Investigation of the anodes of PEM water electrolyzers by operando synchrotron-based photoemission spectroscopy

Viktoriia Saveleva

UNIVERSITÉ DE STRASBOURG

EDSC École Doctorale des Sciences Chimiques

ÉCOLE DOCTORALE SCIENCES CHIMIQUES

Institut de Chimie et Procédés pour l'Energie, l'Environnement et la Santé (ICPEES)

THÈSE présentée par :

Viktoriia SAVELEVA

soutenue le : **29 janvier 2018**

pour obtenir le grade de : **Docteur de l'Université de Strasbourg**

Discipline/ Spécialité : Chimie / Chimie Physique

Etude *in operando* d'anodes d'électrolyseurs de l'eau de type PEM par spectroscopie de photoémission avec le rayonnement synchrotron

Investigation of the anodes of PEM water electrolyzers by *operando* synchrotron-based photoemission spectroscopy

THÈSE dirigée par :

Mme. SAVINOVA Elena	Professeur, Université de Strasbourg
M. ZAFEIRATOS Spyridon	Chargé de recherches, ICPEES

RAPPORTEURS :

M. SCHMIDT Thomas J.	Professeur, Institut Paul Scherrer (CH)
Mme. RUSSELL Andrea E.	Professeur, University of Southampton (UK)

AUTRES MEMBRES DU JURY :

M. KNOP-GERICKE Axel	Chargé de recherches, Fritz Haber Institute (DE)
M. FRIEDRICH Andreas K.	Professeur, German Aerospace Center (DE)

The Obstacle Is the Way

To Philippe

Viktoriia SAVELEVA

Etude *in operando* d'anodes d'électrolyseurs de l'eau de type PEM par spectroscopie de photoémission avec le rayonnement synchrotron

Résumé

Le développement de nouveaux catalyseurs de la réaction de dégagement de l'oxygène (OER) pour les électrolyseurs à membrane échangeuse de protons (PEM) dépend de la compréhension du mécanisme de cette réaction. Cette thèse est consacrée à l'application de la spectroscopie d'émission de photoélectrons induits par rayons X (XPS) et de la spectroscopie de structure près du front d'absorption de rayons X (NEXAFS) *in-situ* sous une pression proche de l'ambiante (NAP) dans le but d'étudier les mécanismes de la réaction d'oxydation de l'eau sur des anodes à base d'iridium et de ruthénium et leurs dégradation dans les conditions de la réaction. Pour les oxydes de ruthénium, nous observons la transition irréversible induite par le potentiel de l'oxyde sous forme anhydre vers l'oxyde hydraté de Ru (IV) par la formation des espèces de Ru avec l'état d'oxydation supérieur à IV. Leurs contributions ne sont pas atténuées par la présence d'Ir, par contre l'Ir stabilise l'oxyde de Ru sous forme anhydre. L'analyse des pics au seuil d'absorption K de l'oxygène (O K edge) obtenus sur les anodes à base d'Ir à différentes tensions démontre la formation d'espèce O^{I-} électrophile comme intermédiaire de la réaction OER, dans une étape électrochimique. Les nanoparticules d'Ir supportées sur dioxyde d'étain dopé à l'antimoine (ATO) sont moins oxydées que les nanoparticules non supportées, ce qui est attribué à l'interaction Ir – ATO. Cette thèse montre les mécanismes différents de la réaction OER pour les anodes à base d'Ir et de Ru impliquant respectivement des transitions anioniques ou cationiques quelle que soit la nature (thermique ou électrochimique) des oxydes.

Mots-clés : réaction de dégagement de l'oxygène (OER) ; électrolyseur de l'eau à base de la membrane échangeuse de protons (PEM) ; oxyde d'iridium ; oxyde de ruthénium ; dioxyde d'étain dopé à l'antimoine (ATO) ; spectroscopie d'émission de photoélectrons induits par rayons X sous une pression proche de l'ambiante (NAP-XPS) ; spectroscopie de structure près du front d'absorption de rayons X (NEXAFS) ; mécanisme de la réaction OER ; dégradation et stabilisation du ruthénium ; Interaction entre le métal et le support ; modélisation des spectres XP

Résumé en anglais

Development of new suitable oxygen evolution reaction (OER) catalysts for proton exchange membrane (PEM) water electrolysis technology depends on the progress in the understanding of the OER mechanism. This thesis is devoted to the application of near-ambient pressure X-ray photoelectron spectroscopy (NAP-XPS) and near edge X-ray absorption fine structure (NEXAFS) techniques for the *in-situ* investigation of the Ir, Ru - based anodes under PEM electrolyzer conditions. For Ru-based systems, we observe the potential-induced irreversible transition of Ru (IV) from an anhydrous to a hydrated form through the formation of high oxidation state species of Ru. The contributions of the latter are not hindered by the presence of Ir, however Ir stabilizes an anhydrous form of Ru oxide. Regarding single Ir-based anodes, the analysis of O K edge spectra under the reaction conditions reveals formation of electrophilic oxygen O^{I-} as an OER intermediate through an electrochemical step. Supported Ir catalysts on antimony-doped tin oxide (ATO) show lower oxidation of Ir nanoparticles in comparison to unsupported ones, which is attributed to the Ir-ATO interaction. This work demonstrates different OER mechanisms on Ir- and Ru-based anodes involving anion and cation red-ox chemistry, correspondingly, regardless the oxide nature (thermal or electrochemical).

Keywords: oxygen evolution reaction (OER); proton exchange membrane (PEM) water electrolysis; iridium oxide; ruthenium oxide; antimony-doped tin oxide (ATO); *in-situ* near-ambient pressure X-ray photoelectron spectroscopy (NAP-XPS); *in-situ* near edge X-ray absorption fine structure (NEXAFS); OER mechanism; degradation and stabilization of ruthenium; metal-support interaction; XP spectra simulation

Acknowledgements

This thesis would not have been possible without continuous support and help of many people. I was very lucky to have you all on this journey.

First of all, I would like to thank the **European project INSIDE** for the financial support during these three years.

My deepest appreciation goes to my PhD supervisors **Elena Savinova** and **Spiros Zafeiratos**. Both of you gave me so much, each in your own way. Whenever I felt discouraged, you were the great example for me. Thank you for believing in me!

I am deeply grateful that **Prof. Thomas Schmidt** from PSI and **Prof. Andrea Russell** from University of Southampton accepted to be the reviewers of my thesis.

I also appreciate the participation of **Prof. Andreas Friedrich** from DLR and **Dr. Axel Knop-Gericke** from FHI in the jury of this thesis.

The synchrotron experiments presented in this thesis would not be possible without help and support of two amazing teams I had an honor to work with at ISISS and TEMPO beamlines of HZB/BESSY II and SOLEIL synchrotrons, correspondingly. Especially I would like to thank **Detre Teschner**, **Michael Hävecker**, **Juan Velasco Vélez**, **Jean-Jacques Gallet** and **Fabrice Bournel**. I am very grateful for your assistance and guidance not only during the measurement sessions but also during our further discussions.

I am very grateful to our partners from the German Aerospace Center, particularly to **Aldo Gago** and **Li Wang**, for providing us the catalysts powders but also for our scientific discussions.

Thanks to **Maria Batuk** and **Joke Hadermann** from University of Antwerp for providing us the necessary microscopic measurements. I am also grateful for the DFT calculations performed by **Travis Jones** from FHI.

I would like to express my gratitude to my colleagues from ICPEES and ICPMS: **Thierry Dintzer**, **Corinne Ulhaq-Bouillet**, **Gwénaëlle Kérangueven**, **Véronique Verkruysse** and **Francine Jacky**.

Special thanks also to **Antoine Bonnefont** from l'Institut de Chimie for being always ready to discuss our results and gave useful advices.

These three years gave me the opportunity to meet extraordinary and hard-working students, some of them have already become Doctors – **Alexandr**, **Sébastien**, **Wen**, **Sylwia** – and the others, who will get their degree pretty soon – **Anna**, **Ivan** and **Basma**.

I want to thank **Sergey Pronkin** and **Nicolas** for all our obstacle races we made together, I have never thought that I would be capable of running 42 km with 100 + obstacles. Special thanks to our HIIT Cronenbourg classes. **Mark**, **François**, **Irene**, without you Tuesday middays would not be so funny.

I also want to thank **CrossFit Strasbourg** for developing not only my physical abilities but also my mental toughness and readiness to unknown and unknowable.

Great thanks to my friends, for their endless encouragement. **Evgeniya**, **Elvira**, **Denis**, **Anton**, **Nasima**, **Selvi**, thank you all for being there for me!

And last but not least. I am very grateful to **my family,** for their understanding and constant support. Special thanks to **Philippe** who became my family here and to whom I dedicated this thesis.

Table of Contents

Acknowledgements 5

List of Abbreviations 12

List of Figures 14

List of Tables 26

General Introduction 28

Chapter 1. Literature Review 30

1.1. Water Electrolysis: Principle and Types 31

1.2. Ir, Ru – based Anodes for PEM Electrolyzers 36

1.2.1. Oxygen Evolution Reaction Mechanisms 43

1.2.2. Metal Support Interaction 55

1.3. Spectroscopies at Near Ambient Pressure conditions 59

1.3.1. X-ray Photoelectron and Near-edge X-ray Absorption Fine Structure Spectroscopies 59

1.3.2. *In-situ* Near Ambient Pressure Spectroscopy 63

1.3.3. Electrochemical Cell for *in-situ* Measurements 67

1.3.3.1. “Dip & Pull” Approach 68

1.3.3.2. Graphene-based Electrochemical Cell 69

1.3.3.3. Electrochemical Cell with Liquid Reservoir 70

1.3.3.4. Three Electrodes Electrochemical Cell 71

1.3.3.5. PEM Fuel Cell Design 72

1.3.3.6. Approach used in this Work 74

1.4. Conclusions of Chapter 1 and Objectives of PhD Thesis 75

Chapter 2. Materials and Experimental Techniques 77

2.1. Materials 78

2.2. *Ex-situ* Material Characterization 80

2.2.1. X-ray Diffraction 80

2.2.2. Scanning Transmission Electron Microscopy and Energy-Dispersive X-ray Spectroscopy 80
2.2.3. Scanning Electron Microscopy 81
2.2.4. X-ray Photoelectron Spectroscopy 82
2.2.5. Characterization in Liquid Electrolyte 83
2.3. Laboratory Set-up for Preliminary Studies 84
2.3.1. Set-up Description 84
2.3.2. Electrochemical Impedance Spectroscopy 85
2.3.3. Nafion or Aquivion? Effect of Humidity 86
2.3.4. Influence of Humidity on the MEA Performance 89
2.4. *In-situ* Synchrotron-based Spectroscopic Studies 92
2.4.1. *In-situ* Near-Ambient Pressure Spectroscopy Set-ups 92
2.4.1.1. HZB/BESSY II – ISISS Beamline 92
2.4.1.2. SOLEIL/UPMC – TEMPO Beamline 92
2.4.2. Analyzed Samples 93
2.4.3. Cyclic Voltammetry and Dynamic Hydrogen Electrode 94
2.4.4. Chronoamperometry 95
2.4.5. Experimental Protocol 96
2.4.5.1. Radiation Damage 96
2.4.5.2. Spectroscopic Measurements 97
2.4.6 Data Processing 98
2.4.6.1. Quantitative Analysis of XPS Results 98
2.3.6.2. Ru3d XP Spectra: Fitting Procedure 99
2.3.6.3. Ir4f XP spectra: Fitting Procedure 103
2.3.6.4. Core-level Spectra Simulation using SESSA Software 108
Chapter 3. Ruthenium-based Anodes for PEM Electrolyzers 113
3.1. Introduction 114
3.2. Material Characterization 116

3.2.1. XRD Analysis....116
3.2.2. Microscopy....117
3.2.3. Electrochemical Tests in Liquid Electrolyte....118
3.2.4. Electrochemical Tests under Gas-phase Water....120
3.3. RuO_2 Anode: Surface Composition....124
3.4. Ru@RuO_x Anode: Surface Composition....127
3.5. *In-situ* NEXAFS Measurements....135
3.6. OER and Degradation Mechanisms of Ru-based Anodes....141
3.7. Conclusions of Chapter 3....146
Chapter 4. Stabilization Mechanism in Bimetallic Iridium-Ruthenium Anodes....147
4.1. Introduction....148
4.2. Material Characterization....150
4.2.1. XRD Analysis....150
4.2.2. TEM / EDX Analysis....151
4.2.3. Electrochemical Characterization in Liquid Electrolyte....154
4.2.4. NAP-XPS measurements: Experimental Protocol and Electrochemical Tests....156
4.3. *In-situ* NAP-XPS studies....159
4.3.1. Evolution of Ru active sites....159
4.3.1.1. Surface vs Sub-surface Composition: Tuning of Photon Energy....162
4.3.1.2. Ru3d XP Spectra: Time Effect....163
4.3.2. Role of Iridium Sites in the OER....164
4.4. Stabilization Mechanism in Bimetallic Anode....168
4.5. Conclusions of Chapter 4....172
Chapter 5. Comparative study of Ir-based anodes under the OER conditions: thermal vs electrochemical oxide....173
5.1. Introduction....174
5.2. Materials Characterization....176

5.2.1. XRD Analysis....176
5.2.2. Transmission Electron Microscopy....177
5.2.3. Electrochemical Characterization in Liquid Electrolyte....178
5.2.4. Electrochemical Analysis in NAP-XPS chamber and Experimental Protocol....181
5.3. *Operando* Spectroscopic Studies of Ir@IrO_x and IrO_2 – based Anodes....185
5.3.1. Oxygen Sites: Absorption and Photoemission Spectroscopies....185
5.3.2. Potential-induced Changes of Ir sites. Ir4f XP spectra Analysis....190
5.4. Nature of OER Active Sites on Ir-based Anodes. Discussion....195
5.5. Conclusions of Chapter 5....200
Chapter 6. Supported Iridium-based Electrocatalyst: SMSI studies....201
6.1. Introduction....202
6.2. Materials and their Characterization....203
6.3. Improvement of the Conductivity of ATO-based catalytic layers....205
6.4. *Operando* Photoemission Studies....207
6.4.1. Electrochemical Response in NAP-XPS Chamber....207
6.4.2. Sn3d XP Spectra Analysis....208
6.4.3. Evolution of Ir/Sn Ratio....211
6.4.4. Influence of the Electrode Potential on the Oxidation State of Iridium....213
6.5. Role of ATO Support in Anode Performance....218
6.6. Conclusions of Chapter 6....227
General Conclusions and Outlook....228
Appendix....231
A.1. XRD Results of metallic Ru Nanoparticles....231
A.2. TEM Analysis: RuO_2 powder....234
A.3. RuO_2 Thickness Calculation: Results....235
A.4. Evolution of O1s XP spectra under polarization. Ru@RuO_x anode....236
A.5. Reference Sample Analysis : RuO_2 and RuO_2 xH_2O....237

A.6. XRD Patterns of Iridium-based compounds....239
A.7. Potential Dependence of the $Ir_{0.7}Ru_{0.3}O_2$ Anode Surface Composition. Surface vs Subsurface....240
A.8. DFT Calculations....241
A.9. O K edge Spectra Background....243
A.10. Ir-based Anodes. O1s XP spectra....244
A.11. Ir-based Reference Samples....245
A.12. STEM/EDX Mapping. Ir/ATO, Post-mortem Analysis....247
A.13. ATO-based anode, Electrochemical Characterization in NAP-XPS chamber....248
A.14. SESSA Simulation: Results....249
A.15. Ir4f XP spectra recorded on Ir/ATO sample with low conductivity....252
A.16. C1s XP spectra recorded on Ir/ATO sample....253
A.17. Sn/Sb Atomic Ratio Evolution....254
References....255
Résumé détaillé....274

List of Abbreviations

AEM	Anion-Exchange Mmembrane
AEY	Auger Electron Yield
AIROF	Anodically Formed Iridium Oxide Film
AP	As Prepared
ATO	Antimony-Doped Tin Oxide
BE	Binding Energy
CA	Chronoamperogram
CCM	Catalyst Coated Membrane
CE	Counter Electrode
CV	Cyclic Voltammogram
DFT	Density Functional Theory
DHE	Dynamic Hydrogen Electrode
EDX	Energy-Dispersive X-Ray Spectroscopy
EELS	Electron Energy Loss Spectroscopy
EIS	Electrochemical Impedance Spectroscopy
EW	Equivalent Weight
FC	Fuel Cell
FWHM	Full Width At Half Maximum
FY	Fluorescence-Yield
GC	Glassy Carbon
HAADF	High Angle Annular Dark Field
HER	Hydrogen Evolution Reaction
HT	High Temperature
ICDD	International Centre for Diffraction Data
ICP-MS	Inductively Coupled Plasma Mass Spectrometer
IMFP	Inelastic Mean Free Path
KE	Kinetic Energy
LSC	Long-Side-Chain
MEA	Membrane-Electrode Assembly
NAP	Near Ambient Pressure
OCV	Open Circuit Voltage

OER	Oxygen Evolution Reaction
PA	Phosphoric Acid
PE	Pass Energy
PEM	Proton Exchange Membrane
PFSA	Perfluorosulfonic Acid
PTFE	Polytetrafluoroethylene
QMS	Quadrupole Mass Spectrometer
RDE	Rotating Disc Electrode
RDS	Rate-Determining Step
RE	Reference Electrode
RH	Relative Humidity
RHE	Reversible Hydrogen Electrode
RRDE	Rotating Ring-Disk Electrode
SEM	Scanning Electron Microscopy
SERS	Surface Enhanced Raman Spectroscopy
SMSI	Strong Metal-Support Interaction
SOEC	Solid Oxide Electrolysis Cell
SSC	Short-Side-Chain
STEM	Scanning Transmission Electron Microscopy
TEY	Total Electron Yield
UHV	Ultra High Vacuum
UPS	Ultraviolet Photoelectron Spectroscopy
VB	Valence Band
WE	Working Electrode
XANES	X-Ray Absorption Near Edge Structure
XAS	X-Ray Absorption Spectroscopy
XPS	X-Ray Photoelectron Spectroscopy
XRD	X-Ray Powder Diffraction
YSZ	Yttria-Stabilized Zirconia

List of Figures

Figure 1. Energy need for the electrolysis reaction as a function of temperature.

Figure 2. Scheme of HT solid oxide electrolysis cell. Taken from[6].

Figure 3. Schematic of the operating principle of an alkaline (A), PEM (B) and AEM (C) water electrolysis cells.

Figure 4.Potential-pH diagram for iridium-(A) and ruthenium-water (B) systems at 25°C. Lines x and y represent the domain of thermodynamic stability of water (25°C, 1 atmosphere). Other lines correspond to the following reactions: $Ir^{+++} + 4H_2O = IrO_4^- + 8H^+ + 3e^-$ (11); $Ir + 2H_2O = IrO_2 + 4H^+ + 4e^-$ (14); $IrO_2 + 2H_2O = IrO_4^{--} + 4H^+ + 2e^-$ (19); $Ru + 3H_2O = Ru(OH)_3 + 3H^+ + 3e^-$ (31); $Ru(OH)_3 = RuO_2 + H_2O + H^+ + e^-$ (32); $RuO_2 + 2H_2O = RuO_4 + 4H^+ + 4e^-$ (33); $RuO_4 + H_2O = HRuO_5^- + H^+$ (34); $RuO_4^- = RuO_4 + e^-$ (35); $RuO_2 + 2H_2O = RuO_4^{--} + 4H^+ + 2e^-$ (36); $RuO_2 + 2H_2O = RuO_4^- + 4H^+ + 3e^-$ (37). Taken from[21].

Figure 5. Amount of dissolved metal from $Ru@RuO_x$, $Ir@IrO_x$, RuO_2, IrO_2 thin films anodes estimated during the transition from 1.2 V vs RHE to the potential corresponded to the current density of 5 mA cm^{-2}. The measurements were performed in 0.1 M H_2SO_4. Taken from[24].

Figure 6. Current-potential curves recorded on $Ru@RuO_x$, $Ir@IrO_x$, RuO_2 and IrO_2 anodes in 0.1 M H_2SO_4 (red) and 0.05 M NaOH (black). Scan rate 10 mV s^{-1}. The potentials were not ohmic drop corrected. Taken from[24].

Figure 7. CVs recorded on Ir electrode (Ir wire) in 0.05 M H_2SO_4 with potential cycling between 0 and 1.5 V (vs RHE) at sweep rate 100 mV s^{-1}. Cycle numbers are provided in the plot. Figure is taken from[40].

Figure 8. Cyclic voltammograms of IrO_2 (oxidized at 500 ^{0}C, shown as a solid line) and AIROF anodes (dashed line) obtained in sulfuric acid (pH = 0.4) and sweep rate 200 and 250 mV s^{-1}, respectively. Taken from[50].

Figure 9. Cyclic voltammetric curves recorded on RuO_2 (A), $Ir_{0.5}Ru_{0.5}O_2$ (B) and IrO_2 (C) anodes at 20 mV s^{-1} in 1 M $HClO_4$ solution. Potential range: [-0.2; 1.4] vs RHE. The current density scale (mA cm^{-2}) is shown for each plot. Taken from[42].

Figure 10. Volcano-shaped curve for the OER activity of the oxides as a function of the enthalpy of their oxidation transition. Alkaline solutions are marked as hollow circles, whereas the acid as black circles. Taken from[79].

Figure 11. Model for the oxygen evolution and corrosion on Ru-based (left-hand panel) and Ir-based (right-hand panel) electrodes proposed by Koetz et al.[22,56]

Figure 12. Ir4f XP spectra recorded on IrO_2 anode under OCV (left-hand panel) and 1.75 V (right-hand panel). The fitting was done using two doublets: Ir (IV) – green and Ir (V) – violet. Photon energy 390 eV. Taken from[101].

Figure 13. Oxidation-reduction cycle of Ir sites derived from the XANES spectra

Figure 14. Low excitation energy region of O K edge recorded on sputtered IrO_x anode under OCV (bottom), 2 V (middle) and 2.5 V (top) polarization conditions. Taken from[108].

Figure 15. Galvanostatic stability test of IrO_x/carbon (black), IrO_x/Com. ATO (red) and IrO_x/ATO (blue) anodes performed in N_2-purged 0.05 M H_2SO_4 at 1 mA cm^{-2} current density and rotation rate of 1600 rpm. t = 25 °C. The inlet shows the magnification over the region 0 – 9 h. Commercial available ATO is marked as Com. ATO. Taken from[75].

Figure 16. In-situ STEM images of Rh/TiO_2 demonstrating the formation of crystalline Ti^{3+} - based (a) and amorphous Ti^{3+}/Ti^{4+}- mixed layer. Taken from[137].

Figure 17. Survey spectrum recorded on IrO_2 catalyst powder under UHV (ICPEES). Photon energy 1486.6 eV, pass energy (PE) = 90 eV.

Figure 18. Scheme of the processes occurring during photoemission and absorption spectroscopies. Fluorescence (photon in/photon out) and electron (photon in/electron out) detection mode are also shown in the right-hand part of the scheme. The scheme was done based on the one shown in[144].

Figure 19. Energy level diagram and schematic photoemission spectra at different photon energies for a sample containing atoms with two core levels A and B and a valence band (VB). Taken from [147].

Figure 20. Schemes of differential pumping systems used in NAP-XPS. Panel A represents a standard analyzer lens with a set of pumping apertures in front of it, while Panel B shows the principle used at ISISS beamline of BESSY II synchrotron with a differentially-pumped lens system. Taken from[155].

Figure 21. Survey spectrum recorded on IrO_2 anode under 3 mbar water vapor and open circuit voltage. Photon energy 820 eV.

Figure 22. Inelastic electron scattering cross-section of the water molecule as a function of electron kinetic energy in the energy range relevant for XPS. Figure was taken from Bluhm[154], where the symbols correspond to the data obtained by others. The total electron scattering cross-section (inelastic, elastic and rotational) is shown by (▰).

Figure 23. Left-hand panel: Schematic of three-electrode electrochemistry set-up in the NAP-XPS chamber.Middle panel: Pt4f and O1s XP spectra of the partially removed electrodes under applied potential and under water vapor (without polarization). Right-hand panel: image of the set-up. Figure was taken from[162].

Figure 24. The scheme of the gas cell (A) and its cross-section (B) used in the AP-XPS set-up. Panels C, D: sketch of the graphene-based membrane. Taken from[174].

Figure 25. The electrochemical cell for in-situ spectroscopic measurements with liquid reservoir. The porosity of the Pt film is shown on the right. Taken from[100].

Figure 26. Left panel: two-electrode electrochemical cell for in-situ NAP-XPS measurements with constant water flow. Right panel: three-electrode cell with an electrolyte. Taken from[108].

Figure 27. Scheme of a model MEA used for in-situ NAP-XPS measurements in[176].

Figure 28. Scheme of the PEM fuel cell set-up for the in-situ NAP-XPS studies. Taken from[179].

Figure 29. Panel A. Pt4f XP spectra recorded on Pt-based MEA (with a PA-imbibed membrane) under 0.11 mbar H_2O/0.16 mbar O_2 at 150°C and 0.8 V vs OCV. The fitting: Pt metal (black); disconnected Pt metal (gray); Pt covered by adsorbed O/OH (red); PtO (blue) and PtO_2 (green). Panel B. SEM image of Pt working electrode where a white circle shows the disconnected particles. Taken from[177].

Figure 30. The BEs of the $Pt4f_{7/2}$ main peak (black), O1s (green), C1s (red), P2p (blue), $Pt4f_{7/2}$ "disconnected" (gray) peaks as a function of the applied voltage. The spectra were collected on Pt-based MEA (with a PA-imbibed membrane). Taken from[177].

Figure 31. Typical SEM images of the WE side of the MEA acquired at different magnifications showing the uniformity and the integrity of the $Ir_{0.7}Ru_{0.3}O_2$ layer.

Figure 32. Left panel: Laboratory set-up for the electrochemical tests of the MEAs under the gas-phase conditions. Right panel: The sample holder containing the MEA.

Figure 33. Nyquist plot obtained on Ir@IrO_x anode under 23.5 mbar water vapor and different potentials shown in the inset. The ohmic resistance was defined as the intercept of the real axis and marked in the plot.

Figure 34. Polymer structure for long-side chain Nafion (left) and short-side-chain Aquivion (right) membranes[186].

Figure 35. Cyclic voltammograms recorded on Pt/C electrode of Nafion-based (black) and Aquivion-based (red) MEA. The Pt loading was 0.1 mg cm^{-2}. The curves were recorded under 3 mbar water vapor and at scan rate 20 mV s^{-1}.

Figure 36. The cyclic voltammograms recorded on Ir@IrO_x electrode under different water vapor pressures: 23.5 mbar (red), 16 mbar (black), 9 mbar (green), 4.5 mbar (blue), 3 mbar (magenta). Panel B represents the magnified Panel A at the potential region [1.3; 1.6] vs DHE. Scan rate 5 mV s^{-1}. The loading 0.1 mg cm^2.

Figure 37. Sketch of the holder used to fix the MEA in the NAP-XPS chamber.

Figure 38. Cyclic voltammograms of the $Ir_{0.7}Ru_{0.3}O_2$ electrode obtained in a NAP-XPS chamber at different ambient conditions: 3 mbar H_2O (black curve); 3 mbar H_2O and 0.5 mbar H_2 (red curve) at a scan rate 5 mV s^{-1}. Catalyst loading 0.1 mg cm^{-2}.

Figure 39. Chronoamperograms obtained in the NAP-XPS chamber at BESSY II synchrotron on $Ru@RuO_x$ anode under 3 mbar water vapor and different polarization conditions: 0.75 V (red); 1.00 V (orange); 1.34 V (yellow); 1.39 V (green); 1.41 V (blue). Solid lines represent the forward scan, the dashed – the backward. The potential is ohmic drop corrected. Temperature 25 °C. Catalyst loading 0.1 mg cm^{-2}.

Figure 40. Potential dependence of Ir/S (black) and Ir/F (red) atomic ratio obtained on IrO_2 anode-based MEA under 3 mbar water vapor. Three different regions are shown in the plot: before the OER onset (marked as forward scan), the OER region and backward scan. The kinetic energy of the emitted electrons was equal to 530 eV.

Figure 41. Incident photon flux vs kinetic energy recorded at ISISS (A) and TEMPO (B) beamlines of BESSY II and SOLEIL synchrotron correspondingly.

Figure 42. C1sRu3d XP spectra for RuO_2 anode in 3 mbar H_2O ambient at E – iR = 1.8 V and photon energy 820 eV. Peak fitting was done using four Ru components: RuO_2 and its satellite (black); $Ru(OH)_x$ (red); Ru(VI) (green); $RuO_{4(s)}$ (blue); and five singlets of carbon (magenta), including the adventitious carbon and the membrane contribution. The experimental data are presented by the black cycles and a summary fitting curve - by a grey line.

Figure 43. Ir4f XP spectra recorded on IrO_2 (A) $Ir@IrO_x$ (B) anodes under 3 mbar water vapor and E – iR = 0 V vs DHE. Panel A: the fitting was done using a main peak of rutile-type IrO_2 (black) and its 2 satellites (red and green); panel B: three different components were distinguished: metallic Ir – grey; Ir (III) – magenta; Ir (IV) – light blue. The experimental data are shown by the black cycles whereas a summary fitting curve by a grey line. Photon energy 595 eV.

Figure 44. Sketch of the models used for photoemission spectra simulation with the SESSA software. Panel A: “layered sphere” morphology, metallic ruthenium particles (d = 2 nm) covered by IrO_2 shell of various thickness.

Figure 45. Sketch of the models used for photoemission spectra simulation with the SESSA software. Panel A: “layered sphere” morphology, metallic iridium particles (d = 2 nm) covered by IrO_2 shell of various thickness, substrate - carbon; Panel B: “spheres” and “layered spheres” morphologies on SnO_2 substrate, in the latter case iridium nanoparticles are covered by tin oxide shell; Panel C: “islands” morphology, varied particles shape with constant volume; Panel D: “spheres” morphology, iridium nanoparticles on tin oxide substrate.

Figure 46. XRD patterns of RuO_2 powder. Pattern markers are provided at the bottom of the image and correspond to: RuO_2 oxide – rutile - 03-065-2824 (black); metallic hcp Ru - 01-089-3942 (red).

Figure 47. STEM images of Ru (A, B) and RuO_2 (C, D) catalysts before (as prepared) (A,C) and after (B, D) in-situ NAP-XPS measurements under the OER conditions.

Figure 48. Current-potential characteristics of the $Ru@RuO_x$ (A) and RuO_2 (B) anodes measured in N_2-saturated 0.05 M H_2SO_4 at 25 °C with a scan rate of 5 mV s^{-1}. Catalysts loading 60 μg cm^{-2}.

Figure 49. Evolution of the mass activity of $Ru@RuO_x$ (black) and RuO_2 (red) electrodes measured at 1.48 V vs. RHE. It should be noted, that due to the extremely high currents obtained on $Ru@RuO_x$ anode during the first cycle the corresponding mass activity is not shown in the plot. Catalysts loading 60 μg cm^{-2}.

Figure 50. CVs obtained on $Ru@RuO_x$ (A) and RuO_2 (B) anodes in the NAP-XPS chamber under 3 mbar of water vapor and 50 mV s^{-1} and 100 mV s^{-1}, respectively. The insert shows a zoomed area of the potential region [0.1; 1.6]. The potential values are Ohmic drop corrected. Catalyst loading – 0.1 mg cm^{-2}.

Figure 51. Chronoamperograms obtained in the NAP-XPS chamber at BESSY II synchrotron on RuO_2 anode under 3 mbar water vapor during the 1st (A) and 2nd OER cycle and different polarization conditions: 0.0 V (red); 1.0 V (orange); 1.5 V (yellow); 1.8 V (green). Solid lines represent the forward scan, the dashed – the backward.

Figure 52. Chronoamperograms obtained in the NAP-XPS chamber at BESSY II synchrotron on $Ru@RuO_x$ anode under 3 mbar water vapor during O K edge (A), C1sRu3d (B) and O1s (C) recording and different polarization conditions: 0.75 V (red); 1.00 V (orange); 1.34 V (yellow); 1.39 V (green); 1.41 V (blue). Solid lines represent the forward scan, the dashed – the backward. Catalyst loading – 0.1 mg cm^{-2}. The potential is ohmic drop corrected. Temperature 25°C. Panel A is duplicating Figure 39.

Figure 53. MS data for the m/z = 32 acquired during the measurements for RuO_2 electrode. The Ohmic drop-corrected potential values are provided at the top of the figure. The OER region is green-filled. The OER onset potential correlates with the MS data on the oxygen and the hydrogen (from the CE - not shown) evolution.

Figure 54. Panel A: fitted C1s-Ru3d XP spectra of RuO_2 electrode at 1.5 V. Experimental XPS data are shown as black cycles, fitted spectrum – as a grey line. For the sake of clarity carbon peaks are not shown. Panel B: Influence of the applied potential on the surface composition of RuO_2 electrode (1st OER cycle). Only forward scan is shown. Measurements were performed in 3 mbar H_2O ambient at a photon energy of 820 eV. The values of potential are iR corrected and are

given on the dynamic hydrogen electrode (DHE) scale. Color codes: RuO_2 (black); $Ru(OH)_x$ (red); Ru(VI) (green); Ru (VIII) abbreviated as $RuO_{4(s)}$ in the text (blue).

Figure 55. Influence of the applied potential on the surface composition of RuO_2 electrode during the backward scan of the first potential cycle (Panel A) and during the second potential cycle (Panel B) under 3 mbar water vapor ambient. Color codes: RuO_2 (black), hydrated RuO_2 (red), Ru (VI) (green), and Ru (VIII) (blue). In case of the 2nd cycle, the potential is increased in a stepwise manner from 0 to 1.8 V and then stepped back to 0 V (marked as 0.0 back). Photon energy 820 eV.

Figure 56. Fitted C1s-Ru3d XP spectra of $Ru@RuO_x$ electrode at 0.75 V before the spectroscopic measurements (Panel A), after the 1st OER cycle – O K edge recording (Panel B), after the 2nd OER cycle – Ru3d XP spectra (Panel C) and after the 3rd – O1s XP spectra (Panel D). Experimental XPS data are shown as black cycles, fitted spectrum – as a grey line. Color code: metallic Ru (grey), RuO_2 (black), hydrated RuO_2 (red), Ru (VI) (green), Ru (VIII) (blue) and carbon species (magenta). Photon energy 820 eV.

Figure 57. O1s XP spectra recorded on $Ru@RuO_x$ anode under 3 mbar of water vapor and 0.75 V vs DHE before the spectroscopic measurements (A); after the 1st OER cycle, O K edge measurements (B); after Ru3d recording, 2nd OER cycle (C) and after the last OER cycle during O1s analysis (D). The fitting was done within three peaks: at 530 eV (red); 531.3 eV (green) and 532.7 eV (blue). Photon energy 1066 eV.

Figure 58. Influence of the applied potential on the surface composition of $Ru@RuO_x$ electrode during the forward (Panel A) and the backward (Panel B) scans of the 2nd OER cycle under 3 mbar water vapor ambient. Color codes: RuO_2 (black), hydrated RuO_2 (red), Ru (VI) (green), and Ru (VIII) (blue). Photon energy 820 eV.

Figure 59. Influence of the potential cycling on the surface composition of $Ru@RuO_x$ electrode obtained based on the corresponding Ru3d XP spectra recorded at 0.75 V (vs DHE) under 3 mbar water vapor ambient. Color codes: RuO_2 (black), hydrated RuO_2 (red), Ru (VI) (green), and Ru (VIII) (blue). The XP spectra were recorded at photon energy of 820 eV.

Figure 60. Potential-induced evolution of O1s components recorded on $Ru@RuO_x$ electrode under 3 mbar water vapor: O_{lat} (red), OH (green), H_2O (blue). Panel A represents the changes depending on the OER cycle under 0.75 V vs DHE, whereas Panel B – during one OER cycle under different polarization conditions.

Figure 61. Low excitation energy region of O K edges (TEY) measured on $Ru@RuO_x$ anode under 3 mbar of water vapor and different polarization: 0.75 V (red); 1.0 V (orange); 1.34 V (yellow); 1.41 V (green); 1.43 V (blue). Two additional spectra were recorded after the 1st

(dashed line) and the 3rd OER cycles (dotted line) at 0.75 V. The potential values are Ohmic drop corrected.

Figure 62. Low excitation energy region of O K edges (TEY) measured on Ru@RuO_x anode under 3 mbar of water vapor and different polarization: 0.75 V (A); 1.0 V (B); 1.34 V (C); 1.43 V (D); back 0.75 V after the 1st OER cycle (E) and after the 3rd OER cycle (F). The fitting was done within three peaks: at 529.2 eV (red); 530 eV (blue) and 531.3 eV (green).

Figure 63. Low excitation energy region of O K edges (TEY) measured on RuO_2 anode under 3 mbar of water vapor and open circuit potential.

Figure 64. Potential-induced evolution of O K edge components located at 529.2 eV (black), 530 eV (red), 531.3 eV (blue). The O K edge spectra were collected at Ru@RuO_x anode under 3 mbar water vapor under different polarization during the 1st OER cycle.

Figure 65. XRD patterns of RuO_2 (bottom) and $Ir_{0.7}Ru_{0.3}O_2$ (top) powders. The asterisks correspond to the following reference ICDD patterns: RuO_2 oxide PDF- 03-065-2824 (black); metallic Ru PDF - 01-089-3942 (blue); IrO_2 oxide – PDF 01-088-0288 (green). XRD pattern of RuO_2 has already been shown in Figure 46.

Figure 66.TEM images of pristine RuO_2 (A,B) and $Ir_{0.7}Ru_{0.3}O_2$ (C,D) samples under different magnifications. Panels A, B reproduce Figure A 2.

Figure 67. STEM images of RuO_2 (A,B) and $Ir_{0.7}Ru_{0.3}O_2$ (C,D) electrodes before (A,C) and after (B,D) the OER studies performed in the NAP-XPS chamber. Note that panels A and B were already shown in Figure 47.

Figure 68. STEM image of the $Ir_{0.7}Ru_{0.3}O_2$ catalyst after the NAP-XPS measurements. Atomic percentage of Ru and Ir in the marked regions as determined by the local EDX analysis is indicated in the figure as well. Similar Ir/Ru distributions were observed in the pristine samples (not shown).

Figure 69. Panel A: CVs (2nd cycle out of 10) for RuO_2 (red) and $Ir_{0.7}Ru_{0.3}O_2$ (black) samples measured in N_2-saturated 0.05 M H_2SO_4 at 25°C at the scan rate of 20 mV s^{-1}. Panel B: Tafel plots constructed from the second current-potential scans. Catalyst loading – 60 μg cm^{-2}. The curve obtained on RuO_2 was previously shown in Figure 50. The data were provided by L. Wang[181].

Figure 70. Current-potential characteristics of the RuO_2 (A), and the $Ir_{0.7}Ru_{0.3}O_2$ (B) anode measured in N_2-saturated 0.05 M H_2SO_4 at 25 °C with a scan rate of 5 mV s^{-1}. Catalyst loading – 60 μg cm^{-2}. The results obtained on monometallic ruthenium oxide were shown in Chapter 3. The data were provided by L. Wang[181].

Figure 71. CVs obtained on $Ir_{0.7}Ru_{0.3}O_2$ (black) and RuO_2 (red) anodes in the NAP-XPS chamber under 3 mbar of water vapor. Scan rate 100 mV s^{-1}. The potential values are Ohmic drop

corrected. Catalyst loading – 0.1 mg cm^{-2}. The electrode area – 0.9 cm^2. The curve obtained on RuO_2 anode was taken from Figure 50.

Figure 72. Chronoamperograms obtained in the NAP-XPS chamber at BESSY II synchrotron on $Ir_{0.7}Ru_{0.3}O_2$ anode under 3 mbar water vapor and different polarization conditions: 0.0 V (red); 1.0 V (orange); 1.5 V (yellow); 1.8 V (green). Solid lines represent the forward scan, the dashed – the backward. The potentials are ohmic drop corrected. Temperature 25°C. Catalyst loading – 0.1 mg cm^{-2}.

Figure 73. MS data acquired during the measurements for (A) RuO_2 and (B) $Ir_{0.7}Ru_{0.3}O_2$ electrodes. The Ohmic drop-corrected potential values are provided at the top of the figure. The OER region is green-filled. The OER onset potential correlates with the MS data on the oxygen and the hydrogen (from the CE - not shown) evolution.

Figure 74. Upper panels: fitted C1s-Ru3d XP spectra of RuO_2 (A) and $Ir_{0.7}Ru_{0.3}O_2$ (B) electrodes at 1.5V. Experimental XPS data are shown as black cycles, fitted spectrum – as a grey line. For the sake of clarity carbon peaks are not shown. Bottom panels: Influence of the applied potential on the surface composition of RuO_2 (C) and $Ir_{0.7}Ru_{0.3}O_2$ (D) electrodes. Only forward scans are shown. Measurements were performed in 3 mbar H_2O ambient at a photon energy of 820 eV. The values of potential are iR corrected and are given on the dynamic hydrogen electrode (DHE) scale. Color codes: RuO_2 (black); $Ru(OH)_x$ (red); Ru(VI); Ru (VIII) or $RuO_{4(s)}$ (blue). Note that Panels A and C was already shown in Figure 54.

Figure 75. Influence of the applied potential on the surface composition of RuO_2 (A) and $Ir_{0.7}Ru_{0.3}O_2$ (B) electrodes in 3 mbar H_2O ambient in the backward scans. Color codes: RuO_2 (black), hydrated RuO_2 (red), Ru (VI) (green), and Ru (VIII) (blue). Photon energy – 820 eV.

Figure 76. Ru3d XP spectra of $Ir_{0.7}Ru_{0.3}O_2$ electrode in 3 mbar H_2O ambient under 1.8 V (A,B) and 2.5 V (C,D) at different photon energies: 820 eV (A,C) and 1300 eV (B,D). Experimental XPS data are shown as black cycles, fitted spectrum – as a grey line. For the sake of clarity carbon peaks are not shown. Color codes: RuO_2 (black); $Ru(OH)_x$ (red); Ru(VI) (green); Ru (VIII) (blue).

Figure 77. Ru3d XP spectra recorded on $Ir_{0.7}Ru_{0.3}O_2$ electrode in 3 mbar H_2O ambient 2 min (A,C) and ca. 50 min (B, D) after the application of potential of 1.0 V (A, B) and 1.5 V (C, D). Experimental XPS data are shown as black cycles, fitted spectrum – as a grey line. Only $Ru3d_{3/2}$ peak of the doublets are shown. Color codes: RuO_2 (black); $Ru(OH)_x$ (red); Ru(VI) (green); Ru (VIII) (blue), carbon (magenta). Photon energy 820 eV.

Figure 78. Ir4f XP spectra obtained on $Ir_{0.7}Ru_{0.3}O_2$ electrode in 3 mbar H_2O ambient at E – iR = 0 V (A, B); 1.5 V (C, D) and 1.8 V (E, F) and two photon energies 595 eV (A, C, E) and 1080

eV (B, D, F). Peak fitting was done using three doublets: main peak of rutile-type IrO_2 (black) and 2 satellites (red and green).

Figure 79. The influence of the applied potential on the Ir/Ru atomic ratio for the $Ir_{0.7}Ru_{0.3}O_2$ catalyst. Forward scan – solid line, backward scan – dashed line. The OER region is marked. The spectra were collected at kinetic energy of 530 eV.

Figure 80. XRD patterns of catalyst powders: metallic Ir (red), thermal oxide IrO_2 (black). The ICDD data for rutile IrO_2 (black, 01-088-0288), face-centered cubic Ir (red, 00-046-1044), $IrCl_3$ (blue, 01-073-0745) are marked in the plot.

Figure 81. STEM images of pristine metallic Ir particles (A), Ir@IrO_x (B) and IrO_2 (C, D) catalyst before (A,C) and after (B, D) in-situ spectroscopic synchrotron measurements.

Figure 82. Cyclic voltammograms obtained in N_2-saturated 0.05 M H_2SO_4 on Ir@IrO_x (A) and IrO_2 (B) anode at the sweep rate of 20 mV s^{-1} under 25 °C. Two cycles are shown for each of the electrodes: the 2^{nd} (dotted line) and the 10^{th} (solid line). Catalyst loading on the GC surface is 60 μg cm^{-2}. Current density is normalized to the geometric surface area of the electrode.

Figure 83. Panel A: The comparison of the 10^{th} CVs recorded on Ir@IrO_x (black) and IrO_2 (red) anodes. The curves were shown in Figure 82. Panel B: OER activity after electrochemically activation measured on Ir@IrO_x anode (black) and IrO_2 (red). The measurements were conducted in N_2-saturated 0.05 M H_2SO_4 with a sweep rate of 5 mV s^{-1}; Catalyst loading on a glassy carbon electrode, 60 μg cm^{-2}; rotating speed, 1600 rpm; measurements temperature, 25 °C.

Figure 84. Tafel slope comparison of Ir@IrO_x (black) and IrO_2 (red) obtained in a three-electrode set-up in N_2-saturated 0.05 M H_2SO_4 at 25 °C. The rotating rate 1600 rpm, scanning rate 5 mV s^{-1}. Catalyst loading on glassy carbon electrode, 60 μg cm^{-2}.

Figure 85. The cyclic voltammograms obtained in the NAP-XPS chamber under 3 mbar water vapor on Ir@IrO_x (A) and IrO_2 (B) anodes. The inset of Panel B represents a magnified voltammogram of the IrO_2 anode. Scan rate 50 mV s^{-1}.

Figure 86. CAs recorded on Ir@IrO_x anode under 3 mbar water vapor and the following potentials: 0 V (red); 0.3 V (orange); 1.0 V (yellow); 1.1 V (green); 1.2 V (cyan); 1.29 V (blue); 1.38 V (violet); 1.43 V (black); 1.48 V (grey). Panel A represents the curves recorded during O K edge measurements, while panel B – during Ir4f spectra collecting. The potentials are iR corrected. Solid lines correspond to the forward scan, dashed lines – to the backward.

Figure 87. CAs recorded on IrO_2 anode under 3 mbar water vapor and the following potentials: 0 V (red); 0.25 V (orange); 0.7 V (yellow); 1.3 V (green); 1.39 V (cyan); 1.48 V (blue); 1.53 V (violet); 1.56 V (black); 1.58 V (grey). Panel A represents the curves recorded during O K edge measurements, while panel B – during Ir4f spectra collecting. The potentials are iR corrected. Solid lines correspond to the forward scan, dashed lines – to the backward.

Figure 88. Low excitation energy of O K edges (TEY) of IrO_2 anode under 3 mbar water vapor and different polarization conditions: 0 V (A); 0.25 V (B); 0.7 V (C); 1.3 V (D); 1.4 V (E); 1.45 V (F); 1.5 V (G): 1.6 V (H). Color code: O^{I-} (magenta), gas-phase O_2 / OH (blue), experimental data (black circles), fitted spectrum (grey).

Figure 89. Low excitation energy of O K edges (TEY) of Ir@IrO_x anode under 3 mbar water vapor and different polarization conditions: 0 V (A); 0.5 V (B); 1.0 V (C); 1.1 V (D); 1.29 V (E); 1.38 V (F); 1.43 V (G); 1.48 V (H); 0 V backward (I). Color code: O^{I-} (magenta), gas-phase O_2 / OH (blue), OH groups at 529.4eV (green) experimental data (black circles), fitted spectrum (grey).

Figure 90. Current values (black) and O^{I-} surface species content (red) versus applied potential for Ir@IrO_x (A) and IrO_2 (B) anodes.

Figure 91. Dependence of the current values recorded on Ir@IrO_x (red) and IrO_2 (black) anodes on the quantity of the formed O^{I-} species.

Figure 92. O1s XP spectra of Ir@IrO_x (C) and IrO_2 (D) anodes under 3 mbar water vapor and 0 V. Color codes: lattice oxygen (red), hydroxide and C=O species (blue), water and H_2O/C-O species (green), experimental points (black cycles), fitted curve (gray line). Photon energy 1066 eV.

Figure 93. Ir4f XP spectra of Ir@IrO_x anode under 3 mbar water vapor and different polarization conditions: A – 0 V; B – 0.4 V; C – 1.1 V; D – 1.3 V; E – 1.4 V; F – 1.43 V; G – 1.5 V; H – 1.1 V (backward scan); I – 0 V (backward scan). Fitting: Ir met – grey, Ir III magenta, Ir IV – cyan. Photon energy 595 eV.

Figure 94. Influence of the applied potential on the surface composition of Ir@IrOx anode. Measurements were performed under 3 mbar water vapor. Photon energy 595 eV. Potentials are ohmic drop corrected, both forward (solid line) and backward (dashed line) scans are shown.

Figure 95. Ir4f XP spectra of Ir@IrO_x anode under 3 mbar water vapor and different polarization conditions: A, D – 1.5 V; B, E – 1.1 V (backward scan); C, F – 0 V (backward scan). Fitting: Ir met – grey, Ir III magenta, Ir IV – cyan. Photon energy: 390 eV (A-C), 595 eV (D-F). Note that the spectra shown in Panels A-C have been demonstrated in Figure 93.

Figure 96. Ir4f XP spectra recorded on IrO_2 anode at different potentials and photon energies of 595 eV (A) and 390 eV (B). Color code for Panel A: 0 V (red); 0.7 V (orange); 1.3 V (yellow); 1.5 V (green); 1.55 V (cyan); 1.6 V (blue). For Panel B: 0 V (black); 1.3 V (red); 1.6 V (blue). The upper part of the panels represents the difference between the spectra obtained under different potentials and the spectrum at the open circuit conditions. Measurements were performed under 3 mbar water vapor. Potentials are Ohmic drop corrected.

Figure 97. Panel A: OER activity of unsupported Ir (black) and Ir/ATO (red) catalysts measured in N_2-saturated 0.05 M H_2SO_4, scan rate 5 mV s^{-1}, rotation rate 1600 rpm. Panel B: Chronopotentiometry results on unsupported Ir (black) and Ir/ATO (red) anodes at current density of 1 mA cm^{-2} in N_2-saturated 0.05 M H_2SO_4. Iridium loading on electrodes: 60 μg cm^{-2} for unsupported Ir and 17 μg cm^{-2} for Ir/ATO. Temperature 25°C. The measurements were performed by L. Wang (DLR).[132]

Figure 98. HAADF-STEM images of Ir/SnO_2:Sb powder scratched from the WE side of the MEAs after in-situ measurements. Ir particles appear brighter on the image. The images were obtained by Dr. M. Batuk (University of Antwerp).

Figure 99. Binding energy shifts relative to the initial potential for Ir4f (red), Sb3d (green), Sn3d (blue), C1s (magenta), Si2p (yellow), O1s (cyan) obtained from the analysis of the NAP-XP spectra measured on Ir/ATO (a) and Ir/ATO + graphene (b) samples. Dotted line corresponds to a 1:1 correlation between the Ohmic-drop corrected voltage and the BE shifts. The kinetic energy of the emitted electrons was ca. 530 eV. Catalyst loading (Ir) 0.5 mg cm^{-2}.

Figure 100. Cyclic voltammogram (A) and chronoamperograms (B) recorded on unsupported iridium anode in the NAP-XPS chamber under 3 mbar water vapor. Scan rate 50 mV s^{-1}. Applied potential for the CAs: -0.25 V (black); 0.85 V (red); 1.05 V (green); 1.40 V (blue). The potentials are Ohmic drop corrected. Catalyst loading (Ir) 0.1 mg cm^{-2}.

Figure 101. Panel A: CV recorded on Ir/ATO anode of the corresponding MEAs in the NAP-XPS chamber under 3 mbar water vapor. Scan rate 20 mV s^{-1}. Panel B: chronoamperograms recorded on Ir/ATO (solid lines) and ATO (dashed lines) in the NAP-XPS chamber under 3 mbar water vapor and different polarization: 0.2 V (black); 1.0 V (red); 1.6 V (green); 1.7 V (blue). The potentials are Ohmic drop corrected.Catalyst loading (Ir) 0.5 mg cm^{-2}.

Figure 102. $Sn3d_{5/2}$ XP spectra recorded on ATO-based MEA under 3 mbar water vapor and different polarization: 0.2 V (grey); 1.0 V (red); 1.6 V (green); 1.7 V (blue). The potential values are Ohmic drop corrected. Kinetic energies of the emitted electrons: 390 eV (Panel A); 530 eV (Panel B); 810 eV (Panel C). The spectra intensities are normalized.

Figure 103. $Sn3d_{5/2}$ XP spectra recorded on Ir/ATO-based MEA under 3 mbar water vapor and different polarization: 0.2 V (grey); 1.0 V (red); 1.6 V (green); 1.7 V (blue). The potential values are Ohmic drop corrected. Kinetic energies of the emitted electrons: 390 eV (Panel A); 530 eV (Panel B); 810 eV (Panel C).

Figure 104. Full width at half maximum of $Sn3d_{5/2}$ XPS peak recorded on ATO (A) and Ir/ATO (B) anodes under different polarization conditions and the following kinetic energies of the emitted electrons: 390 eV (black); 530 eV (red); 810 eV (blue).

Figure 105. Potential-induced changes of the binding energy position of $Sn3d_{5/2}$ XPS peaks recorded on ATO (A) and Ir/ATO (B) anodes under 3 mbar water vapor under different polarization conditions and the following kinetic energies: 390 eV (black); 530 eV (red); 810 eV (blue).

Figure 106. Sn/Ir atomic ratio estimated on the basis of the XP spectra obtained on Ir/ATO anode under 3 mbar water vapor under different polarization conditions and at the kinetic energy of the emitted electrons of 390 eV (black); 530 eV (red); 810 eV (blue). The error bars were estimated from the quality of the corresponding spectra by changing the background.

Figure 107. Ir4f XP spectra recorded on unsupported Ir (A,C,E) and Ir-ATO (B,D,F) anodes under 3 mbar water vapor and -0.25 V and 0.2 V (below peak A_1), correspondingly. The kinetic energies of the emitted electrons was the following: 390 eV (A,B); 530 eV (C,D); 810 eV (E,F). Pass Energy 50 eV. The color code: Ir_{met} - pink, Ir (III) – green, Ir (IV) – violet. Experimental results are shown as circles, while the fitting – grey line.

Figure 108. Potential-induced changes of Ir sites composition estimated on the base of XP spectra recorded on unsupported iridium (A, C, E) and Ir/ATO (B, D, F) anodes under 3 mbar water vapor and the kinetic energies: 390 eV (black); 530 eV (red); 810 eV (blue). Metallic iridium contributions are shown on Panels A, B; Ir (IV) – Panels C, D; Ir (III) – Panels E, F. The potential values are Ohmic drop corrected.

Figure 109. Schematic band structure of SnO_2: undoped (a) and after heavy doping (b,c). Panel (b) shows the filling of the conduction band, while panel (c) demonstrates the results of the many-body interaction, namely the shrinkage of the energy gap. Shaded areas correspond to the occupied regions. Taken from[265].

Figure 110. The energy band gap vs the thickness of SnO_2:Sb films obtained form the valence band XP spectra. The dashed line represents a fit to a power-law function. Taken from[130].

Figure 111. Energy band diagram of metal and n-type semiconductor contacts. E_{vac} – vacuum energy; E_c – energy of conduction band minimum, E_v – energy of valence band maximum, Φ_m and Φ_s work function of metal and semiconductor, correspondingly, χ_s – electron affinity of the semiconductor. Taken from[269].

Figure 112. Schematic diagram of field-effect-induced band bending on an n-type semiconductor with no surface states. Taken from[269].

List of Tables

Table 1. Various paths in the reaction of oxygen evolution and corresponding Tafel parameters. S – catalytically active site. Taken from[70].

Table 2. Tafel slopes observed in the literature on Ir, Ru-based anodes.

Table 3. Influence of water vapor pressure on the Nafion- and Aquivion-based MEAs ohmic resistance. t = 25 °C, $p_{sat}(H_2O)$ = 30 mbar.

Table 4. Influence of water vapor pressure on the MEA (with Ir@IrOx anode catalyst) ohmic resistance and Tafel slopes.

Table 5. Literature $Ru3d_{5/2}$ BE values for different Ru species measured using conventional UHV XPS.

Table 6. Fitting parameters for C1sRu3d XP spectra recorded at 530 eV Kinetic Energy and 20 eV Pass Energy.

Table 7. Literature binding energy values for different Ir species.

Table 8. Fitting parameters for Ir4f recorded at ISISS beamline on thermally obtained IrO_2 anode at 530 eV Kinetic Energy and 20 eV Pass Energy.

Table 9. Fitting parameters for Ir4f recorded at ISISS beamline on thermally obtained IrO_2 anode at 1010 eV Kinetic Energy and 20 eV Pass Energy.

Table 10. Fitting parameters for Ir4f recorded at ISISS beamline on electrochemically obtained Ir@IrO_x anode at 530 eV Kinetic Energy and 20 eV Pass Energy.

Table 11. Fitting parameters for Ir4f recorded at ISISS beamline on electrochemically obtained Ir@IrO_x anode at 330 eV Kinetic Energy and 20 eV Pass Energy.

Table 12. Fitting parameters for Ir4f recorded at TEMPO beamline on electrochemically obtained Ir@IrO_x anode at 530 eV Kinetic Energy and 50 eV Pass Energy.

Table 13. Fitting parameters for Ir4f recorded at TEMPO beamline on electrochemically obtained Ir@IrO_x anode at 390 eV Kinetic Energy and 50 eV Pass Energy.

Table 14. Fitting parameters for Ir4f recorded at TEMPO beamline on electrochemically obtained Ir@IrO_x anode at 820 eV Kinetic Energy and 50 eV Pass Energy.

Table 15. Parameters used for simulation of the XP spectra recorded at ISISS and TEMPO beamlines in SESSA software.

Table 16. Atomic ratio estimated on the basis of Ru3d, C1s and O1s fitted spectra for Ru@RuO_x at different stages of the electrode analysis.

Table 17. Atomic ratio estimated on the basis of Ru3d and O K edge fitted spectra for different states of the Ru@RuO_x electrode.

Table 18. Inelastic mean free path calculated for Ir and IrO_2 based on TPP2M formula[197].
Table 19. Literature values of the work functions.

General Introduction

Utilization of non-renewable energy sources such as fossil fuels creates environmental and economic problems, while the global energy demand is continuously growing. Hydrogen can be a key solution for the world's energy problem. Hydrogen production by means of water electrolysis is attracting an increasing interest due to its potential output capacity and environmental friendliness. Nevertheless, currently available water electrolyzers require further research and development in order to achieve sustainable hydrogen production at the megawatt level. Among the low temperature devices, two technologies are commercially available nowadays – alkaline and proton exchange membrane (PEM)-based electrolyzers. The latter possess several advantages as compared to alkaline systems such as higher current densities and operating pressures, lower gas cross-over, compact system design, etc.

Improving the oxygen evolution reaction (OER) kinetics is one of the barriers to a widespread market penetration of the PEM water electrolysis technology. Among other requirements, the OER catalysts should withstand harsh acidic and oxidizing environment of the anode of a PEM electrolyzer and possess low OER overpotential. Ir,Ru - based oxides are among the few most active anode materials, however both noble elements are among the scarcest and the most expensive materials. Development of new suitable anode catalysts for PEM electrolyzers depends on the progress in the understanding of the OER mechanism and key reactive intermediates of this complex electrocatalytic process. Moreover, studies of the catalysts degradation under the reaction conditions are required for the development of durable anode materials.

Despite much effort and a variety of the applied analytical techniques and methods, the mechanism of the heterogeneous electrocatalytic OER is still insufficiently understood, largely due to the difficulties in identifying active surface states and detecting the reaction intermediates.

The invention of near-ambient pressure X-ray photoelectron spectroscopy (NAP-XPS) systems allowed studying the chemical composition and the reactions at gas/solid and gas/liquid interfaces. Recent integration of the electro-analytical set-ups into the NAP-XPS end-stations extended the application of this approach to *operando* studies of the electrochemical devices such as electrolyzers, fuel cells, batteries, providing information on the surface composition of the corresponding catalysts under operating conditions. The application of photoemission spectroscopy is governed by the high surface sensitivity of XPS and its capability to provide the information on the electronic structure of materials. Thus, its application for the studies of the

electrode/electrolyte interfaces *in-situ* under the operation conditions may shed light on the reaction mechanisms.

The present thesis is based on the application of the NAP-XPS approach to study the Ir,Ru-based anodes *operando* under PEM electrolyzer conditions.

Chapter 1 contains two sections, the first being devoted to the review of PEM water electrolysis technology focusing on the OER electrocatalysts, and the second reviewing near ambient pressure spectroscopy approach used in this work for *operando* studies.

The materials, the state-of-the-art as well as advanced synchrotron-based techniques used in this work are described in **Chapter 2**. The experimental protocol of *operando* measurements and data processing procedures are also mentioned there.

The following four Chapters are devoted to the results of *operando* spectroscopic measurements performed on Ir, Ru-based anodes. Particularly, **Chapter 3** is related to the elucidating of the OER and degradation mechanisms of Ru-based single oxides. Based on these results, the analysis of the stabilizing role of iridium admixtures in Ru-based anodes is performed in **Chapter 4**. The comparison of the behavior of thermal and electrochemical iridium oxides under OER conditions is presented in **Chapter 5** and includes the discussion of the OER mechanism. Finally, **Chapter 6** is related to the analysis of supported iridium catalysts and the role of metal-support interaction in determing activity-stability properties.

This work was done in the framework of the European project INSIDE (European Union's Seventh Framework Programme (FP7/2007-2013) for Fuel Cell and Hydrogen Joint Technology Initiative under Grant No. 621237). This R&D project is devoted to *in-situ* diagnostics of water electrolyzers. One of the partners, the German Aerospace Center, DLR (Stuttgart, Germany), provided us the catalyst powders used for *in-situ* analysis and performed their characterization in the presence of liquid electrolyte. The preparation of the membrane-electrode assemblies and their further characterization by *ex-situ* and *in-situ* methods, the electrochemical tests under water vapor conditions in the laboratory set-up as well as the analysis of the obtained results were performed by myself. Scanning and transmission electron microscopy measurements were performed at ICPEES and IPCMS (Strasbourg, France) in collaboration with our colleagues. Additional microscopic analysis of the pristine and post-mortem samples containing supported iridium catalysts was done at the University of Antwerp (Belgium).

Chapter 1. Literature Review

1.1. Water Electrolysis: Principle and Types

Renewable and clean energy sources, such as wind and solar, have vast potential to reduce current dependence on fossil fuels and related greenhouse gas emissions. However, solar and wind power are intermittent and depend on geography, and thus are not reliable for instantaneous supply of energy. To take full advantage of renewable energies even on a rainy or windless day, electrical grids need to store the power previously produced. A variety of grid-scale storage technologies are currently available, including pumped hydro, compressed air, and various types of battery storage[1]. However, the shortcomings of battery storage are low storage capacity, short equipment life, and considerable amount of wastes generated. Hydrogen possesses the highest energy density and is considered as a potential alternative fuel and energy carrier in the chemical energy storage issue. Currently, hydrogen is mainly produced by natural gas reforming process, which is neither renewable nor clean. A more environmentally friendly manner of hydrogen production is water splitting. Beside this, other advantages of the electrocatalytic splitting of water technology are high hydrogen purity, simplicity of the process and abundant water resources[2,3].

Hydrogen regenerated in a water electrolyzer by applying an electric current is further compressed and stored in gas tanks and can be used in a fuel cell to generate electricity, forming a regenerative hydrogen fuel cell system[4].

The core of an electrolyzer unit is an electrochemical cell, which is filled with pure water and has two electrodes connected to an external power supply. When a certain potential difference is applied between the two electrodes, they start to produce hydrogen gas at the negatively biased electrode and oxygen gas at the positively biased electrode. The overall reaction is given by:

$$H_2O_{(liq)} \rightarrow H_{2\,(g)} + 0.5\ O_{2\,(g)} \quad (Eq.\ 1)$$

Electrolysis of water can be realized either at low temperature using liquid water or at high temperature (HT) using steam. The temperature regime affects both the overall efficiency and the costs. Figure 1 shows the electrolysis energy need as a function of temperature. The energy required for water electrolysis reaction at constant temperature and pressure is determined by the change of enthalpy ΔH resulting from the changes of the Gibbs free energy ΔG (electric input) and the thermal input $T\Delta S$ (T – the temperature and ΔS – the entropy change), which can be expressed by the following equation:

$$\Delta H = \Delta G + T\Delta S \quad (Eq.\ 2)$$

The standard free energy of reaction ΔG^0 (at 25 °C, 1 atm) equal to 237 kJ/mol corresponds to theoretical cell potential $E^0 = \Delta G^0/zF$ = 1.23 V (where z – the number of electrons transferred per hydrogen mole and equal to 2, F – Faraday constant), i.e. the lowest required voltage for the

electrolysis to take place. In most commercial electrolyzers, the thermal energy $T\Delta S$ required for the electrolysis process is provided by means of electricity. In this case, the minimum required voltage, which is now called thermo-neutral, is equal to 1.48 V. However, the presence of the additional energy consumption factors increases the cell voltage. Increasing of the temperature leads to a decrease of ΔG, while the heat energy demand is growing (Figure 1). Based on this, the main advantage of the high temperature technology is less electrical energy expenses for steam dissociation. Additionally, the $T\Delta S$ demand can be partially replaced by less expensive heat sources than electricity, increasing the efficiency of the electrolyzer and diminishing the cost of hydrogen production itself, as over two thirds of the cost arises from the use of electricity[5].

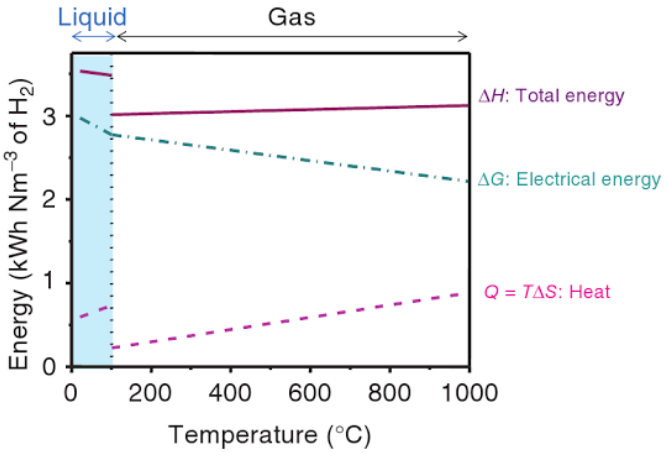

Figure 1. Energy need for the electrolysis reaction as a function of temperature. ΔH – enthalpy; ΔG – Gibbs free energy; ΔS – entropy. Taken from[6].

The operating temperature of HT devices is normally in the range 700 – 900°C. Figure 2 shows the schematic view of a single electrochemical cell operated at HT in a solid oxide electrolysis cell (SOEC) and the reactions taking place at the anode and cathode sides of the cell[6]. The SOEC contains three ceramic layers: a dense electrolyte and two porous electrodes placed on both sides of the electrolyte. One of the main advantages of the SOECs is avoiding the need for noble metals as electrode catalysts[7]. Typically, the cathode side is made of a nickel/yttria-stabilized zirconia (YSZ) cermet, where an ionic conductor, YSZ, acts as an electrolyte, possessing high thermal and chemical stability. For the anode side, the perovskite-based materials are generally used in order to provide both electronic and ionic conductivities of the layer[5]. Beside steam electrolysis, SOECs are also capable of electrolyzing carbon dioxide to carbon monoxide and oxygen ($CO_2 \rightarrow CO + 1/2\ O_2$)[8]. While the HT regime provides the main benefits of the SOECs as reduced electricity demand, the main degradation mechanisms of these devices are also related to the elevated temperatures. Among the others, one may mention the delamination at the anode/electrolyte interface, formation of the pores in the electrolyte layer and of the volatile $Ni(OH)_2$ species.[9]

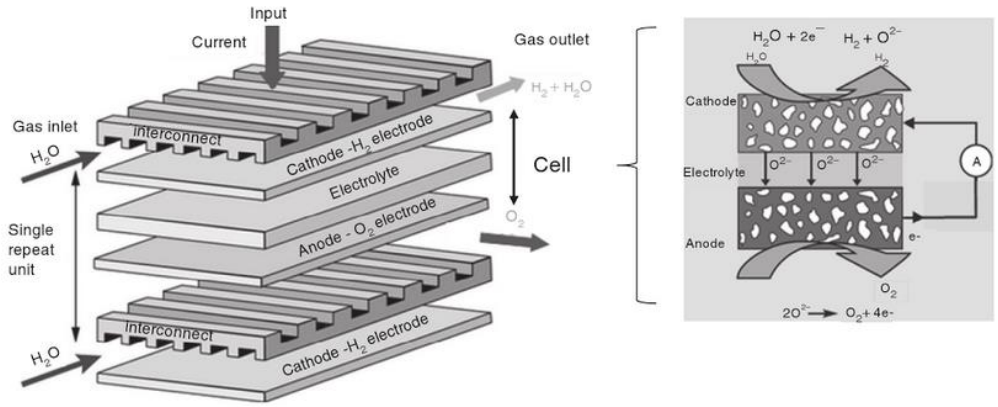

Figure 2. Scheme of HT solid oxide electrolysis cell. Taken from[6].

In case of low temperature electrolyzers two technologies are currently commercially available – alkaline and proton exchange membrane (PEM)-based electrolyzers. A third approach, which is relatively new compared to PEM technology, is based on anion-exchange membranes (AEMs) and is expected to combine the benefits of the devices mentioned above. The schemes of all three approaches are shown in Figure 3.

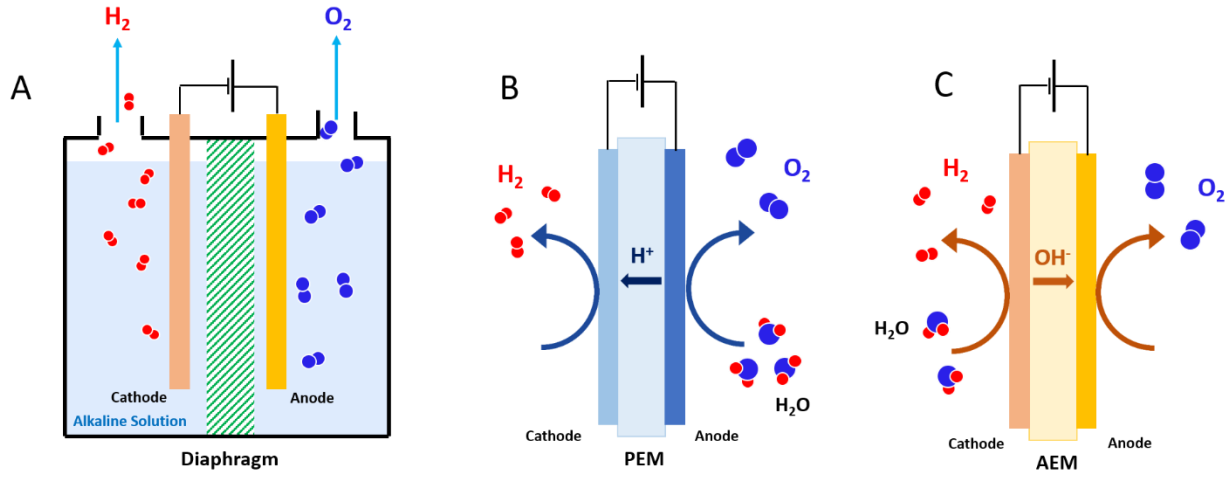

Figure 3. Schematic of the operating principle of an alkaline (A), PEM (B) and AEM (C) water electrolysis cells.

Alkaline electrolyzer (Panel A of Figure 3) is a commercially more mature technology among the others and contains two electrodes immersed in a liquid alkaline electrolyte. The electrons flow from the source to the cathode side where they are consumed by water molecules producing hydrogen molecules according to the reaction:

$$2\ H_2O_{(liq)} + 2e^- \rightarrow H_{2\,(g)} + 2\ OH^- \quad (Eq.\ 3)$$

Hydroxide ions move through the electrolyte solution to the anode side at which they give away electrons and form oxygen:

$$2\ OH^- \rightarrow H_2O_{(liq)} + 0.5\ O_{2\,(g)} + 2e^- \quad (Eq.\ 4)$$

By the use of a diaphragm (see Figure 3, *Panel A)*, the evolved hydrogen and oxygen gases are not intermixed, however, the absence of a complete cross-diffusion cannot be ensured, since the disequilibrium of the gas pressures leads to the crossover of hydrogen molecules[10]. The diffusion of hydrogen to the oxygen evolution part of the cell leads to a decrease of the efficiency of the latter and to the formation of the hydrogen-oxygen explosive mixture. Moreover, the hydrogen permeability through the diaphragm does not depend on the rate of hydrogen and oxygen evolution. This fact complicates the start-up/shut-down of the alkaline electrolyzers and the overall management of the liquid electrolyte supply as it cannot be ramped quickly. Thus, the minimum partial load of alkaline electrolyzers is limited by the diaphragm, which cannot completely prevent the product gasses from cross-diffusing through it. Currently two types of alkaline electrolyzers are presented on the market – atmospheric and pressurized (e.g. NEL, Hydrogenics), where the outlet hydrogen pressure of the latter is varied in the range 30 – 200 bar g, avoiding the additional compression step. To achieve so high gas pressures, the separated diaphragm typically used in low pressure electrolyzers should be replaced by a membrane, providing protection from hydrogen-oxygen recombination, such as the ion-exchange membrane IMET utilized by Hydrogenics.

Potassium hydroxide is the most commonly used electrolyte due to the high mobility of hydroxide ions. However, the ohmic losses across the liquid electrolyte as well as the diaphragm are still relatively high and limit the range of the operating current density. The current values available in alkaline electrolyzers are in the range of 0.2 – 0.4 mA/cm^2.[10] The liquid alkaline electrolyte should be kept away from the air or other sources of CO/CO_2 which lead to the formation of insoluble carbonates, in case of potassium hydroxide - K_2CO_3. Their precipitation in the porous catalysts layers leads to the blocking of the active surface and consequently to decreasing the overall electrolyzer performance[11]. From the other hand, the alkaline media allows utilization of low cost catalysts such as nickel and nickel-based materials for hydrogen evolution reaction (HER)[12,13] and transition metal-based oxides for oxygen evolution reaction (OER)[14]. In general, the alkaline electrolysis technology is associated with relatively low investment costs (1000 – 1200 Euro / kW)[15] in comparison to PEM technology which will be discussed further.

The introduction of a solid polymer electrolyte into water electrolyzer (Figure 3, Panel B) allowed overcoming of the drawbacks of alkaline technology, such as gas crossover, low pressure operation, high overpotential and the complexity of the cell design. The compact design of PEM electrolyzers also allow one to achieve high operational pressures (the differential pressures of 100 bar and more[15]). The presence of a thin layer of the polymer membrane leads to lower ohmic losses (in comparison to alkaline electrolyzer) allowing the achievement of high current densities (> 2 A cm^{-2}) and thus reducing the overall energy cost. Unlike the diaphragm used in alkaline electrolyzer, the proton transport across the membrane responds quickly to the power input and can operate at

practically full nominal power density range and facilitates the electrolyzer management. The direct production of highly pressurized hydrogen from PEM electrolyzer also economizes the energy required for gas compressing for its further storage in the tanks. However, the high operation pressure enhances the gas cross-permeation requiring the usage of thicker membranes, i.e. increasing of their resistance.

The acid media of PEM technology requires materials with high corrosion resistance. The utilization of noble metal catalysts, current collectors and separator plates contributes to a high investment cost of 1900 – 2300 Euro / kW[15]. Moreover, in comparison to alkaline systems the overall lifetime of PEM electrolyzers is lower. Thus, the current development of PEM technology is mainly focused on the reduction of the costs and the improvement of performance and durability.

The scheme of a PEM electrolysis cell is shown in Panel B of Figure 3 and consists of the catalyst coated membrane (CCM), where the latter acts as a proton conductor and gas separator. The CCM is further compressed between two porous transport layers (not shown in the scheme) providing the transport of water and produced oxygen/hydrogen gasses as well as the electrical contact between the catalyst layer and external bipolar plates. Liquid water is introduced to the anode side of the cell, where it is oxidized producing oxygen, electrons and protons:

$$H_2O_{(liq)} \rightarrow 0.5\ O_{2\,(g)} + 2\ H^+ + 2e \quad \textit{(Eq. 5)}$$

The protons and water are further transported through the membrane to the cathode side of the cell and are reduced to molecular hydrogen:

$$2\ H^+ + 2e \rightarrow H_{2\,(g)} \quad \textit{(Eq. 6)}$$

Typical cathode electrocatalysts are platinum black or carbon supported platinum. For the anode side, the most active and stable catalysts are iridium or iridium/ruthenium mixed oxides[10]. The properties of the state-of-the-art membrane Nafion and its analogue will be discussed further.

Combination of the advantages of alkaline and PEM technologies is expected for anion-exchange membrane-based electrolyzers (Panel C of Figure 3). The substitution of the liquid electrolyte by a solid one would increase the operational current densities and simplify the cell management[16]. The membrane resistance and the low gas cross-over would also allow the operation at higher pressures in comparison to a liquid cell[17]. The possibility of using non-precious metals in AEM technology reduces costs. The AEMs are typically based on the quaternary ammonium ion. Thus, the absence of metal cations excludes the formation of carbonate precipitation as is the case for the liquid alkaline media. Regardless all these advantages, further development of AEMs is required as the currently available membranes exhibit poor stability under the operation conditions limiting the lifetime of the electrolyzer.

1.2. Ir, Ru – based Anodes for PEM Electrolyzers

Ru- and Ir-based oxides are amongst the few most active electrode materials, which can withstand the harsh acidic and oxidizing environment of the anode of a PEM electrolyzer, and have thus been the focus of detailed investigations (see [10,14,18–20] and Refs therein). Whilst RuO_2 is more active and cheaper than IrO_2, the former is prone to electrochemical corrosion. In that perspective, the fundamental understanding of the ruthenium dissolution mechanism can be considered as the key in the development of novel, more stable catalysts, as well as in the determination of optimal operating conditions for PEM fuel cells and electrolyzers.

For Ir, Ru-based anodes of PEM electrolyzers, two oxide types are taken into consideration, thermal and electrochemical. The former is obtained by oxidation of metallic particles in the presence of oxygen or air leading to the formation of a rutile structure. We will refer to these oxides as IrO_2 and RuO_2. In contrast, the electrochemical oxide is not a phase oxide and this abbreviation is used for the oxygen-containing layer (hydrated oxide or oxyhydroxide) formed on metallic particles under electrochemical treatment (potential cycling, applying of constant potential) resulting in a structure named here as $Ir@IrO_x$ and $Ru@RuO_x$. It should be also noted that the thickness of the electrochemical oxide and its composition will depend on the electrochemical treatment.

Figure 4 represents the Pourbaix diagrams for iridium and ruthenium, correspondingly. Taking into account the acidic conditions of the PEM electrolyzer we will only discuss possible red-ox states of Ir and Ru under these conditions. In case of iridium, in the range of the potentials shown in panel A of Figure 4, we observe the following states: metallic iridium, Ir (III) mentioned in the Figure as Ir^{+++}, Ir (IV) – as IrO_2 and Ir (VI) abbreviated as IrO_4^{--}. The absence of a proper oxide structure for Ir (III) and Ir (VI) species on this diagram is related to the absence of corresponding data on their thermodynamic stability and existing forms. The presence of two lines in Figure 4 between IrO_2 and IrO_4^{--} is related to different concentrations of the latter in equilibrium with the former. *Pourbaix et a*l.[21] also mentioned the existence of IrO_4^- ions (Ir (VII) species), however due to the absence of any thermodynamic data on these species, they were not included into the plot.

The red-ox behavior of ruthenium (Panel B of Figure 4) is more complex due to the number of valence states inherent to it: metallic Ru, Ru (III) abbreviated as $Ru(OH)_3$, Ru (IV) shown as hydrated oxide RuO_2 $2H_2O$, Ru (VIII) – RuO_4. The latter compounds are prone to dissolution forming either vapor or soluble products. One may notice that the region of RuO_4 species existence and consequently of the corrosion of ruthenium coincides with the OER. The coincidence of the OER onset and RuO_4 formation was discussed later by other groups[22,23] .

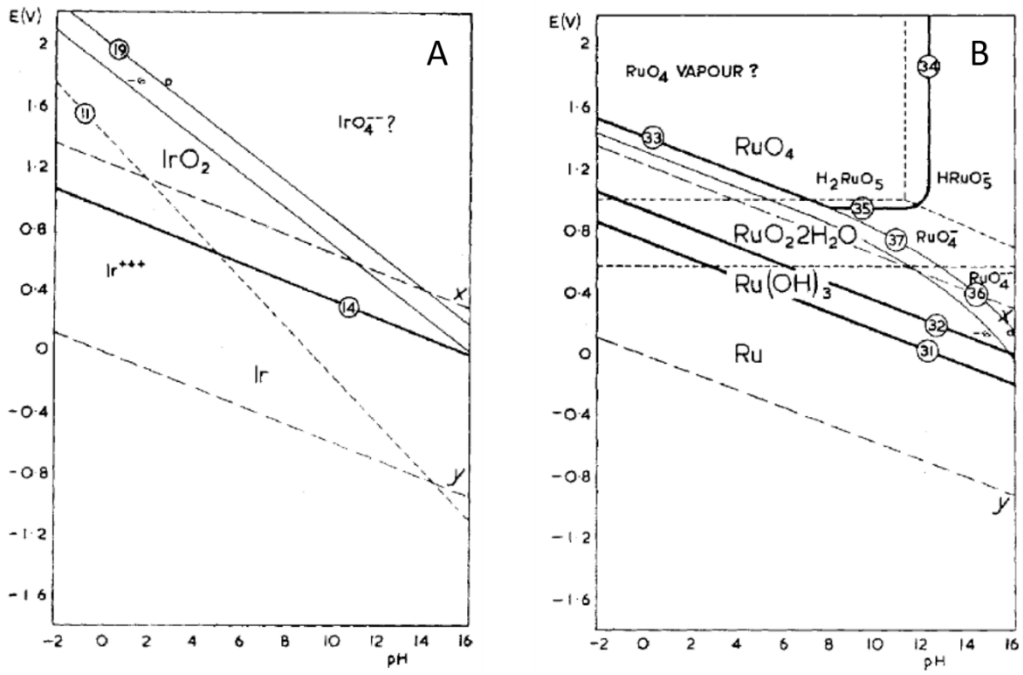

Figure 4.Potential-pH diagram for iridium-(A) and ruthenium-water (B) systems at 25°C. Lines x and y represent the domain of thermodynamic stability of water (25°C, 1 atmosphere). Other lines correspond to the following reactions: $Ir^{+++} + 4H_2O = IrO_4^- + 8H^+ + 3e^-$ *(11);* $Ir + 2H_2O = IrO_2 + 4H^+ + 4e^-$ *(14);* $IrO_2 + 2H_2O = IrO_4^{--} + 4H^+ + 2e^-$ *(19);* $Ru + 3H_2O = Ru(OH)_3 + 3H^+ + 3e^-$ *(31);* $Ru(OH)_3 = RuO_2 + H_2O + H^+ + e^-$ *(32);* $RuO_2 + 2H_2O = RuO_4 + 4H^+ + 4e^-$ *(33);* $RuO_4 + H_2O = HRuO_5^- + H^+$ *(34);* $RuO_4^- = RuO_4 + e^-$ *(35);* $RuO_2 + 2H_2O = RuO_4^{--} + 4H^+ + 2e^-$ *(36);* $RuO_2 + 2H_2O = RuO_4^- + 4H^+ + 3e^-$ *(37). Taken from*[21].

The analysis of the Pourbaix diagrams show that both Ir and Ru catalysts are prone to corrosion at high anodic potentials and acidic media of PEM water electrolyzers. *Cherevko et al.*[24] obtained the dissolution profiles for both thermal and electrochemical oxide-based electrodes during a potential ramp from 1.2 V to the potential corresponding to a current density of 5 mA cm^{-2} (shown in Figure 5). One may clearly see the increasing stability in the following order: $Ru@RuO_x << Ir@IrO_x < RuO_2 << IrO_2$. Wherein the more stable against dissolution thermally prepared rutile phase oxides RuO_2 and IrO_2 are less active than the electrochemically formed oxides $Ru@RuO_x$ and $Ir@IrO_x$ which are prone to higher corrosion rates[22–29]. Figure 6 shows current-potential curves for Ir,Ru-based electrodes measured in acidic and alkaline electrolytes demonstrating the decreasing of activity in the order of $Ru@RuO_x > Ir@IrO_x \approx RuO_2 > IrO_2$[24]. The comparison of two media did not reveal drastic differences in the shape of the recorded curves and their position on the potential scale except for IrO_2. Its atypical behavior in alkaline electrolyte is probably related to the specific pretreatment or experimental conditions, while other results obtained in acid and alkaline media did not reveal any differences in the OER onset for IrO_2-based nanoparticles[30]. Based on the results shown here and discussed in literature[31–33], it is clearly seen that the electrochemical activity of metallic particles covered by a thin oxide layer formed

electrochemically under operation conditions is higher compared to conventional oxide anodes with a rutile structure. However, the stability of these oxides decreases in the opposite way to their activity, i.e. activity-stability properties are generally assumed to be in an inverse relationship.[14,25]

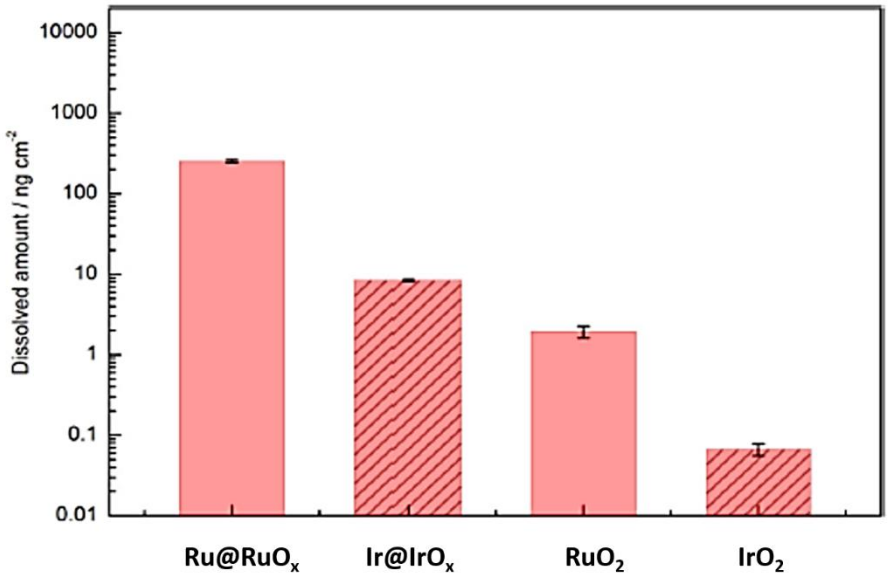

Figure 5. Amount of dissolved metal from $Ru@RuO_x$, $Ir@IrO_x$, RuO_2, IrO_2 thin films anodes estimated during the transition from 1.2 V vs RHE to the potential corresponded to the current density of 5 mA cm^{-2}. The measurements were performed in 0.1 M H_2SO_4. Taken from[24].

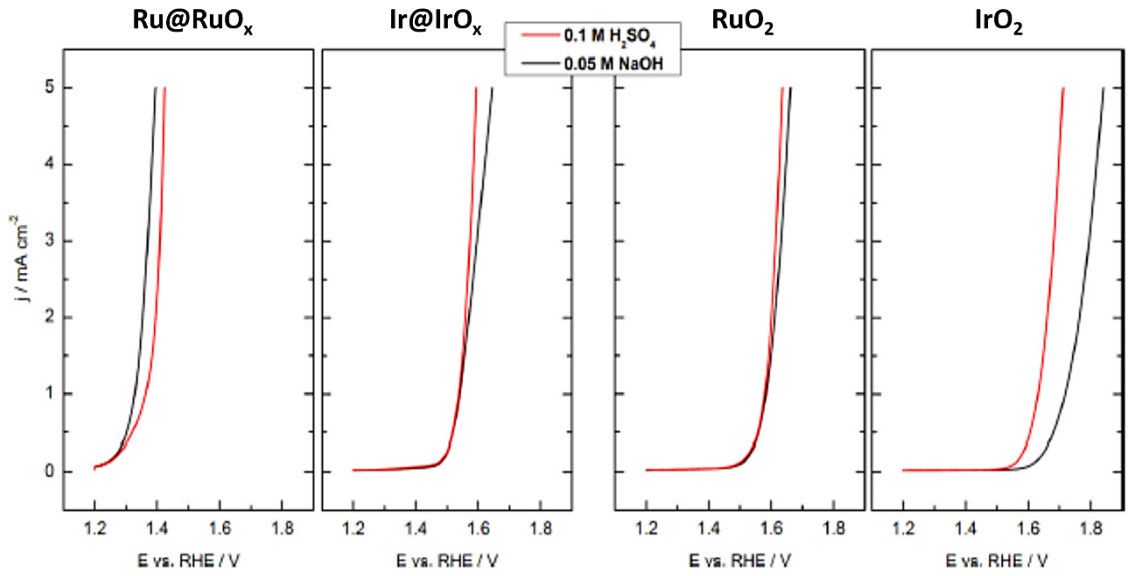

Figure 6. Current-potential curves recorded on $Ru@RuO_x$, $Ir@IrO_x$, RuO_2 and IrO_2 anodes in 0.1 M H_2SO_4 (red) and 0.05 M NaOH (black). Scan rate 10 mV s^{-1}. The potentials were not ohmic drop corrected. Taken from[24].

Regardless of the outstanding OER activity of metallic ruthenium, its poor stability prevents the utilization of single Ru-based anodes in practice and requires their further development. One of the ways to improve the stability of Ru-based anodes without compromising their OER activity is the synthesis of binary (or ternary) metal oxide catalysts. It has been shown

that the introduction of such metals as Ir[34,35],Ta[36],Co[37],Cu[37],Pt[38] allowed not only improvement of the stability of the obtained multicomponent systems but also maintenance of the high activity level of the mixed electrocatalyst. Amongst the others, bimetallic anodes based on Ru and Ir oxides have attracted considerable attention[14,18,34,35,39] and will be discussed in detail.

The analysis of cyclic voltammograms recorded on the corresponding anodes may provide useful information regarding the surface processes taking place on the electrode. It should be noted that the shape of the recorded curves as well as the position of the characteristic peaks depend on the electrode material synthesis (metal[40,41], thermally[42] or anodically grown oxide, sputtered deposited oxide[43], electrodeposited oxide film[44]), pretreatment procedure, measurement protocol and conditions. The assignment of the peaks observed on Ir- and Ru-based electrode voltammograms is not well established and the reports discussed in the literature are quite contradictory. Below we will consider some of them to facilitate our future discussions.

Figure 7 shows the evolution of the current-voltage response on an Ir wire electrode obtained by *Birss et al.*[40]. Three pairs of peaks are typically observed on this type of the anode: A_0/C_0, A_1/C_1, A_2/C_2 (note that C_0 is not shown in Figure). One may see that their intensity is increasing with the number of cycles (and thus, the oxide film thickness).

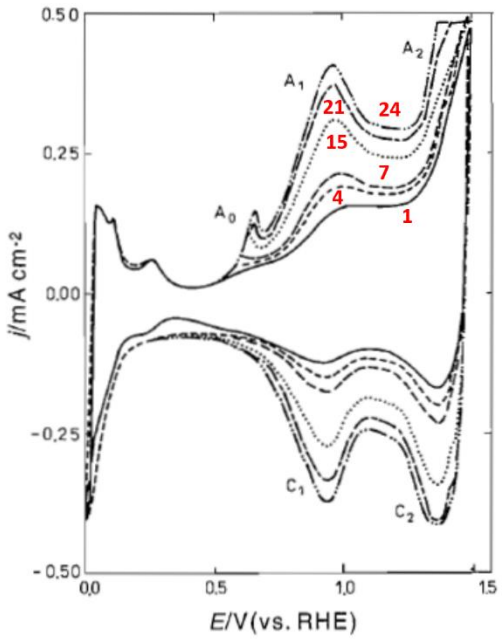

Figure 7. CVs recorded on Ir electrode (Ir wire) in 0.05 M H_2SO_4 with potential cycling between 0 and 1.5 V (vs RHE) at sweep rate 100 mV s^{-1}. Cycle numbers are provided in the plot. Figure is taken from[40].

It should be noted, that iridium-based as well as ruthenium-based hydrous oxides (discussed further) are known as pseudocapacitive materials, where the energy storage occurs due to the proton intercalation and migration and red-ox transition[45]. Thus, the voltammograms recorded on Ir / Ru – based electrodes should reflect all these processes.

Conway et al.[46,47] considered the peak A_0 as a pre-peak to A_1. Increasing the sweep rate leads to an anodic shift of the former emphasizing its slow kinetics. Following this discussion, *Birss et al.*[40] proposed a slow electron transfer reaction Ir (III) / Ir (IV) accompanied by deprotonation (reverse to proton intercalation taking place in C_0 also related to Ir (III) / Ir (IV) red-ox transition). *Birss et al.*[40] also proposed a different degree of the involvement of electrolyte anions in the processes associated with peaks A_0/C_0 and A_1/C_1, correspondingly. This process was followed by a fast film hydration process resulting in the well-defined peak A_1. *Burke* and *Whelan*[48] suggested it as the main charge storage peak as well. Another possibility of the presence of two peaks A_0 and A_1 is the presence of energetically different sites[40]. According to the others, the peak A_0 was considered as O/OH chemisorption while the transition Ir (III) / Ir (IV) was referred to peak A_1[41,49].

Figure 8 demonstrates the comparison of the curves obtained on anodically formed iridium oxide films (AIROF) and thermal nanostructured iridium oxide[50]. The curve recorded on IrO_2 electrode does not contain the pre-peak discussed previously for the hydrous iridium oxide film (peak A_0)[51]. Furthermore, the reduced form of Ir oxide, i.e. Ir (III), possesses lower conductivity in comparison to that of the higher oxidation state Ir (IV). The impedance spectroscopy analysis performed on (AIROF)[52,53] and nanostructured IrO_2 oxide[51] revealed the evolution of the conductivity with applied potential, while IrO_2 did not display any changes. Thus, according to *Sunde et al.*[51], the proton intercalation and corresponding reduction of Ir sites (Ir (IV) / Ir(III) transition) do not seem to occur on anhydrous crystalline iridium oxide.

The third peak pair A_2/C_2 observed in the voltammogram of iridium (Figure 7) is generally attributed to further oxidation of iridium sites up to Ir (V) or Ir (VI)[40,54]. *Cherevko et al.*[41] also proposed the formation of oxyhydroxide Ir (V) – IrO_2OH – at these potentials, however this high oxidation state complex was considered as short-lived and prone to decomposition forming oxygen molecules and an iridium complex with a lower oxidation state. The formation of high oxidation state iridium species (> IV) and their participation in the OER is highly debated in the literature[55–57].

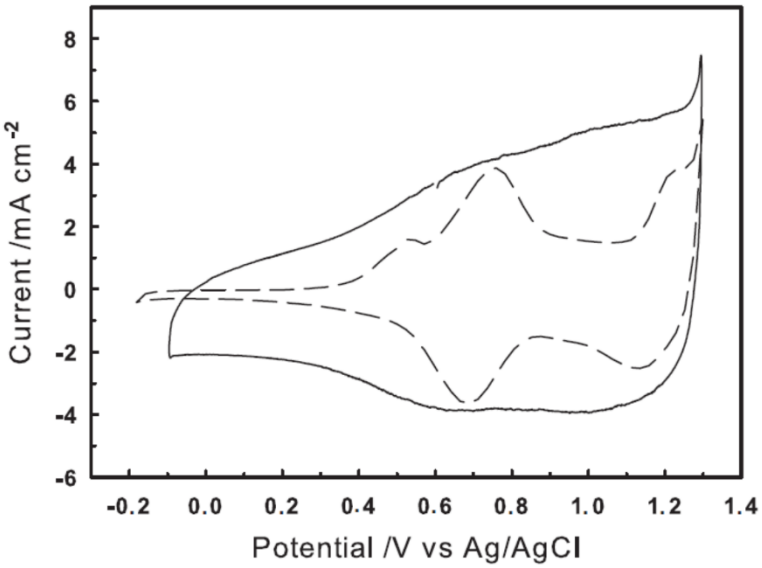

Figure 8. Cyclic voltammograms of IrO_2 (oxidized at 500 ^{0}C, shown as a solid line) and AIROF anodes (dashed line) obtained in sulfuric acid (pH = 0.4) and sweep rate 200 and 250 mV s^{-1}, respectively. Taken from[50].

Now we can compare the behavior of pure IrO_2 with pure RuO_2 and their mixed oxides. The voltammograms are shown in Figure 9[42]. All the electrodes were prepared from metallic precursors by their thermal treatment in the presence of oxygen at 400 ^{0}C. One may see the presence of a unique peak in the middle of the voltammogram for the three electrodes, however this peak shifts depending on the electrode composition from ca. 0.7 V on RuO_2 to ca. 1.1 V vs RHE on IrO_2. *Kodintsev et al.*[42] attributed these peaks to the corresponding III / IV red-ox transitions.

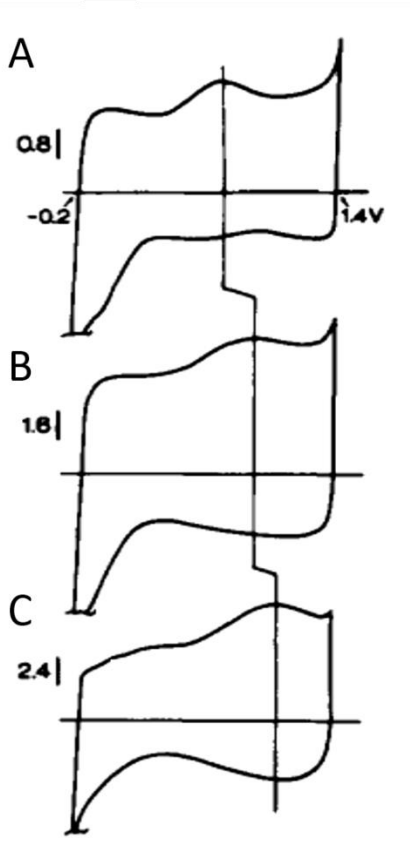

Figure 9. Cyclic voltammetric curves recorded on RuO_2 (A), $Ir_{0.5}Ru_{0.5}O_2$ (B) and IrO_2 (C) anodes at 20 mV s^{-1} in 1 M $HClO_4$ solution. Potential range: [-0.2; 1.4] vs RHE. The current density scale (mA cm^{-2}) is shown for each plot. Taken from[42].

While the voltammogram obtained on the thermally prepared RuO_2 electrode shown in Figure 9 possesses only one red-ox peak, the behavior of the similar electrodes analyzed by *Audichon et al.*[49] and *Reier et al.*[58] was described by two transitions at 0.6 V and 0.8 V vs RHE attributed to Ru (III) / Ru (IV) and Ru (IV) / Ru (VI). The curves obtained on thermally oxidized Ru-based oxide by *Lyons et al.*[54] exhibit even three distinct red-ox processes attributed to Ru (III) / (IV), Ru (IV) / (VI) and Ru (VI) / (VII) or Ru (VI) / Ru (VIII) surface transitions. The presence or the absence of the peaks is strongly related to the experimental protocol and to the pretreatment procedure.

The discussion of the surface evolution of Ru-based electrodes, especially of the hydrous oxide, cannot be performed without mentioning their pseudocapacitance properties associated with the electron (Ru^{2+}, Ru^{3+}, Ru^{4+}) accompanied by the proton transfers[45,59]. The charge exchange occurring at the $RuO_2 \cdot H_2O$ electrode/electrolyte interface at a constant rate results in well-defined features in the corresponding cyclic voltammograms. The charge storage mechanism on ruthenium oxide proposed by *Trasatti*[60] is expressed by the following redox reaction:

$$RuO_x(OH)_y + \delta H^+ + \delta e \leftrightarrow RuO_{x-\delta}(OH)_{y+\delta} \quad (Eq.\ 7)$$

$$Ru^{4+}\text{-}O^{2-} + H^{+} + e \leftrightarrow Ru^{3+}\text{-}OH^{-} \quad (Eq.\ 8)$$

What is interesting to note, is that the capacitance values obtained on hydrated $RuO_2 \cdot H_2O$ electrode are much larger than those recorded on anhydrous RuO_2. *Zheng et al.*[61] explained the greater proton exchange of the former by facile reduction of Ru ions and proton permeability of the hydrated oxide structure. The lattice of crystalline ruthenium oxide is rigid and is difficult to expand, while $RuO_2 \cdot H_2O$ structure can be rearranged when H^+ ions are intercalated[61]. Moreover, the DFT calculations performed on RuO_2 structure by *Liu et al.*[62] revealed quite high migration barrier for hydrogen limiting proton diffusion in bulk RuO_2.

The hydrous-anhydrous transition of Ru (IV) oxide prior to the OER region was also discussed by *Juodkazytė et al.*[63] on the basis of the microgravimetric analysis coupled with the conventional electrochemical cell.

1.2.1. Oxygen Evolution Reaction Mechanisms

Improving of the OER kinetics is one of the barriers to a widespread market penetration of the PEM water electrolysis technology[14]. For this reason, the attention of the scientific community has grown in order to elucidate the reaction mechanism of the OER. A number of OER mechanisms have been reported and discussed in the literature based on both experimental and theoretical results[18]. The first discussions of the OER mechanism were based on the Tafel slope analysis[64], which we will briefly discuss below.

In case of a single outer-sphere electron transfer reaction, its rate can be described by the Butler-Volmer equation[65]:

$$j = j_0 \{exp(\beta_f f \eta) - exp[-\beta_b f \eta]\} \quad (Eq.\ 9)$$

where j – the current density;

j_0 – exchange current density;

β – symmetry factors of a single electron transfer reaction (f – forward, b – backward);

$f = F/RT$;

F – Faraday's constant;

R – universal gas constant;

T – absolute temperature;

η – overpotential.

Considering the higher reaction rates of the forward reactions than those of the backward reactions at high anodic overpotentials the second term in the brackets of Eq. 9 is very small and we obtain the following equation for the overpotential:

$$\eta = \frac{2.303RT}{\beta_f F} log(j_0) - \frac{2.303RT}{\beta_f F} log(j) \quad (Eq.\ 10)$$

For simplicity, this equation can be rewritten as:

$$\eta = a + b\ log\ (j) \quad (Eq.\ 11)$$

where $a = \frac{2.303RT}{\beta_f F} \log(j_0)$. The intercept obtained from the plot of η vs log j can be converted into the exchange current density j_0 known as a descriptor of the catalytic activity[66]. The second term of Eq. 11 is known as Tafel slope and can be determined as:

$$\delta\eta/\delta log\ i = 2.303RT / \beta_f F \quad (Eq.\ 12)$$

Based on the Tafel slope values, one may also compare the electrocatalytic activity and analyze the reaction mechanism. The analysis of the multistep reactions is more complex and for their description, we should make some additional assumptions. The exchange current of the rate-determining step (rds) is assumed to be at least two orders of magnitude smaller than other "fast" reactions and the rds is the same for forward and backward scans. The electrode surface is assumed to be free of any adsorbed species and the reaction is in the steady state[65]. Thus, the rate of the overall reaction will be described the following way:

$$j = j_0 \{exp(\alpha_f f\eta) - exp[-\alpha_b f\eta]\} \quad (Eq.\ 13)$$

where α_f and α_b – the apparent transfer coefficient of the overall forward and backward reactions, correspondingly[67]. These composite terms are related to the symmetry factors[68]:

$$\alpha_f = n_p + n_q\beta_f \quad (Eq.\ 14)$$

$$\alpha_b = n_r + n_q\beta_f \quad (Eq.\ 15)$$

n_p and n_r - the number of electrons transferred prior to and after the rate-determining step (rds), respectively. While the number of electrons transferred during one elementary rds is marked as n_q.

In order to illustrate the principle of the Tafel analysis, we will examine few simple model systems with different rate-determining steps.

1. The reaction sequence consists of the electrochemical and chemical steps while the latter is rds. This leads to the following numbers: $n_p = 1$, $n_q = 0$ and $n_r = 0$. The Tafel slope does not depend on the symmetry factor β and is equal to:
   $\delta V/\delta \log i = 2.303RT / \alpha_f F = 2.303RT / 1\ F =$ ***60 mV dec^{-1}***
2. The same reaction scheme as in the previous case however, the rds is the electrochemical step. Then $n_p = 0$, $n_q = 1$, $n_r = 0$ and the Tafel slope:
   $\delta V/\delta \log i = 2.303RT / \alpha_f F = 2.303RT / \beta_f F = 60 / \beta_f$

Assuming a symmetric electron transfer (β_f = ½), the slope is estimated as ***120 mV dec^{-1}***

3. The last scheme considered here contains two electrochemical steps, where the second is the rds. The electrons transferred in these reactions: $n_p = 1$, $n_q = 1$, $n_r = 0$. Taking in consideration β_f = ½ the Tafel slope will be equal to:
   $\delta V/\delta \log i = 2.303RT / \alpha_f F = 2*2.303RT / 3F =$ ***40 mV dec^{-1}***

In spite of the numerous OER mechanisms proposed in the literature (see few examples shown in Table 1), most of them include the participation of the same intermediates as S-OH and S-O, where S is the catalytically active surface site. The main difference is related to the reaction resulting in the oxygen formation, either it is formed through the direct recombination of two SO intermediates according to the reaction:

$$S\text{-}O \rightarrow 2S + O_2 \quad (Eq.\ 16)$$

or by involving another intermediate, SOOH, which is decomposed to O_2:

$$S\text{-}OOH \leftrightarrow S + O_{2\,(g)} + H^+ + e \quad (Eq.\ 17)$$

Table 1 also contains the Tafel slopes estimated for each of the reaction steps both for anodic and cathodic directions assuming symmetry factor of 0.5. Thus, for example, for the electrochemical oxide path route, *Trasatti et al.* suggested the formation of surface-bonded *O* species as a rate determining step[69]:

$$S\text{-}OH \rightarrow S\text{-}O + H^+ + e \ (Eq.\ 18)$$

Table 1. Various paths in the reaction of oxygen evolution and corresponding Tafel parameters. S – catalytically active site. Taken from[70].

	$\delta V/\delta \ln i$	
	Anodic	**Cathodic**
(1) Oxide path		
$S + H_2O \rightarrow SOH + H^+ + e$	**2RT/F**	**2RT/F**
$2SOH \rightarrow SO + SH_2O$	**RT/2F**	∞
$2SO \rightarrow O_2 + 2S$	**RT/4F**	∞
(2) Electrochemical Oxide path		
$S + H_2O \rightarrow SOH + H^+ + e$	**2RT/F**	**2RT/3F**
$SOH + S + H_2O \rightarrow SO + SH_2O + H^+ + e$	**2RT/3F**	**2RT/F**
$2SO \rightarrow O_2 + 2S$	**RT/4F**	∞
(3) Metal Peroxide path		
$4S + 4H_2O \rightarrow 4SOH + 4H^+ + 4e$	**2RT/F**	**2RT/F**

$SOH \rightarrow SO + SOOH$	**RT/2F**	**RT/2F**
$SO + SOH \rightarrow S + SOOH$	**RT/3F**	**RT/F**
$SOOH + SOH \rightarrow O_2 + S + SH_2O$	**RT/4F**	∞
(4) Electrochemical Metal Peroxide path / Four Concerted		
Proton–Electron Transfer path	**2RT/F**	**6RT/5F**
$S + H_2O \rightarrow SOH + H^+ + e$	**RT/2F**	**RT/2F**
$SOH \rightarrow SO + H^+ + e$	**2RT/5F**	**2RT/3F**
$SO + H_2O \rightarrow SOOH + H^+ + e$	**RT/4F**	∞
$SOOH \rightarrow S + O_2 + H^+ + e$		

The analysis of the Tafel plots obtained for different electrocatalytic systems showed their dependence on the applied potential, especially at high anodic polarizations. This can be explained by several reasons: the changes of the reaction path or the rate-determining step, modification of the surface state of the electrode either due to the coverage by the intermediates or to the changes of the electrode itself (e.g. formation of other oxide phases)[67,70,71]. Formation of the gas-phase oxygen or of the corrosion products during the reaction may also affect the kinetics of the OER and consequently alter the measured Tafel slope. The coverage of the intermediate species is a potential-dependent value, however in the above Tafel analysis it is assumed as constant (either 0 or 1) leading to an incomplete description of the actual surface kinetics. The variety of the experimental procedures and the electrochemical cell configurations results in differences between the ideal and real electrochemical response corrected by means of the ohmic drop. The correct estimation of the latter is also not trivial under the OER condition resulting in the incorrect conclusions regarding the reaction mechanism[72].

The complexity of the oxygen evolution reaction and other processes taking place at the electrode/electrolyte interface coupled with the assumptions of the model used in the Tafel slope interpretation[66] require additional approaches in order to understand the OER mechanism, e.g. microkinetic modelling[66].

In spite of the drawbacks of the Tafel analysis approach mentioned above regarding the determination of the OER mechanism, it cannot be neglected from the analysis of the electrochemical behavior of Ir- and Ru-based anodes presented in this thesis. The literature values obtained at different types of these anodes are presented in Table 2. The analysis of Ru-based anodes showed the values of ca. 40 mV dec^{-1} regardless the electrode (oxide or metallic) nature. In contrast, a vast variety of Tafel slopes observed on Ir-based anodes emphasizes their dependence on the electrode structure and composition. However, the differences in the Tafel slopes observed on single Ir- and Ru-based electrodes can be used in the analysis of the active sites in the mixed

Ir, Ru system by the comparison of the obtained slopes[73]. Thus, the Tafel analysis performed on $Ru_{0.5}Ir_{0.5}O_2$ anodes provided in the works of *Kötz et al.* and *Audichon et al.* proposed a IrO_2-like OER mechanism under low overpotentials[49,74]. In case of homogeneous samples the following trend has been observed for the mixed oxides: the increasing of the iridium content leads to the gradual growth of Tafel slope from 39 mV dec^{-1} corresponding to pure RuO_2 up to 58 mV dec^{-1}, typical value of pure IrO_2[54].

The changes of the Tafel slope under the operation can be also indirectly correlated to the stability of the catalyst as was demonstrated for supported Ir-based catalysts by *Oh et al*.[75]

Table 2. Tafel slopes observed in the literature on Ir, Ru-based anodes.

Anode	Tafel Slope / mV dec^{-1}	Suggested rate-determining step	Ref
Bulk Ru	44	S-HO* → S-O* + H^+ + e	58
RuO_2 nanoparticles	30 – 40		36
Ir nanoparticles	60	Chemical step	58,76
IrO_2 nanoparticles	58		54,77
$Ru_{0.5}Ir_{0.5}O_2$	60		49,74
Ir oxide nanoscale film		Depends on the electrode structure	78
$t_{calcination}$ < 450°C	40 – 60		
$t_{calcination}$ = 550°C	72		
IrO_x/ATO	57 – 60	Chemical step	75

Despite the difference in the oxygen formation step, the common opinion is that the electrocatalysis of the OER is a heterogeneous reaction, in which the bonding interactions within the intermediates' (SOH, SO and SOOH) are crucial for the overall electrocatalytic ability. Further steps in the OER mechanism development were related to the construction of the plots linking the catalyst activity and the intermediates bonding energy, i.e. creation of volcano-shaped plots.

The first trials were inspired by plots constructed for the hydrogen evolution reaction between the HER activity obtained experimentally and calculated heat of hydrogen adsorption. In case of the OER, the strength of OH adsorption was used as a descriptor, however the difficulties in its accurate determination did not allow the development of this idea[79].

The next idea was to associate the overpotential with the oxygenated intermediates (SOH) removal rather than their adsorption as was considered before[79]. It was claimed that during the formation of SO intermediates on metal oxide surfaces MO_x, the adsorbed oxygen is not bound on the surface of the oxide in its low oxidation state MO_x, but rather as in the higher oxide MO_{x+1}.

Based on this, the volcano plot shown in Figure 10 was created based on the enthalpy of the transition MO_{x-1} to MO_x and the OER activity of the latter. It should be noted, that the ΔH values are referred to the transition from the next lower oxide to the nominal oxide, while the opposite is expected under the oxidative conditions of the reaction. For example, in case of RuO_2 oxide, the enthalpy of transition Ru_2O_3 – RuO_2 was used in the plots shown in Figure 10. This was related to the oxygen deficient nature of the metal oxides. Based on this suggestion, the increase of the OER overpotential observed on the metal oxides with the operation time was attributed to the formation of stoichiometric oxide reducing the catalytic activity[71].

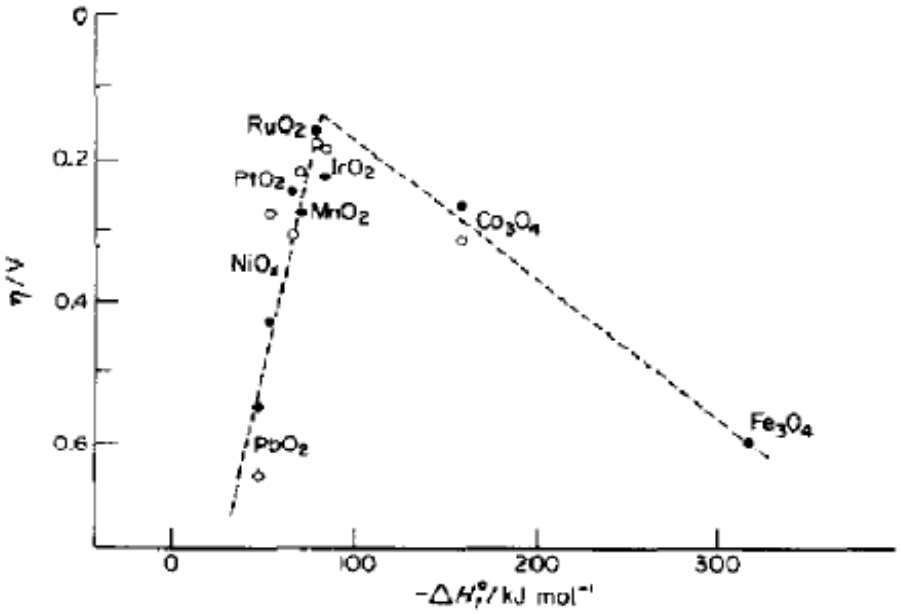

Figure 10. Volcano-shaped curve for the OER activity of the oxides as a function of the enthalpy of their oxidation transition. Alkaline solutions are marked as hollow circles, whereas the acid as black circles. Taken from[79].

Following the idea of the OER mechanism consisting of four concerted proton–electron transfer steps OER mechanism (through the formation of OOH peroxide intermediate, see Table 1)[80,81], the stability of different intermediates (O, OH, OOH) on metal and metal oxides surfaces was estimated by means of density functional theory (DFT) calculations.[82] Based on the obtained results, *Rossmeisl et al.* proposed the transformation of adsorbed O species into OOH as a rate determining step:

$$SO + H_2O_{(liq)} \leftrightarrow SOOH + H^+ + e \quad (Eq.\ 19)$$

Later, based on the linear relations between the O species binding energy and the binding energy of two other species relevant to the oxidation of water (HO and HOO) obtained on rutile-type structure oxides (IrO_2, RuO_2, TiO_2), *Rossmeisl et al.* proposed to use the binding energy of O to the surface to describe the trends in the OER activity.[83]

The application of the electrochemical methods for the studies of the oxygen evolution reaction mechanism is not limited to the Tafel analysis. The analysis of cyclic voltammograms recorded on the electrode can be used to: (i) elucidate the oxidative/reductive processes taking place at the electrode interfaces; (ii) evaluate thickness of the oxide films formed under potential cycling; (iii) estimate integrated voltammetric charge; (iv) follow the evolution of the electrochemical activity and overpotential[41,54,84,85]. Amongst the hydrodynamic electrochemical methods, the rotating disc electrode (RDE) is applied in order to provide a well-defined and steady-state mass-transport regime[25,86,87]. Another method, the rotating ring-disk electrode (RRDE) technique, can be used in order to estimate the catalyst selectivity. The observed anodic currents in the OER region (above 1.4 V vs RHE) can be originated from the OER occurrence as well as from the catalyst oxidation or corrosion. Thus the evolved oxygen can be measured by the oxygen reduction reaction occurring on a Pt-ring electrode[14].

While the electrochemical methods are very sensitive to the processes taking place on the electrode surface, the qualitative as well as quantitative analysis of the reaction products are necessary to fully understand the reaction mechanism. One of the most common approaches is the introduction of the online mass spectrometer[23,88]. The inductively coupled plasma mass spectrometer (ICP-MS)[26,41] can be directly connected to the electrochemical chamber to perform the corresponding analysis. Partial substitution of oxygenated species by the isotopes coupled with mass spectrometry studies allows differentiating their roles in the reaction. An example of these results will be discussed later[23].

The implementation of various spectroscopic techniques into the electrochemical cell contributed to the following discussion of the oxygen evolution reaction mechanisms proceeding on the metal oxide surfaces. Surface enhanced Raman spectroscopy (SERS)[89,90] was one of the first techniques used for *in-situ* analysis as it is not affected by the presence of the aqueous solutions or gas phases. SERS is typically applied for the detection of the adsorbate species and of the red-ox state transitions. The interpretation of the frequency shifts obtained in Raman spectra is based on the comparison with reference spectra, while the analysis of the multicomponent systems is rather complicated and requires additional theoretical calculations[91].

Based on the results obtained by *in-situ* Raman spectroscopy performed on the OER anodes and supported by the corresponding DFT calculations, oxygen evolution was proposed to be a result of the decomposition or disproportionation of the surface oxide forming under reaction conditions[89]. Moreover, this oxide was considered to possess a 3D non-ordered structure containing surface peroxide structures *SOOH* observed by means of SERS. While the direct recombination of oxygen atoms to form O_2 was not considered as the reaction mechanism due to

a large activation barrier associated with this process estimated by DFT calculations[82], the evolved oxygen can be originated both from water and surface lattice oxygen[89].

The participation of the lattice oxygen in the OER observed on IrO_2[92] and RuO_2[23] anodes was confirmed by means of isotopic labelling studies. This direct involvement of the oxygen atoms from the oxide structure during the reaction can lead to the catalyst dissolution and was observed not only for ruthenium[26,93] and iridium-based[41,94] catalysts but also for other systems irrespective of the pH values. Based on these and other results, the instability of the lattice oxygen under the OER conditions was also discussed in the framework of a of thermodynamic approach.[95]

The DFT analysis of different coordination sites of ruthenium oxide possessing various activity-stability properties[27] revealed that in case of low-coordinated sites (such as the case of amorphous oxide formed under electrochemical treatment, $Ru@RuO_x$) the lattice oxygen exchange mechanism is more probable than on other sites[96].

One of the first works discussing the changes of the oxidation states of ruthenium sites in the OER cycle was done by *O'Grady et al.*[97] and was further developed by *Koetz et al.* for both Ir and Ru-based oxides based on results of X-ray photoelectron spectroscopy (XPS) performed under ultra high vacuum (UHV) conditions[22,98].

The OER mechanisms on Ru- and Ir- based anodes proposed by *Koetz et al.* [22,56] are shown in Figure 11[22,56]. The potential cycling of a metallic ruthenium electrode is pruposed to lead to the formation of a hydrous oxide layer. Prior to the oxygen evolution reaction, Ru is assumed to be in the formation of Ru (VI) – $RuO_2(OH)_2$ – while under the reaction conditions it is further oxidized forming Ru (VII) and Ru (VIII) oxides. The latter is considered as a corrosion product and an OER intermediate dissociating into oxygen and Ru (VI) completing the OER cycle (see left hand-side panel of Figure 11). The *ex-situ* XPS measurements performed in vacuum by *Kötz et al.* did not confirm the presence of Ru (VII) and Ru (VIII) species, while the latter was observed by the same group later by means of *in-situ* reflectance spectroscopy[84]. The main advantages of this technique is its surface sensitivity, and its differential nature allows eliminating any undesirable signals. However, this technique is suitable for the particular substances possessing high extinction coefficient in the ultraviolet/visible region such as ruthenium species[84]. While the formation of Ru (VIII) under the OER conditions has been confirmed, other potential-induced red-ox transitions proposed in the tentative reaction mechanism were not detected *in-situ* yet.

The understanding of the OER and degradation mechanisms of ruthenium oxide can be directly related to the stabilization mechanism of IrO_2 admixtures in $Ir_xRu_{1-x}O_2$ mixed oxides. While this effect has been demonstrated by several groups[49,77], its reliable and consistent explanation is still missing. As it was shown in the scheme of the OER on Ru-based electrodes proposed by *Kötz et al.*[22,84], RuO_4 is considered as the main corrosion product. By performing

similar *ex-situ* spectroscopic analysis on a mixed $Ir_xRu_{1-x}O_2$ anode, the authors suggested that the presence of iridium diminishes the formation of Ru (VIII). The additional ultraviolet photoelectron spectroscopy (UPS) measurements realized on Ir,Ru-based oxides showed the formation of a common valence in case of a mixed oxide, due to which iridium limits the oxidation of Ru to higher states, particularly to Ru (VIII)[34].

The changes of the electronic structure of the mixed oxide in the presence of IrO_2 admixtures proposed by *Koetz et al.* were later disputed by *Kasian et al*[99]. Based on the electrochemical results coupled with inductively coupled plasma mass spectrometry studies, the authors confirmed the dissolution of ruthenium regardless the composition of mixed $Ir_xRu_{1-x}O_2$ oxide. The improved stability of the mixed oxides was attributed to lower corrosion of iridium sites rather than to any stabilizing effect of the latter. The dissolution of ruthenium results in IrO_2-like electrochemical performance of the anodes.

While *Koetz* and coworkers linked the degradation of Ru-based anodes to the formation of Ru (VIII) containing components, *Yeo et al.*[36] considered the oxidation of trivalent ruthenium cations present in thermal single oxide RuO_x ($x < 2$) as the main reason of its poor stability. Thus, the stabilization of Ru (III) / Ru (IV) transition by iridium or/and tantalum admixtures was suggested to improve the stability of the corresponding mixed oxides.

Going back to the scheme proposed by *Koetz*, similar to Ru, the OER mechanism on Ir anodes was supposed to include several red-ox transitions[56]. Initially the surface of an iridium anode was found to contain hydrous oxide layer with Ir (III) species. Increasing the potential leads to its oxidation up to Ir (IV) and Ir (VI), where the latter is assumed as an OER intermediate disproportionating to Ir (IV).

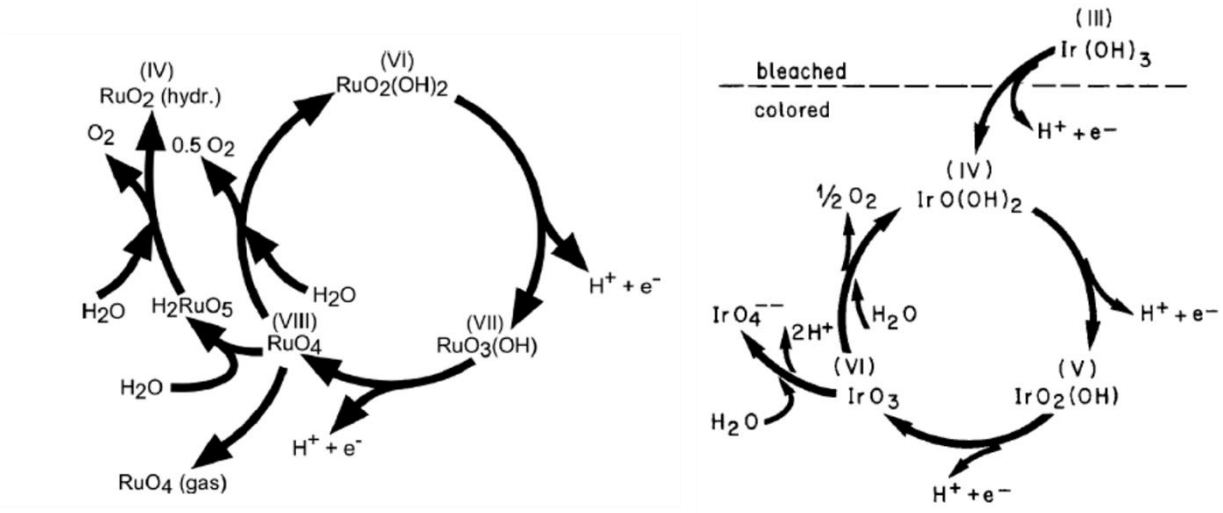

Figure 11. Model for the oxygen evolution and corrosion on Ru-based (left-hand panel) and Ir-based (right-hand panel) electrodes proposed by Koetz et al.[22,56]

Photoemission and absorption spectroscopies are the most powerful techniques for the analysis of the surface red-ox states. Recent instrumentation development allowed their *in-situ* applications to study the electrode-electrolyte interfaces under reaction conditions[100–102]. The details of these approaches and the configurations of the corresponding electrochemical cells will be discussed later in detail, while here we will mainly focus on the results obtained on Ir- and Ru-based electrodes regarding the OER and degradation mechanisms. Due to the poor stability of the ruthenium-based anodes, their *in-situ* studies are quite rare. Recently, *Pederson et al.*[103] demonstrated the results obtained by *operando* X-ray absorption spectroscopy (XAS) on metallic Ru nanoparticles prepared by magnetron sputtering and on RuO_2 nanoparticles prepared by thermal treatment of the former. While typically, the XAS measurements (photon-in-photon-out mode) are considered as bulk sensitive, the high surface-to-bulk ratio of the analyzed Ru nanoparticles (5 nm diameter) allowed the authors to perform surface sensitive measurements. The analysis of metallic ruthenium particles is complicated by their fast dissolution under the OER conditions, however the authors managed to follow the formation of Ru (IV) oxide phase at 1.5 V vs RHE. Increasing the applied potential further stepwise led to complete loss of Ru species. In contrast, the white line position of thermally oxidized RuO_2 nanoparticles shifts to lower energy values, witnessing the decreasing in oxidation state, under the highest applied potential of 1.9 V vs RHE. This counterintuitive phenomenon was explained using a free energy diagram composed on the basis of the proposed DFT model[83]. At the potentials where all the reaction steps are downhill in energy, the driving force to oxygen evolution is very high, consequently the surface coverage of Ru by adsorbed oxygen is decreasing, i.e. the average oxidation state is diminishing. However, no red-ox transformation has been observed prior to the OER onset where Ru is tetravalent.

One of the first works performed on IrO_2 anodes using *in-situ* near ambient pressure (NAP) XPS approach was done by the group of *Nilsson*[101]. Based on the analysis of the XP spectra recorded under open circuit potential and under OER conditions (Figure 12), the authors proposed the formation of Ir (V) as an intermediate of the OER similar to the mechanism proposed by *Koetz et al.* for Ir-based anodes. Due to the absence of the reference materials containing Ir in a valence state higher than IV, the attribution of the additional doublet observed under the reaction conditions to Ir (V) species has been done based on the oxidation trends observed on other metals like platinum. However, the analysis of the XP spectra of Ir-based samples coupled with the DFT calculations demonstrated the inverse behavior of the binding energy position of the peak and the oxidation state of iridium, particularly for Ir (III) and Ir (IV) species[104].

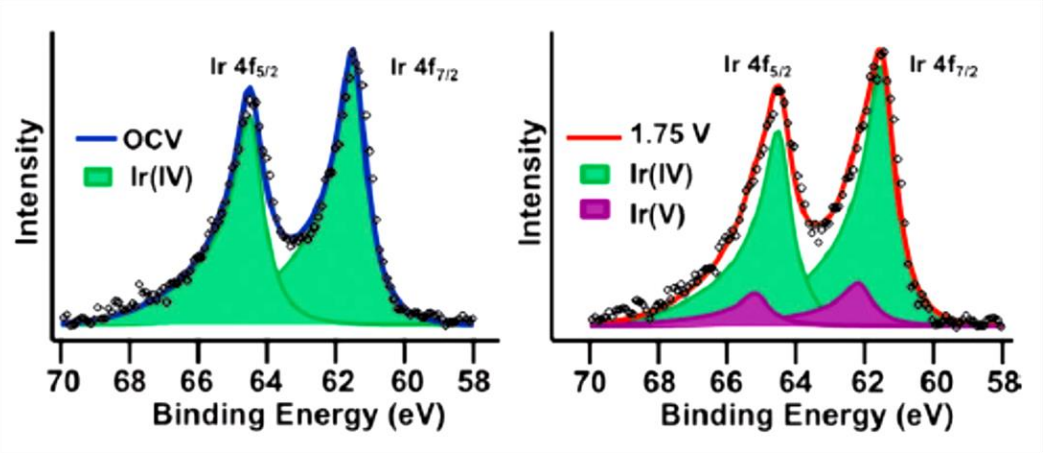

Figure 12. Ir4f XP spectra recorded on IrO_2 anode under OCV (left-hand panel) and 1.75 V (right-hand panel). The fitting was done using two doublets: Ir (IV) – green and Ir (V) – violet. Photon energy 390 eV. Taken from[101].

The *in-situ* analysis of hydrated iridium oxide by means of X-ray absorption near edge structure (XANES) performed by *Minguzzi et al.*[55] also revealed similar iridium red-ox transitions under polarization. The electrodeposited iridium films used in this work initially contained Ir (III) species. The authors suggest the formation of Ir (V) species prior to the OER and their further participation in the reaction cycle according to the scheme presented in Figure 13. Analogous to the previous work, the position of Ir (V) in the Ir-L_{III} edge spectra was not supported by any reference materials. The appearance of Ir (III) species under oxidation conditions of the reaction is counterintuitive and can be related to the corrosion of Ir film or to the degradation under the X-ray beam during the measurements. Additionally the hard X-rays used in this work in order to penetrate the X-ray window and the electrolyte solution[105] diminish the surface sensitivity of this approach.

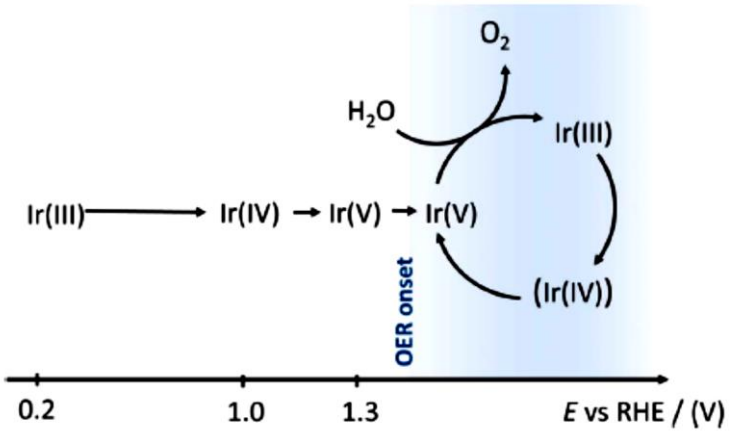

Figure 13. Oxidation-reduction cycle of Ir sites derived from the XANES spectra recorded in[55].

In contrast, *in-situ* XAS studies performed on a thin sputtered IrO_x film by *Pederson et al.*[103] did not confirm either decrease or increase of the oxidation state of iridium in the OER

region. Nevertheless, the authors expect the formation of low oxidation state (< IV) iridium species at higher overpotential (> 1.9 V vs RHE) as a result of the OER.

The alternative view on the potential-induced transitions occurring during the OER cycle is related to the involvement of the anion red-ox chemistry in the reaction mechanism as has been demonstrated for the perovskite families used in low temperature[106] and high temperature[107] electrochemical devices based on the experimental results and theoretical calculations. For Ir-based anodes, the idea of anion red-ox transitions and their direct involvement in the reaction mechanism has been recently demonstrated by *Pfeifer et al.*[108]

The role of oxygen red-ox states in the OER mechanism on Ir-based anodes has been also discussed based on the *in-situ* near ambient pressure spectroscopic measurements performed on a sputtered Ir film[108]. Soft X-ray absorption spectroscopy (electron detection mode) was applied in order to follow the changes of O K edge spectra depending on the applied potential. The example of the spectra under open circuit voltage (OCV) and OER conditions is shown in Figure 14. The attribution of the newly formed peak at ca. 529 eV to O^{I-} species was done based on the DFT calculations of defect Ir oxides containing these fragments. It was also observed, that these species are present on the surface of the anode only under the OER conditions, while returning to the initial OCV conditions results in their disappearance. Regarding the red-ox states of iridium, the analysis of the Ir4f XP spectra also performed in this work did not reveal the presence of the oxidation state of iridium higher than IV.

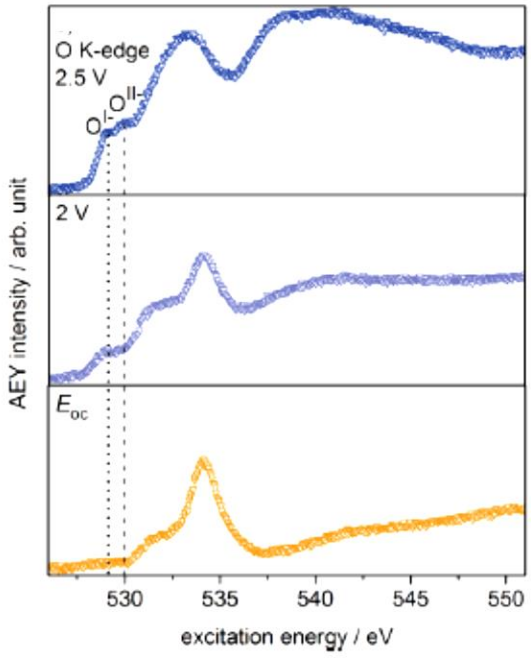

Figure 14. Low excitation energy region of O K edge recorded on sputtered IrO_x anode under OCV (bottom), 2 V (middle) and 2.5 V (top) polarization conditions. Taken from[108].

The contradictions of the results obtained *in-situ* on Ir-based anodes by various methods described earlier do not allow us to make any clear conclusions on the mechanism of the OER and

require further investigations of Ir-based anodes. Due to the low stability of Ru-based anodes under PEM electrolyzer conditions, this electrocatalytic system did not attract so much interest of the research community as iridium. However, better understanding of the processes taking place at Ru-based anodes and the comparison with Ir may shed light on the path of the OER and contribute to the development of new catalysts.

1.2.2. Metal Support Interaction

In spite of the fairly good activity-stability properties of Ir-based catalysts their direct implementation in PEM electrolysis technology is hindered by high cost and scarcity of iridium metal. In order to improve the utilization of the iridium surface, the main strategies are related to the decreasing the particles size[27], development of core-shell structures[109,110], changing the phase structure to more active amorphous oxides[24,25] or using support materials[75,109,111].

Carbon-based support materials commonly used in the fuel cell technology[112,113] cannot be applied under the harsh conditions of the oxygen evolution reaction. Typically used electrocatalyst supports are based on TiO_2[114,115] or Magnéli phases of titanium oxide Ti_4O_7[116,117]; WO_3[118] and SnO_2[75,119–121]. Doped tin oxide has attracted significant attention due to its high electronic conductivity and electrochemical stability[119,121–123]. Doping is a general technique in order to modify in a desired way the properties of oxide materials. The introduction of such elements as antimony[119], niobium[123], fluorine[124], indium[122] etc. in the rutile structure of SnO_2 improves the electronic conductivity of the support and enhances the activity and the stability of the corresponding catalyst-support composite[111,123]. Antimony-doped tin oxide (ATO) is considered as one of the promising support materials for the oxygen evolution reaction.[75,125]

Tin oxide is a nonstoichiometric oxygen deficient oxide semiconductor ($SnO_{2-\delta}$). Its isolated oxygen vacancies are compensated by the electron charge and result in n-type conductivity[126]. Antimony doping changes the electronic conductivity of SnO_2, however it strongly depends on the oxidation state of Sb[127,128].

Antimony is a multivalent element with two common oxidation states of Sb (V) and Sb (III). It was observed that both oxidation states can be present in the ATO and the Sb (V) / Sb (III) ratio depends on doping level[129–131]. The lower the doping level – the higher is the contribution of Sb (V) species. The substitution of tetravalent Sn by pentavalent Sb leads to the formation of the positively charged defects compensated by the creation of tin vacancies. Further, these vacancies can react with the oxygen vacancies present initially in the nonstoichiometric tin oxide leading to the diminishing of the latter. The decrease of the oxygen vacancies leads to higher concentration of the electrons, i.e. the electronic conductivity of ATO increases. In contrast, a high doping level of antimony leads to a predominant contribution of Sb (III) atoms in Sb (III) / Sb (V) ratio. In this

case, tetravalent tin atoms are substituted by trivalent antimony. In its turn, this induces the formation of additional oxygen vacancies, decreasing the amount of the available electrons and diminishing the conductivity[128].

As was previously mentioned, the introduction of the support leads to the improvement of the composite stability. Figure 15 shows the results of galvanostatic stability tests performed on carbon- and ATO-supported iridium catalysts at 1 mA cm^{-2} current density during 15 hours[75]. The stability of synthesized ATO support (sample IrO_x/ATO) was compared to a commercially available one referred in the Figure as Com. ATO. While carbon-supported catalyst possesses the poorest stability (confirmed also by ICP-MS measurements), one may also notice lower degradation of a synthesized ATO-based anode in comparison to a commercial-based electrode.

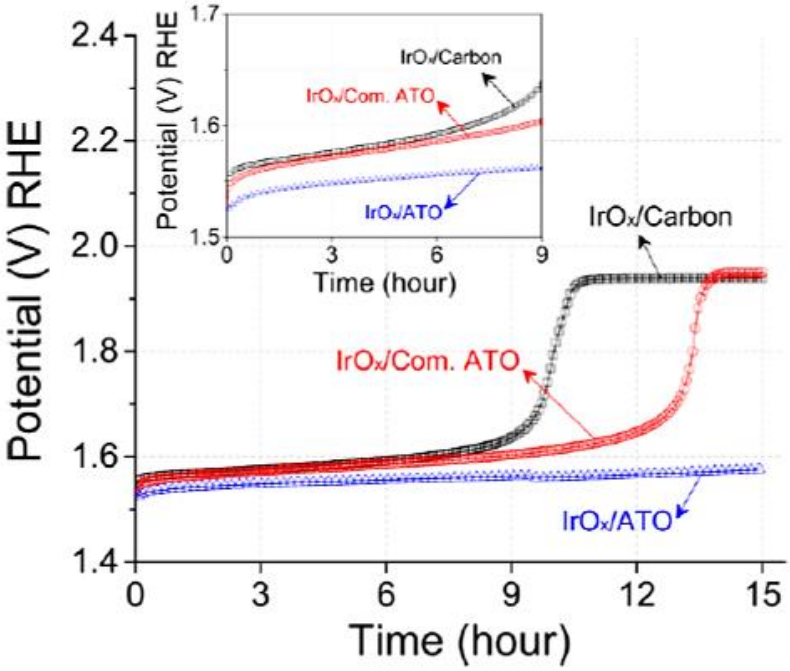

Figure 15. Galvanostatic stability test of IrO_x/carbon (black), IrO_x/Com. ATO (red) and IrO_x/ATO (blue) anodes performed in N_2-purged 0.05 M H_2SO_4 at 1 mA cm^{-2} current density and rotation rate of 1600 rpm. t = 25 °C. The inlet shows the magnification over the region 0 – 9 h. Commercial available ATO is marked as Com. ATO. Taken from[75].

Geiger et al.[120] analyzed the behavior of the ATO support in the absence of any catalyst under different electrochemical conditions. The ATO was stable under potential cycling in the range [0.36; 1.1] vs RHE, however the broadening of the potential interval up to [-0.29; 1.45] vs RHE led to the formation of a SnO_2 rich layer due to partial Sb dissolution confirmed by ICP-MS data.[120] The formation of antimony depletion region on the ATO surface has been also observed by *Fabbri et al.*[121] as a result of potential cycling of the ATO-based catalyst in the potential region [0.05; 1.6] vs RHE. The improvement of the activity of ATO-supported iridium catalysts in comparison to the unsupported counterpart has been demonstrated by different groups.[75,132,133]

The influence of reducible supports on the activity of metal nanoparticles was discovered by *Tauster et al*.[134,135] and was referred as strong metal-support interaction (SMSI). The SMSI may induce the *charge transfer* between the metal nanoparticles and the substrate due to the mixing of their orbitals[75], partial or complete *encapsulation* of the metallic particles[136,137], *alloys formation* etc. All these factors may contribute to the electrochemical performance of the catalysts and consequently of the electrolyzer.

One of the most typical SMSI effects observed in heterogeneous catalysis is the formation of a thin support layer on the surface of the metallic nanoparticles of the catalyst. This layer may act as an anchor to avoid the particles detachment and thus improving the stability of the electrode.[138] However, in order to maintain the activity of the particles, the encapsulation should be either partial or through the formation of a porous layer enabling the access for the reactants. Examples of a support layer covering Rh nanoparticles are shown in Figure 16[137]. The presented scanning transmission electron microscopy (STEM) images were *obtained in-situ* for the dense crystalline Ti-based oxide and for its amorphous porous layer. While the crystalline shell leads to the blocking of the active surface of the nanoparticles, the amorphous porous layer enhances the activity-stability properties of Rh catalyst.[137]

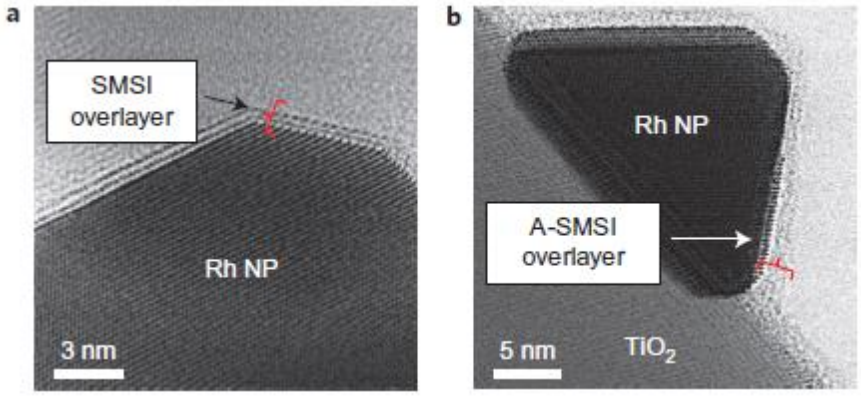

Figure 16. In-situ STEM images of Rh/TiO_2 demonstrating the formation of crystalline Ti^{3+} - based (a) and amorphous Ti^{3+}/Ti^{4+}- mixed layer. Taken from[137].

Regarding Ir/ATO system, the nature of the improved OER activity has not been established yet. *In-situ* XAS measurements coupled with *ex-situ* XPS studies performed by *Oh et al.*[75] revealed a lower mean oxidation state of iridium nanoparticles in case of the supported catalyst. The depth analysis of the photoemission spectra also shows a decrease of the thickness of the oxide shell on iridium. Based on these data, the authors proposed the charge donation from ATO to IrO_x nanoparticles and also suggested that the degradation of iridium electrocatalysts is related to the presence of high oxidation state of iridium (> III) while the presence of the ATO support stabilizes Ir in its lower valence state, Ir (III), and improves its stability. However, the presence of Ir (III) species was not confirmed by XPS measurements.

The lack of comprehensive studies of semiconductor/metal interface and particularly of Ir/ATO system as a promising catalyst for energy conversion application motivated us to include it in our *in-situ* investigation.

1.3. Spectroscopies at Near Ambient Pressure conditions

The complexity of the processes taking place during the OER, the uncertain reaction mechanism and dynamic evolution of the catalyst surface has motivated the use of advanced surface-sensitive studies of the electrode/electrolyte interface under operating conditions. Section 1.3.1 describes the basic concepts of X-ray photoelectron and Near-edge X-ray absorption fine structure spectroscopies and Section 1.3.2 gives the explanation of the near ambient pressure approach while the examples of the electrochemical cells used for *in-situ* spectroscopic measurements are overviewed in Section 1.3.3.

1.3.1. X-ray Photoelectron and Near-edge X-ray Absorption Fine Structure Spectroscopies

X-ray photoelectron spectroscopy is the most popular spectroscopic technique for defining the elemental composition of the outer 1-10 nm of a solid surface. The inelastic mean free path (IMFP) of the photoelectrons excited by soft X-rays leads to their strong interaction with surrounding atoms. Based on the energy analysis of the emitted photoelectrons it can provide the following information on the surface elemental analysis (both qualitative and quantitative): the oxidation state of the elements, the presence of the adsorbed species and formation of the alloys[139].

In XPS, the sample surface is irradiated with photons of the energy *hv*, which directly interact with electrons of the sample atoms (see scheme in Figure 18). As a result, ionized states are created and the photoelectrons are emitted with specific kinetic energy (KE) E_{kin}, which depends on their binding energy (BE) E_{bin} and the work function φ (depending on both sample and spectrometer)[140]:

$$E_{kin} = hv - E_{bin} - \varphi \quad (Eq.\ 20)$$

X-ray photoelectron spectra are displayed as plots of the number of photoelectrons (intensity) as a function of their binding energy or, alternatively, their kinetic energy. Figure 17 represents the survey spectrum recorded on IrO_2 catalyst powder under UHV conditions at the laboratory XPS (ICPEES, France). The observed peaks correspond to the elements originating both from the electrode (Ir4f, O1s) and adventitious carbon (C1s). The typical step-like shape of the background is related to the inelastic photoemission of the photoelectrons (energy losses within the solid).

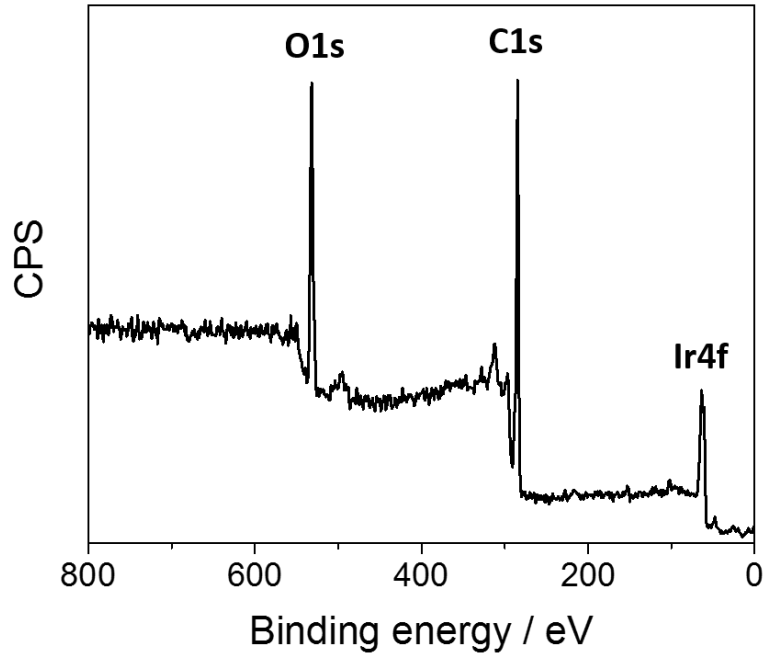

Figure 17. Survey spectrum recorded on IrO_2 catalyst powder under UHV (ICPEES). Photon energy 1486.6 eV, pass energy (PE) = 90 eV.

XPS makes the quantitative analysis of the surface composition possible, and provides information about the chemical state of elements through the detection of ‘‘chemical shifts’’ in the BE of the photoelectrons. The binding energy shifts observed in XPS core levels can be due to initial- or final-state effects. *Initial-state effects* are dominated by the properties of the atom prior to the photoemission process. For example, different oxidation states of a material move the energy level of the electrons inside the atom. In contrast, *final-state effects* are caused by phenomena occurring after the photoemission process. *Shake-up satellites* may occur when the outgoing core photoelectron interacts with a valence electron and excites it to a higher energy level, thus the energy of the former is reduced resulting in a satellite structure to low kinetic energy of the primary photoelectron peak. Moreover, the valence electrons can be completely ionized, i.e. excited to an unbounded continuum state. This process is referred as *shake-off*, but they are rarely discerned in the spectrum as the energy separation is much greater than the primary peak[140,141].

While in XPS, core electrons are ejected above the vacuum level by the excitation of a photon with sufficiently high energy, in X-ray absorption spectroscopy the core electrons are lifted into unoccupied bound states above the Fermi level or into the quasicontinuum just above the ionization threshold (see Figure 18). Depending on the analysis purpose and the investigated samples, several detection modes can be applied. Standard XAS experiments are performed in transmission mode where the intensity of the photons is measured after the monochromator (before the interaction with the sample) and after the sample. The main limitations of this method are the

homogeneity and the thickness of the sample and the necessity of the hard X-rays (> 4500 eV) in order to penetrate the sample.

The formation of the core hole gives rise to the emissions of the photons (fluorescence-yield mode, FY) or secondary electrons (total electron yield mode, TEY). Measuring of these decay products has advantage over the transmission detection as one may measure samples of arbitrary thickness. In case of the photon-in-photon-out[142] technique (FY mode) the mean free path of the emitted photons is of the same order of magnitude as the incoming X-rays, decreasing the surface sensitivity of FY. In this case, surface sensitivity can be achieved by increasing the surface-to-volume ratio of studied materials. In contrast, the analysis of the electrons emerging from the sample surface provides information of the surface / sub-surface composition due to the fact that the photons are less attenuated than electrons. The comparison of the photon and electron decay intensities show the domination of the latter for all core levels below 1 keV[143].

Short mean free paths of the electrons require ultra-high vacuum conditions in the measurement chamber. The development of the particular TEY detectors[142] allowed utilization of the soft X-rays (250 eV < $h\upsilon$ < 1000 eV) for the measurements of gas/solid reaction conditions initiating the *in-situ* studies of the catalysts surface and enhancing the surface sensitivity of the method.

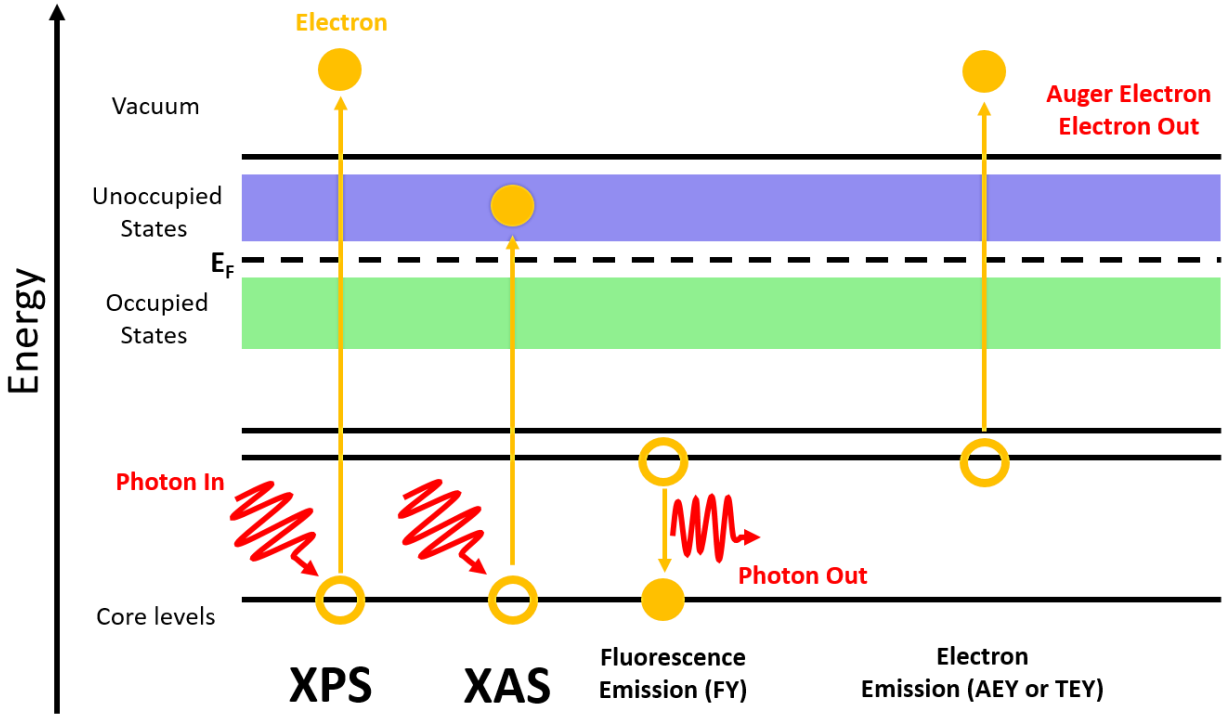

Figure 18. Scheme of the processes occurring during photoemission and absorption spectroscopies. Fluorescence (photon in/photon out) and electron (photon in/electron out) detection mode are also shown in the right-hand part of the scheme. The scheme was done based on the one shown in[144].

Near-edge X-ray absorption fine structure is a surface-sensitive X-ray absorption spectroscopy. The NEXAFS spectrum exhibits strong and distinctive features in the energy region just below and up to about 30 eV above the absorption edge[145,146], providing complementary information about the local structure[147]. Particularly, analysis of the O K edge spectra in combination with theoretical calculations allows to distinguish the oxygen sites of different binding configuration and environments.[148]

The reason of high surface sensitivity of NEXAFS technique is the relatively low kinetic energies of the electrons and the corresponding mean free path in the matter, similar to XPS. The surface sensitivity of this method can be further enhanced by recording electrons with particular kinetic energy. In Auger Electron Yield (AEY) mode only elastically scattered Auger electrons are recorded and this provides higher surface sensitivity than the total electron yield mode[145]. If all escaping electrons are counted so the energy of the measured electrons is not selected – Total Electron Yield mode detection – the signal-to-noise ratio is much higher in comparison to AEY but the surface sensitivity is lower[149]. The probing depth depends on the material, but the average values estimated for AEY are ca. 2-3 nm, while for TEY – 4-10 nm[149]. The comparison of these detection modes as well as the schematic presentation of XPS process and the Auger electrons (originated from the decay of valence electron into the core hole with transfer of the decay energy to another valence electron) ejection is shown in Figure 19[147].

The short inelastic mean free paths of the electrons emitted from the surface limit the application of XPS and NEXAFS (electron detection modes) techniques to ultrahigh vacuum conditions. In case of high pressure conditions, the electrons will be gas-scattered, however this problem was resolved in near-ambient pressure approach, whose development and the basic concept will be discussed in detail below.

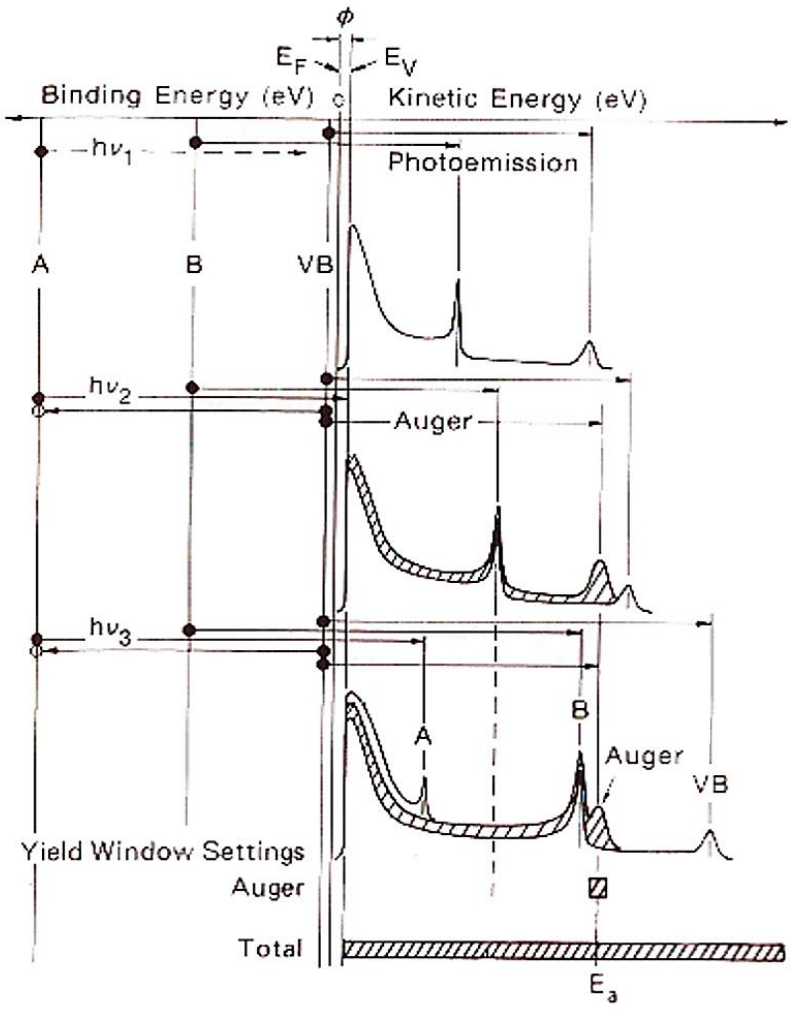

Figure 19. Energy level diagram and schematic photoemission spectra at different photon energies for a sample containing atoms with two core levels A and B and a valence band (VB). Taken from [147].

1.3.2. *In-situ* Near Ambient Pressure Spectroscopy

The first attempts to study the electrode/electrolyte interfaces "quasi" *in-situ* involved the following approaches:

- emersion techniques, involved the removing of an electrode from the electrolyte under the certain potential for subsequent analysis in UHV system[150];
- fast-freezing, consisting in injection of the aqueous solution onto cold sample holder in the measurement chamber and the UHV-XPS measurements were performed at liquid nitrogen temperature. This technique is capable to preserve the chemical speciation of the solutes and to prevent crystallizing of the solution[151];
- ionic liquids/electrode interface analysis under UHV[152].

The main obstacle for studying the real electrode/electrolyte interface under operational conditions was so-called "pressure difference" between the electrolyte solution and surface

characterization conditions. First, the introduction of the gas molecules into the XPS chamber will lead to the scattering of the photoelectrons before they reach the electron analyzer. Second, the X-ray source, the electron detector and analyzer must be kept under vacuum conditions.

The attenuation of the electrons due to scattering by gas molecules can be reduced by minimizing the path length of the electrons in the high-pressure region. This can be achieved by bringing the sample surface close to a differentially-pumped aperture (see the examples in Figure 20), behind which the pressure drops by several orders of magnitude[153–155]. Each differential pumping stage can provide pressure differentials of about 10^{-2} to 10^{-5} depending on the experimental conditions. This approach is known as near-ambient pressure XPS.[155–157] The upper pressure limit in NAP-XPS experiments can be increased by decreasing the size of the first aperture, which improves differential pumping as well as reducing the path length of the electrons through the high-pressure region. This allowed to increase the operating pressure limit up to 130 mbar[155]. In order to avoid significant loss of signal in the pumping stages, the photoelectrons are focused onto the differentially-pumped apertures using electrostatic lenses. Moreover, the utilization of high brilliance third generation synchrotrons (such as BESSY II, SOLEIL) provide intense X-rays, which makes possible the use of small front aperture diameters without diminishing of the photoelectron intensities[153].

The inelastic scattering of the photoelectrons by gas molecules obscures the sample photoemission spectrum. Figure 21 shows the example of the survey spectra recorded on IrO_2-based anode under 3 mbar water vapor and open circuit conditions. The introduction of the water vapor leads to the changing of the background shape due to the inelastic scattering. Molecular ionization is the dominant energy-loss mechanism for electrons with KE greater than a few times the ionization threshold, which is typically ca. 10 eV. The electron mean free path in a gas atmosphere defined as[153]:

$$\lambda_{electron} = k_B\, T / P\, \sigma_{electron} \quad (Eq.\ 21)$$

where P – working pressure; $\sigma_{electron}$ – the electron-molecular scattering cross-section. The scattering depends critically on the type of gas which determines σ[154]. Particularly, Figure 22 shows the inelastic cross-section values for water vapor by electrons with kinetic energies from 2 to 1000 eV. The shape of the curves means that in the most surface sensitive XPS measurements the attenuation of the electrons by the gas will be the strongest. The gas scattering of the X-ray photons is generally much weaker than for the photoelectrons (the cross-sections of the former are several orders of magnitude smaller)[153].

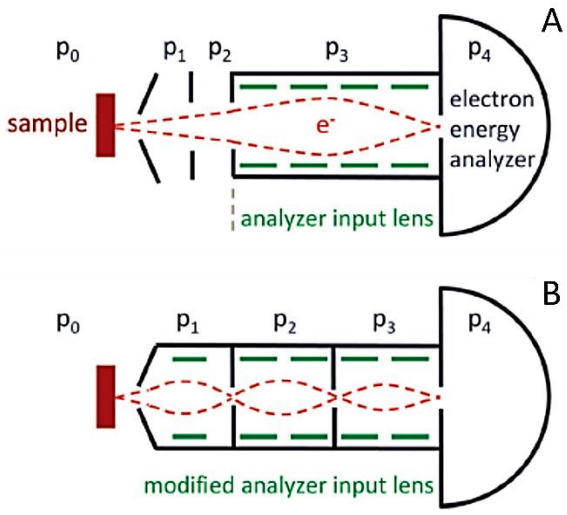

Figure 20. Schemes of differential pumping systems used in NAP-XPS. Panel A represents a standard analyzer lens with a set of pumping apertures in front of it, while Panel B shows the principle used at ISISS beamline of BESSY II synchrotron with a differentially-pumped lens system. Taken from[155].

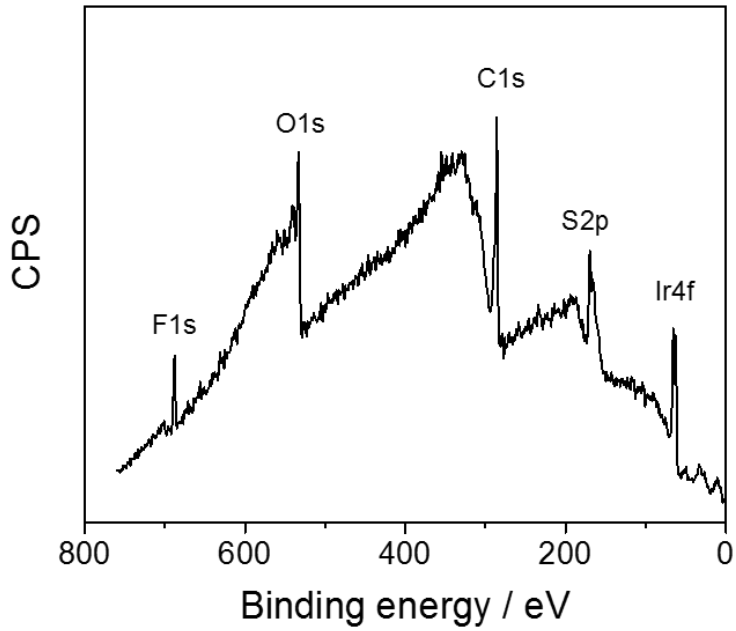

Figure 21. Survey spectrum recorded on IrO_2 anode under 3 mbar water vapor and open circuit voltage. Photon energy 820 eV.

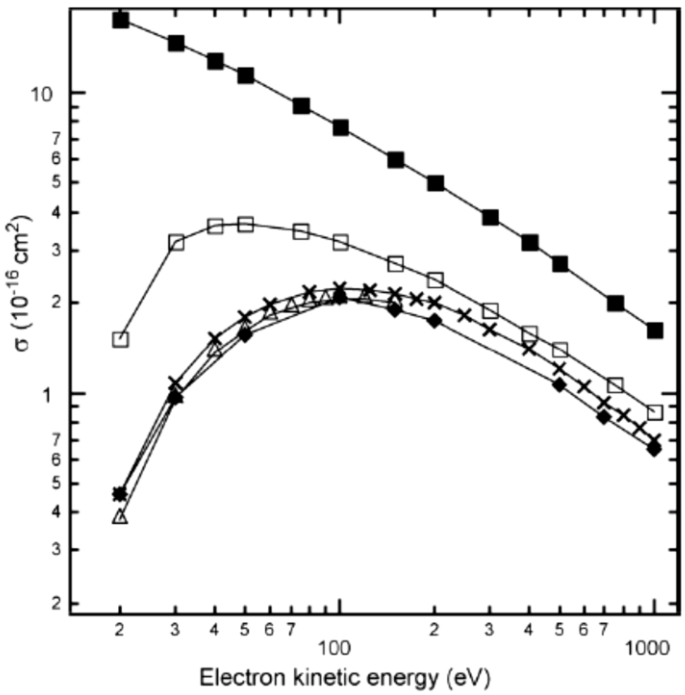

Figure 22. Inelastic electron scattering cross-section of the water molecule as a function of electron kinetic energy in the energy range relevant for XPS. Figure was taken from Bluhm[154]*, where the symbols correspond to the data obtained by others. The total electron scattering cross-section (inelastic, elastic and rotational) is shown by (■).*

Regardless of the large range of the pressures currently available in the NAP-XPS, the threshold value used in real measurements is defined by the signal-to-noise ratio of the obtained photoemission spectra. In its turn, the latter depends on the kinetic energy of the emitted electrons. The electrons with higher KE are less gas scattered, meanwhile their surface sensitivity will be diminished. Besides, the pressure limit used in NAP-XPS studies is determined by the gas ambient (the scattering cross section changes with the gas type), by the core-level cross-section of the analyzed elements and by the experimental parameters such as the electron flux and the beam size.

The introduction of differential-pumping system can be realized by various schemes. The most basic contains two or more pumping stages placed between the sample and the entrance to the electron analyzer input lens. The scheme of this design is shown in Panel A of Figure 20. This configuration is quite simple as no modifications of the lens system are required and the differential pumping stages can be easily added to the system. However, this configuration limits the efficiency of the electron detection. This drawback has been overcome by the integration of the differential pumping directly into the electrostatic lens system[158]. Panel B of Figure 20 shows the example of this system currently in use at the ISISS beamline of BESSY II synchrotron. This scheme provides a pumping difference of 10^{-8} between the *in-situ* cell and the hemisphere analyzer and allows an increase of the detection efficiency of photoelectrons, as compared to panel A design, by up to few orders of magnitude[155].

In addition to the electron detector, the X-ray source also has to be kept under vacuum conditions. This can be achieved either by differential pumping stages (NAP-XPS set-up at TEMPO, SOLEIL), or by the use of X-ray transparent windows such as silicon nitride (used at ISISS, BESSY II), aluminum or polymer membranes with thickness of a few hundreds of nanometers and an active window area in the square millimeter range[154,155].

Further development of the NAP-XPS approach is not limited to the variation of the differential pumping schemes, but also includes the evolution of *in-situ* cells used in the NAP-XPS studies. The specific designs allow controlling the environment of the sample more precisely and broadening the variety of the analyzed samples and systems. The cell can be designed in a way to perform the particular sample preparation or pretreatment, to do the analysis of more complex systems such as fuel cells/electrolyzers what will be discussed later in details.

By pushing the operating pressure to higher values and continuous development of the instruments and experimental cells, the NAP-XPS technique became an important *in-situ* tool for studies of the solid/gas and solid/liquids interfaces vital for many research fields, including the electrochemical conversion devices[155,159]. It should be mentioned, that besides photoemission studies, the near-ambient pressure approach can be applied to AEY mode of the absorption spectroscopy technique. The application of photon-in-electron-out mode provides the surface sensitivity similar to XPS, thus, adding the additional information, e.g. related to the changes in the structure[160].

In the last decades the development of NAP-XPS spectrometers was mainly done for the synchrotron-based radiation sources, while currently the interest to the high pressure laboratory-based instruments is also growing[161].

1.3.3. Electrochemical Cell for *in-situ* Measurements

The configuration of the cells used for *in-situ* spectroscopic studies of gas/solid (liquid/solid) interfaces can be realized either by separation of the vacuum analyzing chamber and the sample under the ambient conditions or by implementation of the differential pumping system discussed previously. The following sub-sections are devoted to the various electrochemical cells developed for *in-situ* NAP-XPS measurements of energy conversion devices. Considering their vast variations depending on the analyzed systems, only the ones applied to the water electrolysis/fuel cell technologies are overviewed and discussed relating to the approach used in this work.

1.3.3.1. “Dip & Pull” Approach

The principle of the “dip & pull” method is based on the emersion electrode technique[150] used previously for quasi *in-situ* studies before the NAP-XPS approach introduction. The set-up developed at Lawrence Berkeley National Laboratory (USA) allows study of the solid-liquid interface of a thin layer of the electrolyte (10-30 nm) on the electrodes surface[162]. The advantage of this configuration is the availability of the reference electrode absent in the Nafion-based cells discussed further (see the scheme in Figure 23). In order to penetrate the thin liquid layer of the electrolyte on the solid surface the “tender” X-ray synchrotron radiation (X-ray energy from 2 keV to < 7 keV, between soft and hard X-rays) is applied.

This method was successfully used to the investigation of the following electrochemical processes: Pt oxidation in KF[162] and in alkaline electrolyte[163], oxidation-reduction cycles of Ni–Fe oxyhydroxide electrode in KOH solution[164] and the energy-band relations of semiconductor and metal-covered semiconductor interfaces in the direct contact with liquid electrolyte[165]. This approach was also used to study the potential distribution in the electrochemical double layer at a solid/liquid interface.[166]

In spite of the numerous successful *in-situ* spectroscopic studies performed by this method, the most challenging part is still the integrity of the electrolyte film throughout the experiments and the reproducibility of the electrolyte film of the same thickness and consequently of the results obtained. Another drawback of this set-up geometry is high values of the ohmic losses through the liquid film and diffusion of the ions into and out of the film is slow. Moreover, due to the distribution of the ohmic losses along the electrode surface, their contribution cannot be taken into account for by iR corrections[164]. The redistribution of the ions and potential drop also lead to the changes in the local pH of a thin electrolyte film affecting the measurements. Thus, all the sites are exposed to different polarization conditions and will contribute to the average XPS signal obtained in this set-up complicating the data interpretation.

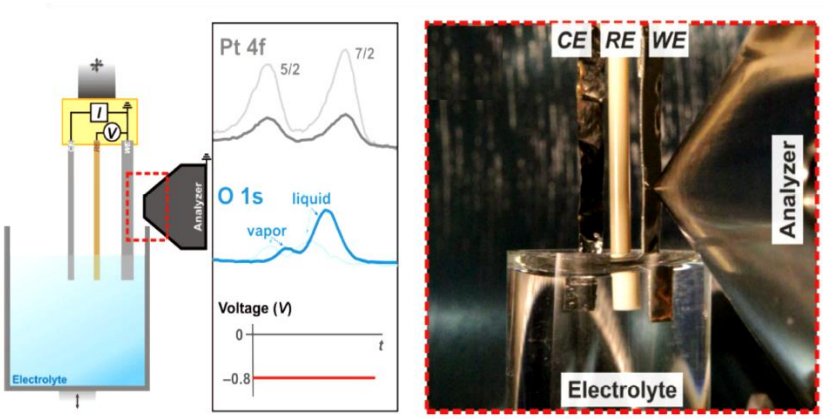

Figure 23. Left-hand panel: Schematic of three-electrode electrochemistry set-up in the NAP-XPS chamber.Middle panel: Pt4f and O1s XP spectra of the partially removed electrodes under applied potential and under water vapor (without polarization). Right-hand panel: image of the set-up. Figure was taken from[162].

1.3.3.2. Graphene-based Electrochemical Cell

The separation of the electrochemical cell and the vacuum measurement chamber with electron transparent membranes such as SiN_x and graphene-based compounds has been successfully realized in various configuration for *in-situ* HR TEM measurements.[167–169] Recently, the same approach was applied for liquid/solid interface studies by soft X-rays XAS.[170,171]

Among other materials, recently developed graphene oxide based membranes possess the following properties: superior mechanical stability, gas impermeability and transparency to the X-rays in the region of 100 – 1000 eV. Thus, these membranes have been considered as promising candidates for the electrochemical cell fabrication applied in different types of spectroscopies and microscopies[172]. The ultrathin mono- and bilayer graphene films allows the photoelectrons escaping from the sample surface to be detected on the vacuum side wherein the kinetic energies of the emitted photoelectrons should be higher than 400 eV in order to penetrate this membrane. Figure 24 shows an example of the set-up containing a catalyst layer deposited on a graphene-based separated membrane, while the latter is on silicon nitride grid (see panel C of Figure 24)[173]. This approach was developed at the Department of Inorganic Chemistry of FHI (Berlin, Germany).

The feasibility of the use of graphene-based membranes in the analysis of the liquid/solid and gas/solid interfaces using XPS has been demonstrated by several model studies on sputter-deposited nanoparticles of gold[172], iridium and copper[174] placed on the back side of the membrane. However, the configuration of the graphene-based cell defines and consequently limits the type of the catalysts available for the deposition on the membrane.

This approach allows analysis of the gas/solid and liquid/solid interfaces by means of XPS and surface sensitive XAS (photon-in-electron-out detection mode) without implemented differential pumping system of the spectrometer. The principle of the cell is similar to the one used

in the electrochemical flow cell introduced by *Binninger et al.*[171] for *in-situ* XAS studies in a transmission detection mode (PSI, Villigen, Switzerland).

Among the limitations of the graphene-based window for this kind of *in-situ* studies is the poor stability of the graphene structure to the presence of any cross-contamination[175]. The reproducibility of the prepared defect-free graphene layers and their stability in various experiments and consequently of the obtained results remain a great challenge for their wide application.

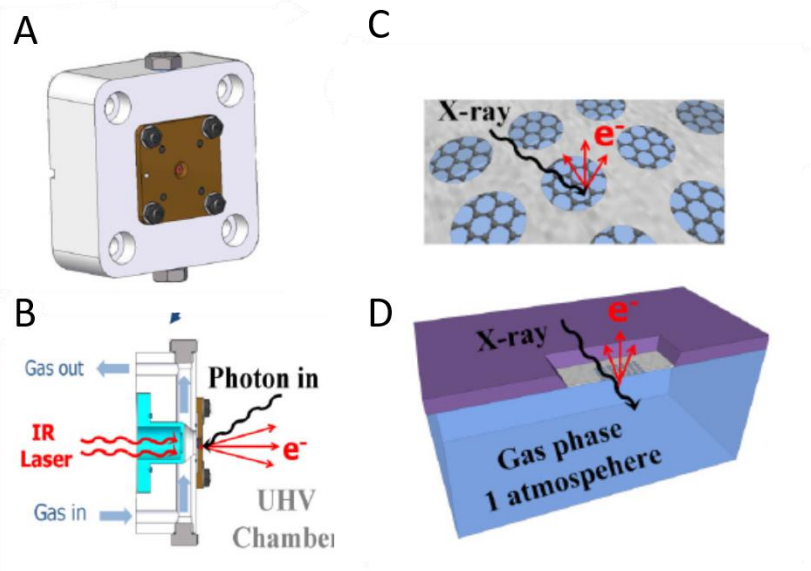

Figure 24. The scheme of the gas cell (A) and its cross-section (B) used in the AP-XPS set-up. Panels C, D: sketch of the graphene-based membrane. Taken from[174].

1.3.3.3. Electrochemical Cell with Liquid Reservoir

The principle of the cell used for the *in-situ* studies of the gas-phase water electrolysis developed at FHI (Berlin, Germany) was based on the water permeability of the proton exchange membrane[100]. Figure 25 shows the sketch of this cell, consisting of a Pt-coated Nafion membrane which is sealed on one side with the liquid water reservoir. The electrode side is exposed to the spectrometer and does not have any gas/water vapor suppliers. The Pt film is porous enough to permit the diffusion of water from the liquid reservoir side to the analyzed electrode side in virtue of the pressure difference leading to the pressure in the measurement chamber up to 10^{-2} mbar. The cell was designed in the way to allow switching the working electrode (WE) and counter electrode (CE) sides allowing studying both hydrogen and oxygen evolution reactions.

The main disadvantage of this cell configuration is the reservoir volume leading to quite short measurement times and the difficulties in the data reproducibility since the reservoir dried out very fast. This affects also the distribution of the water in the membrane. The improvement of this cell using the continuous flow of water is shown in Figure 26 (left)[108]. This allowed increasing

the time frames of the experiment and improving the reproducibility of the obtained results. However, the distribution of water along the membrane and consequently the distribution of the conductivity and ohmic losses still cannot be neglected and must be taken into account.

Regarding the sample preparation, the absence of the ionomer in the catalyst layer limits the electrode/electrolyte interface, while the deposition of the porous and continuous electrode film used in these studies is difficult to reproduce restricting the choice of the analyzed samples.

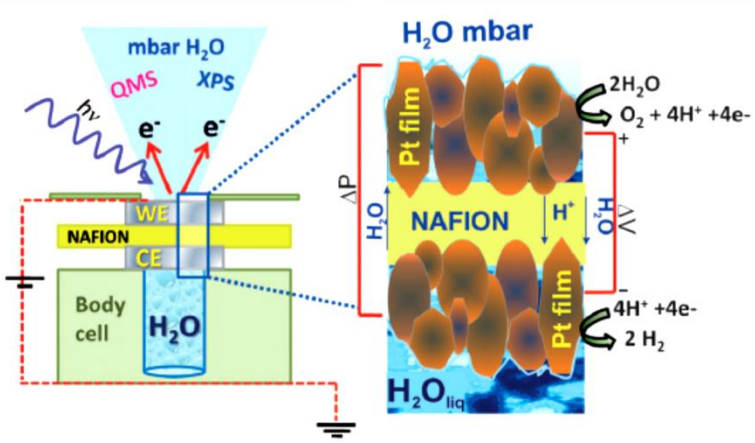

Figure 25. The electrochemical cell for in-situ spectroscopic measurements with liquid reservoir. The porosity of the Pt film is shown on the right. Taken from[100].

1.3.3.4. Three Electrodes Electrochemical Cell

The cell with the liquid water flow was further improved by the addition of the micro reference electrode (FHI, Berlin) and replacement of water by liquid electrolyte[108]. The introduction of the reference electrode led to an additional modification of the cell. In order to decrease the distance between the working and the reference electrodes, Pt counter electrode was removed from the back side of the Nafion membrane (left Panel of Figure 26) and was replaced by an external Pt wire. The scheme of a new set-up is presented on the right Panel of Figure 26. The configuration of the cell allows study of different catalysts system by varying of the electrolyte type. Particularly, this set-up was used for *in-situ* investigation of iridium film electrode surfaces under the OER conditions[108].

The presence of the reference electrode can be considered as the main advantage of this cell in comparison to other Nafion-based cell configurations discussed in this section. Nevertheless, the presence of liquid electrolyte flowing through the cell increases the overall ohmic losses and complicates the management of the set-up. The time frames of the experiment are constrained by the volume of the electrolyte and the flow rate. The presence of the gas bubbles in the electrolyte flow leads to the electrode disconnection and consequently to the interruption of the experiment.

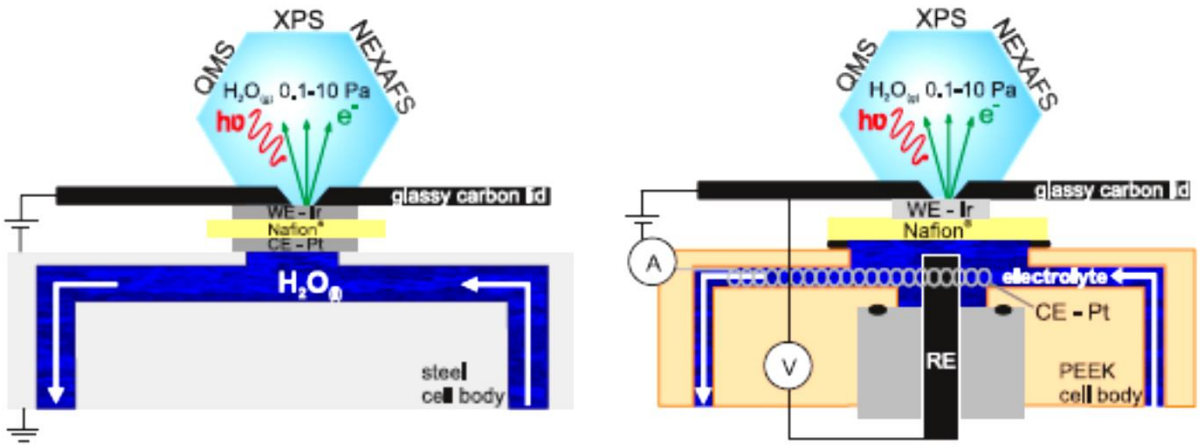

Figure 26. Left panel: two-electrode electrochemical cell for in-situ NAP-XPS measurements with constant water flow. Right panel: three-electrode cell with an electrolyte. Taken from[108].

1.3.3.5. PEM Fuel Cell Design

Another attempt to provide an insight into the potential-induced changes in liquid/solid interface was performed at ICPEES (Strasbourg) using phosphoric acid (PA) – imbibed membrane used for HT PEM FCs. The main advantage of this type of the membrane for relatively dry ambient conditions of experimental XPS chamber is its excellent proton conductivity and low vapor pressure of phosphoric acid H_3PO_4. The sketch of the membrane-electrode assembly (MEA) consisting of the PA-imbibed membrane coated by the catalyst/ionomer layer from the both sides is shown in Figure 27[176]. The working electrode is coated by the catalyst of interest, while the counter electrode was covered by Pt. The loading of Pt on the CE side of the MEA was ca. 10 times higher than the loading of the WE. This allowed reducing the overpotential on the CE.

The main difference of this configuration in comparison to the similar set-ups discussed earlier is the exposure of the anode and cathode sides to the same ambient conditions avoiding the water distribution across the membrane. It is also important that the cell design allows investigation of a wide range of fuel cell and electrolysis cell systems under conditions comparable to their conventional operation. Another advantage of the cell and the sample prepared for this set-up is its simplicity. This design allowed performing the *in-situ* measurements of various catalyst systems operating at high temperatures as it was shown for Pt[176,177], PtAu[102], PtRu[178]. Among the main disadvantages of this approach for *operando* studies is the absence of the reference electrode (RE) and the issues related to the PA electrolyte itself.

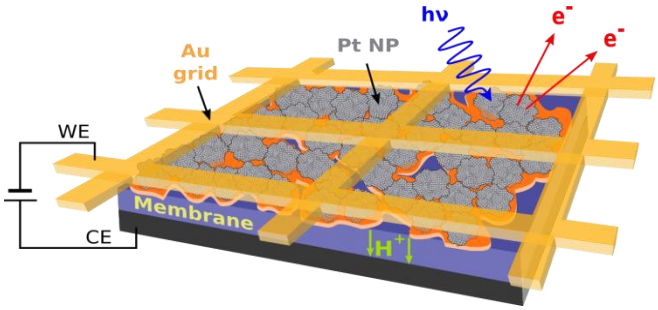

Figure 27. Scheme of a model MEA used for in-situ NAP-XPS measurements in[176].

Another design of fuel cell developed in Joint Center for Artificial Photosynthesis and SLAC National Accelerator Laboratory was based on the same principle of the Nafion membrane permeability discussed above, while the anode and the cathode sides are exposed to different atmospheres. The scheme is shown in Figure 28, where the Nafion membrane coated on both sides with Pt nanoparticles, cathode and anode sides of the fuel cell. The anode was sealed within a chamber filled with humidified 95% N_2 / 5% H_2 gas mixture flow. The other side (cathode) was exposed to the XPS chamber filled only with the oxygen gas. One of the main improvements of this cell in comparison to the ones discussed above was the introduction of the Nafion ionomer in the catalyst layer enhancing the utilization of the catalyst active surface[179]. The presence of hydrogen on the CE side allows using this Pt electrode as a pseudo-reference.

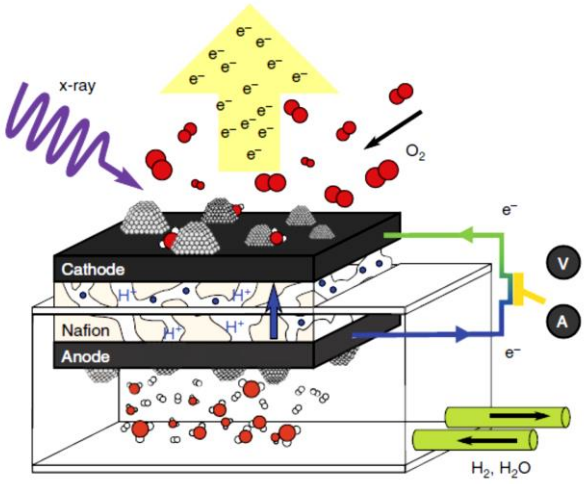

Figure 28. Scheme of the PEM fuel cell set-up for the in-situ NAP-XPS studies. Taken from[179].

This design allowed application of the set-up to other systems, e.g. water electrolyzers. IrO_2 anode was analyzed using *in-situ* NAP-XPS under open circuit and OER conditions[101]. The humidification of the Nafion membrane was realized from both electrode sides in a different way. The anode side exposed to the measurement chamber was humidified by water vapor (10 Torr = 13.3 mbar, ca. 50% relative humidity (RH) at 25 °C) meanwhile the Pt-containing cathode side

was sealed within the back-side chamber and filled by the saturated water vapor. Nafion ionomer was used on both electrode sides.

While the overall principle of the set-up is quite simple, the preparation of the corresponding sample sealed between two chambers is not straightforward, as well as the exchange of the analyzed sample is time consuming.

1.3.3.6. Approach used in this Work

In order to choose the appropriate set-up for the *operando* studies of OER anodes for PEM water electrolysis performed in this work, the pros and cons of each of the approaches had to be taken into account.

The utilization of liquid water instead of water vapor would improve the reliability of the performed measurements but the presence of liquid film on the electrode surface requires hard/tender X-rays (as it was shown in Dip & Pull method) that would decrease the surface sensitivity of the XPS.

The introduction of reference electrode resolves the problem of the potential scale definition, while many of the studies mentioned above were done in two-electrode set-ups where the potential of the working electrode was not well determined. In most cases, the polarization conditions were correlated to the corresponding gas phase evolution obtained by mass spectrometer online to the measurement chamber to analyze the ambient. The introduction of the third electrode requires a modification and further development of the set-up.

The preparation of the appropriate MEA for *operando* spectroscopic measurements is another important issue. Both catalyst layers (anode and cathode side) have to be prepared using the corresponding ionomer solution in an appropriate ratio and the sprayed layer should possess an optimal thickness to avoid either the presence of disconnected particles or the blocking of the electrode/electrolyte interface.

In this work we used the design proposed by *Law et al.*[176], where the PA-imbibed membrane was substituted by a proton exchange membrane. The catalyst layers were prepared the same way as for the real PEM electrolyzer. In order to obtain the appropriate humidification of the membrane and delivery of the reactant molecules the MEA was exposed to the same ambient in the NAP chamber and no separation of the WE and CE chambers was used. The presence of Pt on the CE side of the MEA and its higher loading (approximately one order of magnitude) in comparison to the WE side allowed us to use it as a dynamic hydrogen electrode under the OER conditions. This and other details of the cell configuration used in this work and further information on the analyzed materials, the setup, and measurement techniques will be given in Chapter 2.

1.4. Conclusions of Chapter 1 and Objectives of PhD Thesis

The main obstacle on the road to the full transition to the renewable energy is an appropriate grid-scale chemical energy storage solution. In this case, hydrogen is playing the key role and the easiest way of its storage is the electrocatalytic splitting of water into hydrogen and oxygen. Despite the well-established and durable alkaline electrolysis technology, the issues in gas purity, safety and response time have pushed the research and the industrial interest toward the PEM electrolysis technology. PEM water electrolyzers have a relevant technological potential because of their theoretical high efficiency, compact design, simplicity of the auxiliary system, easy maintenance, rapid response and wide dynamic operation range. However, questions related to their efficient performance as well as durability and degradation are still not fully answered. One of the major problems is the high-cost of iridium used as a state-of-the-art anode catalyst for the OER. Numerous attempts on the development of active and stable alternative catalysts have been made. The complexity of the oxygen evolution reaction coupled with the constant evolution of the catalysts surface under the reaction conditions perplex the understanding of the processes taking place at the electrode/electrolyte interface during the reaction. Meanwhile without the corresponding understanding of the OER mechanism and the behavior of state-of-the-art electrodes further progress in PEM electrolysis development will be highly limited.

Recent development of the surface-sensitive methods instrumentation, such as XPS and soft X-rays NEXAFS, resulted in the increase of the operation pressure, allowing *in-situ* studies of the solid/gas interfaces under operation conditions. The vast variety of the electrochemical cells constructed for these measurements is related to the specificity of the analyzed systems as well as to some technical issues.

This thesis is devoted to the application of NAP-XPS and NEXAFS techniques for the *in-situ* investigation of the OER anodes for the PEM water electrolyzer in order to shed light on the following issues remained controversial and unanswered by the time the work started:

- OER mechanism on Ir and Ru-based catalysts: similarities and differences, nature of the active sites;
- Degradation of Ru-based catalysts under the OER conditions and the role of Ir in stabilization of Ru oxide;

- Impact of the catalyst composition (oxide nature) on the OER activity and stability: electrochemically and thermally formed oxides;
- Enhanced activity and stability of the supported iridium-based catalyst, metal support interaction phenomena.

Chapter 2. Materials and Experimental Techniques

2.1. Materials

The unsupported single and mixed Ir-, Ru-based metallic nanoparticles and oxides as well as supported Ir-based catalysts studied in this work were synthesized at DLR (Stuttgart, Germany) by L. Wang by direct sodium borohydride reduction of Ir and Ru salts in the presence of a surfactant agent in a water-free environment[117,180]. Anhydrous Iridium Chloride ($IrCl_3$, Alfa Aesar) and Ruthenium Chloride ($RuCl_3$, Alfa Aesar) were used as the precursors. For the mixed $Ir_{0.7}Ru_{0.3}$ nanoparticles, the analogous procedure was applied by using the same precursors with a stoichiometric Ir:Ru atomic ratio of 7:3. In order to obtain Ir, Ru-based oxides the corresponding metallic Ir, Ru and IrRu nano-particles were oxidized in a furnace under air by using a ramp of 5 °C min^{-1} and a dwell time of 0.5 h at 490 °C[110,181]. The maximum temperature of 490 °C was chosen in order to minimize the surface area decrease through particle agglomeration and coalescence. The electrcatalysts obtained by such thermal oxidation are labeled as "thermal" (RuO_2, IrO_2, $Ir_{0.7}Ru_{0.3}O_2$). The electrochemical treatment (potential cycling as electrode pretreatment, electrode polarization during the spectroscopic measurements) of metallic Ir,Ru-based electrode materials leads to the formation of an oxide layer on the surface of the particles. These materials are referred as "electrochemical" oxides (marked as $Ru@RuO_x$, $Ir@IrO_x$), however their structure mostly corresponds to a metallic core covered by a thin oxide layer.

The SnO_2:Sb aerogels used as the support material for the Ir catalyst were prepared by G. Ozouf at MINES ParisTech (Sophia Antipolis, France)[123]. The powders were synthesized by an acid-catalyzed sol–gel route starting with metal alkoxides, tin isopropoxide (Alfa Aesar, 99% (metals basis)) and antimony (III) isopropoxide (Alfa Aesar, 99.9% (metals basis)), as precursors. The supported Ir catalyst (Ir/SnO_2-Sb) was further synthesized by $NaBH_4$ reduction via adding the SnO_2:Sb aerogel to the $IrCl_3$ ethanol solution[132], the iridium loading was 30 % wt.

The membrane-electrode assemblies were fabricated by myself using the catalyst-coated membrane method. The E87-05S Aquivion membrane and Aquivion dispersion D72-25BS (Solvay™) were chosen as the solid electrolyte. Catalyst inks were prepared by mixing the synthesized catalyst powders (in a metallic or oxide forms) for the working electrode and HiSpec4000 Pt 40 wt.% Pt/C from Johnson Matthey for the counter electrode, isopropyl alcohol (AMRESCO) and ultra-pure water with the ratio 1:1, and an Aquivion dispersion (20 wt.%. relative to the total solid content of the ink). The prepared inks were sonicated for 1 h and sprayed on the membrane with a spraying gun Iwata (Japan) at 100°C followed by the pressing procedure (5 minutes at 5 bar). The catalyst loading on the WE was controlled at 0.1 mg cm^{-2}, whereas platinum loading on the CE was 1 mg cm^{-2}. In case of Ir/ATO catalyst system, the precious metal loading was 0.5 mg cm^{-2}. Higher loading of the CE was chosen intentionally in order to minimize

overpotential of the corresponding hydrogen evolution reaction. In this way, it was possible to use the CE as a dynamic hydrogen electrode what will be discussed later in detail. The geometric area of the electrodes was 0.9 cm^2.

2.2. *Ex-situ* Material Characterization

Pristine and post-mortem catalysts powders and membrane-electrode assemblies have been characterized *ex-situ* using methods described in the following subsections.

2.2.1. X-ray Diffraction

The phase composition of the catalyst powders were studied with X-ray powder diffraction (XRD) using a Bruker D8 Advance diffractometer with a Cu source. The reference data were taken from the database of the International Centre for Diffraction Data (ICDD).

2.2.2. Scanning Transmission Electron Microscopy and Energy-Dispersive X-ray Spectroscopy

The analysis of the particle shape and size distributions as well as the elemental mapping were performed by Transmission and scanning transmission electron microscopy coupled with the energy-dispersive X-ray spectroscopy (EDX) analysis. In order to study the electrocatalyst particles after their operation, the corresponding WE sides of the MEAs were scratched with a diamond pen and the obtained powders were transferred to a copper grid for further microscopy measurements. The analysis was done at IPCMS (France) and at the University of Anwerp (Belgium).

Except for Ir/ATO catalyst system, the STEM was performed with a LaB6-JEOL 2100 microscope operating at 200 kV with a point to point resolution of 0.1 nm. TEM was carried out with JEOL 2100F instrument operating at 200 kV with a 0.2 nm resolution. The measurements were performed by Corinne Ulhaq-Bouillet (IPCMS, France). The Fast Fourier Transformation and the microscopy images treating and analysis were done using the DigitalMicrograph software.

The microscopic analysis performed at Electron Microscopy for Materials Science group (University of Anwerp, Belgium) was performed by Maria Batuk. Transmission electron microscopy images, high angle annular dark field scanning transmission electron microscopy (HAADF-STEM) images and energy dispersive X-ray maps were acquired using a FEI Titan 80-300 “cubed” microscope equipped with a Super-X detector and operated at 300 kV. The probe current was 150 pA. Sn-L (3.44 keV), Sb-L (3.50 keV), Ir-L (9.17 keV) and O-K (0.52 keV) lines were used for the chemical maps.

2.2.3. Scanning Electron Microscopy

The success of the *in-situ* spectroscopic studies of the MEAs strongly depends on their quality, in particular on the integrity of the catalyst layer. The previous results performed by our group[176,177] have demonstrated the complexity of the NAP-XPS data interpretation when disconnected particles are present within the electrode film. The configuration of the set-up was close to the one used in this work, where the WE is grounded through the potentiostat. This means that during XPS measurements the BE position of the elements originated from the WE will not be shifted with polarization. On the other hand the BE of the elements arising from the ionomer should be shifted by the potential difference applied between the WE and the CE. However, the results obtained on Pt-based electrodes shown in[176,177] revealed the presence of an additional doublet in the Pt4f spectra, which shifted with the applied potential the same way as the electrolyte-originating elements (see the BE shifts for different elements in Figure 30). This shifting component observed in Pt4f XP spectra (Panel A of Figure 29) was attributed to the disconnected particles or agglomerates which are not in contact with the current collector (see scheme in Figure 27) observed later on this electrode by means of SEM analysis (Panel B of Figure 29).

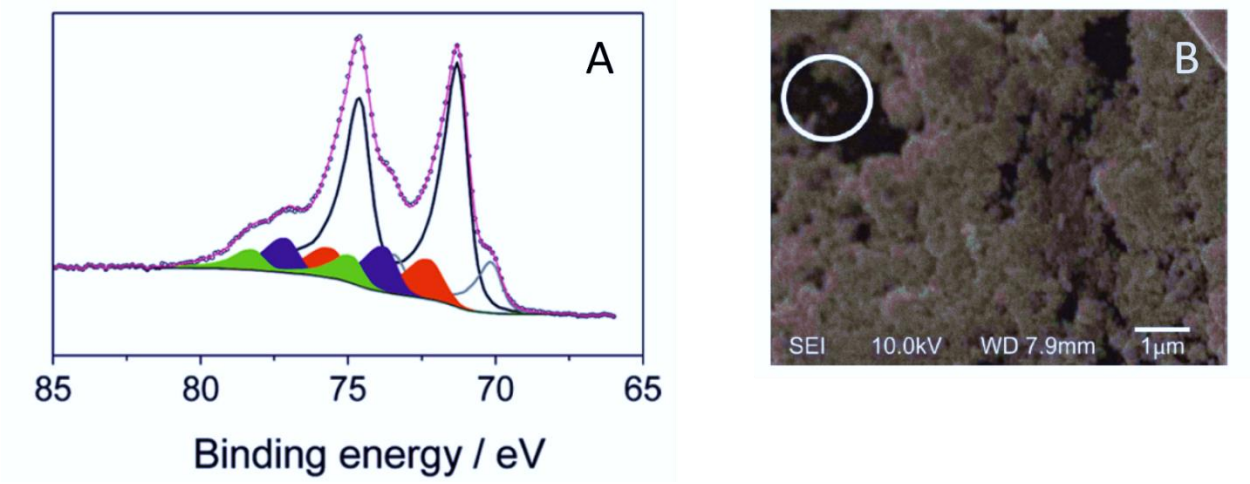

Figure 29. Panel A. Pt4f XP spectra recorded on Pt-based MEA (with a PA-imbibed membrane) under 0.11 mbar H_2O/0.16 mbar O_2 at 150°C and 0.8 V vs OCV. The fitting: Pt metal (black); disconnected Pt metal (gray); Pt covered by adsorbed O/OH (red); PtO (blue) and PtO_2 (green). Panel B. SEM image of Pt working electrode where a white circle shows the disconnected particles. Taken from[177].

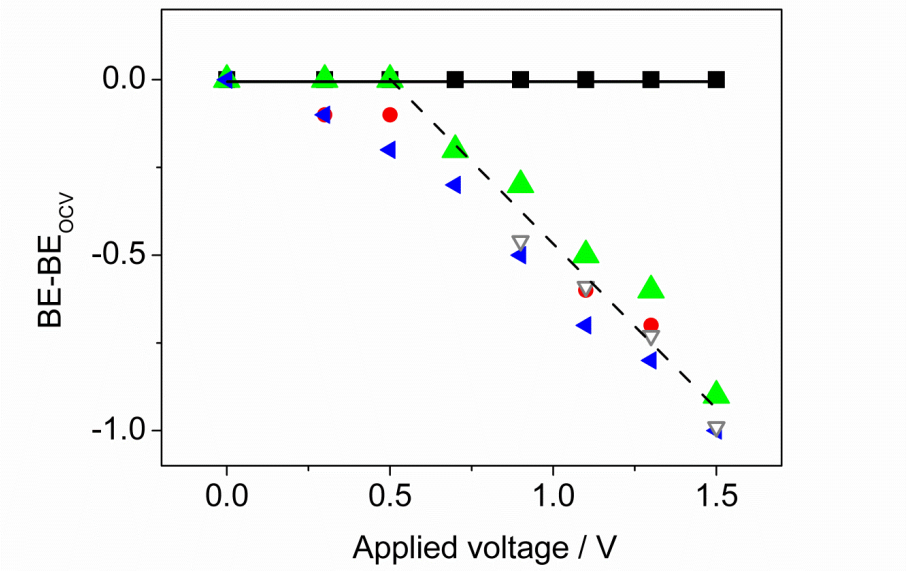

Figure 30. The BEs of the Pt4f$_{7/2}$ main peak (black), O1s (green), C1s (red), P2p (blue), Pt4f$_{7/2}$ "disconnected" (gray) peaks as a function of the applied voltage. The spectra were collected on Pt-based MEA (with a PA-imbibed membrane). Taken from[177].

Thus, the distribution of the sprayed WE catalyst along the membrane has been verified for each MEA batch prepared for the studies at the synchrotron facilities by scanning electron microscopy (SEM). An example of a characteristic SEM image of a uniform catalyst layer is shown in Figure 31.

Throughout this work, two instruments were used: Jeol JSM-6700F (Japan) and Zeiss Gemini SEM 500 both with a lattice resolution of 1 nm. The measurements were done by Thierry Dintzer (ICPEES and IPCMS, France).

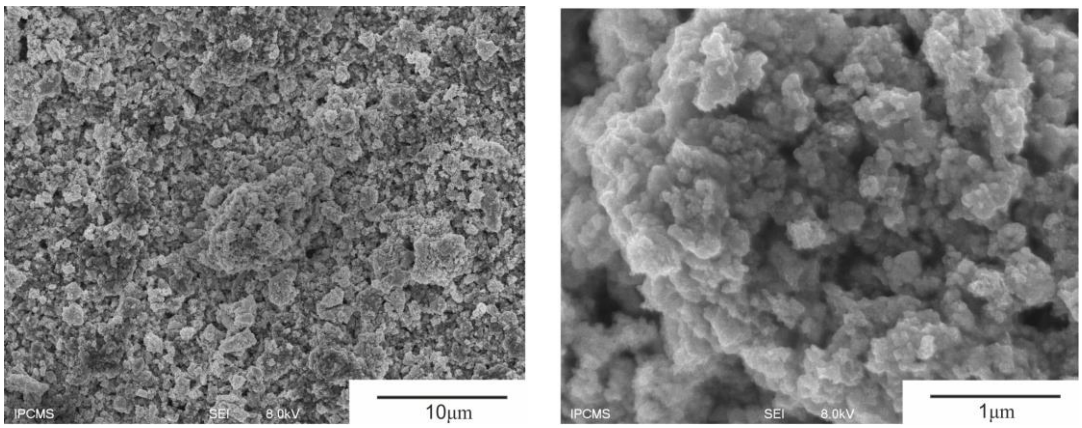

Figure 31. Typical SEM images of the WE side of the MEA acquired at different magnifications showing the uniformity and the integrity of the Ir$_{0.7}$Ru$_{0.3}$O$_2$ layer.

2.2.4. X-ray Photoelectron Spectroscopy

The XPS analysis of the pristine and post-mortem catalyst powders under UHV conditions (10^{-9} mbar) was performed with a Multilab 2000 Thermoelectron spectrometer (ICPEES, France)

by myself and a Thermo Scientific ESCALAB 250 instrument (DLR, Germany) by Pawel Gazdzicki. In both cases, Al Kα radiation was used as the X-ray Source. The analysis of the XP spectra will be discussed for each particular case in the next chapters.

2.2.5. Characterization in Liquid Electrolyte

The electrochemical characterization of the Ir,Ru-based catalysts in liquid electrolyte discussed in this Thesis was done by L. Wang (DLR). The measurements were conducted in N_2-saturated 0.05 M H_2SO_4 at 25°C. The rotating disc electrode studies were performed using an Autolab PGSTAT12 potentiostat while the electrochemical impedance spectroscopy (EIS) analysis was carried out with a Zahner IM6 electrochemistry workstation. The catalyst-contained ink was prepared following the same procedure as the one used for the MEAs fabrication and was deposited on a glassy carbon rotating disk electrode (GC-RDE, PINE, 0.196 cm^2) used as a support. The catalyst loading was 60 $\mu g\ cm^{-2}$. Pt foil was used as a counter electrode and reversible hydrogen electrode (RHE) – as a reference. For reproducibility, at least 4 independent electrodes were prepared and measured for each catalyst sample. The ohmic resistance of the electrolyte between the working and the reference electrode was determined by EIS before each measurement and used for the iR corrections. The corresponding values are provided for each catalyst system.

2.3. Laboratory Set-up for Preliminary Studies

Besides the physical chemistry characterization of the catalysts powders and the corresponding MEAs, their electrochemical performance has been studied in the laboratory set-up simulating the conditions of the NAP chamber used at synchrotron facilities. The MEA resistance was examined by means of high frequency impedance spectroscopy measurements depending on the relative humidity level of the surrounding environment. The difference between Nafion- and Aquivion-based MEAs regarding their response to low humidity conditions studied by cyclic voltammetry and electrochemical impedance spectroscopy is also shown in this section.

All electrochemical measurements during the laboratory tests and *in-situ* synchrotron measurements were performed using a μ-AutoLab potentiostat from Metrohm.

2.3.1. Set-up Description

The set-up designed by W. Doh at ICPEES (Strasbourg, France) for the MEA tests under the low humidity ambient conditions consists of a stainless steel cylindrical chamber equipped with a sample holder, oxygen-free liquid water reservoir, capacitance gauge CMR 392 and control unit RVC 300 (Pfeiffer Vacuum), vacuum pipeline valve PV25MK (Edwards) and a dual stage rotary vane vacuum pump 5 E2M5 (Edwards). The MEA is placed on the ceramic sample holder and is covered by two stainless steel plates from both sides. The Au grid is used as the current collector and placed between the MEA and covering plates from both electrode sides. The plates are connected through the corresponding wires to the potentiostat. The photos of the set-up and the sample holder are shown in Figure 32.

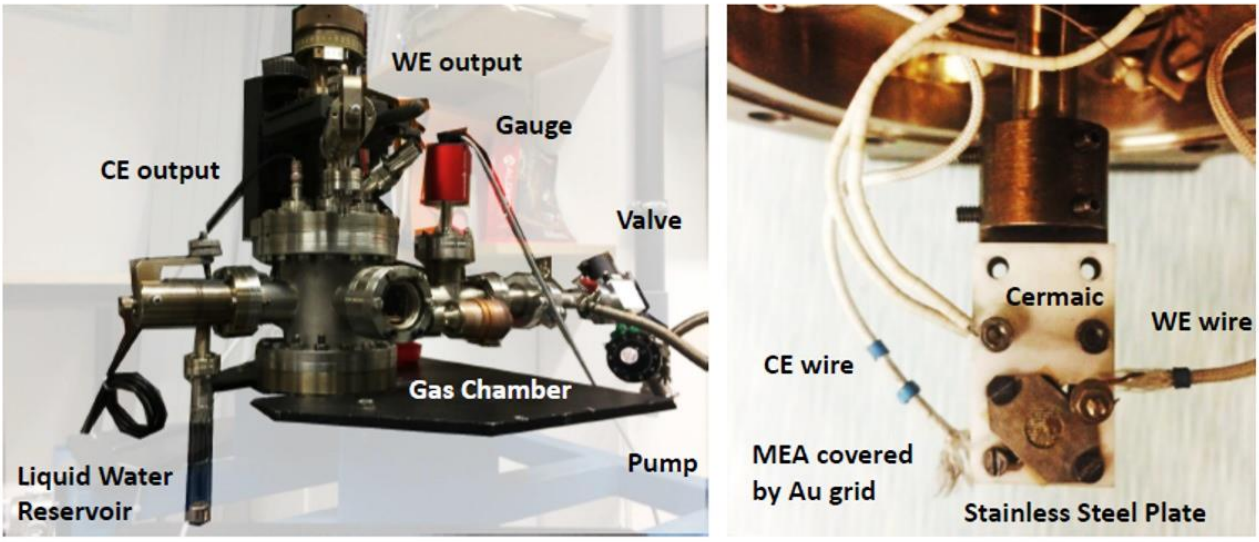

Figure 32. Left panel: Laboratory set-up for the electrochemical tests of the MEAs under the gas-phase conditions. Right panel: The sample holder containing the MEA.

Water vapor was introduced into the chamber from the liquid water reservoir through the leak valve. Before the measurements, the dissolved gasses were removed from liquid water by the degasification process based on the decreasing of oxygen solubility with temperature dropping. The procedure consisted of several cycles of liquid reservoir freezing using liquid nitrogen followed by pumping out non-dissolved gasses. Except for the water vapor, for some experiments we also introduced hydrogen into the chamber through another leak valve connected to the chamber. The measurements in the laboratory set-up were performed in a batch mode, while the NAP-XPS measurements were done in a flow mode.

The preliminary tests of the MEAs pursued the following purposes:

- analyze the effect of the water vapor pressure on the MEA performance;
- define the potential scale of the two-electrode cell by comparing the CVs recorded in a standard three-electrode cell with liquid electrolyte;
- evaluate the ohmic resistance losses and their dependence on the humidity level.

2.3.2. Electrochemical Impedance Spectroscopy

The membrane conductivity under relatively dry ambient conditions plays the key role in the overall MEA performance. The ohmic resistance of the electrolyte was determined by electrochemical impedance spectroscopy measured in the potential region close to the OER onset in the frequency region from 100 kHz to 0.01 Hz. The example of the Nyquist plot obtained for Ir@IrO_x anode under 23.5 mbar water vapor and different polarization conditions is shown in Figure 33. High frequency intercept on the real axis of the Nyquist plot was taken as the ohmic resistance value. For more precise determination of the membrane resistance fitting of the EIS spectra with equivalent circuits is required, but was not applied in this work. At 23.5 mbar of water vapor (ca. 80% RH) it was estimated as 11 Ohm. Analogous to the CV recording, the EIS measurements were also used as the indicator of the MEA stability during synchrotron measurements. No changes in the membrane resistance value were observed before and after the experiments for all the samples presented in this work.

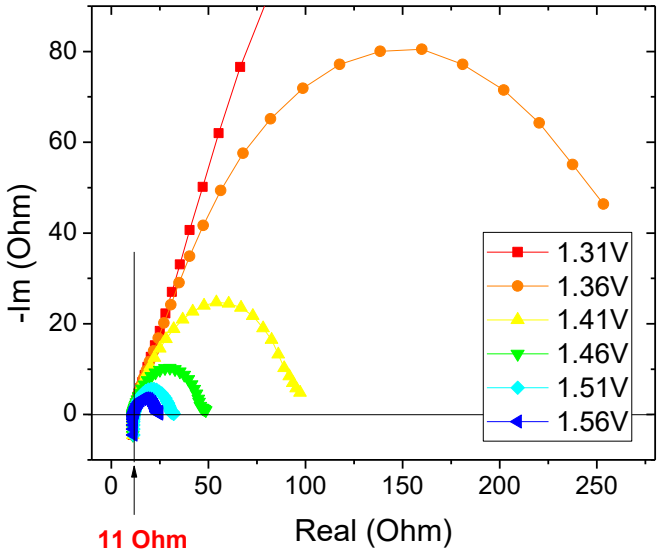

Figure 33. Nyquist plot obtained on Ir@IrO_x anode under 23.5 mbar water vapor and different potentials shown in the inset. The ohmic resistance was defined as the intercept of the real axis and marked in the plot.

2.3.3. Nafion or Aquivion? Effect of Humidity

Aquivion ionomer used in this work has similar structure as the state-of-the-art PEM ionomer Nafion (DuPont™). It represents a perfluorosulfonic acid (PFSA) consisting of a polytetrafluoroethylene (PTFE) backbone responsible for the mechanical and chemical stability and perfluorinated side chains with a sulfonic acid end groups providing the proton transport (Figure 34). The ionomer dispersion is added in the catalyst ink in order to provide not only the conductivity between the catalysts particles but also as a particles binder[15]. The proton transfer occurs through the membrane comprising $–SO_3^-H^+$ functional groups via Grotthuss[182] and translational diffusion or vehicle mechanisms[183]. At high relative humidities Grotthuss mechanism or hopping is considered as the dominant, where the protons detach from the $–SO_3^-H^+$ functional groups and combine with water molecules forming H_3O^+ complexes[182]. On the contrary, according to the vehicle model, the proton is bonded to a "vehicle" such as H_2O forming Brønsted base and moving through the channel[183]. Thus for both mechanisms, the conductive properties of the PFSA-based membranes and ionomers depend on the water content and the concentration of sulfonic acid functional groups providing the protons.

By changing the side chain length of the PFSA one may influence the concentration of $–SO_3^-H^+$ functional groups, which is related to the equivalent weight (EW). The EW is defined as a mass of dry polymer per mole of sulfonic acid groups. Typically, depending on the length of the side chains, the PFSA ionomer can be divided into the long-side-chain (LSC) such as a benchmark *Nafion* and short-side-chain (SSC) membranes, e.g. *Aquivion*[184,185] (Figure 34). In comparison to

the LSC, the SSC-based ionomer has larger crystallinity, higher glass transition temperature, lower gas cross-over and higher mechanical resistance. Higher concentration of sulfonic groups in SSC ionomers improves their conductivity especially under low and medium humidity level and decreases their ohmic resistance.[186,187] The SSC-based clusters formed in the presence of water are well dispersed and high concentration of sulfonic groups in these clusters and channels provides higher diffusion coefficient of water and H_3O^+ ions in comparison to LSC-based ionomers[188]. Higher water absorption of SSC-based ionomers also contributes to their improved conductivity at low humidity level[189].

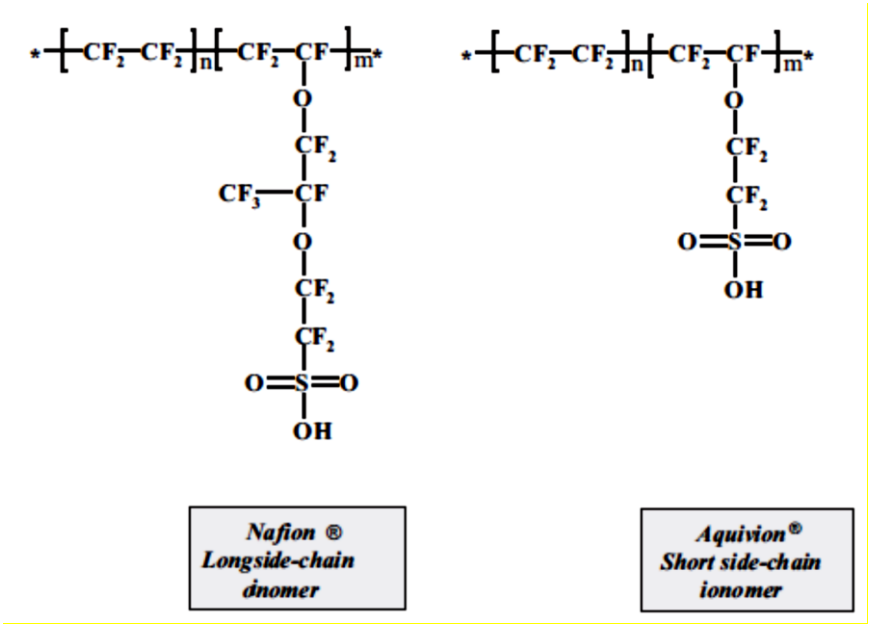

Figure 34. Polymer structure for long-side chain Nafion (left) and short-side-chain Aquivion (right) membranes[186].

In order to compare the conductive properties of the membranes under different ambient conditions we prepared two MEAs based on Nafion and Aquivion ionomer and membranes, correspondingly. Two electrochemical techniques have been chosen for the analysis – cyclic voltammetry and EIS. As a model MEA system, we have deposited Pt/C catalysts on both WE and CE sides. The advantage of Pr is related to the well-defined shape of its CV facilitating the analysis. An example of the curves recorded on Nafion-based and Aquivion-based MEAs with Pt/C electrocatalysts under 3 mbar of water vapor is shown in Figure 35.

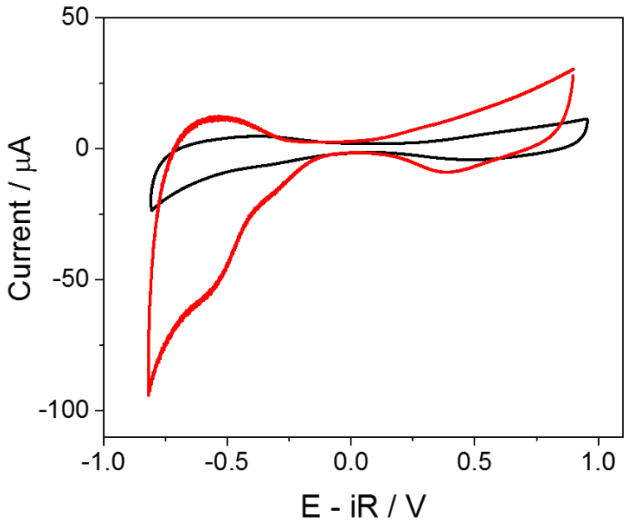

Figure 35. Cyclic voltammograms recorded on Pt/C electrode of Nafion-based (black) and Aquivion-based (red) MEA. The Pt loading was 0.1 mg cm^{-2}. The curves were recorded under 3 mbar water vapor and at scan rate 20 mV s^{-1}.

The upper potential limit was chosen prior to the OER region in order to avoid the irreversible oxidation of Pt. The EIS measurements were done at potentials corresponding to the electrical double layer interval in order to avoid the presence of the adsorbate species. The influence of humidity on the MEA resistance is shown in Table 3. One may clearly see the increasing of the resistance value with the water vapor pressure decreasing. Moreover, the increase of the membrane resistance with the decrease of RH is much less abrupt for Aquivion compared to Nafion. Besides the EIS analysis, we also compared the shape and the current values of the CVs (Figure 35) recorded on the MEAs under these conditions as an indicator of the electrochemical activity. This allows measurements at much lower RH values for Aquivion which has been chosen for our NAP-XPS measurements.

Analysis of the CV presented in Figure 35 also shows the limitations of the 2-electrode cell (absence of the RE), whereby the CE is capable to function as the DHE only when the WE is polarized positively.

Table 3. Influence of water vapor pressure on the Nafion- and Aquivion-based MEAs ohmic resistance. t = 25 °C, $p_{sat}(H_2O)$ = 30 mbar.

Water Vapor Pressure / mbar	**Relative Humidity / %**	**Impedance / Ohm**	
		Nafion – based	Aquivion – based
24	80	33	10
17	60	52	15
12	40	54	14
9	30	160	20
7	20	210	27
5	17	730	57
3	10	3 500	160
1	3	100 000	2 000
0.5	1.7	-	8 000
0.3	1	-	25 500

2.3.4. Influence of Humidity on the MEA Performance

Dry conditions (ca. 10% RH) of *in-situ* experiments performed in this work lead to the diminishing of the membrane conductivity. As was previously discussed in Chapter 1, the Tafel slope analysis can be used to compare the electrocatalytic activity of the catalysts as well as to define the reaction rate-determining step and the reaction mechanism. In that perspective, the evolution of this parameter with the changes of the ambient conditions may shed light on the relevance of the *in-situ* spectroscopic measurements for the real PEM water electrolyzer system. is not straightforward and the differences in the estimated values cannot be fully related to the changes of the rds or the overall reaction mechanism.

Table 4 contains the Tafel slopes calculated from the CVs measured on Ir@IrO_x anode at slow scan rate of 5 mV s^{-1} and different humidity level (Figure 36). While the obtained values are not strongly influenced by the RH level, one may see the increasing of the difference in the slopes for forward and backward scan of the CVs with the decreasing of the humidity level. Besides the results obtained under water vapor conditions, the resistance and the Tafel slope estimated in the presence of liquid electrolyte are also presented in Table 4. Moreover, the measurements were also performed in a water electrolyzer cell. For the experiments in the electrolyzer, the MEAs were prepared the same way (with the same catalyst loadings) as for the NAP-XPS measurements.

The Tafel slope estimated from water electrolyzer tests is larger than the one obtained for RDE measurements. The most crucial difference between these tests is the preparation of the

electrode, where the MEA was used in the former case, while in the latter - the catalyst ink was directly deposited on a glassy carbon electrode. Another difference is related to the electrolyte: solid polymer in the electrolyzer tests and aqueous H_2SO_4 in RDE studies. Under water vapor conditions, the Tafel slope measured on the MEA is even higher than the one obtained in a liquid water electrolyzer. These changes of the values can be related to the catalyst particle interconnection issues. In case of the RDE measurements, the particles are uniformly deposited on the GC electrode, which is directly connected to the current collector. In case of water electrolyzer and *in-situ* cell for the NAP-XPS measurements, the MEAs are fixed between the plates (with gas diffusion layers and golden meshes in between, correspondingly) in order to provide the conductivity between the particles through the intermediate layer and potentiostat. The configuration of the *in-situ* cell contains also a circular opening for the X-rays (see Figure 37) creating pressure distribution and consequently resistance distribution in the catalyst layer. In addition, proton transport may become limiting during measurements performed at low RH values. All these factors might influence the changes of the Tafel slopes.

Based on the results presented here we can make the following conclusions:

- for Aquivion-based MEAs ohmic resistance increases with decreasing the humidity from 80 down to 10 % by ca. an order of magnitude;
- diminishing of the catalyst activity from 80% down to 10% RH is not drastic;
- comparison of the Tafel slopes obtained under gas-phase electrolysis conditions with the data obtained in liquid electrolyte is not straightforward and the differences in the estimated values cannot be fully related to the changes of the rds or the overall reaction mechanism.

Table 4. Influence of water vapor pressure on the MEA (with Ir@IrOx anode catalyst) ohmic resistance and Tafel slopes.

Water Vapor Pressure / mbar	**RH / %**	**Resistance / Ohm**	**Tafel slope, mV dec^{-1}**	
			Forward scan	Backward scan
23.5	80	11	112	116
16	50	11	104	121
9	30	17	96	122
4.5	15	60	111	160
3	10	90	**120**	152
Liquid electrolyte - RDE measurements		0.026	**44**	-
Water electrolyzer cell		0.56	**73**	78

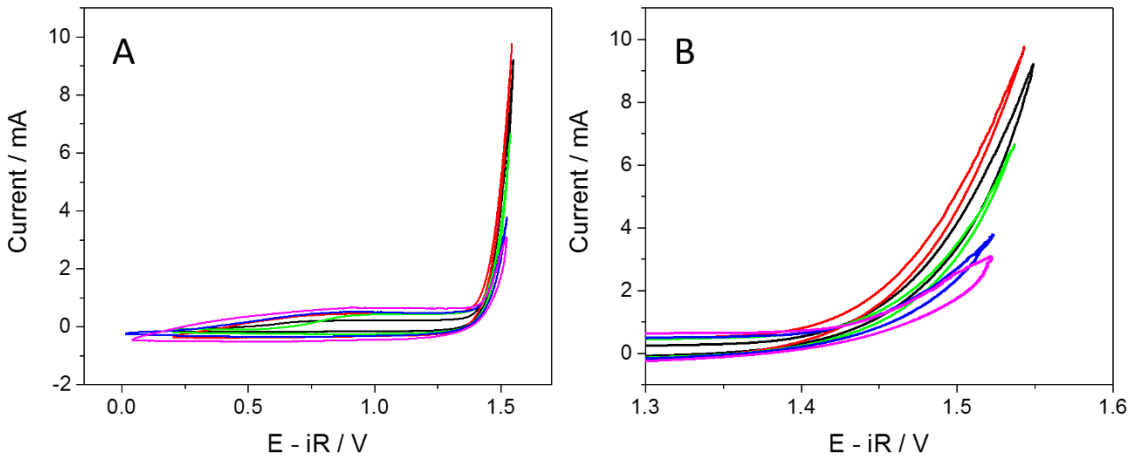

Figure 36. The cyclic voltammograms recorded on Ir@IrO$_x$ electrode under different water vapor pressures: 23.5 mbar (red), 16 mbar (black), 9 mbar (green), 4.5 mbar (blue), 3 mbar (magenta). Panel B represents the magnified Panel A at the potential region [1.3; 1.6] vs DHE. Scan rate 5 mV s^{-1}. The loading 0.1 mg cm^2.

2.4. *In-situ* Synchrotron-based Spectroscopic Studies

2.4.1. *In-situ* Near-Ambient Pressure Spectroscopy Set-ups

In-situ near ambient pressure XPS and NEXAFS measurements were performed at the third generation synchrotron facilities: HZB/BESSY II (Berlin, Germany) and SOLEIL/UPMC (Gif-sur-Yvette, France). The unique properties of synchrotron radiation are wide-energy tunability, high brilliance and high photon flux.[140,190] The set-ups and instrumentations of the beamlines as well as the measurement conditions are described below.

2.4.1.1. HZB/BESSY II – ISISS Beamline

The *in-situ* measurements of Ir, Ru-based anodes were performed at the ISISS (Innovative station for *in-situ* spectroscopy) beam line at the Inorganic Chemistry department of the FHI. The configuration of the used set-up allowed the recording of the photoemission and absorption spectra at the gas-phase pressure up to few mbars due to 3 stages differential pumping and electrostatic lens system[156,191]. The Phoibos 150 electron analyzer (SPECS) is equipped with a 2D Delay Line detector from Surface Concept. The gases were introduced into the NAP-XPS chamber through the leak valves using the mass flow controllers Bronkhorst. The composition of the ambient in the analyzing chamber was constantly monitored by an on-line quadrupole mass spectrometer (QMS, Prisma, Pfeiffer Vacuum, Inc., Germany). The QMS was used to continuously record the traces of H_2O, H_2 and O_2 during the measurements.

The photoelectrons produced in the water vapor/oxygen ambient of the NAP-XPS chamber introduce lines in the corresponding spectrum from the material surface, particularly in the O1s XP spectra[192]. By applying an acceleration voltage between the investigated surface and the grounded entrance slit of the spectrometer (the nozzle), the KE of the gas phase peaks were shifted resulting in the separation between the gas phase and the surface peaks.

For NEXAFS studies, the Auger electron yield was measured with the electron spectrometer. To partly suppress the contribution of gas-phase oxygen and water the kinetic energy of the collected electrons was set to 385 eV with a PE of 100 eV[144]. The total electron yield was collected via a Faraday cup via the first aperture of the differential pumping system with an applied accelerating voltage.

2.4.1.2. SOLEIL/UPMC – TEMPO Beamline

The TEMPO beamline[193] of the SOLEIL synchrotron was used to carry out the NAP-XPS measurements of unsupported and supported Ir-based catalyst. The analysis chamber of the NAP-

XPS is equipped with a SPECS Phoibos 150-NAP hemispherical electron analyzer including an electrostatic lens with four differential pumping stages allowing a pressure up to 20 mbar during acquisition. The aperture size is 300 μm and the beam resolution – 100 μm. A windowless beamline entrance with 3 differential pumping stages secure the pressure of the beamline below a limit of 5×10^{-8} mbar. The analyzer is equipped with a Delay Line detector from Surface Concept. The NAP-XPS chamber of TEMPO beamline is also equipped by QMS allowing constant controlling of the gas-phase composition of the chamber. The water vapor was introduced into the chamber through a leak valve; the experiments were performed in a flow mode.

2.4.2. Analyzed Samples

In-situ investigation of Ir, Ru-based anodes for PEM water electrolyzers under OER conditions was performed on the membrane-electrode assemblies, consisting of Aquivion membrane, counter (Pt/C) and working electrodes. In this work, the following anode catalysts were studied:

- thermal RuO_2 and electrochemical $Ru@RuO_x$ oxides (Chapter 3);
- mixed Ir,Ru-based thermal oxide (Chapter 4);
- thermal IrO_2 and electrochemical $Ir@IrO_x$ oxide (Chapter 5);
- Ir catalyst supported on SnO_2-Sb aerogel (ATO) (Chapter 6).

MEAs with the geometric catalyst surface area of 0.9 cm^2 were integrated in the electrochemical cell, which was introduced in the chamber of the NAP spectrometer.

The sketch of the sample holder used in the NAP-XPS of ISISS beamline is shown in Figure 37. The same principle is utilized at TEMPO beamline of SOLEIL synchrotron. The contacts insolation is provided by using the sapphire body of the sample holder containing stainless steel screws to join the golden current collectors, stainless steel masks and the potentiostat.

All the experiments presented in this work were performed under the constant flow of water vapor in the NAP chamber maintaining the pressure of 3 mbar corresponding to ca. 10% RH at room temperature and both electrodes were exposed to the same ambient atmosphere. Spectroscopic measurements were performed under potential-controlled conditions.

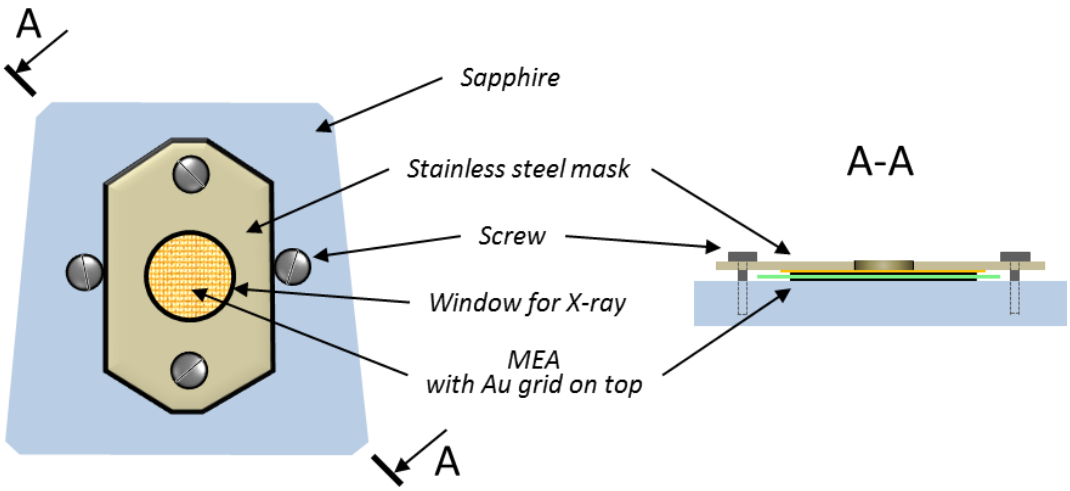

Figure 37. Sketch of the holder used to fix the MEA in the NAP-XPS chamber.

The electrochemical activity of the MEAs was measured by cyclic voltammetry. The current flow was controlled by means of chronoamperometry (CA) during the spectroscopic measurements. The EIS measurements were also performed for the ohmic drop correction. The latter and CVs recording allowed monitoring the performance of the MEA and detect eventual degradation throughout the experiments.

2.4.3. Cyclic Voltammetry and Dynamic Hydrogen Electrode

An example of the current-voltage curves obtained in a NAP-XPS chamber under 3 mbar water vapor and water/hydrogen mixture conditions on $Ir_{0.7}Ru_{0.3}O_2$ anode is shown in Figure 38. Since the measurements were carried out in a two-electrode set-up, it was necessary to define the potential of the working electrode against a well defined reference. In order to do that, a hydrogen-water mixture was introduced into the chamber after the NAP-XPS measurements allowing one to use the CE side of the MEA as a dynamic hydrogen electrode (DHE)[177]. The stability of $Ir_{0.7}Ru_{0.3}O_2$ catalyst under water/hydrogen ambient was confirmed by XP spectra. The potential difference between the OER onset in water and in water-hydrogen ambient was estimated as not exceeding 20 mV at the sweep rate of 5 mV s^{-1}. The potential scale was then recalculated into the DHE via the iR correction and neglecting the ca. 20 mV shift. Comparison of the OER onset potential obtained on this electrocatalyst in the presence of water vapor (1.4 V vs DHE) and liquid electrolyte (1.45 V vs RHE)[181] allowed us to use the potential scale without further corrections. It should be noted that the counter electrode behaves as a DHE even at the absence of additional hydrogen flow. As it was mentioned in Material section, the catalyst loading of the CE is much higher than the on the WE in order to avoid the overpotential on the former electrode. The amount

of the hydrogen evolved during the HER on the cathode side is enough for the CE to act as the DHE.

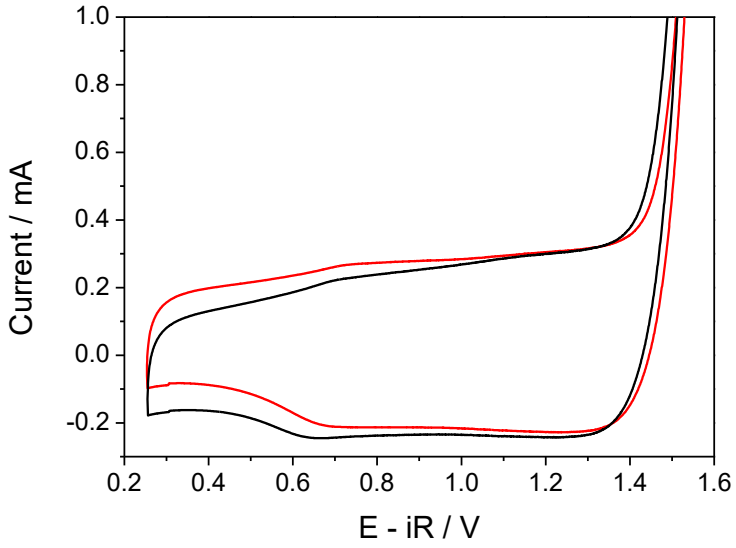

Figure 38. Cyclic voltammograms of the $Ir_{0.7}Ru_{0.3}O_2$ electrode obtained in a NAP-XPS chamber at different ambient conditions: 3 mbar H_2O (black curve); 3 mbar H_2O and 0.5 mbar H_2 (red curve) at a scan rate 5 mV s^{-1}. Catalyst loading 0.1 mg cm^{-2}.

2.4.4. Chronoamperometry

In-situ NAP-XPS/NEXAFS measurements were performed under constant voltage applied between the working and counter electrodes. The example of the current transients at selected voltage values for Ru@RuO_x anode obtained in the NAP chamber at BESSY II synchrotron is represented in Figure 39. The recording of the corresponding spectra was initialized after the stabilization of the current values (ca. 2-3 min after the potential application). Decreasing of the current transients during the backward scan can be explained by continuous degradation of the Ru catalyst. This topic will be discussed in more detail in Chapter 3.

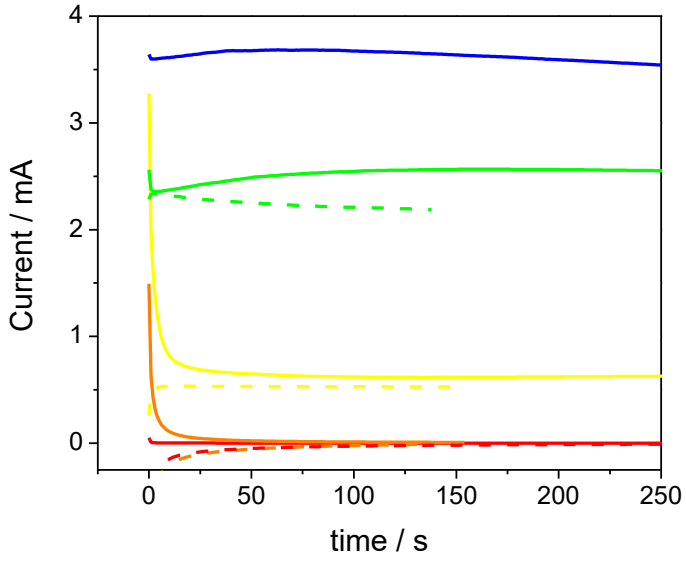

Figure 39. Chronoamperograms obtained in the NAP-XPS chamber at BESSY II synchrotron on Ru@RuO_x anode under 3 mbar water vapor and different polarization conditions: 0.75 V (red); 1.00 V (orange); 1.34 V (yellow); 1.39 V (green); 1.41 V (blue). Solid lines represent the forward scan, the dashed – the backward. The potential is ohmic drop corrected. Temperature 25 °C. Catalyst loading 0.1 mg cm^{-2}.

2.4.5. Experimental Protocol

While the specific measurement sequences will be discussed further in each particular case, the general protocol followed in this work is briefly presented here. Before performing any spectroelectrochemical measurements all the MEAs have been pretreated by cycling in the potential region from open circuit voltage of 0 V to 1 V vs DHE (10 cycles) directly in the NAP-XPS chamber under 3 mbar water vapor in order to obtain stable and reproducible surface state. The potential of 1V vs DHE was chosen in order to avoid the oxygen evolution region. Such a potential cycling leads to the formation of electrochemical oxide in case of metallic nanoparticles and/or hydroxylation of the oxide surface[194]. Besides the initial pretreatment, periodic recording of the CVs and impedance measurements during the experiments allowed us following the MEA stability.

In-situ spectroscopic measurements were performed under constant voltage applied between working and counter electrodes. The acquisition of the spectra was initialized after the stabilization of the current values controlled by means of chronoamperometry.

2.4.5.1. Radiation Damage

To be sure that the observed changes of the recorded spectra are mostly originated from the applied potential rather than from the radiation damage of the X-rays[195], the spectra acquisition

of the analyzed elements was done by moving the sample in such a way that different spots on the WE surface were exposed to the beam, followed by the quantitative analysis – atomic ratio calculations. While the analyzed catalysts were stable to the X-ray exposure throughout the experiments, the analysis of S2p XP spectra originating from the Aquivion ionomer / membrane revealed quite poor stability of the sulfonic acid groups, observed previously on other PFSA-based membranes[196]. Figure 40 shows the evolution of Ir/S and Ir/F atomic ratio under different polarization conditions including the OER region measured at one spot. The spectroscopic and electrochemical results obtained on IrO_2 anode confirmed its stability during the measurement time frame, thus this electrode was chosen for the analysis of the polymer degradation. One may notice a drastic decreasing of the sulfur contribution with time of the electrochemical measurements. However, the Ir/F ratio increases two times only. This can also be related to the cleaning of the IrO_2 particles surface under potential cycling.

In order to reduce the radiation damage, the analyzed spot was constantly switched during the measurements and the beam shutter was kept closed unless during the spectra acquisition.

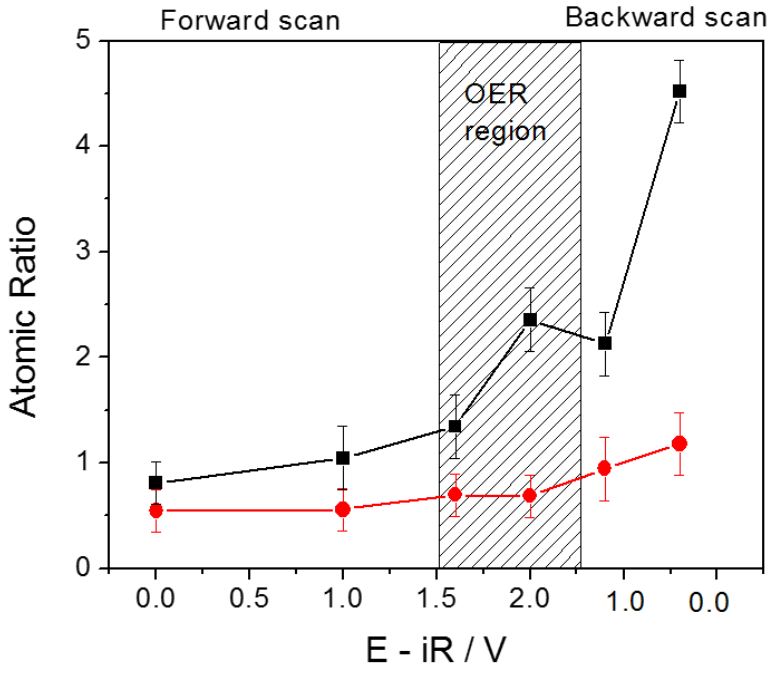

Figure 40. Potential dependence of Ir/S (black) and Ir/F (red) atomic ratio obtained on IrO_2 anode-based MEA under 3 mbar water vapor. Three different regions are shown in the plot: before the OER onset (marked as forward scan), the OER region and backward scan. The kinetic energy of the emitted electrons was equal to 530 eV.

2.4.5.2. Spectroscopic Measurements

For XPS measurements performed at ISISS and TEMPO beamlines, pass energies of 20 eV and 50 eV were used correspondingly. If not otherwise stated, Ru3d, Ir4f, C1s, O1s, Sn3d,

Sb3d, F1s and S2p spectra were recorded using selected excitation photon energies so that the photoelectrons were emitted at a kinetic energy of ca. 530 eV. The corresponding inelastic mean free paths (IMFP) of the emitted electrons were estimated using QUASES-IMFP-TPP2M software for metallic Ir and Ru[197]. The analysis depth was calculated as three times the IMFP. The depth-dependent measurements were carried out using photon energies 460 eV, 595 eV and 1080 eV for Ir4f spectra (corresponding to 1.9, 2.3, 3.6 nm of the analysis depth for metallic Ir, respectively); 820 eV and 1300 eV for C1sRu3d spectra (4.4 nm and 6.3 nm analysis depth for metallic Ru); 880 eV, 1020 eV and 1300 eV for Sn3d (1.9, 2.3 and 3.1 nm analysis depth for tin oxide). A binding energy calibration of the spectra was realized by measuring the valence band spectrum.

NEXAFS measurements were performed in the same NAP-XPS chamber. Both the Auger and total electron yield (AEY and TEY) were registered at the same time. O K edge was recorded in the photon energy range [520 eV; 560 eV] at the kinetic energy of the collected electrons of 385 eV and the pass energy 50 eV. The energy was chosen in order to avoid the superposition with the oxygen Auger peak and in order to suppress the contribution of the photoelectrons originating from the gas-phase (for the AEY mode) as it was shown in *Hävecker et al.*[148]

2.4.6 Data Processing

This Section demonstrates the fitting procedure used in this Thesis for the analysis of Ir4f and C1sRu3d XP spectra. The deconvolution was done using CasaXPS software. The literature values of the binding energies for various Ir,Ru substances are also presented here. The simulation of the XP spectra performed in this work is discussed at the end of the section.

2.4.6.1. Quantitative Analysis of XPS Results

The surface atomic ratios were estimated based on the intensities of the XP spectra using the following equation[139]:

$$\frac{n_1}{n_2} = \frac{I_1/(f_1 \cdot \sigma_1)}{I_2/(f_2 \cdot \sigma_2)}$$

where $\frac{n_1}{n_2}$ is the atomic ratio of elements (1) and (2); I – the spectral intensities obtained at the same kinetic energies of the emitted photoelectrons; f – the energy dependent incident photon flux, measured using a gold foil with known quantum efficiency at each beamline; σ – the photoelectric cross-section for the interested atomic orbital taken from[198]. The incident photon fluxes recorded at BESSY II and SOLEIL synchrotrons are shown in Figure 41.

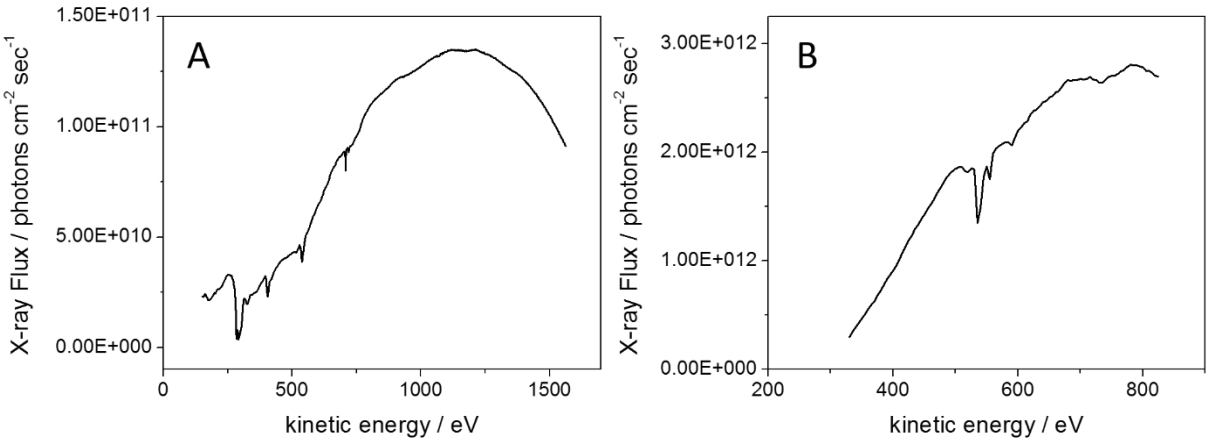

Figure 41. Incident photon flux vs kinetic energy recorded at ISISS (A) and TEMPO (B) beamlines of BESSY II and SOLEIL synchrotron correspondingly.

2.3.6.2. Ru3d XP Spectra: Fitting Procedure

The peak fitting of Ru3d XP spectra is complicated by the presence of Ru in various oxidation states and the overlap with the C1s peaks. The carbon peaks originate from the adventitious carbon[199] as well as from the Aquivion ionomer and membrane. The contribution of the latter can be estimated using the F1s XPS peak area, fully originating from the membrane. Accepting the atomic ratio C:F = 1:2[200] for the membrane, the expected area of the carbon peak originating from CF_2 groups of the membrane was calculated and constrained for the further peak fitting. As it was shown in the previous part, the polymer backbone containing fluorine can be slightly damaged under the X-rays exposure what was taken into consideration in the C1s analysis. Since the WE of the MEA is grounded the peaks originating from the WE (Ru3d and C1s from adventitious carbon) are not expected to shift with the applied potential. Meanwhile the membrane components shift following the cell voltage[176], and this was also taken into account during the C1sRu3d spectra fitting. Other C1s components from the membrane were neglected due to their low contributions.

The assignment of the Ru-based peaks was based on the literature data (Table 5). The peak fitting of Ru3d XP spectra presented in this work required at least four peak doublets. The parameters used for the fitting were partly taken from the work of *Morgan*[201] and are presented in Table 6. The presence of anhydrous RuO_2 could be revealed by a $Ru3d_{5/2}$ peak at 280.6 eV accompanied by a shoulder, while hydrated RuO_2 ($Ru(OH)_x$) clearly showed up by a $Ru3d_{5/2}$ peak at 281.4 eV (see Figure 42). The Ru (VIII) component appeared as a well-defined no carbon-overlapping $Ru3d_{3/2}$ shoulder in the XP spectra. One of the open questions discussed by *Cox et al.*[202] was related to the attribution of the peak, which was observed 1.6 eV positive of the 3d doublet of RuO_2. Literature data was contradictory, some authors attributing the peak to Ru in the

valence state (VI), RuO_3, the other to a RuO_2 satellite. Indeed, presence of a shake-up satellite in the Ru3d spectrum of RuO_2 oxide is expected[201]. However, the analysis of Ru3d spectra for different samples at various applied potentials revealed presence of an additional (beyond the RuO_2 satellite) potential-dependent doublet at the same BE (1.6 eV positive of the Ru3d doublet of RuO_2), which was especially intense for RuO_2 during and after the OER. Thus, self-consistent peak fitting of Ru3d spectra was only possible if four doublets were considered: (i) RuO_2 in an anhydrous form (with a shake-up satellite), (ii) hydrous Ru (IV) oxide denoted for the moment as $Ru(OH)_x$, (iii) Ru (VI) denoted as RuO_3, and (iv) Ru (VIII), which we attribute to a surface $RuO_{4(s)}$. The formation of Ru (VIII) phase as RuO_4 on Ru-based electrodes has been proposed by *Kötz et al*[84,203]. The volatile anhydrous Ru (VIII) oxide has been analyzed by spectroscopic methods[204,205], however the structure of the oxide is still under question. In the presence of liquid water Ru (VIII) forms soluble compounds[33]. The existence of a RuO_3 phase has been largely debated in the literature. According to the present understanding, Ru (VI) does not form a thermodynamically stable solid RuO_3 phase, but may rather exist as a metastable phase or a defective RuO_2 phase[202]. Formation of RuO_3 on Ru anodes has been postulated based on *ex-situ* XPS data[22,206], and many authors claim that its presence impacts the stability of the anodes. It has also been documented that Ru (VI) may disproportionate into a Ru (IV) and a higher Ru oxide. *Kötz et al.*[22] observed Ru (VI) on the surface of a RuO_2 anode exposed at ca. 1.74 V *vs.* RHE using post-mortem XPS characterization. Note that the presence of Ru (VI) and Ru (VIII) satellites cannot be excluded, but was neglected in this work due to their negligible contribution and their overlap with the C1s peaks. In addition, we considered the C1s singlets originating from the membrane and C1s singlets of the adventitious carbon (in C-C and in oxidized form[199]). The example of this peak fitting is shown in Figure 42 and the fitting parameters – in Table 6.

The correct fitting of the C1s XP spectra remains complicated due to the contributions of carbon atoms involved in different bonds present on the material surface[207,208]. According to the study of *Estrade-Szwarckopf*[208], the carbonaceous materials have at least three contributions in the C1s XP spectra originating from graphitic carbon (sp^2 configuration), defective structures with sp^3 configuration and π- π^* levels transition peak. For graphitic carbon, *Blume et al.*[207] distinguish sp^2, disordered and defective carbon. The asymmetric peak of graphitic sp^2 carbon was explained on the basis of core holes left after excitation of photoelectrons.[209] However, as it was shown in[207], the asymmetry also depends on the surface geometry of the graphitic carbon. Moreover, the tail of this peak created the quasi background signal for C-O / C=O symmetric peaks.[208]

Overlapping with Ru3d peaks and the presence of various carbon contribution (graphitic, hydrocarbons, membrane originating), all these factors perplex an exact evaluation of the line shapes used in the fitting procedure. In this work, we do not analyze carbon species behavior and

the C1s peaks mostly overlap with $Ru3d_{3/2}$ part of the doublet, so the asymmetry factor was neglected from the C1s peaks analysis.

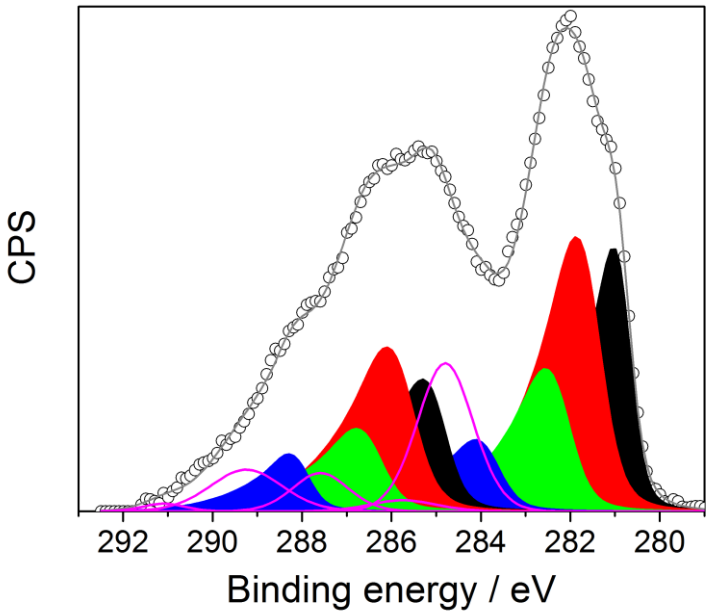

Figure 42. C1sRu3d XP spectra for RuO_2 anode in 3 mbar H_2O ambient at E – iR = 1.8 V and photon energy 820 eV. Peak fitting was done using four Ru components: RuO_2 and its satellite (black); $Ru(OH)_x$ (red); Ru(VI) (green); $RuO_{4(s)}$ (blue); and five singlets of carbon (magenta), including the adventitious carbon and the membrane contribution. The experimental data are presented by the black cycles and a summary fitting curve - by a grey line.

Table 5. Literature $Ru3d_{5/2}$ BE values for different Ru species measured using conventional UHV XPS.

Binding energy $Ru3d_{5/2}$ / eV					Sample	Ref
Ru^0	Ru (IV)		Ru (VI)	Ru (VIII)		
	Anhydrous RuO_2	Hydrated RuO_2	RuO_3	RuO_4		
279.95 281.55 (sat)	280.77 282.22 (sat)	282.30			Ru rod RuO_2 anhydrous (commercial) Hydrated RuO_2 (commercial)	210
279.8	280.6 282.5(sat)	280.8 282.7 (sat)			Ru (0001) (commercial) RuO_2 anhydrous (commercial) Hydrated RuO_2 (commercial)	201
279.91		280.68	282.38		Ru powder Hydrated RuO_2 (commercial)	211
280.0	280.7	281.4	282.5	283.3	RuO_2 anhydrous (thermally obtained, 900°C, air) Hydrated RuO_2 xH_2O (commercial) RuO_4 obtained by low temperature (-80°C) vapor deposition of a commercial sample	205
279.9	280.7	281.0	282.4		Ru subjected to 1.5 V vs Saturated Calomel Electrode in 1N H_2SO_4 RuO_2 anhydrous (thermally obtained, 500°C, air)	203
280.2		281.9			Ru subjected to thermal oxidation at 500°C in O_2 presence	212
	280.5 – 280.9		282.5-282.8		RuO_2 (110) and (100) single crystals	206
	280.7		282.3	283.6	5 nm Ru nanoparticles, 10 nm RuO_2 nanoparticles	213

Table 6. Fitting parameters for C1sRu3d XP spectra recorded at 530 eV Kinetic Energy and 20 eV Pass Energy.

Component	Line shape	FWHM / eV		Binding energy / eV	
		$3d_{5/2}$	$3d_{3/2}$	$3d_{5/2}$	$3d_{3/2}$
Ru $_{metallic}$	LF(0.8,1.125,500,180)	0.77	0.85	280.1	284.3
RuO_2	LF(0.25,1,45,280)	0.85	1.14	280.6	284.8
RuO_2 satellite	LF(0.25,1,45,280)	1.23	1.24	282.2	286.4
$Ru(OH)_x$	LF(0.25,1,45,280)	1.16	1.24	281.4	285.6
Ru(VI)	LF(0.25,1,45,280)	1.23	1.24	282.2	286.4
$RuO_{4(s)}$	LF(0.25,1,45,280)	1.20	1.30	283.8	288.0
Adventitious carbon					
C-C	GL(30)	1.46		284.8	
C-O-C	GL(30)	1.75		285.7	
C-OH	GL(30)	1.67		287.4	
O-C=O	GL(30)	1.90		289.0	
Proton exchange membrane (BE value for E-iR = 1.8V)					
$-CF_2-$	GL(30)	1.4		290.4	

2.3.6.3. Ir4f XP spectra: Fitting Procedure

Figure 43 shows the Ir4f XP spectra obtained on IrO_2 and $Ir@IrO_x$ anodes at the ISISS beamline under 3 mbar water vapor and OCV. The fitting was performed using a Shirley background. The fitting of the spectra recorded on rutile-type iridium oxide (Panel A of Figure 43) was done using three doublets: main core-level doublet and two satellites, correspondingly. The analysis of the Ir4f spectra obtained on $Ir@IrO_x$ anode was performed using five doublets: three main peaks and two satellites. The fitting parameters were based on the procedures described by *Pfeifer et al.*[214]. The typical asymmetric core-level line shapes used here for iridium components is normally attributed to the d-electron many-body screening response[215,216]. The peak separation and the peak area ratios between the Ir $4f_{7/2}$ and the Ir $4f_{5/2}$ components were constrained to 3 eV and 4:3, respectively. The area ratio between the main core-level peak and the satellite 1 and 2 was maintained constant and was equal to 5.6 and 11.1, respectively. The assignment of the peaks was done according to the literature data (Table 7) and the employed fit parameters for two different energies depending on the beamline where the spectra were recorded are listed in Tables 9 – 15. The BE offset applied in the Ir4f XP spectra fitting is related to the nature of the Doniach-Sunjic

line shape used here which does not reach zero at high BE values. The difference in the fitting of the spectra recorded at ISISS and TEMPO beamlines are mostly related to different pass energies used there. The latter leads to the changes in the FWHM values. Slight increasing of the peaks width at kinetic energy of 1010 eV is attributed to the broadening of the X-ray beam at higher photon energies[217]. It is worth to note the difference in the fitting of Ir (IV) peak (the BE position, the FWHM, peak shape) used for the analysis of the thermal and electrochemical Ir oxides. While XPS cannot distinguish crystalline and amorphous structures, the hydration of the oxide affects the obtained spectra (similar to the case discussed before for Ru (IV) oxides). While IrO_2 is an anhydrous rutile oxide, the oxide layer formed on metallic iridium under potential cycling ($Ir@IrO_x$ anode) is hydrated (see Chapter 5). Another issue related to the analysis of XP spectra is the position of Ir (III) component. By combining the XPS measurements with DFT calculations *Pfeifer et al.*[108,218] have demonstrated that, due to the final state effects, the BE of the Ir (III) component is higher than that of Ir (IV), on the contrary to the work of *Casalongue et al.*[101], where the high BE component was referred to the formation of Ir (V) species. Here we present the fitting data used in this work for the analysis of Ir4f spectra, while the assignment of the components and their potential evolution is discussed in detail in Chapter 5.

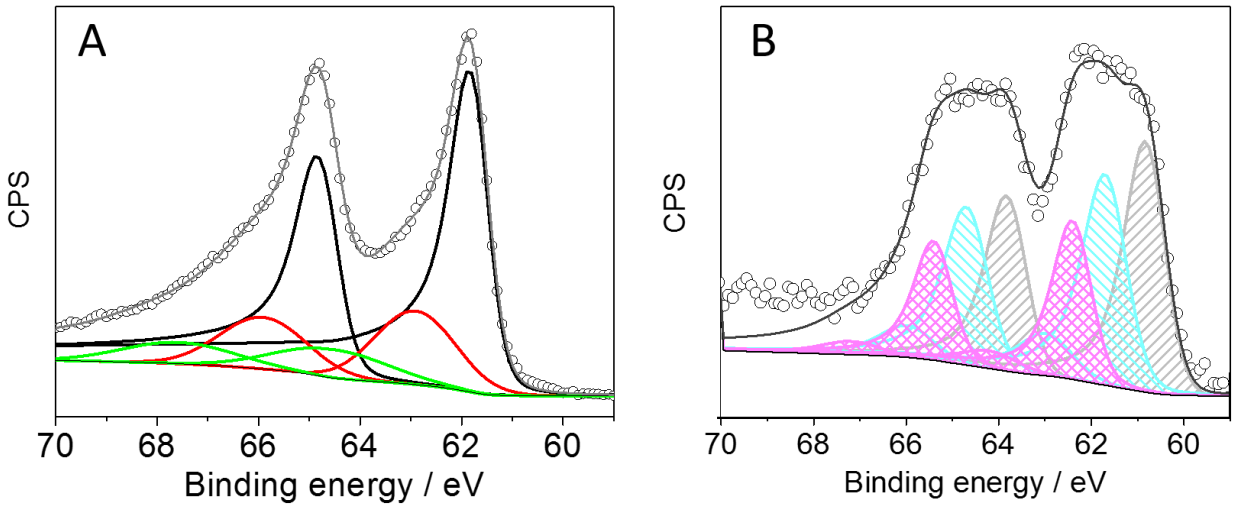

Figure 43. Ir4f XP spectra recorded on IrO_2 (A) $Ir@IrO_x$ (B) anodes under 3 mbar water vapor and E – iR = 0 V vs DHE. Panel A: the fitting was done using a main peak of rutile-type IrO_2 (black) and its 2 satellites (red and green); panel B: three different components were distinguished: metallic Ir – grey; Ir (III) – magenta; Ir (IV) – light blue. The experimental data are shown by the black cycles whereas a summary fitting curve by a grey line. Photon energy 595 eV.

Table 7. Literature binding energy values for different Ir species.

Binding Energy $Ir4f_{7/2}$ / eV					Sample description	Conditions	Ref
Ir (0)	Ir (III)	Ir (IV)	Ir (V)	Ir (VI)			
60.9		61.9			Bulk IrO_2 (commercial)	UHV	[219]
		61.9			IrO_2 (thermally obtained, 900K in O_2)		
		61.2			Electrochemically oxidized in 1 M H_2SO_4 at 3 V vs SHE		
60.8		61.7			IrO_2 nanoparticles (thermally obtained in air)	UHV, synchrotron radiation	[78]
60.9		62.1			IrO_2 + RuO_2 / Ti (thermally obtained in O_2)	UHV	[42]
61.1	61.6	62.7		64.3	Ir foil, Ir_2O_3, IrO_2 (commercial)	UHV	[32]
		62.9		64.3	Electrochemically oxidized Ir electrode in 0.5M H_2SO_4 under potential cycling [0.05;1.45] vs RHE		
		62.5		64.2	IrO_2 (thermally obtained in air)		
	62.1	61.5			IrO_2 (thermally obtained in air)	UHV, synchrotron radiation	[220]
60.9		61.5	62.2		IrO_2 nanoparticles (commercial) Potentials: OCV, 1.75 V (OER conditions)	NAP-XPS, 10 Torr Water Vapor	[101]
60.5					Ir metal (commercial)	UHV	[221]
		61.5			Thermally obtained IrO_2 (commercial)		
60.7					Sputtered Ir foil	UHV	[222]
		61.0			Rutile IrO_2 (commercial)	UHV	[216]
		61.8 62.9(sat) 67.9 (sat)			Rutile IrO_2 (commercial)	UHV	[104]
60.8	62.3 63.3(sat)	61.8 62.8(sat) 65.8(sat)			Sputtered-deposited Ir electrode. Potentials: OCV, 2 V, 2.5 V	NAP-XPS, 5 Pa water vapor	[108]
60.8					Ir foil (commercial)	UHV	[223]
		61.9 63.2(sat)			Anhydrous IrO_2 *		
		62.5			Hydrated IrO_2 *		
	62.6 71.6(sat)				Hydrated $IrCl_3$ *		
	62.4				Anhydrous $IrCl_3$ * (*the samples are commercial)		

Table 8. Fitting parameters for Ir4f recorded at ISISS beamline on thermally obtained IrO_2 anode at 530 eV Kinetic Energy and 20 eV Pass Energy.

Component	Line shape	FWHM / eV		Binding energy / eV	
		$4f_{7/2}$	$4f_{5/2}$	$4f_{7/2}$	$4f_{5/2}$
Ir (IV)	DS(0.2, 230)SGL(45)	0.85	0.93	61.9	64.9
Ir (IV) sat 1	GL(0)	1.88	2.00	63.0	66.0
Ir (IV) sat 2	GL(0)	2.60	2.60	64.7	67.7

Table 9. Fitting parameters for Ir4f recorded at ISISS beamline on thermally obtained IrO_2 anode at 1010 eV Kinetic Energy and 20 eV Pass Energy.

Component	Line shape	FWHM / eV		Binding energy / eV	
		$4f_{7/2}$	$4f_{5/2}$	$4f_{7/2}$	$4f_{5/2}$
Ir (IV)	DS(0.2, 230)SGL(45)	1.00	1.08	61.9	64.9
Ir (IV) sat 1	GL(0)	2.85	2.68	63.0	66.0
Ir (IV) sat 2	GL(0)	2.60	2.40	64.7	67.7

Table 10. Fitting parameters for Ir4f recorded at ISISS beamline on electrochemically obtained Ir@IrO_x anode at 530 eV Kinetic Energy and 20 eV Pass Energy.

Component	Line shape	FWHM / eV		Binding energy / eV	
		$4f_{7/2}$	$4f_{5/2}$	$4f_{7/2}$	$4f_{5/2}$
Ir_{met}	DS(0.01, 100)SGL(0)	1.00	1.00	60.85	63.85
Ir (IV)	DS(0.02, 100)SGL(20)	1.08	1.08	61.70	64.70
Ir (IV) sat	DS(0.02, 100)SGL(20)	1.35	1.35	63.00	66.00
Ir (III)	DS(0.02, 100)SGL(20)	0.95	0.95	62.40	65.40
Ir (III) sat	DS(0.02, 100)SGL(20)	1.45	1.45	64.20	67.20

Table 11. Fitting parameters for Ir4f recorded at ISISS beamline on electrochemically obtained Ir@IrO_x anode at 330 eV Kinetic Energy and 20 eV Pass Energy.

Component	Line shape	FWHM / eV		Binding energy / eV	
		$4f_{7/2}$	$4f_{5/2}$	$4f_{7/2}$	$4f_{5/2}$
Ir_{met}	DS(0.01, 100)SGL(0)	0.90	0.90	60.85	63.85
Ir (IV)	DS(0.02, 100)SGL(20)	1.06	1.06	61.76	64.76
Ir (IV) sat	DS(0.02, 100)SGL(20)	1.26	1.26	63.05	66.05
Ir (III)	DS(0.02, 100)SGL(20)	1.05	1.05	62.40	65.40
Ir (III) sat	DS(0.02, 100)SGL(20)	1.45	1.45	64.20	67.20

Table 12. Fitting parameters for Ir4f recorded at TEMPO beamline on electrochemically obtained Ir@IrO_x anode at 530 eV Kinetic Energy and 50 eV Pass Energy.

Component	Line shape	FWHM / eV		Binding energy / eV	
		$4f_{7/2}$	$4f_{5/2}$	$4f_{7/2}$	$4f_{5/2}$
Ir_{met}	DS(0.01, 100)SGL(0)	1.29	1.29	60.6	63.6
Ir (IV)	DS(0.02, 100)SGL(20)	1.24	1.24	61.9	64.9
Ir (IV) sat	DS(0.02, 100)SGL(20)	1.13	1.13	63.3	66.3
Ir (III)	DS(0.02, 100)SGL(20)	0.95	0.95	62.5	65.5
Ir (III) sat	DS(0.02, 100)SGL(20)	1.55	1.55	64.3	67.3

Table 13. Fitting parameters for Ir4f recorded at TEMPO beamline on electrochemically obtained Ir@IrO_x anode at 390 eV Kinetic Energy and 50 eV Pass Energy.

Component	Line shape	FWHM / eV		Binding energy / eV	
		$4f_{7/2}$	$4f_{5/2}$	$4f_{7/2}$	$4f_{5/2}$
Ir_{met}	DS(0.01, 100)SGL(0)	1.29	1.29	60.7	63.7
Ir (IV)	DS(0.02, 100)SGL(20)	1.24	1.24	62.0	65.0
Ir (IV) sat	DS(0.02, 100)SGL(20)	1.35	1.35	63.3	66.3
Ir (III)	DS(0.02, 100)SGL(20)	0.95	0.95	62.6	65.6
Ir (III) sat	DS(0.02, 100)SGL(20)	1.55	1.55	64.4	67.4

Table 14. Fitting parameters for Ir4f recorded at TEMPO beamline on electrochemically obtained Ir@IrO_x anode at 820 eV Kinetic Energy and 50 eV Pass Energy.

Component	Line shape	FWHM / eV		Binding energy / eV	
		$4f_{7/2}$	$4f_{5/2}$	$4f_{7/2}$	$4f_{5/2}$
Ir_{met}	DS(0.01, 100)SGL(0)	1.29	1.29	60.6	63.6
Ir (IV)	DS(0.02, 100)SGL(20)	1.24	1.24	62.0	65.0
Ir (IV) sat	DS(0.02, 100)SGL(20)	1.35	1.35	63.3	66.3
Ir (III)	DS(0.02, 100)SGL(20)	0.95	0.95	62.5	65.5
Ir (III) sat	DS(0.02, 100)SGL(20)	1.55	1.55	64.4	67.4

2.3.6.4. Core-level Spectra Simulation using SESSA Software

In order to reproduce the experimental results or estimate the oxide thickness layer formed on the particles under the reaction conditions we performed the simulation of the photoemission spectra by means of the SESSA software (Version 2.0)[224]. This software is capable of simulating the photoelectron intensities of nanostructures such as islands, rods, spheres, layered spheres on different surfaces - substrates and contains the vast database needed to perform quantitative interpretation of the spectra such IMFP etc. A simulation module provides an estimate of individual peak intensities as well as the XP spectra[225]. The configurations of the sample, analyzer etc. has been selected close to the real set-up used in ISISS and TEMPO beamlines and shown in Table 15. The sketches of the morphologies used for the calculations of Ru-based and Ir-based systems are shown in Figure 44 and Figure 45, respectively.

Table 15. Parameters used for simulation of the XP spectra recorded at ISISS and TEMPO beamlines in SESSA software.

Configuration Parameters	ISISS beamline	TEMPO beamline
Orientation of sample surface normal:		
Phi / deg	0.000	0.000
Theta / deg	90.000	0.000
Rot / deg	-	-
Orientation of analyzer axis:		
Phi / deg	0.000	0.000
Theta / deg	90.000	0.000
Orientation of source axis		
Phi / deg	55.000	180.000
Theta / deg	90.000	35.300
Orientation of polarization vector		
Phi / deg	-	90.000
Theta / deg	-	54.700
Aperture		
Lower phi / degree	0.000	0.000
Lower Theta / degree	0.000	0.000
Upper Phi / degree	360.000	360.000
Upper Theta / degree	22.000	22.000

Figure 44. Sketch of the models used for photoemission spectra simulation with the SESSA software. Panel A: "layered sphere" morphology, metallic ruthenium particles (d = 2 nm) covered by IrO_2 shell of various thickness.

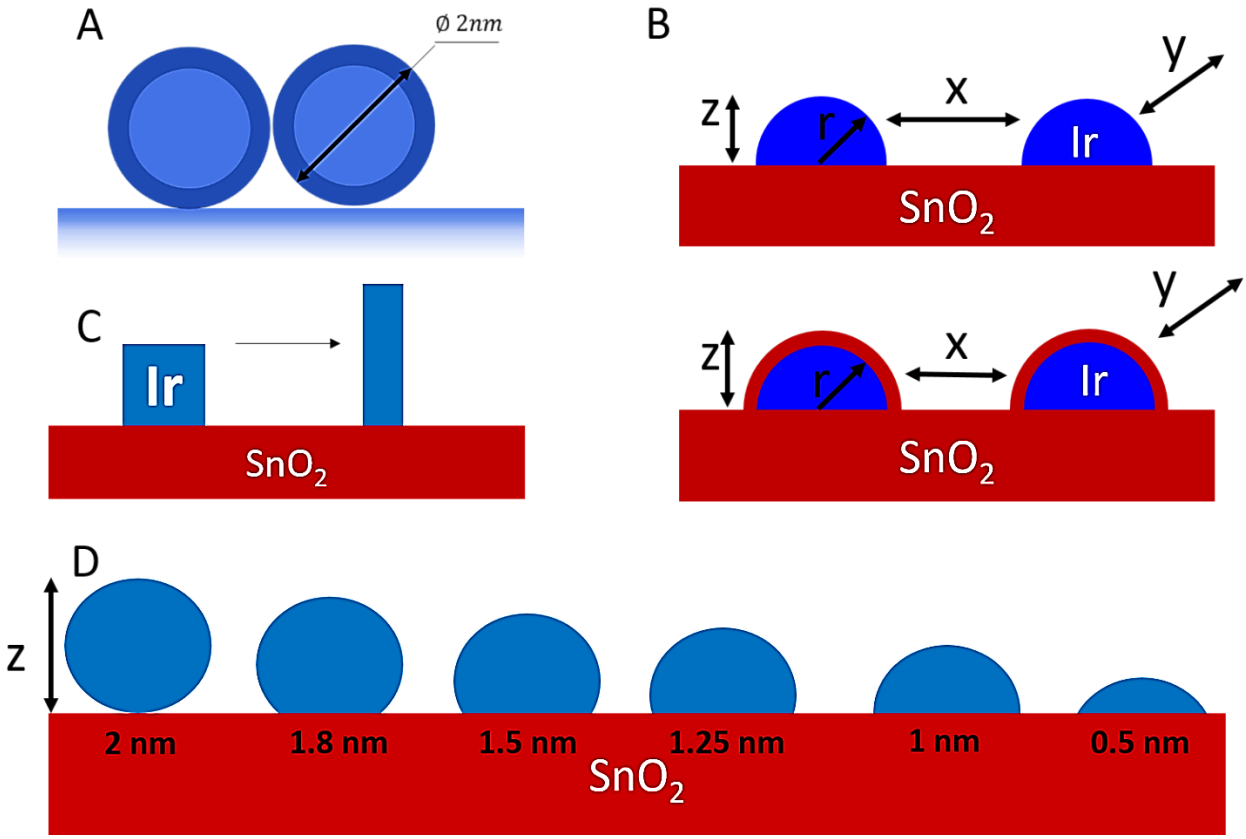

Figure 45. Sketch of the models used for photoemission spectra simulation with the SESSA software. Panel A: "layered sphere" morphology, metallic iridium particles (d = 2 nm) covered by IrO_2 shell of various thickness, substrate - carbon; Panel B: "spheres" and "layered spheres" morphologies on SnO_2 substrate, in the latter case iridium nanoparticles are covered by tin oxide shell; Panel C: "islands" morphology, varied particles shape with constant volume; Panel D: "spheres" morphology, iridium nanoparticles on tin oxide substrate.

2.3.6.4.1. Ruthenium Oxide Thickness Estimation

The thickness of the oxide layer formed on Ru (as prepared, AP) catalyst under the electrochemical oxidation was estimated on the basis of a "layered spheres" morphology (see the sketch in Figure 44). For simplicity, the oxide shell was considered to consist only of RuO_2. The particles diameter was maintained constant at the value of 2.6 nm, while the thickness of the oxide layer and the diameter of the metallic ruthenium core was varied accordingly. The calculations were done for the photon energy of 820 eV. The density of metallic Ru was taken as 12.45 g/cm^3 = 7.4 * 10^{22} atoms/cm^3, of RuO_2 – 6.97 g/cm^3 = 3.2 * 10^{22} atoms/cm^3.

2.3.6.4.2. Iridium Oxide Thickness Estimation

In order to estimate the thickness of the oxide layer formed on iridium nanoparticles under the OER conditions, we used a "layered spheres" morphology. The spherical particles of metallic iridium were covered by iridium oxide layer of various thickness. The substrate used in these

calculations was carbon (Panel A of Figure 45). Particularly, we used the following parameters and assumptions during the calculations:

- diameter of the metallic iridium core of 2 nm (corresponding to the mean diameter of the pristine Ir nanoparticles) was kept constant throughout the modeling;
- density of metallic iridium nanoparticles was taken as 22.42 g/cm^3 = 7 * 10^{22} atoms/cm^3, of carbon substrate – 2.2 g/cm^3 = 1.1 * 10^{23} atoms/cm^3;
- iridium oxide shell contained only Ir (IV) species as the calculations were done for the OER region where Ir (III) is absent (for the data see Chapter 5 and 6);
- thickness of the oxide layer was varying from 0 nm to 0.35 nm;
- XP spectra were simulated for the photon energies of 460 eV, 595 eV, 1080 eV at which the experimental data were obtained;
- oxide/metal interface is considered as continuous and well-defined, meanwhile in real system gradients and mixed regions may exist at the interface.

2.3.6.4.3. Tin Oxide Segregation on Metallic Iridium Particles

Chapter 6 is devoted to the *in-situ* studies of supported iridium catalyst on antimony-doped tin oxide. The experimental results discussed there revealed a potential-induced evolution of the Sn/Ir atomic ratio. Moreover, its behavior depends on the used photon energy, i.e. the analytical depth. One of the attempts made for the experimental data interpretation was related to the simulation of Ir4f and Sn3d XP spectra for different morphologies in order to visualize the observed changes.

The first model (Panel B of Figure 45) used for the calculations was intended to simulate the full encapsulation of iridium nanoparticles by tin oxide layer:

- antimony was excluded from the calculations;
- radius of iridium nanoparticles was varied from 10 to 30 Å;
- photon energies used in modeling for Ir4f and Sn3d XP spectra corresponded to the kinetic energies of the emitted electrons of 390 eV; 530 eV; 810 eV according to the experimental data;
- metallic iridium nanoparticles density was taken as 22.42 g/cm^3 = 7 * 10^{22} atoms/cm^3, tin oxide – 6.8 g/cm^3 = 2.8 * 10^{22} atoms/cm^3;
- tin oxide layer thickness was varied in the range 3 – 9 Å.

The next trial was related to the changes of iridium particle shapes at a constant volume. For this, the “islands” morphology was applied (Panel C of Figure 45). The volume was estimated for spherical particles of 2 nm and maintained constant through the calculations while the

parallelepiped dimensions were varied accordingly. The distance between iridium particles, abbreviated as x and y in the software was maintained constant at 90 Å. The other parameters (such as densities, photon energies etc.) were used analogous to the previous model.

The main drawback of the SESSA software is a limited set of morphologies available for the calculations. The simulation of partial surface segregation of tin oxide was realized by a “spheres” morphology (see Panel D of Figure 45) by changing the protruding height of iridium nanoparticles above the substrate. The diameter of the particles was equal to 2 nm and the height (parameter z) of the particles protruding above the substrate was varied from 2 nm down to 0.5 nm. The distance between iridium particles, abbreviated as x and y in the software was kept constant at 85 Å.

The results of the modeling are presented and discussed in Chapter 6.

Chapter 3. Ruthenium-based Anodes for PEM Electrolyzers

3.1. Introduction

Ru-based catalysts are the most active materials for the anodes of PEM water electrolyzers, however due to their poor stability, the direct utilization of pure ruthenium oxides is not reliable. In order to develop more stable Ru-based catalysts without compromising their electrochemical activity, the understanding of their degradation mechanism is necessary and requires thorough studies.

In this work, we combine near-ambient pressure XPS and NEXAFS techniques in order to perform *operando* studies of the membrane electrode assemblies with Ru-based oxide anodes under water splitting conditions. The results discussed in this Chapter allowed us to shed light on the degradation mechanism of Ru-based electrodes and propose tentative mechanism of the oxygen evolution reaction.

Two main types of the catalysts have been chosen for the analysis – RuO_2 oxide with rutile structure obtained by thermal oxidation of Ru nanoparticles on the one hand and metallic Ru nanoparticles (Ru (AP), as – prepared), which were oxidized electrochemically under the reaction conditions. Under the experimental conditions (potential cycling, oxygen evolution reaction conditions) the surface of the latter is covered by an electrochemically formed oxide and the anode is abbreviated as $Ru@RuO_x$ emphasizing formation of an oxide layer on the metal surface, which was confirmed by NAP-XPS. Investigation of these two types of Ru-based materials helped us to uncover species responsible for the degradation and for the OER electrocatalysis.

In-situ studies of RuO_2 and $Ru@RuO_x$ anodes were performed at the ISISS beamline at BESSY II synchrotron facilities during two different beamtimes (November 2015 for RuO_2 and May 2017 for $Ru@RuO_x$, correspondingly). The analysis of the results obtained on RuO_2-based MEAs provided us with new important information regarding the chemical state of Ru during the OER. The unfortunate presence of a Si contamination did not allow us, however, to obtain reliable information on the nature of oxygen-containing species on the anode surface during the November 2015 beamtime session, which we tried to recover in May 2017. This, as well as differences in the electrochemical stability of the two anodes prompted us to modify the experimental procedure during the later beamtime session. For RuO_2 (in November 2015) only photoemission spectra were collected. The whole set of the core-levels of the elements present on the electrode surface (Ru3d, C1s, O1s, F1s, S2p, Si2p) were collected for each applied potential and their potential-induced evolution was followed during two OER cycles. This study allowed us to observe red-ox transitions of Ru during the OER. However, recent discussions of the OER mechanism on transition metal oxides emphasize the role of oxygen anion red-ox transitions[108]. Considering this, during the second synchrotron session in addition to NAP-XP we also collected NEXAFS spectra

at the O K edge. Poor stability of the Ru@RuO_x anode results in its fast degradation under the OER conditions, which prompted us instead of collecting all spectra at a constant applied potential to perform several consecutive OER cycles. Thus, for Ru@RuOx the measurement protocol was the following: during the first OER cycle only O K edge spectra were recorded, during the second – Ru3d XP spectra, during the third – O1s XP spectra, allowing more facile comparison of the similar spectra. The state of the anode between the cycles was controlled by collecting all relevant photoemission and absorption spectra.

Comprehensive analysis of the photoemission and absorption spectra obtained for RuO_2 and Ru@RuO_x anodes in the presence of water vapor under electrochemical control allowed us to reveal formation of different valence states of Ru, follow their evolution under the potential cycling and correlate these results with the stability of the materials. The *ex-situ* characterization such as microscopy and X-ray diffraction as well as various electrochemical tests performed for each of the electrodes are also discussed here.

The objective of the work presented in this Chapter is to understand the behavior of Ru-based anodes and the dependence of their structure and electrode polarization. By combining the near ambient pressure XPS and NEXAFS measurements for the *in-situ* studies of thermally (RuO_2) and electrochemically obtained (Ru@RuO_x) oxides anodes we aimed to:

- study the red-ox transformations of ruthenium- and oxygen-based species;
- follow the evolution of the surface species under the operation conditions;
- understand the nature of the OER active sites;
- study the reversibility of the processes taking place at the electrode/electrolyte interface;
- analyze the influence of oxide nature (thermally or electrochemically formed) on the overall performance;
- correlate the changes mentioned above with the catalytic activity of the catalysts and their stability.

This chapter is based on the published article: Saveleva, V. A.; Wang, L.; Luo, W.; Zafeiratos, S.; Ulhaq-bouillet, C.; Gago, A. S.; Friedrich, K. A.; Savinova, E. R. Uncovering the Stabilization Mechanism in Bimetallic Ruthenium − Iridium Anodes for Proton Exchange Membrane Electrolyzers. *Phys. Chem. Lett.* **2016**, *7*, 3240–3245[181] and completed with unpublished results.

3.2. Material Characterization

This section contains the results obtained on pristine as well as post-mortem Ru@RuO_x and RuO_2 catalyst powders by means of XRD and microscopy. The results of the electrochemical tests performed in a three-electrode standard cell in the presence of aqueous 0.05 M H_2SO_4 electrolyte and in a two-electrode configuration under water vapor ambient using a MEA configuration are also discussed here.

3.2.1. XRD Analysis

Ru-based catalysts were synthesized according to the method described in Chapter 2. As prepared Ru (AP) and thermally obtained RuO_2 nanoparticles were characterized by means of X-ray powder diffraction and their diffractograms are shown in Figure A1 of the Appendix and Figure 46, correspondingly. As it will be shown in the next section, the mean particle size of Ru (AP) is ca. 2.6 nm can explain the absence of sharp peaks in the corresponding diffractogram. In case of thermal Ru oxide, we observed the well-defined reflections of the rutile RuO_2 phase. Additional reflections at 2Θ=44 and 59° may be attributed to a small admixture of unreacted metallic Ru. The XRD patterns used for the phase identification are shown in Table A 1, Table A 2 and Table A 3 of the Appendix. The XPS analysis discussed further did not reveal presence of metallic ruthenium on the surface of the RuO_2 sample, even during the depth profiling measurements. We suggest that the metallic reflections observed in diffractograms are most likely coming from the metallic core of the particles. It appears that the temperature of 490°C applied during the thermal oxidation was not sufficient to fully oxidized Ru nanoparticles into the RuO_2 phase. However, we preferred to avoid higher temperature treatment in order to limit sintering and undesired growth of the particles, which was observed already under the applied conditions. Already under the conditions applied here, the particles of RuO_2 are rather big, with the length up to 90 nm (see details in the next section).

The analysis of Ru (AP) diffractogram shows the presence of unreacted salt $RuCl_3$. However, the pattern of RuO_2 powder prepared from Ru (AP) does not contain any reflections corresponding to $RuCl_3$. We suppose that during the thermal treatment of metallic Ru, ruthenium chloride was decomposed with a release of chlorine gas. The photoemission measurements performed on electrochemical and thermal Ru oxides did not reveal the presence of chlorine species on the anode surface regardless the applied potential. Additionally, no chlorine evolution controlled by mass spectrometry (controlled at m/z = 35 and 37) was observed during the OER.

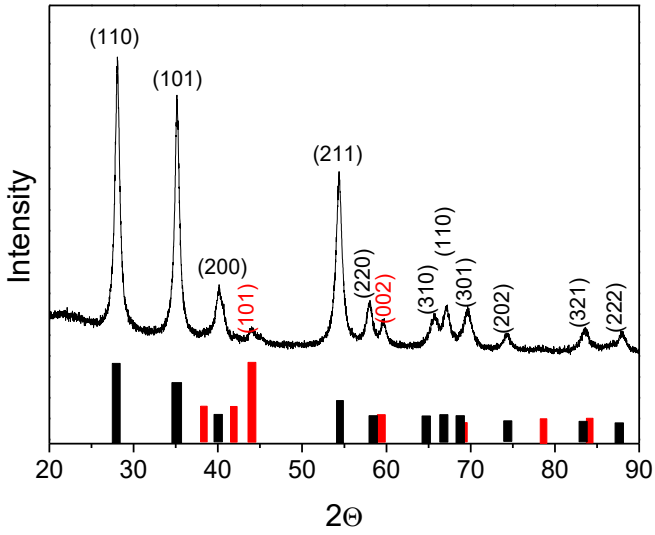

Figure 46. XRD patterns of RuO_2 powder. Pattern markers are provided at the bottom of the image and correspond to: RuO_2 oxide – rutile - 03-065-2824 (black); metallic hcp Ru - 01-089-3942 (red).

3.2.2. Microscopy

Typical TEM images of as prepared Ru and thermally obtained RuO_2 particles before any electrochemical tests are shown in Figure A 2. Initially the Ru (AP) sample is in the form of nanoparticles with a mean diameter of ca. 2.6 nm. For the RuO_2 sample, one may notice that the catalyst comprises a fraction of small round-shaped (or facetted) particles with the size of ca. 7 nm, as well as rod-shaped particles, with diameter 9 - 16 nm and the length varying from 10 to 90 nm with a mean value of 15 nm.

The STEM analysis was performed on both catalysts in pristine form and after the samples had been subjected to NAP-XPS measurements under electrochemical control in the potential interval of the OER. The typical images obtained for Ru-based samples are shown in Figure 47. In case of Ru (AP) powder, the application of potential leads to the formation of an oxide layer on metallic Ru particles as revealed by NAP-XPS measurements and discussed below. We define these nanoparticles as $Ru@RuO_x$ sample. However, STEM analysis of the latter did not allow us to distinguish the oxide layer coating the metallic core of Ru nanoparticles. This can be attributed either to the fact that the oxide layer on the metal surface is very thin (according to NAP-XPS data it does not exceed 2 monolayers, the results of oxide thickness estimation are provided in Figure A 3 of the Appendix), which is beyond the resolution of our STEM measurements, or (most likely) to the oxide instability under a focused electron beam (due to its reduction) during the microscopy measurements. Nevertheless, the mean diameter of $Ru@RuO_x$ remained the same as in the initial

Ru (AP) powder. In a similar way for RuO_2 electrocatalyst, no significant difference either in the particle size or in the shape of the particles was observed after the NAP-XPS measurements.

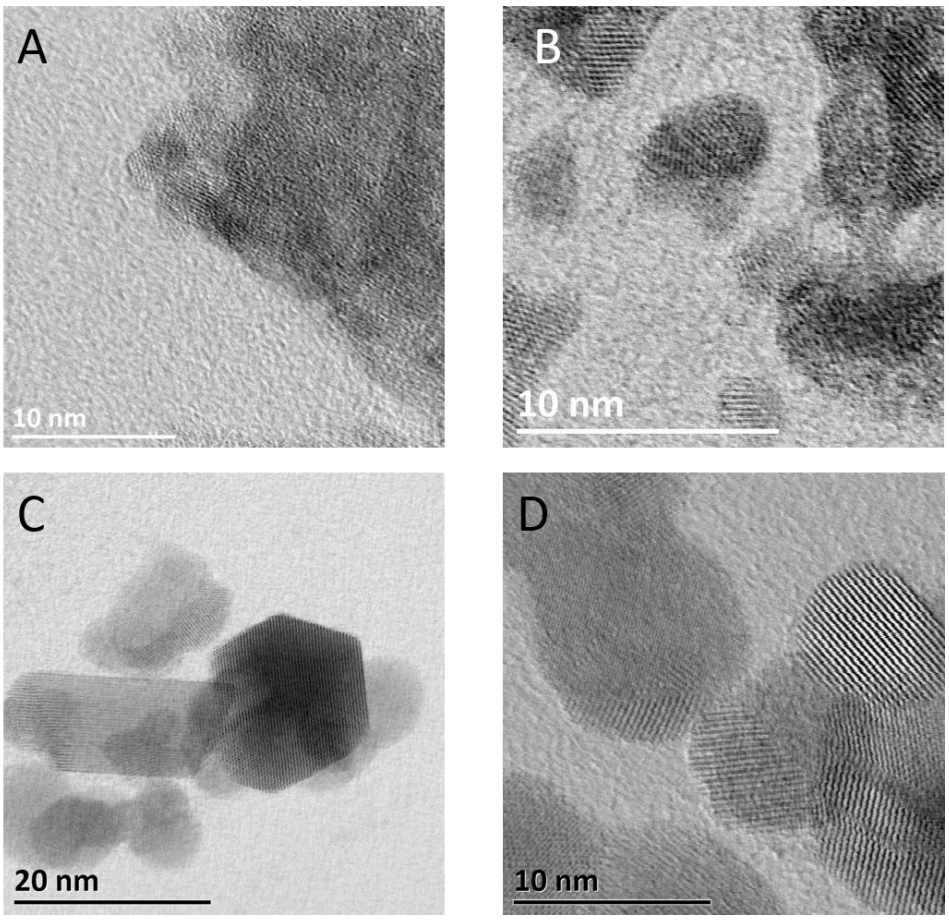

Figure 47. STEM images of Ru (A, B) and RuO_2 (C, D) catalysts before (as prepared) (A,C) and after (B, D) in-situ NAP-XPS measurements under the OER conditions.

3.2.3. Electrochemical Tests in Liquid Electrolyte

All the electrochemical measurements of the catalyst powders in a three-electrode glass electrochemical cell in the presence of 0.05 M H_2SO_4 were performed by L. Wang (DLR, Stuttgart). The experimental details were mentioned in Chapter 2.

Figure 48 compares the rotating disc electrode data obtained on Ru (AP) catalyst (transformed into $Ru@RuO_x$ under the cycling as further confirmed by NAP-XPS measurements) and RuO_2 electrodes in 0.05 M H_2SO_4. One may clearly see a drastic decrease of the electrochemical activity for both anodes and especially for metallic Ru following consecutive excursions in the OER potential interval. The $Ru@RuO_x$ anode demonstrates higher activity during the first and the second cycles in comparison to the RuO_2 anode in agreement with the literature data[27,226,227], however further cycling in the same potential interval (from 1.00 V to

1.45 V vs RHE) inverts the relation. The evolution of the mass activity with potential cycling for both anodes is shown in Figure 49. Ru@RuO_x shows ca. 40 times higher activity than RuO_2 during the second cycle; however, the activity ratio drops down to 3 in the 4th cycle and one during the 8th cycle. The data obtained suggest faster degradation of electrochemical compared to thermal oxide anodes under potential cycling in the OER interval in agreement with the literature. This will be further corroborated by the NAP-XPS data.

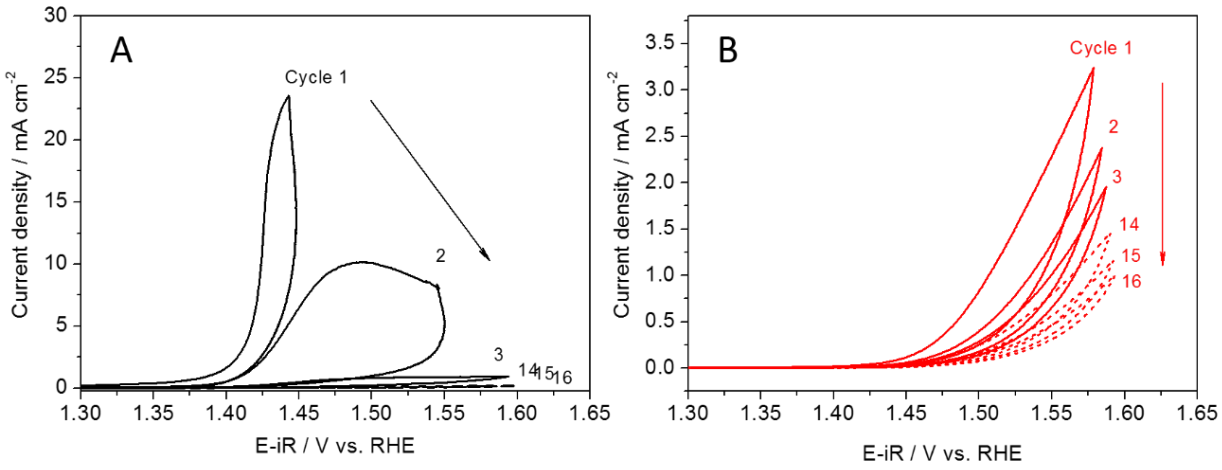

Figure 48. Current-potential characteristics of the Ru@RuO_x (A) and RuO_2 (B) anodes measured in N_2-saturated 0.05 M H_2SO_4 at 25 °C with a scan rate of 5 mV s^{-1}. Catalysts loading 60 μg cm^{-2}.

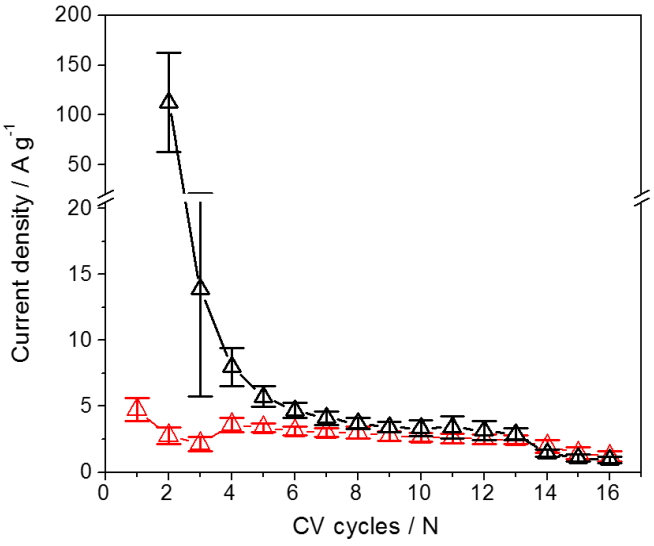

Figure 49. Evolution of the mass activity of Ru@RuO_x (black) and RuO_2 (red) electrodes measured at 1.48 V vs. RHE. It should be noted, that due to the extremely high currents obtained on Ru@RuO_x anode during the first cycle the corresponding mass activity is not shown in the plot. Catalysts loading 60 μg cm^{-2}.

Constant evolution of the $Ru@RuO_x$ anode with potential cycling does not allow a meaningful Tafel slope analysis in order to discuss the rate determination step and/or the reaction mechanism. Estimation of the Tafel slopes from voltammograms presented in Figure 48 shows their continuous evolution suggesting an occurrence of non-steady state (degradation) processes. While the thermal ruthenium oxide is also prone to corrosion as previously discussed and shown in the corresponding data, the Tafel slope values in the potential interval from 1.4 V to 1.6 V vs RHE remained relatively constant and equal to 60 ± 5 mV dec^{-1}. However due to the degradation processes taking place at the electrode surface under high anodic potentials we also observed an increase of the slope up to 100 mV dec^{-1} at potentials above 1.5 V vs RHE. In the literature[69] the Tafel slope of 60 mV dec^{-1} was interpreted by an OER mechanism involving a reversible electrochemical step followed by a slow chemical step. However, considering the complexity of the OER process and a concomitant electrode degradation it is hardly possible to make reliable conclusions regarding the OER mechanism based on the Tafel slope analysis. This emphasizes the necessity of the *in-situ* studies using surface-sensitive techniques.

3.2.4. Electrochemical Tests under Gas-phase Water

Before the spectroscopic measurements, Ru-based anodes were pretreated by means of potential cycling in the NAP-XPS chamber under 3 mbar of water vapor in order to stabilize the electrode surface. The typical CVs for $Ru@RuO_x$ and RuO_2 anodes are shown in Figure 50. Considering increase of the membrane resistance with the decrease of the relative humidity the potential scale was Ohmic drop-corrected. The MEA resistance determined by the EIS in the NAP-XPS chamber of ca. 80 Ohm for $Ru@RuO_x$ and ca. 60 Ohm for RuO_2 anodes was used for the iR corrections. The EIS measurements were performed before and after the spectroscopic measurements in order to assess the state of the MEA, and no changes in the values were observed for any of the samples discussed here.

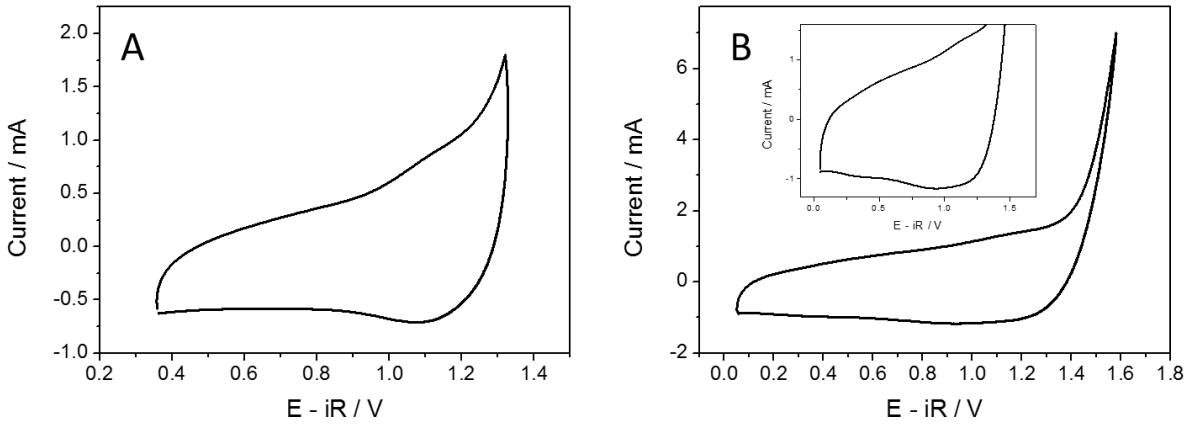

Figure 50. CVs obtained on Ru@RuO_x (A) and RuO_2 (B) anodes in the NAP-XPS chamber under 3 mbar of water vapor and 50 mV s^{-1} and 100 mV s^{-1}, respectively. The insert shows a zoomed area of the potential region [0.1; 1.6]. The potential values are Ohmic drop corrected. Catalyst loading – 0.1 mg cm^{-2}.

The RuO_2 anode exhibited stable CVs upon potential cycling in the interval from ca. 0 V to ca. 1.6 V. The CV of RuO_2 shows broad ill-defined anodic and cathodic peaks in the interval from ca. 0.4 to ca. 1.3 V. The anodic peak at 0.6 – 0.7V vs RHE is typically attributed to Ru (III) / Ru (IV) transition accompanied by proton insersion[42,49]. However *Lyons et al*.[54] proposed that this red-ox transition occurs earlier at ca. 0.4 V vs RHE, while the peak at 0.65 V vs RHE was attributed to the Ru (VI) / Ru (VII) transition. The anodic peak observed prior to the OER, around ca. 1.1 V vs. RHE, most likely corresponds to the oxidation of Ru to an oxidation state above IV. Thus, *Lyons et al*. attributed it to the Ru (VI) / Ru (VIII) transition[54].

Considering fast degradation of Ru@RuO_x in the potential interval of the OER observed in the liquid electrolyte, and its reduction to metallic Ru at potentials below ca. 0.38 V, potential cycling was performed in a limited interval from 0.35 V to 1.32 V vs DHE. In this potential interval only one anodic peak at 1.1 V vs DHE could be observed for the Ru@RuO_x anode. The attribution of the voltammetric features will be discussed later based on the NAP-XPS results.

The spectroscopic measurements have been performed under potentiostatic conditions by varying potential in an incremental fashion. The corresponding chronoamperograms recorded on Ru@RuO_x and RuO_2 anodes under consecutive OER cycles are shown in Figure 51 and Figure 52, respectively. The spectroscopic measurements were initiated 200 s after the potential application. In order to evaluate the degradation rate of Ru-based anodes under gas-phase water electrolysis conditions, we will compare the current values at the time of the XP and XA spectra recording, i.e. at 200 s. For the RuO_2 anode, the current was relatively stable at E – iR = 1.5 V. However, increasing the electrode potential up to E – iR = 1.8 V resulted in a much stronger current decay. In the 2nd OER cycle currents at 1.5 and 1.8 V decreased by ca. 25-30% compared to those

observed in the 1st OER cycle. In case of Ru@RuO_x anode, relatively stable OER currents were observed in the 1st OER cycle at E-iR up to 1.41 V. However, currents were noticeably smaller in the subsequent OER cycles with ca. 25% drop in the 2nd and ca. 40 – 50% drop from their initial values (E – iR = 1.39 V and 1.41 V vs DHE) in the 3rd OER cycle. It should be also noted that due to the lower stability of Ru@RuO_x anode, the anodic potential used for the *in-situ* NAP-XPS studies of this sample was limited to 1.41 V (to avoid strong corrosion of the catalyst) in comparison to 1.8 V used in case of RuO_2 electrode.

As it was mentioned in Chapter 2, the NAP-XPS chamber was equipped by mass spectrometer in order to monitor the gas-phase composition in the chamber and particularly to follow the oxygen and hydrogen evolution. Figure 53 shows the example of MS data obtained on RuO_2 anode at different potential (E - iR) values. Oxygen evolution is clearly observed at 1.5 and 1.8 V vs. DHE. At 1.5 V the MS signal for the m/z = 32 is stable indicating that the electrocatalytic production of oxygen is also stable during the time of the measurement. However, at the very high anodic potential of 1.8 V the ionic current decays most probably due to the electrochemical corrosion of RuO_2. This should be compared with the chronoamperograms, which show relatively stable currents at 1.5 and fast current decay at 1.8 V.

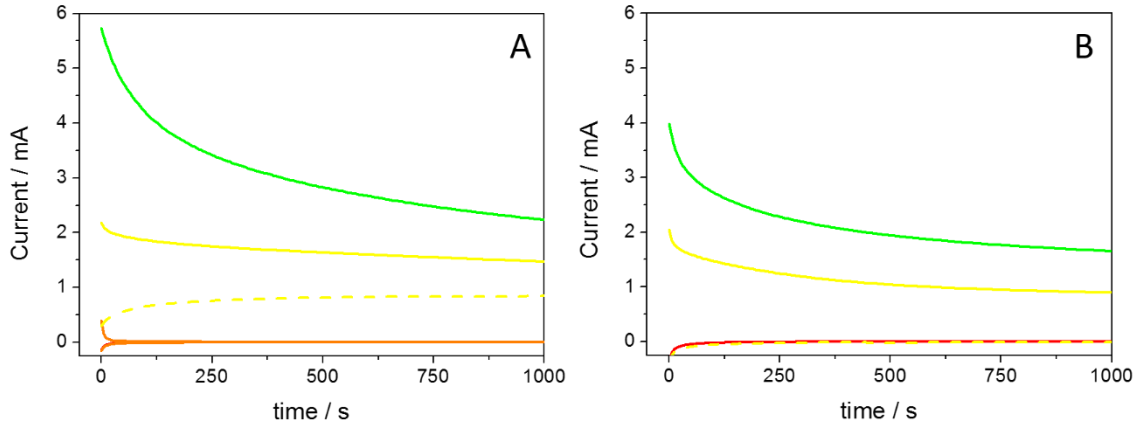

Figure 51. Chronoamperograms obtained in the NAP-XPS chamber at BESSY II synchrotron on RuO_2 anode under 3 mbar water vapor during the 1st (A) and 2nd OER cycle and different polarization conditions: 0.0 V (red); 1.0 V (orange); 1.5 V (yellow); 1.8 V (green). Solid lines represent the forward scan, the dashed – the backward. Catalyst loading – 0.1 mg cm^{-2}. The potential is ohmic drop corrected. Temperature 25°C.

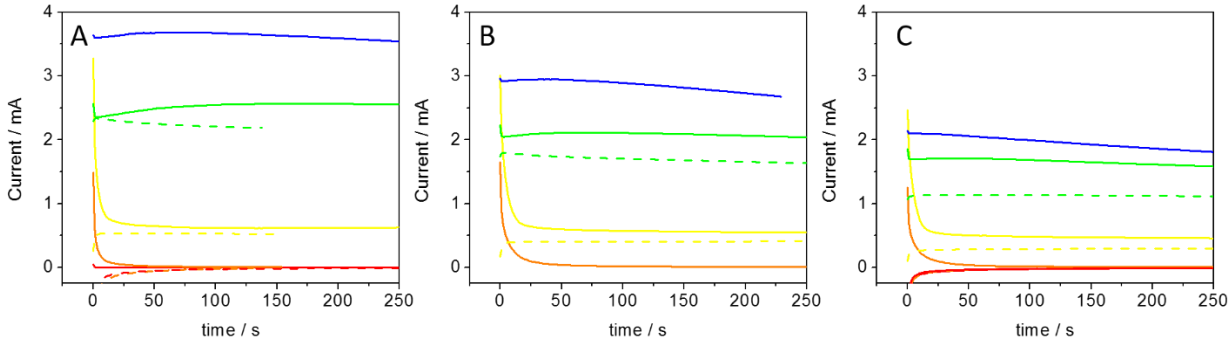

Figure 52. Chronoamperograms obtained in the NAP-XPS chamber at BESSY II synchrotron on Ru@RuO_x anode under 3 mbar water vapor during O K edge (A), C1sRu3d (B) and O1s (C) recording and different polarization conditions: 0.75 V (red); 1.00 V (orange); 1.34 V (yellow); 1.39 V (green); 1.41 V (blue). Solid lines represent the forward scan, the dashed – the backward. Catalyst loading – 0.1 mg cm^{-2}. The potential is ohmic drop corrected. Temperature 25°C. Panel A is duplicating Figure 39.

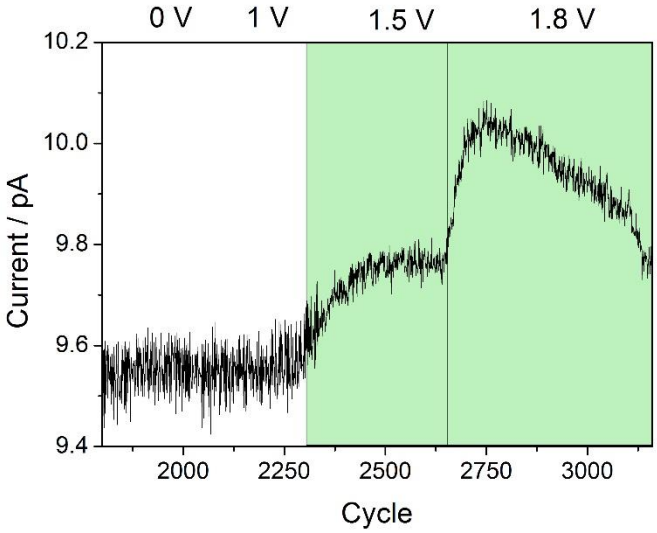

Figure 53. MS data for the m/z = 32 acquired during the measurements for RuO_2 electrode. The Ohmic drop-corrected potential values are provided at the top of the figure. The OER region is green-filled. The OER onset potential correlates with the MS data on the oxygen and the hydrogen (from the CE - not shown) evolution.

3.3. RuO_2 Anode: Surface Composition

The measurement protocol for *in-situ* photoemission studies on RuO_2 electrode comprised of the measurements of all core-level spectra (Ru3d, C1s, O1s, F1s, S2p, Si2p) under each potential. The potential was switched in a stepwise manner and the potential-induced changes were followed during two OER cycles.

We will start from the analysis of Ru3d XP spectra obtained on a RuO_2 anode under different polarization conditions. Panel A of Figure 54 shows the fitted spectra of the RuO_2 electrode exposed to a potential of 1.5 V (vs. DHE), whereby the OER was confirmed by the mass spectrometer integrated in the measurement chamber (Figure 53). While the detailed fitting procedure of Ru3d spectra is discussed in the corresponding section of Chapter 2, here we will briefly explain the methodology. The complexity of the Ru3d fitting is related to numerous possible oxidation states of Ru and to overlapping of this peak with C1s. Another core-level peak of Ru – Ru3p – is less sensitive to the changes in the oxidation state, so it will not be discussed here. The contribution of carbon-based ionomer was included in the fitting and its intensity was estimated based on the F1s XP spectra. Four peak doublets have been used to perform the fitting of Ru3d XP spectra presented in this work. Their attribution to different oxidation states of ruthenium was done based on the literature data and on a self-consistent analysis of the spectra obtained at different potentials. The fitting parameters are presented in Table 6. Particularly, on the RuO_2 anode surface under OER conditions (Panel A of Figure 54) we detected the following components: rutile-type RuO_2, hydrous Ru (IV) oxide $Ru(OH)_x$, as well as Ru in higher oxidation states (VI) and (VIII). The latter is typically abbreviated as RuO_4 in the literature (even if neither its structure nor its exact composition are fully understood yet), while the existence of Ru (VI) oxide in the form of RuO_3 is still debated, so we will refer it as Ru (VI) species.

Panel B of Figure 54 demonstrates the gradual transformation of the Ru (IV) oxide into other species as the potential is increased positive of 0 V. It is notable that Ru (VIII) species are detected at 1.0 V, i.e. below the standard potential of the RuO_4 phase formation reported in the literature (1.387 V[21]). This can be rationalized by the formation of either a thin surface layer or islands of $RuO_{4(s)}$ (rather than a RuO_4 phase), strongly interacting with the underlying RuO_2 substrate. The interaction of the overlayer with the substrate is likely to account for the potential shift from the thermodynamic value.[228] Note also that RuO_4 species are unstable, which may jeopardize the determination of the Nernst potential for the Ru (IV)/Ru (VIII) transition.

While electrochemical formation of RuO_4 has been postulated in previous publications, it has never been detected on the anode surface by means of XPS either during or after the electrolysis, likely due to its instability at room temperature. *Kötz et al.* observed formation of

dissolved corrosion products in the vicinity of the RuO_2 anode simultaneously with the OER and hypothesized on the RuO_4 generation and the OER occurring through common intermediates (Ru (VI) and Ru (VII) in the Kötz' scheme).[98]

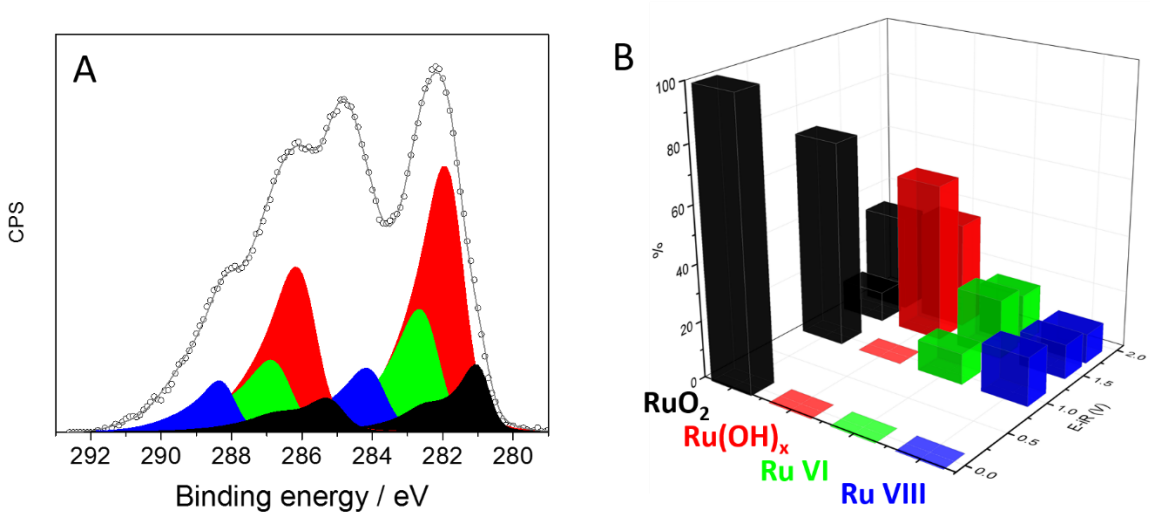

Figure 54. Panel A: fitted C1s-Ru3d XP spectra of RuO_2 electrode at 1.5 V. Experimental XPS data are shown as black cycles, fitted spectrum – as a grey line. For the sake of clarity carbon peaks are not shown. Panel B: Influence of the applied potential on the surface composition of RuO_2 electrode (1st OER cycle). Only forward scan is shown. Measurements were performed in 3 mbar H_2O ambient at a photon energy of 820 eV. The values of potential are iR corrected and are given on the dynamic hydrogen electrode (DHE) scale. Color codes: RuO_2 (black); $Ru(OH)_x$ (red); Ru(VI) (green); Ru (VIII) abbreviated as $RuO_{4(s)}$ in the text (blue).

As the electrode potential is shifted positive, the contribution of $RuO_{4(s)}$ surface species declines. This fact, along with the emergence of $RuO_{4(s)}$ below the OER onset, might suggest that $RuO_{4(s)}$, which is generated in an electrochemical step acts as an intermediate in the OER. Evidence provided by the isotope labeling experiments[23,92] advocates the so-called lattice oxygen evolution reaction, whereby the OER results from the higher to lower oxide decomposition:[95]

$$RuO_2 + 2H_2O \rightarrow RuO_{4(s)} + 4H^+ + 4e^- \quad (Eq.\ 22)$$

$$RuO_{4(s)} \rightarrow RuO_2 + O_2 \quad (Eq.\ 23)$$

Note however that the presence of $RuO_{4(s)}$ on the backward scan observed for RuO_2 (Panel A of Figure 55), $Ru@RuO_x$ (see the next Section) and $Ir_{0.7}Ru_{0.3}O_2$ (see Chapter 4) anodes challenges this hypothesis.

Next we would like to focus on the changes in the atomic contributions of rutile-type anhydrous RuO_2 and hydrous $Ru(OH)_x$ oxide. One may notice that a significant growth of $Ru(OH)_x$ starts at the OER onset potential. The stepwise decreasing of the potential presented in Panel A of Figure 55 shows that the potential reversal did not result in the restoration of the initial

composition, RuO_2 accounting to ca. 40 and $Ru(OH)_x$ ca. 45 %. Moreover, the contribution of the hydrated phase does not descend but continuously increases after consecutive potential cycles suggesting the irreversibility of the anhydrous-to-hydrous oxide transition as can be seen from Panel B of Figure 55, representing the results of the second potential cycle. We thus conclude that $Ru(OH)_x$ is formed as a result of the catalytic OER cycle and its transformation from anhydrous oxide is irreversible. The effect of the surface hydration on the activity of Ru-based catalysts has been discussed previously,[54] but not yet unequivocally confirmed by *in-situ* analytical methods. The changes of the hydration level of Ru (IV) oxide should be also observed in the O1s XP spectra recorded together with Ru3d. Unfortunately, the presence of Si cross contamination observed on the electrode surface under polarization did not allow us to perform any quantitative analysis of oxygen-containing species, as Si is present to be in the form of SiO_x dominating the intensity of the O1s XP spectra.

As to the Ru (VI) species, which in the literature is often denoted as RuO_3, it shows up at 1 V, simultaneously with $RuO_{4(s)}$, its contribution above the OER onset increasing for the RuO_2 electrode (Figure 54). Upon the reversal of the voltage bias, the Ru (VI) component still persists on the RuO_2 electrode (Panel A, Figure 55). Such a behavior suggests that in contrast to the accepted opinion (see recent review[14] and references therein) RuO_3 is not the OER intermediate.

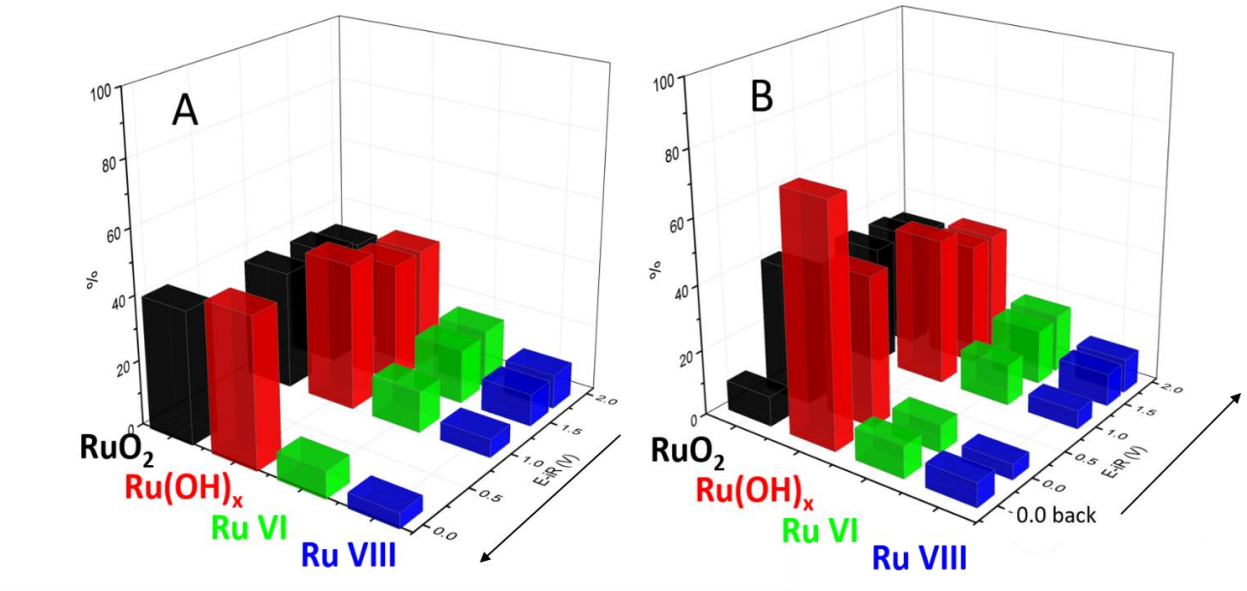

Figure 55. Influence of the applied potential on the surface composition of RuO_2 electrode during the backward scan of the first potential cycle (Panel A) and during the second potential cycle (Panel B) under 3 mbar water vapor ambient. Color codes: RuO_2 (black), hydrated RuO_2 (red), Ru (VI) (green), and Ru (VIII) (blue). In case of the 2nd cycle, the potential is increased in a stepwise manner from 0 to 1.8 V and then stepped back to 0 V (marked as 0.0 back). Photon energy 820 eV.

3.4. $Ru@RuO_x$ Anode: Surface Composition

In this section, we will present surface analysis of the electrochemical $Ru@RuO_x$ oxide during the OER.

As it was already mentioned in the introduction, poor stability of $Ru@RuO_x$ anode, consisting of metallic Ru core covered by the oxide formed under the potential cycling, forced us to modify the measurement protocol in comparison to the one used for RuO_2 anode. Three OER potential cycles in the range [0.75; 1.45] V vs DHE have been performed on $Ru@RuO_x$ electrode. During the first one, only O K edge spectra were recorded under different polarization conditions, while the second and the third were devoted to the measurements of Ru3d and O1s spectra, correspondingly. The overall composition of the electrode surface has been controlled by the measurements of all core-level spectra between the OER cycles under 0.75 V vs DHE. This potential has been chosen in order to avoid the reduction of Ru species.

Panel A of Figure 56 shows the C1s-Ru3d XP of a $Ru@RuO_x$ electrode at 0.75 V before the spectroscopic measurements, which suggests the presence of metal Ru, RuO_2 and hydrated $Ru(OH)_x$ species. The details of the fitting are discussed in Chapter 2. Even if the quantitative analysis of the initial Ru3d spectrum is complicated by the significant carbon contribution, it is apparent that potential cycling of the electrode initially composed of metal Ru in the interval from 0.3 to 1.0 V does not result in its transformation into anhydrous RuO_2, but rather leads to the formation of a mixture of hydrous Ru and anhydrous Ru oxides. This conclusion is in agreement with the literature[22,26,229]. The formation of the hydrous Ru oxide is also supported by the O1s spectrum (panel A of Figure 57), which shows the presence of both O and OH species (for more details see below). The contribution of the hydrous Ru oxide increases, while the contribution of anhydrous Ru oxide decreases after consecutive OER cycles as one can see from panels B, C and D of Figure 56.

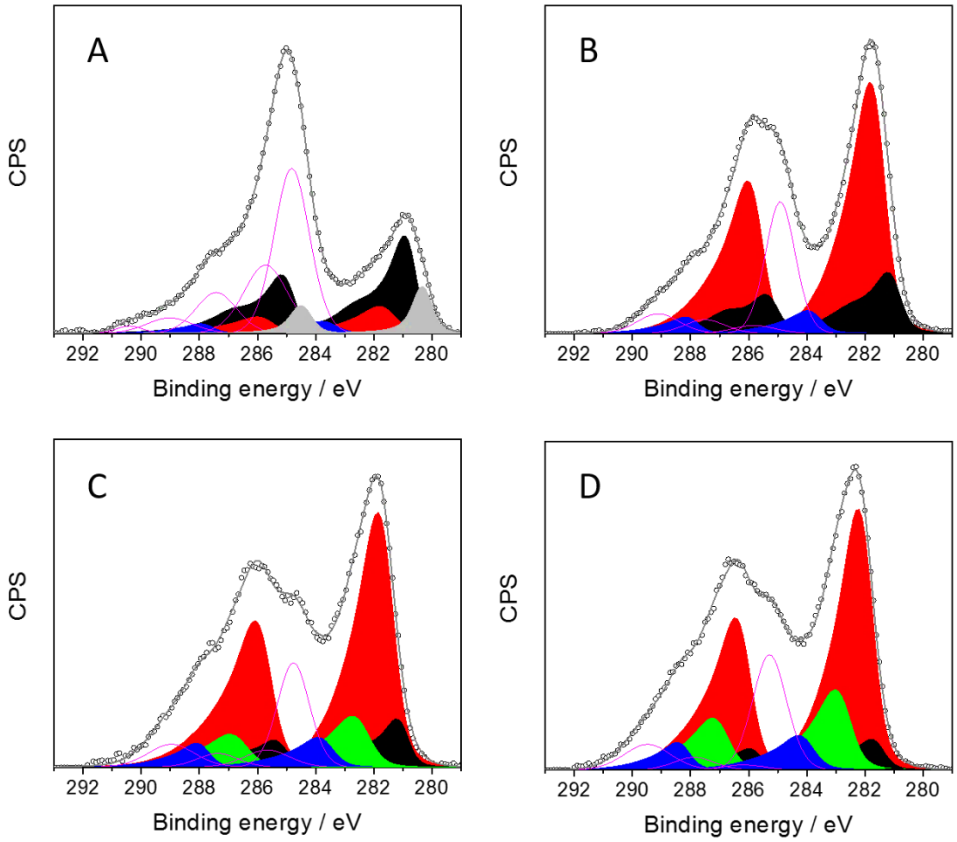

Figure 56. Fitted C1s-Ru3d XP spectra of Ru@RuO_x electrode at 0.75 V before the spectroscopic measurements (Panel A), after the 1st OER cycle – O K edge recording (Panel B), after the 2nd OER cycle – Ru3d XP spectra (Panel C) and after the 3rd – O1s XP spectra (Panel D). Experimental XPS data are shown as black cycles, fitted spectrum – as a grey line. Color code: metallic Ru (grey), RuO_2 (black), hydrated RuO_2 (red), Ru (VI) (green), Ru (VIII) (blue) and carbon species (magenta). Photon energy 820 eV.

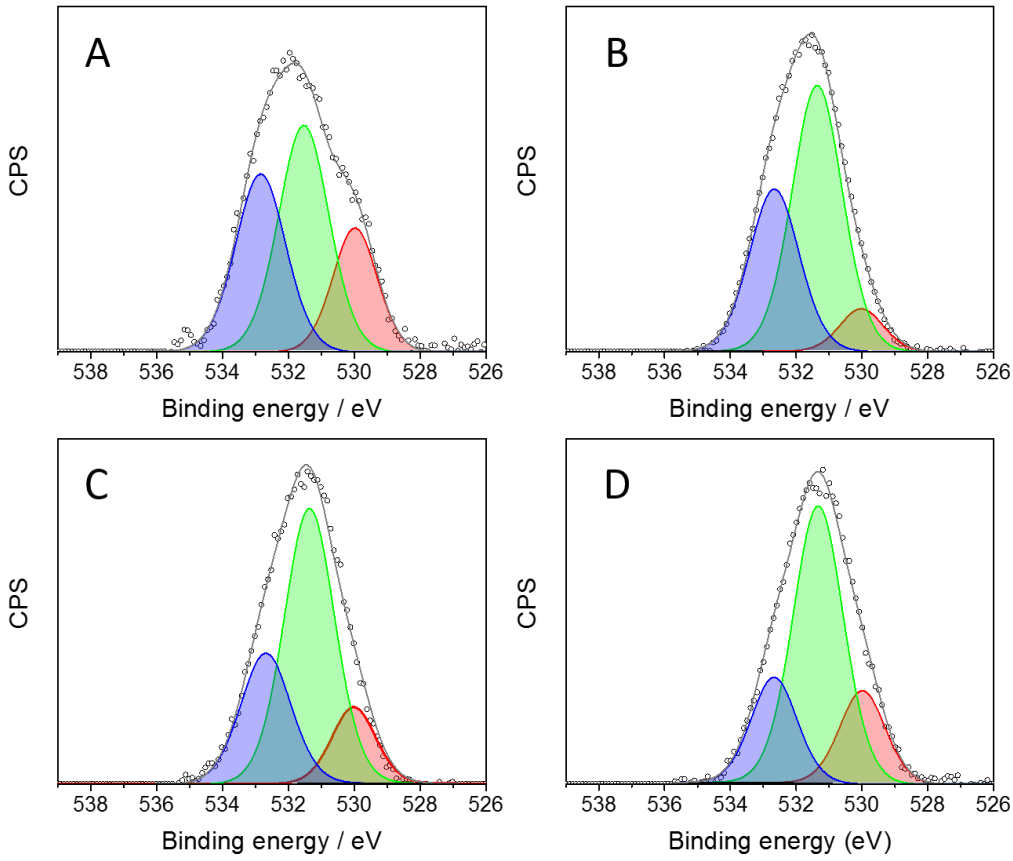

Figure 57. O1s XP spectra recorded on Ru@RuO_x anode under 3 mbar of water vapor and 0.75 V vs DHE before the spectroscopic measurements (A); after the 1st OER cycle, O K edge measurements (B); after Ru3d recording, 2nd OER cycle (C) and after the last OER cycle during O1s analysis (D). The fitting was done within three peaks: at 530 eV (red); 531.3 eV (green) and 532.7 eV (blue). Photon energy 1066 eV.

Before we follow the evolution of the surface composition resulting from consecutive OER cycles in more detail, we will discuss the influence of the applied potential on the evolution of Ru-based species obtained from the analysis of Ru3d XP spectra of Ru@RuO_x electrode.

The contribution of different components under polarization during the forward and the backward scans are shown in Figure 58. First of all, one may notice that the surface is dominated by the hydrous Ru oxide, while the contribution of the anhydrous oxide continuously decreases from ca. 20 down to ca. 9%. Significantly higher contribution of the hydrous oxide on the Ru@RuO_x – compared to the RuO_2 anode corroborates lower stability of the former under the OER conditions. For $Ru(OH)_x$ species one may notice their slight descent with the potential in the OER region, also observed on the RuO_2 anode, which can be explained by their oxidation into Ru (VI) and Ru (VIII) species.

Regarding the formation of Ru in high (above IV) oxidation states, the behavior is similar to the one observed for the RuO_2 anode. One may clearly see a constant presence of Ru (VIII)

species, abbreviated in this work as surface oxide $RuO_{4(s)}$, even at the initial potential. Please recall that the potential-induced changes of Ru3d spectra have been recorded during the second OER cycle. Based on the results obtained on RuO_2 anode, the following red-ox transitions are supposed to take place during the potential cycling: RuO_2 / $Ru(OH)_x$ – Ru (VI) – Ru (VIII). Moreover, the presence of Ru (VI) and Ru (VIII) species on the RuO_2 anode surface has been confirmed during the backward scan; even under 0V (see Figure 55). Thus, small traces of Ru (VIII) on $Ru@RuO_x$ anode of ca. 7% at 0.75 V (vs DHE) can be related to the previous OER cycle as well as to rather high initial potential of 0.75 V used in the study where Ru (VIII) species formed during the 1st OER cycle probably cannot be fully reduced.

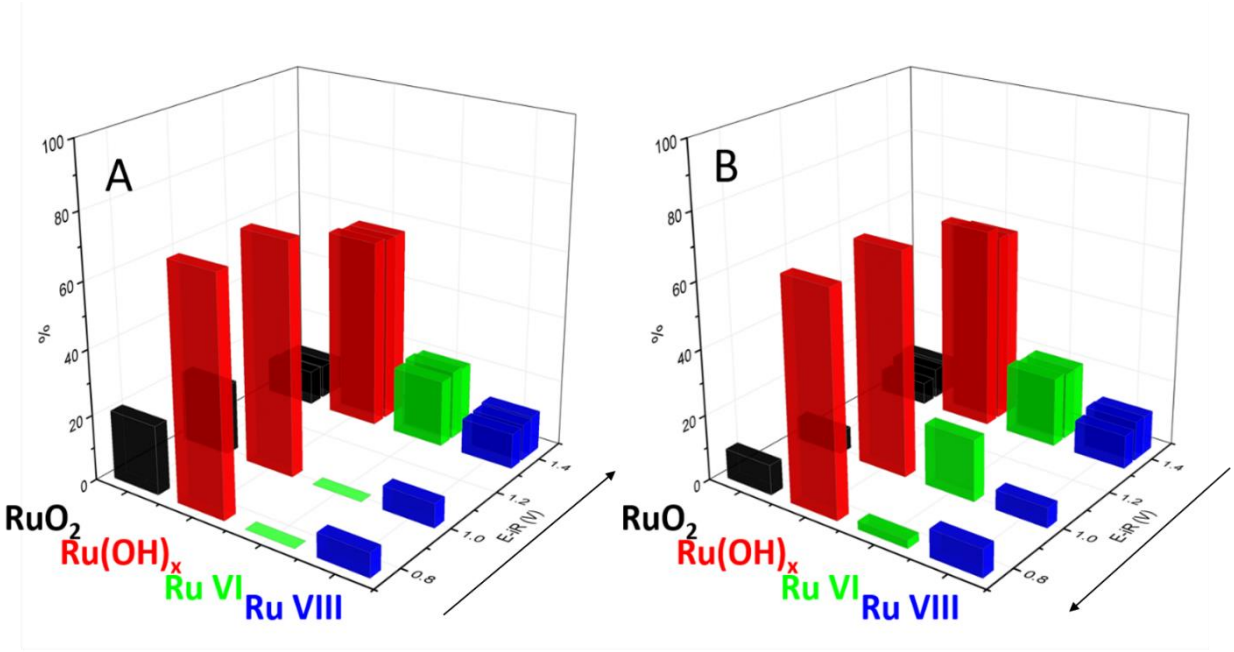

Figure 58. Influence of the applied potential on the surface composition of $Ru@RuO_x$ electrode during the forward (Panel A) and the backward (Panel B) scans of the 2nd OER cycle under 3 mbar water vapor ambient. Color codes: RuO_2 (black), hydrated RuO_2 (red), Ru (VI) (green), and Ru (VIII) (blue). Photon energy 820 eV.

One may see that increase of the applied potential leads to the formation of Ru (VI) species prior to the OER region (at 1.31 V vs DHE) which remains on the electrode surface under the potential reversal similar to what was observed for the RuO_2 anode. The amount of Ru (VIII) species is not strongly affected by the polarization and stays at the level of 7-9 %. Such a behavior is in contrast to the one exhibited by the RuO_2 anode in the first OER cycle (Figure 54) but is similar to the one observed in the 2nd OER cycle (Figure 55B). The fact that Ru (VIII) is observed on the electrode surface outsides the OER region cast doubt on our suggestion of the role of Ru (VIII) as an OER intermediate, which generates O_2 by decomposing into RuO_2 (Eq 23).

Let us turn again to the evolution of the Ru3d spectra resulting from consecutive OER cycles (Figure 58 and Figure 59). One of the most noticeable changes is related to the contribution of the hydrous Ru (IV) oxide, which significantly increases after the 1st OER cycle but then

stabilizes at ca. 65 – 70 %. The contribution of anhydrous RuO_2 is gradually decreasing with the number of cycles from initial ca. 60 % down to ca. 5 % after the 3rd OER cycle. For high oxidation states of ruthenium, the amount of Ru (VIII) species is stabilized on the electrode surface at the level of ca. 8 % and stays relatively constant. Meanwhile Ru (VI) species contribution is growing after the 2nd and 3rd cycles, which is probably related to the strong degradation of the sample.

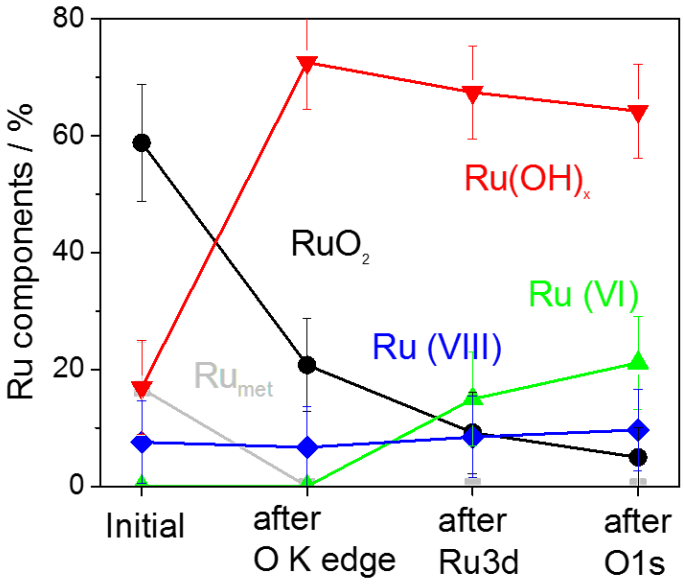

Figure 59. Influence of the potential cycling on the surface composition of Ru@RuO_x electrode obtained based on the corresponding Ru3d XP spectra recorded at 0.75 V (vs DHE) under 3 mbar water vapor ambient. Color codes: RuO_2 (black), hydrated RuO_2 (red), Ru (VI) (green), and Ru (VIII) (blue). The XP spectra were recorded at photon energy of 820 eV.

Overall, the evolution of Ru3d XP spectra with polarization and with the number of OER cycles followed on Ru@RuO_x confirmed the results obtained for the RuO_2 anode, the major difference residing in the higher contribution of the $Ru(OH)_x$ on the electrochemical compared to the thermal Ru oxide. However, the weak point of the *in-situ* analysis of the RuO_2 anode was the difficulty to analyze the O1s spectra due to the cross-contamination by SiO_x species. The constant control of Ru@RuO_x anode surface under different polarization did not reveal the presence of Si or other extrinsic species, which allowed us to discuss the evolution of the O1s XP spectra and correlate their changes with the results obtained from the Ru3d spectra analysis. Figure 57 shows the spectra recorded for the Ru@RuO_x anode before (Panel A) and after each of the three consecutive OER cycles (Panels B-D). The fitting was done using three peaks located at 530 eV, 531.3 eV and 532.7 eV. The Gaussian-Lorentzian (GL(30)) functions and Shirley background subtraction were used for the fitting. The FWHM was in the range of 1.6 – 1.8 eV (FWHM constraints ± 0.1 eV). The low-binding energy peak, located at 530 eV is typically related to the

lattice oxygen peak, assigned as O_{lat}[212], while two others are considered as OH groups (531.3 eV) and water molecules (532.7 eV). It should be also mentioned, that the two high binding energy peaks may also contain contribution from the oxidized carbon-based species. The water gas-phase peak is shifted to higher BE values due to the accelerated voltage applied to the nozzle, consequently it can be excluded from the consideration.

Now we can turn to the quantitative analysis of the O1s spectra evolution at different lifetime of the $Ru@RuO_x$ electrode shown in Figure 60. Panel A displays the changes of the O1s components ratio depending on the OER cycle at 0.75 V vs DHE. One may notice the growth of the OH species after consecutive OER cycles, while the contribution of the O_{lat} is quite stable with small deviations. Panel B of Figure 60 represents the potential-induced changes of oxygen core-level spectra recorded during the 3rd OER cycle. The fitted spectra are shown in Figure A 4. The amount of OH species is potential-independent, however the contribution of O_{lat} is increasing in the interval from 1.0 to 1.3 V.

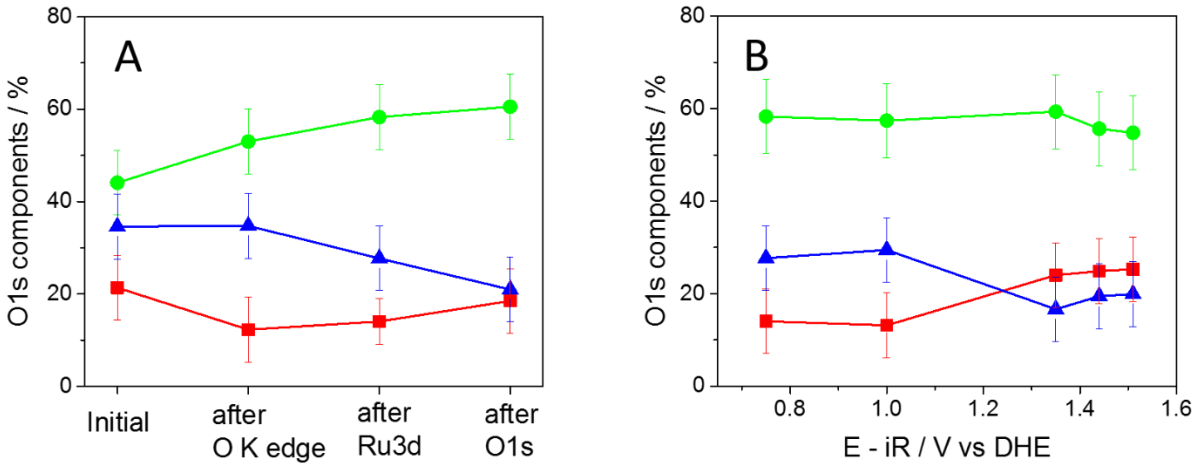

Figure 60. Potential-induced evolution of O1s components recorded on $Ru@RuO_x$ electrode under 3 mbar water vapor: O_{lat} (red), OH (green), H_2O (blue). Panel A represents the changes depending on the OER cycle under 0.75 V vs DHE, whereas Panel B – during one OER cycle under different polarization conditions.

Table 16 shows the calculated atomic ratios on the basis of the quantitative analysis of Ru3d, C1s and O1s spectra recorded on $Ru@RuO_x$ at the same kinetic energy of the emitted electrons of 530 eV and the electrode potential of 0.75 V vs DHE after consecutive OER cycles. The error bar estimated from the XP spectra fitting is ca. ± 0.05, except for the first column values which will be discussed later. For comparison the results obtained on two reference samples – RuO_2 and RuO_2 xH_2O (Alfa Aesar) – as well as the corresponding fitted photoemission spectra are shown in the Appendix in Table A 4 and in Figure A 5, respectively. The exact composition of the purchased hydrated RuO_2 was not specified by the supplier, however the analysis of the XP spectra revealed the presence of both forms of Ru (IV) oxide – anhydrous and hydrated. The

presence of Ru (III) hydrous oxide species cannot be excluded either, but considering absence of reliable reference data we refrain from its consideration.

Now we can turn to the discussion of the data shown in Table 16. The decreasing of C/Ru ratio with potential, estimated from the overall intensities of C1s and Ru3d spectra, can be attributed to the cleaning of the electrode surface after consecutive OER cycles. While the anhydrous Ru (IV) oxide can be attributed to RuO_2, the compositions of the high oxidation state components (Ru (VI) and Ru (VIII)) and hydrated Ru (IV) oxide have been debated in the literature.

We will start with the analysis of the anhydrous and hydrated Ru (IV) oxides, assuming that the latter is in a hydroxide form. The quantitative analysis of O1s XP spectra allows us to distinguish two form of the species – oxide/hydroxide – and their ratio is provided in Table 16. For comparison the ratio between two ruthenium components $RuO_2/Ru(OH)_x$ obtained from the fitting of Ru3d species was also estimated and included in the Table. It should be noted that before the excursions into the OER interval ("initial state") the contribution of carbon species in the overlapping XP spectra of C1sRu3d is quite high (C / Ru = 12.9), decreasing the accuracy of the Ru3d fitting for this spectrum (see Panel A of Figure 56). Besides, the cross-sections used here for the quantitative analysis were estimated for the metallic Ru rather than for the Ru oxides, which may be quite different[230]. Despite some errors, the overall decrease of the $RuO_2/Ru(OH)_x$ ratio after consecutive OER cycles seems undisputable. Meanwhile the O_{lat}/OH ratio estimated from O1s spectra does not show such a clear trend. Indeed, it decreases from ca. 0.48 down to 0.23 after the first OER cycle, and is then relatively constant after the 2nd and the 3rd OER cycle. Based on this, we propose that not only RuO_2 gives the contribution to the O_{lat} species intensity. In order to clarify this below we compare the evolution of the Ru3d and O1s spectra with the electrode potential.

In order to attribute the high oxidation state ruthenium species to oxide or hydroxide form, one should analyze the potential evolution of Ru3d and O1s XP spectra. While the data were collected at different periods (during the 2nd OER cycle for Ru3d and the 3rd OER cycle for O1s), one can still compare the results qualitatively. The analysis of Panel A of Figure 58 shows that the contributions of $Ru(OH)_x$ and RuO_2 species are decreasing with the electrode potential while those of Ru (VI) and Ru (VIII) components start increasing at E ≥ 1.34 V. If we go back to the Panel B of Figure 60, we will see that the lattice oxygen peak also demonstrates an increase in the potential interval from 1 to 1.41 V. Since the contribution of RuO_2 species is expected to decrease rather than to increase at E > 1 V, we assume that Ru (VI) and Ru (VIII) species are likely to be present in an oxide form rather than in a hydroxide one, which would account for the increase of the O_{lat} component with the electrode potential. The atomic ratio (RuO_2 + Ru (VI) + Ru (VIII)) /$Ru(OH)_x$

estimated from Ru3d spectra was also included in the Table 16. Although quantitatively different from that of the O_{lat}/OH ratio, it shows the same qualitative trend: after the 1st OER cycle it exhibits only a small increase.

We thus conclude that the evolution of the O1s spectra either with the potential or as a result of consecutive OER cycles is overall in agreement with the changes of the Ru3d spectra, even if the former is less sensitive to the changes in the anode composition.

Table 16. Atomic ratio estimated on the basis of Ru3d, C1s and O1s fitted spectra for Ru@RuO_x at different stages of the electrode analysis.

Atomic Ratio	**Ru@RuO_x**			
	Initial state	After the 1st OER (O K edge)	After the 2nd OER (Ru3d)	After the 3rd OER (O1s)
C1s / Ru3d	12.90 ± 7.0	3.07 ± 0.5	2.64 ± 0.5	1.71 ± 0.5
Ru3d (RuO_2) / Ru3d ($Ru(OH)_x$)	3.46 ± 1.5	0.29 ± 0.05	0.23 ± 0.05	0.12 ± 0.05
O1s (O_{lat}) / O1s (OH)	0.48 ± 0.1	0.23 ± 0.07	0.24 ± 0.07	0.31 ± 0.07
Ru3d components : (RuO_2 + Ru (VI) + Ru (VIII)) / $Ru(OH)_x$	3.89 ± 1.5	0.44 ± 0.05	0.55 ± 0.05	0.59 ± 0.05

3.5. *In-situ* NEXAFS Measurements

The analysis of the O K edge spectra can provide additional information on the composition of the electrode during the OER. O K-edge spectra provide information on the amount of O-2p holes induced by covalence in the transition metal – oxygen bond[231]. The absorption results obtained on Ir-based anodes which will be discussed in Chapter 5, allowed us to follow the evolution of oxygen red-ox transitions and to discuss the OER mechanism based on these results. These findings motivated us to perform similar measurements of Ru-based anodes, particularly the Ru@RuO_x electrode. The attempts to perform *in-situ* NEXAFS measurements on thermal ruthenium oxide were not successful due to some technical issues, however we were able to collect the reference spectrum of RuO_2 measured at the same water ambient conditions.

It should be noted, that the main contribution to the O K edge intensity is originating from the gas-phase present in the measurement chamber – the water/oxygen mixture. However, by measuring the reference gas phase NEXAFS spectra we confirmed that low energy features, which we were interested in, are not overlapping with the gas-phase peaks. Here we discuss only the total electron yield (TEY) mode, due to its higher signal-to-noise ratio in comparison to the Auger electron yield, while the latter is more surface sensitive as it was discussed in Chapter 1.

The evolution of O K edge spectra (TEY mode) with polarization recorded on Ru@RuO_x anode is shown in Figure 61. All spectra were normalized to their integrated intensity. The dashed and the dotted lines represent the state after the 1st and the 3rd OER cycles, respectively.

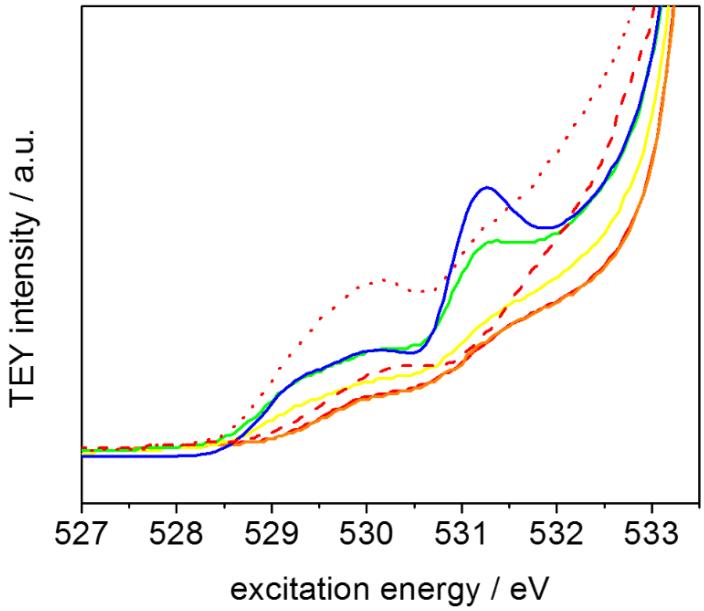

Figure 61. Low excitation energy region of O K edges (TEY) measured on Ru@RuO$_x$ anode under 3 mbar of water vapor and different polarization: 0.75 V (red); 1.0 V (orange); 1.34 V (yellow); 1.41 V (green); 1.43 V (blue). Two additional spectra were recorded after the 1st (dashed line) and the 3rd OER cycles (dotted line) at 0.75 V. The potential values are Ohmic drop corrected.

One may clearly observe the presence of at least three components with the peak positions at 529.2 eV, 530 eV and 531.3 eV. The latter also involves the gas-phase oxygen contribution evolved during the OER as confirmed by *Pfeifer et al.*[108] One may observe the increasing of this peak intensity at 1.41 V and 1.43 V corresponding to the oxygen evolution confirmed by the online mass-spectrometry data. The energy of 531.3 eV also correlated with the OH component of the O1s XP spectra, thus the peak may include both species – OH groups and gas-phase oxygen evolved on the electrode. The literature data related to the O K edge spectra of Ru-based compounds are very scarce. *Hu et al.*[232] performed XAS analysis of the polycrystalline bulk RuO_2 sample and observed a peak at 529 eV, which they attributed to the lattice oxygen.

For our further discussions, we performed the fitting of the corresponding O K edge spectra recorded on Ru@RuO$_x$ anode under different polarization conditions and at 0.75 V before and after the 1st and the 3rd OER cycles. After the normalization to the incident photon flux and to the gas-phase peak intensity the corresponding background was subtracted from each O K edge spectra in the interval [526; 533] eV (the example of same BG subtraction is shown in Figure A 8 for Ir-based sample). As it was previously mentioned, only the spectra recorded in the TEY mode were chosen due to their better signal-to-noise ratios, which is critical for the analysis of small intensities of the pre-edge region.

Three peaks located at 529.2 eV, 530 eV and 531.3 eV were fitted with Gaussian/Lorentzian GL(30) function of the constant width (FWHM = 1 eV) for the first two components. The shape of the peaks was considered based on the results obtained for Ir-based samples (discussed in detail in Chapter 5) Small variations of the width of the high-energy peak located at 531.3 eV were attributed to the background subtraction. Taking into account the low intensity of the pre-edge we also estimated the error of 25 % of the value by performing the O K edge fitting by changing the fitting parameters several times. The fitted absorption spectra are shown in Figure 62. One may clearly see that all three components are present on the electrode surface, their intensities depending on the applied potential and/or the number of the OER cycles. Considering that all of these species are present already at the initial potential of 0.75 V, none of them can be directly attributed to an OER intermediate.

NEXAFS measurements under 3 mbar water vapor were also performed on the RuO_2-based MEA. Due to some technical problems, the analysis under potential control was not possible for this sample. However, we can still use the spectrum collected at the open circuit voltage as a reference. The O K edge spectrum of RuO_2 was fitted according to the procedure mentioned above (see Figure 63). Unlike for the electrochemical ruthenium oxide, only two peaks – at 530.0 eV and 531.3 eV - were observed in case of thermal ruthenium oxide sample. We consider the former peak as oxygen coming from the lattice oxide, while the latter is originated from the OH groups. As it was mentioned before, the electrochemical tests on RuO_2-based MEA were not performed and the anhydrous-hydrous Ru (IV) oxide transition does not occur in the absence of polarization. The analysis of the photoemission spectra (C1sRu3d) also recorded on RuO_2 sample revealed high surface content of carbon-based species (atomic ratio C/Ru = 77). Thus, one cannot exclude contribution of the oxygen-containing carbon species to the peak at 531.3 eV.

Figure 64 shows the potential dependence of the O K edge components for the $Ru@RuO_x$ anode. The peak located at 531.3 eV, which contains the contributions of the OH species on the electrode surface as well as the of the gas-phase oxygen (which is present in the chamber in the potential interval of the OER). One may notice a slight decrease of this peak as the electrode potential is increased from 1.0 up to 1.34 V, which correlates with the diminishing of the $Ru(OH)_x$ contribution observed earlier during the analysis of Ru3d spectra (Figure 58). Under the potentials of the OER, the intensity of the peak at 531.3 eV is increasing due to the contribution of the evolved oxygen. Based on the analysis of O1s XP spectra and the O K edge spectra recorded on the reference sample we propose that lattice oxygen contributes to the peak at 530 eV. The slight shift of the resonance position of O_{lat} species in comparison to the literature data can be explained by the differences in the oxide structure/composition, its thin layer (in case of the $Ru@RuO_x$ anode) and also by the presence of other species on the surface.[147] In addition, possible surface

reconstructions under water ambient may also have an impact on the energy shifts and intensities changes of the O K edges[233]. The decrease of this peak with potential can be compared to similar behavior of RuO_2 species (see Figure 58A) under polarization, confirming its attribution to the lattice oxygen species.

The third peak observed at low excitation energy of 529.2 eV strongly depends on the applied potential. Analysis of Figures 61 and 63 suggests that the 529.2 eV/530.0 eV peak ratio increases in the OER interval (*cf.* Panels C, D with Panels A, B of Figure 62), and drops with the potential reversal (Panel E of Figure 62). Comparing O K edge spectra under polarization with the potential evolution of Ru species with potential (Panel A of Figure 58), one may notice that only the contributions of Ru (VI) and Ru (VIII) species are increasing in this potential region. Based on this analysis, we propose that the low energy peak at 529.2 eV in the O K-edge spectrum is related to the presence of high oxidation state Ru oxides on the electrode surface. The shift of this peak to lower energies compared to the lattice oxygen in RuO_2 (530.0 eV, see Figure 63) may be explained to an enhancement of covalence of the Ru-O bond accompanying an increase in the oxidation state of Ru. This assumption is in agreement with the literature data comparing O K-edge spectra for Ru(IV) and Ru(V) compounds[232] and for transition metal (Cu, Ni, Co) oxides.[231] While for the O K edge spectra we distinguish two lattice oxygen peaks corresponding to Ru in different oxidation states, the analysis of O1s XP spectra discussed in the previous section was done only with one component at 530 eV. The low binding energy region of the oxygen core-level peak does not exhibit two well-distinguished peaks, however the presence of an additional component at 529.2 eV cannot be excluded.

The recording of the Ru3d, O1s and O K edge spectra under different polarization was not performed at the same time perplexing their direct quantitative comparison due to the constant evolution of the electrode surface. However, we can analyze the spectra collected between the OER cycling as we did for the O1s data discussed before. Table 17 displays the ratio between two low excitation energy peaks in the O K-edge spectra of $Ru@RuO_x$ electrode located at 529.2 eV and 530 eV before and after consecutive OER cycles. Following the attribution of these peaks to high Ru oxidation state oxides and ruthenium (IV) oxide, respectively, the ratio between these two peaks is also included in the Table. The intensity of the peaks observed in the O K edge spectra is not directly related to the amount of certain species, but depends on the concentration of the induced holes. Consequently, the data obtained by photoemission and absorption spectroscopy cannot be compared quantitatively, but only qualitatively.

From the data presented in Table 17 one may notice the increasing of the O K edge peak (529.2 eV / 530 eV) ratios with the number of OER cycles. A similar trend is observed for Ru

species, where the amount of high oxidation state (Ru (VI) and Ru (VIII)) oxides is growing and the quantity of RuO_2 is decreasing.

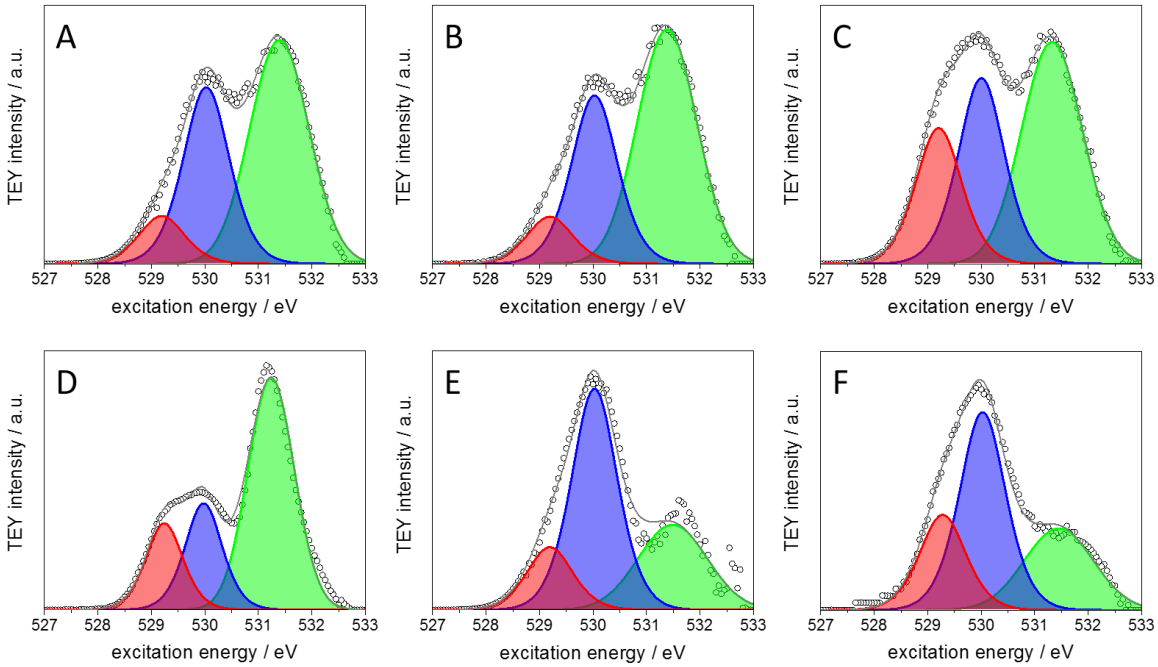

Figure 62. Low excitation energy region of O K edges (TEY) measured on Ru@RuO_x anode under 3 mbar of water vapor and different polarization: 0.75 V (A); 1.0 V (B); 1.34 V (C); 1.43 V (D); back 0.75 V after the 1st OER cycle (E) and after the 3rd OER cycle (F). The fitting was done within three peaks: at 529.2 eV (red); 530 eV (blue) and 531.3 eV (green).

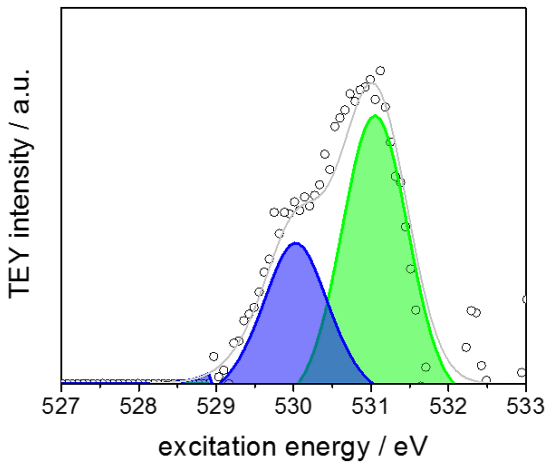

Figure 63. Low excitation energy region of O K edges (TEY) measured on RuO_2 anode under 3 mbar of water vapor and open circuit potential.

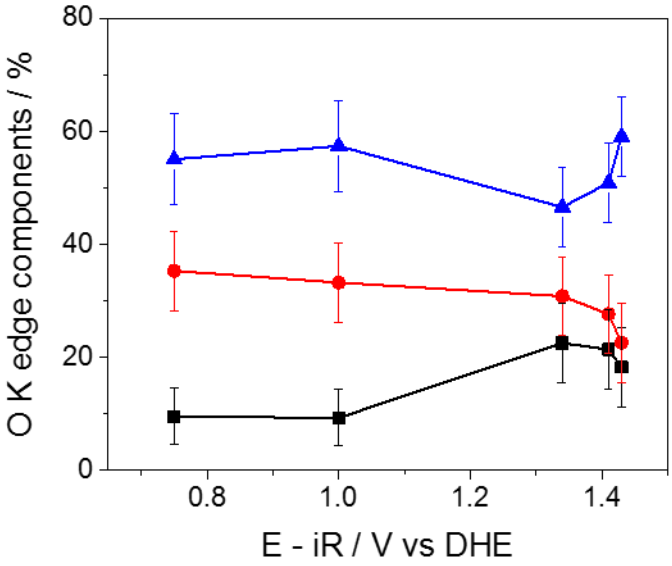

Figure 64. Potential-induced evolution of O K edge components located at 529.2 eV (black), 530 eV (red), 531.3 eV (blue). The O K edge spectra were collected at Ru@RuO_x anode under 3 mbar water vapor under different polarization during the 1st OER cycle.

Table 17. Atomic ratio estimated on the basis of Ru3d and O K edge fitted spectra for different states of the Ru@RuO_x electrode.

Ratio	Initial State	After the 1st OER cycle (O K edge)	After the 3rd OER cycle (O1s)
O K edge components:			
529.2 eV / 530 eV	0.27 ± 0.03	0.28 ± 0.03	0.48 ± 0.05
Ru3d components :			
Ru (VI) + Ru (VIII) / RuO_2	0.12 ± 0.05	1.77 ± 0.05	3.72 ± 0.05

3.6. OER and Degradation Mechanisms of Ru-based Anodes

The synthesized metallic Ru and prepared from it thermal oxide RuO_2 powders have been characterized by means of XRD revealing the presence of small particles of hexagonal Ru and rutile-type oxide, respectively. The microscopic analysis of these powders revealed the mean particle size of ca. 2.6 nm in case of initial metallic powder, while their thermal treatment led to their growth up to 7 nm in case of round shaped particles and up to 10 – 90 nm in case of rod-shaped with a diameter of 14 nm. The post-mortem STEM analysis performed on the electrocatalysts after their *in-situ* spectroscopic studies did not reveal any noticeable changes either in the particles size or in their shape.

Now we turn to the discussion of the electrochemical behavior of the anodes in liquid electrolyte and under water vapor conditions. Literature data have revealed an inverted relationship between the electrochemical activity and stability of Ru-based anodes, where metallic particles covered by a thin oxide layer formed electrochemically possess higher activity in comparison to the rutile-type oxides obtained thermally, while the former are prone to much faster corrosion[31–33].

The decay of the activity of Ru-based electrodes with time either under potentiostatic or potentiodynamic conditions has been confirmed for both liquid (see the RDE measurements shown in Figure 48) and gas-phase conditions (see the recorded chronoamperograms shown in Figure 51 and Figure 52). In order to estimate the corrosion rate, we have compared the currents obtained at 1.5V vs RHE (vs DHE in the MEA configuration) during the first and the second OER cycle on rutile oxide.

Discussion of the Tafel slopes for Ru-based anodes are ambiguous due to their fast degradation and due to the superposition of the currents related to the OER and to the Ru oxidation/reduction. Nevertheless for comparing the data with the literature, we roughly estimated the Tafel slopes for the OER on $Ru@RuO_x$ and RuO_2 in liquid electrolyte as 40 and 60 mV dec^{-1}. The value obtained for $Ru@RuO_x$ is in agreement with the literature data,[46] while that for RuO_2 is ca. 30-40 mV dec^{-1} higher than the one observed in the literature for this type of the anodes.[36,234] This difference may be be related to the oxide structure[27] and the experimental procedure, e.g. the electrolyte pH, ionomer content, the electrode preparation (MEA or thin layer deposited on glassy carbon) and its pretreatmnet[235]. In the literature, the slope of 40 mV dec^{-1} is usually attributed to the electrochemical rate-determination step described by the following reaction:

$$S\text{-}HO^* \rightarrow S\text{-}O^* + H^+ + e, \text{ (Eq. 24)}$$

while for 60-70 mV dec^{-1}, the chemical step of oxygen surface recombination is typically considered as the rate determining for the OER[236,237]. The differences in Tafel slopes observed here and in the literature as well as their evolution with the electrode state under potential cycling emphasize the complexity of the processes taking place at the electrode surfaces and the necessity of additional analytical techniques for the analysis of the OER mechanism.

Except for the Tafel analysis, cyclic voltammetry can also provide additional information regarding the red-ox transitions taking place at the electrode/electrolyte interface. The shapes of the CVs as well as the position of the corresponding anodic and cathodic peaks observed for RuO_2 and Ru@RuO_x anodes in liquid electrolyte (not shown) and gas-phase ambient (Figure 50) are quite similar. However, the consistent attribution of these peaks is currently absent in the literature, while the analysis of the *in-situ* spectroscopic data presented in this work may contribute to the understanding.

The analysis of the *in-situ* spectroscopic data obtained on RuO_2 and Ru@RuO_x anodes revealed both similarities and differences of their behavior under the OER conditions. Due to the differences in the measurement protocols a direct quantitative comparison is not reliable, however qualitatively the results complement each other.

Now we move to the discussion of the spectroscopic data. The analysis of Ru3d XP spectra confirmed the presence of all four Ru species on both anodes abbreviated as anhydrous RuO_2, hydrated $Ru(OH)_x$, Ru (VI) and Ru (VIII). For Ru@RuO_x anode, we also observed presence of the metallic component at the initial stage before the application of high anodic potentials (Panel A of Figure 56), however after potential excursions into the OER interval the metallic component vanished.

One of the most noticeable effects of the polarization is related to the transformation of anhydrous rutile-type oxide RuO_2 into its hydrated state – $Ru(OH)_x$. This transition is initiated by the applied potential and as it was shown for RuO_2 anode, starts in the OER region. The contribution of $Ru(OH)_x$ does not decrease but continuously increases upon potential cycling which can be clearly noticed from the data obtained on RuO_2 electrode (Figure 54 and Figure 55) suggesting the irreversibility of the anhydrous-to-hydrous oxide transition. The growth of hydrated form of Ru (IV) oxide under applied potential is less noticeable in case of the Ru@RuO_x anode (Figure 58) in comparison to RuO_2 anode. This can be attributed to the different nature of the studied oxides. While the thermal oxide is initially present in the form of the rutile RuO_2 phase, the electrochemical oxide consists of a hydrous Ru oxide even before cycling in the OER potential interval (Figure 56, Figure 59). Nevertheless in case of electrochemically formed oxide Ru@RuO_x, one may see a drastic increase of the $Ru(OH)_x$ contribution already after the 1st OER cycle. The amount of RuO_2 component is constantly decreasing under potential cycling, while the quantity of

hydrated $Ru(OH)_x$ maintains constant. All these data support the idea of the irreversibility of the $RuO_2/Ru(OH)_x$ transition confirmed for both electrochemical and thermal oxides. The hydroxylation of Ru-based electrode surface under the reaction conditions has been proposed previously,[54] however solid experimental evidences has not been provided yet.

In order to confirm the formation of hydrous Ru (IV) oxide, $Ru(OH)_x$, we performed the comparative analysis of O1s, Ru3d and O K edge spectra recorded at 0.75 V after consecutive OER cycles for the $Ru@RuO_x$ anode. The fitting of O1s spectra was done using three peaks attributed to lattice oxygen, OH-groups and adsorbed water. The O K edge spectra were also fitted with three peaks, where two low energy peaks were assigned to lattice oxygen originating from Ru in different oxidation states and the high-energy peak to OH and gas-phase oxygen. The comparison of the atomic ratio estimated from the fitted photoemission and absorption spectra at different stages of the experiments presented in Table 16 and Table 17 supports the idea that the component abbreviated as $Ru(OH)_x$ may be considered as hydrous oxide.

Increasing of the applied potential leads also to the oxidation of Ru sites, forming Ru (VI) and Ru (VIII). We will start the discussion from the latter. The formation of Ru (VIII) species on rutile-type RuO_2 anode below the corresponding thermodynamic potential[228] (see Figure 54) can be rationalized by the formation of either a thin surface layer or islands of $RuO_{4(s)}$ (rather than a RuO_4 phase), strongly interacting with the underlying RuO_2 substrate (under potential oxidation). The analysis of the Ru3d spectra recorded on $Ru@RuO_x$ demonstrates the constant presence of Ru (VIII) species on the electrode surface, however its amount does not exceed 10-15 % (Figure 58). Since for $Ru@RuO_x$ the potential dependence of the Ru3d spectra was studied in the second OER cycle, Figure 58 must be compared with Figure 55B (2^{nd} OER cycle for RuO_2). Similar surface composition and behavior of the two anodes suggests that during the OER the more stable RuO_2 oxide with rutile structure transforms into a less stable hydrous Ru (IV) oxide (most likely amorphous, even if XPS cannot provide direct information regarding the crystalline structure).

The electrochemical formation of $RuO_{4(s)}$ on Ru-based anodes has been postulated in previous publications, however it has never been detected on the anode surface either during or after the electrolysis, likely due to its instability at room temperature. *Kötz et al.* detected formation of dissolved corrosion products in the vicinity of the RuO_2 anode simultaneously with the OER and hypothesized on the RuO_4 generation and the OER occurring through common intermediates (Ru (VI) and Ru (VII) in the Kötz' scheme shown in Figure 11).[98]

As the electrode potential is shifted positive to the OER region, the contribution of $RuO_{4(s)}$ surface species slightly declines in case of RuO_2 anode. The slight increasing of the Ru (VIII) surface contribution with increasing of the applied potential observed on $Ru@RuO_x$ anode is within the experimental and fitting error (of 5 – 10 %).

The decreasing of $RuO_{4(s)}$ under the oxygen evolution reaction conditions observed for the RuO_2 anode was initially attributed to its direct participation in the OER as an active intermediate. We also observed an increasing of RuO_2 and RuO_3 components at more positive bias which can be explained by decomposition of higher Ru (VIII) to lower Ru (IV) and Ru (VI) species (Eq. 23)[95]. The idea of the decomposition of higher to lower oxidation state oxides coupled with the oxygen release can be supported by the previous results obtained by means of isotope labeling measurements discussed in[23,92]. The role of Ru (VIII) species as OER intermediates based on the results obtained on RuO_2 anode was proposed in our manuscript *Saveleva et al.*[181] However, the analysis of Ru3d XP spectra collected later on $Ru@RuO_x$ anode (Figure 58 and Figure 59) revealed the constant presence of Ru (VIII) species on the electrode surface. Thus, our attribution of $RuO_{4(s)}$ to the OER intermediate cannot be supported by these results. It is interesting to note that the amount of Ru (VIII) species formed on the electrode surface does not depend on the oxide nature, moreover it is even larger for more stable thermally prepared RuO_2 anode. Thus, the amount of $RuO_{4(s)}$ cannot be directly related to the propensity of the Ru electrode to degradation as it was proposed previously in the literature[84].

The role of Ru (VI) in the OER mechanism as well as the composition of these species were widely discussed in the literature[14] however to the best of our knowledge no unambiguous experimental evidences were obtained. On the RuO_2 anode, Ru (VI) species form simultaneously with RuO_4 prior to the OER and these red-ox transitions can be related to the peak at ca 1.1 V observed in the CV (Figure 50). The analysis of the surface evolution of the $Ru@RuO_x$ anode under the potential cycling reveals the accumulation of Ru (VI) species on the surface, also excluding their attribution to the oxygen evolution reaction intermediate.

While the existence of high oxidation state ruthenium oxides (VI, VII, VIII) has been discussed in the literature, their exact composition and structure were not yet defined[204,205]. Ru (VI) species are generally considered as a deficient oxide RuO_3, while the composition of Ru (VIII) is displayed as RuO_4. By comparing the potential-induced XPS and XAS results (Table 16 and Table 17), we propose that both Ru (VI) and Ru (VIII) are most likely in the form of oxides rather than hydroxides. The low energy peak observed in the O K edge spectra regardless the potential value at 529.2 eV was attributed to these high oxidation state oxides. The assignment of the O K edge components was done based on the experimental spectroscopic data, however, to further confirm the assignment, DFT calculations are highly desirable.

To sum up, the most noticeable changes observed on Ru-based anodes with polarization are related to $Ru(OH)_x$ component and its irreversible growth with potential cycling. Formation of $Ru(OH)_x$ can be further correlated with the diminishing of the currents observed from the

corresponding chronoamperograms. We assume that transformation of rutile RuO_2 into hydrous Ru (IV) oxide to be largely responsible for the electrode degradation.

On the basis of the obtained results, we propose the following OER and degradation mechanisms for ruthenium containing anodes based on the Ru cation red-ox chemistry. RuO_2 anode with the rutile structure seems to be rather stable below ca. 1.0 V vs. DHE, which is the potential where a re-ox wave is observed in CVs. At $E \geq 1.0$ V vs. DHE, we observe formation of Ru in high oxidation states, which based on the available literature references were attributed to Ru (VI) and Ru (VIII). Further increase of the electrode potential results in the O_2 formation, which is accompanied by a decrease of the contribution of Ru (VI) and Ru (VIII) and an emergence of a peak of hydrous Ru (IV) oxide. From this, we conclude that the OER catalytic cycle is based on the Ru-cation red-ox chemistry whereby Ru (IV) is oxidized to an active Ru intermediate in a high oxidation state, probably, Ru (VII) as earlier postulated by *Koetz et al*. This short-lived intermediate cannot be detected, since it is rapidly transformed into long-lived Ru species, releasing O_2. Ru (VI) and Ru (VIII) are formed either within the catalytic cycle (in this case the O_2 formation must occur in an electrochemical step in order to explain the presence of Ru (VI) and Ru (VIII) on the surface outside the OER potential interval) or as corrosion byproducts. However, neither of these seems to be an active OER intermediate since both of them are present on the surface outside the OER potential interval. It is essential that after closing the catalytic cycle Ru (IV) does not return to the anhydrous Ru (IV) oxide but rather forms a hydrous Ru (IV) oxide, which is much less stable to corrosion than the pristine anhydrous Ru (IV). Based on the observed correlation between the $Ru(OH)_x$ formation and decrease of the electrochemical activity, we propose these species to be responsible for the degradation of Ru-based anodes.

3.7. Conclusions of Chapter 3

In-situ near ambient pressure spectroscopic analysis performed in this work on Ru-based anodes allowed us to follow significant potential-dependent changes in the valence state as well as the degree of hydration of Ru and correlate these with activity/stability properties of these oxides, which cannot be detected using *ex-situ* methods.

First, in this work we show that the behavior of the studied catalysts under the operation conditions and the OER mechanism do not depend on the oxide nature. We also discovered a new degradation mechanism of Ru-based anodes. By combining XPS and NEXAFS measurements *operando*, we demonstrate that under operation an anhydrous form of Ru (IV) oxide gradually and irreversibly transforms into a hydrous Ru (IV) hydroxide form. The differences in the stability properties of the Ru@RuO_x and RuO_2 catalysts, confirmed by the corresponding measurements both in 0.05 M H_2SO_4 and under water vapor ambient, were also attributed to the formation of these hydroxide surface species rather than to the formation of RuO_4 proposed earlier in the literature. The constant presence of high oxidation state ruthenium oxides on the electrode surface does not support the idea of their role as the reaction intermediates, however their accumulation under the potential cycling is considered as the result of the decomposition of other short living active species. By analyzing the oxygen NEXAFS spectra, we also confirm that the OER mechanism is based on the red-ox chemistry of ruthenium.

The results presented herein contribute to the overall understanding of the processes taking place at Ru-based electrode/electrolyte interface of the PEM electrolyzers and give a clue to the development of more stable anodes for this technology. Particularly, the stabilization mechanism of rutile RuO_2 oxide by the presence of Ir admixtures will be discussed in the next Chapter.

Chapter 4. Stabilization Mechanism in Bimetallic Iridium-Ruthenium Anodes

4.1. Introduction

Recent years have witnessed an increased interest in Ir, Ru-based oxide anodes as oxygen evolution catalysts due to their improved stability in comparison to pure RuO_2 coupled with high catalytic performance[49,77]. However, an optimal catalyst composition should be also defined with respect to its costs. Four times higher price of iridium catalysts in comparison to ruthenium requires its economical utilization. The role of iridium admixtures in the enhanced properties of the mixed Ir, Ru-based oxide catalyst is not fully understood yet, the results reported in the literature being quite contradictory[36,84,99]. The lack of the proper understanding of the stabilization mechanism hinders further development of active and stable anode catalysts for PEM electrolyzers.

The objective of the studies discussed in this Chapter is to unveil the stabilization mechanism of iridium in mixed Ir, Ru-based oxide under water electrolysis conditions. In order to do this we performed NAP-XPS measurements on rutile-type single RuO_2 and mixed $Ir_{0.70}Ru_{0.3}O_2$ anodes *operando* under water electrolysis conditions. The measurements for the two types of catalysts were done during the same beam time at BESSY II synchrotron. Before the spectroscopic measurements, the surface of the anodes was stabilized by potential cycling in the potential interval from 0 to 1.6 V (including the OER region). The acquisition of the XP spectra was initiated several minutes after the application of the potential, and the core-levels of all elements presented on the electrode surfaces were recorded successively.

In this Chapter, we discuss the following results obtained by means of *in-situ* NAP-XPS:

- surface state of iridium and ruthenium under different polarization conditions;
- depth propagation of the catalytic active layer of the catalysts by tuning the energy of the photoelectrons;
- time and reversibility effects on the anode surface composition.

Even though the results obtained on the RuO_2 anode have already been shown and discussed in detail in Chapter 3, some of them will be repeated here to facilitate the comparison of single and bimetallic Ru-based anodes.

The analysis of the photoemission spectra recorded on single and bimetallic anodes under different experimental conditions allowed us to unveil the stabilization effect of the iridium admixtures in bimetallic Ir,Ru-based anode and discuss the role of Ir and Ru sites in the oxygen evolution reaction. Tuning of the photon energy gave us the opportunity to analyze the sub-surface composition of the Ru(Ir)-based catalysts and define the interface-localized processes. The results obtained on mixed $Ir_{0.70}Ru_{0.3}O_2$ confirm the degradation mechanism proposed for Ru-based anodes in Chapter 3.

This chapter is based on the published article: Saveleva, V. A.; Wang, L.; Luo, W.; Zafeiratos, S.; Ulhaq-bouillet, C.; Gago, A. S.; Friedrich, K. A.; Savinova, E. R. Uncovering the Stabilization Mechanism in Bimetallic Ruthenium − Iridium Anodes for Proton Exchange Membrane Electrolyzers. *Phys. Chem. Lett.* **2016**, *7*, 3240–3245[181].

4.2. Material Characterization

Here we present the *ex-situ* XRD and microscopy characterization of the single RuO_2 and mixed $Ir_{0.70}Ru_{0.3}O_2$ catalyst powders. The comparison of the electrochemical tests performed on the anodes based on these catalysts in liquid electrolyte and under water vapor conditions is also provided here. In order to facilitate the discussion, part of the figures devoted to the RuO_2 characterization are duplicated from Chapter 3.

4.2.1. XRD Analysis

A mixed Ir,Ru-based oxide catalyst has been synthesized in a similar way as single Ru oxide by direct reduction of the corresponding salts first forming metallic nanoparticles followed by their thermal oxidation under the air (see the procedure in Chapter 2). The nominal stoichiometric ratio of Ir:Ru for the bimetallic sample was equal to 7:3.

Figure 65 shows the diffractograms obtained on monometallic Ru and bimetallic Ir,Ru-based oxides. RuO_2 pattern has already been discussed in the previous chapter and consists of a rutile-phase oxide with small traces of metallic ruthenium (reflection at $2\Theta = 44$). The latter most probably originates from the metallic core due to the incomplete oxidation of metallic ruthenium nanoparticles. In case of $Ir_{0.70}Ru_{0.3}O_2$ powder diffractogram shown on the top of Figure 65, no traces of either metallic iridium or metallic ruthenium were detected. The reference powder diffraction patterns of rutile RuO_2 and IrO_2 from ICDD, which were used for the analysis, are shown in Table A 1 and Table A 5 of Appendix, respectively. The reflections observed on these oxides are very close due to their similar lattice parameters. For tetragonal RuO_2 (space group P42/mnm): a = 4.520 Å and c = 3.116 Å, while for IrO_2: a = 4.505 Å and c = 3.159 Å. One may notice the difference in the peaks width what can be related to the differences in the crystals size (see the next Section). The changes in the peak intensities observed for some of the reflections for RuO_2 and $Ir_{0.70}Ru_{0.3}O_2$ may be attributed to the overlapping of the corresponding peaks (for the XRD patterns, see the Tables in Appendix). Thus, based only on the XRD results, one cannot distinguish between formation of a mixed Ir,Ru oxide or separated Ir and Ru oxide phases. In order to distinguish the formation of a mixed Ir,Ru oxide from a mixture of Ir and Ru oxide phases, we performed the transmission electron microscopy coupled with energy-dispersive spectroscopy analysis discussed below.

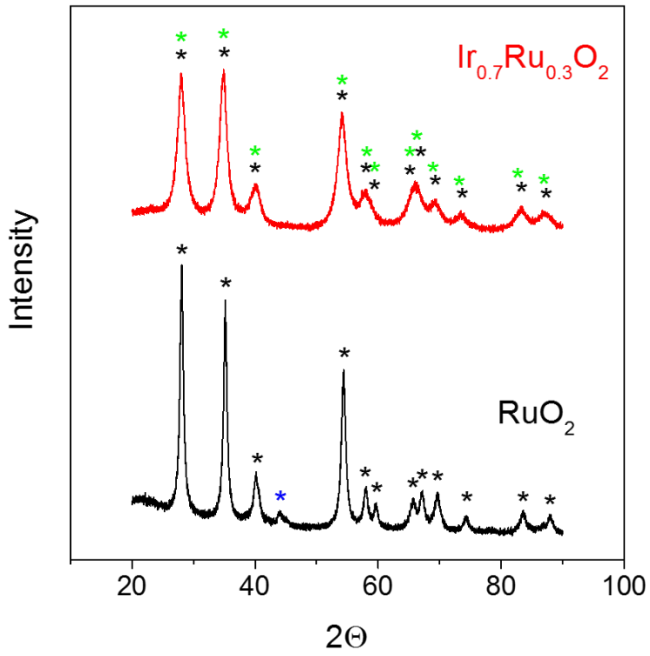

Figure 65. XRD patterns of RuO_2 (bottom) and $Ir_{0.7}Ru_{0.3}O_2$ (top) powders. The asterisks correspond to the following reference ICDD patterns: RuO_2 oxide PDF- 03-065-2824 (black); metallic Ru PDF - 01-089-3942 (blue); IrO_2 oxide – PDF 01-088-0288 (green). XRD pattern of RuO_2 has already been shown in Figure 46.

4.2.2. TEM / EDX Analysis

Both transmission and scanning transmission electron microscopy coupled with the EDX analysis were used to characterize the catalyst powders before the MEA fabrication as well as post-mortem by scraping the catalyst particles from the WE surface of the MEAs after the *in-situ* NAP-XPS measurements.

Typical TEM and STEM images obtained on RuO_2 and $Ir_{0.70}Ru_{0.3}O_2$ catalyst powders are shown in Figure 66 and Figure 67, correspondingly. Smaller size of $Ir_{0.70}Ru_{0.3}O_2$ particles ranging from 3 to 9 nm in comparison to elongated RuO_2 particles of the length from 10 to 90 nm witnesses the limited growth of the oxides crystals in the presence of iridium.

The EDX analysis revealed a homogeneous sub-nm scale distribution of Ir and Ru along the sample, suggesting formation of a single $Ir_{0.7}Ru_{0.3}O_2$ phase rather than a mixture of two separated RuO_2 and IrO_2 phases in the bimetallic sample (the example of the post-mortem EDX analysis is shown in Figure 68). No significant difference either in the particle size or in the elemental distribution was observed after the samples had been subjected to NAP-XPS measurements under electrochemical control in the potential interval of the OER (Panels B,D in Figure 67, Figure 68).

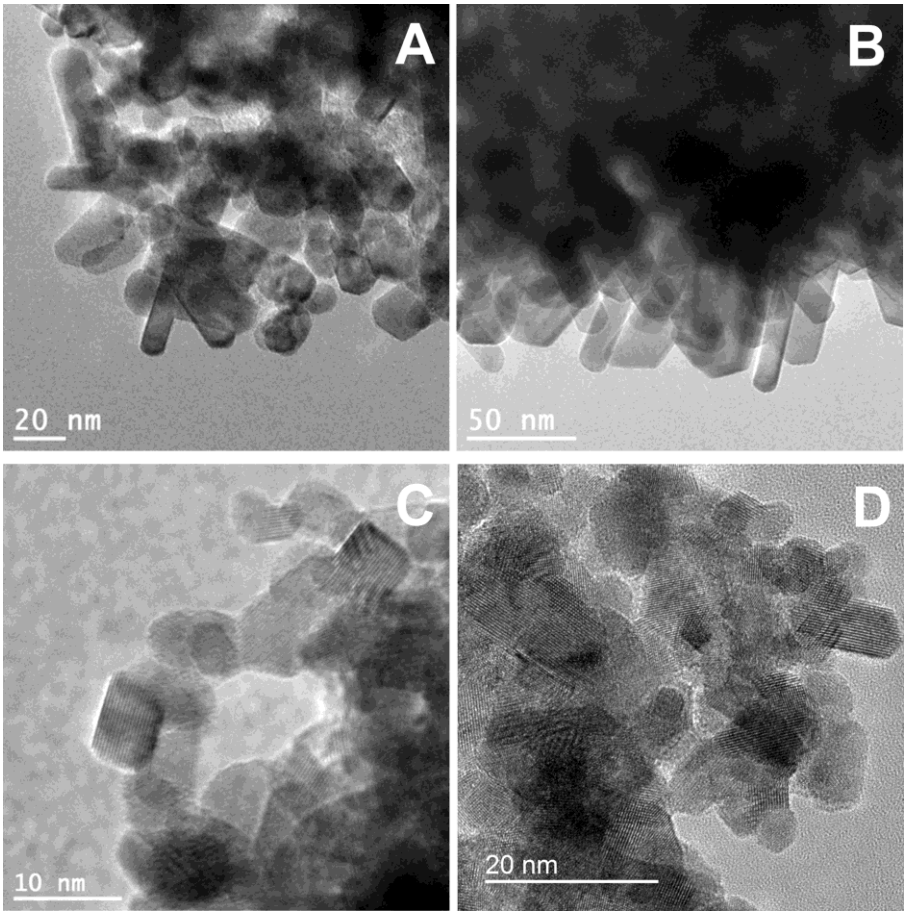

Figure 66.TEM images of pristine RuO_2 (A,B) and $Ir_{0.7}Ru_{0.3}O_2$ (C,D) samples under different magnifications. Panels A, B reproduce Figure A 2.

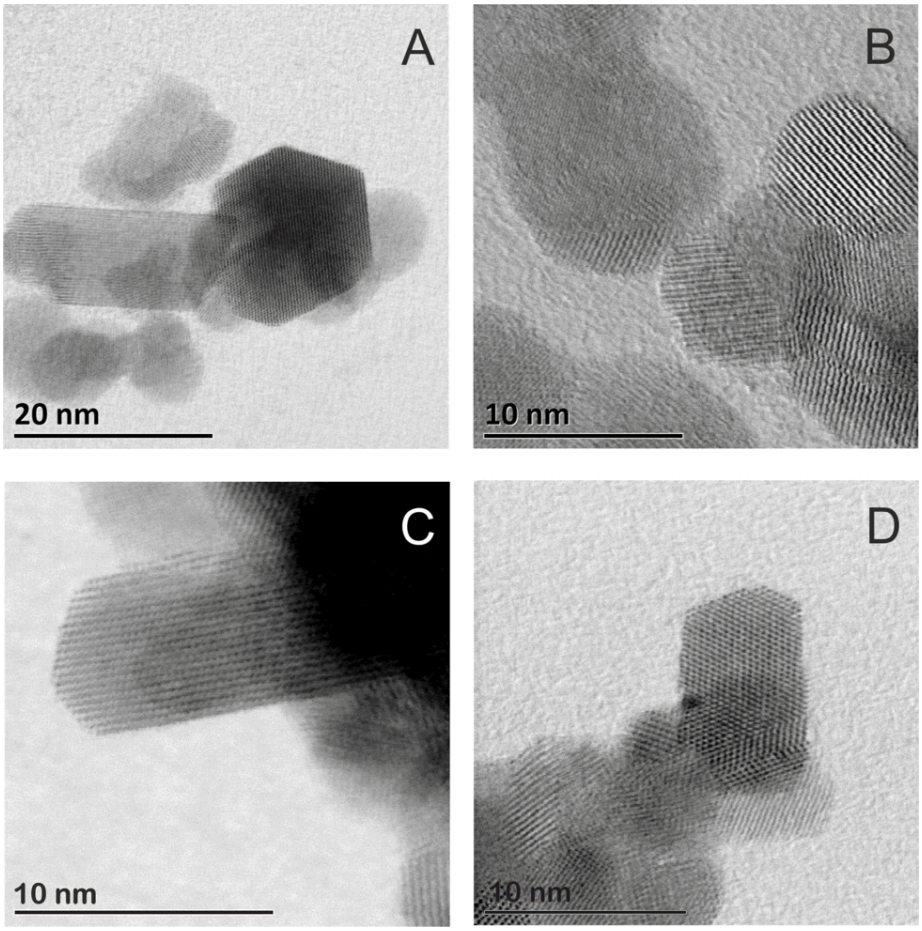

Figure 67. STEM images of RuO_2 (A,B) and $Ir_{0.7}Ru_{0.3}O_2$ (C,D) electrodes before (A,C) and after (B,D) the OER studies performed in the NAP-XPS chamber. Note that panels A and B were already shown in Figure 47.

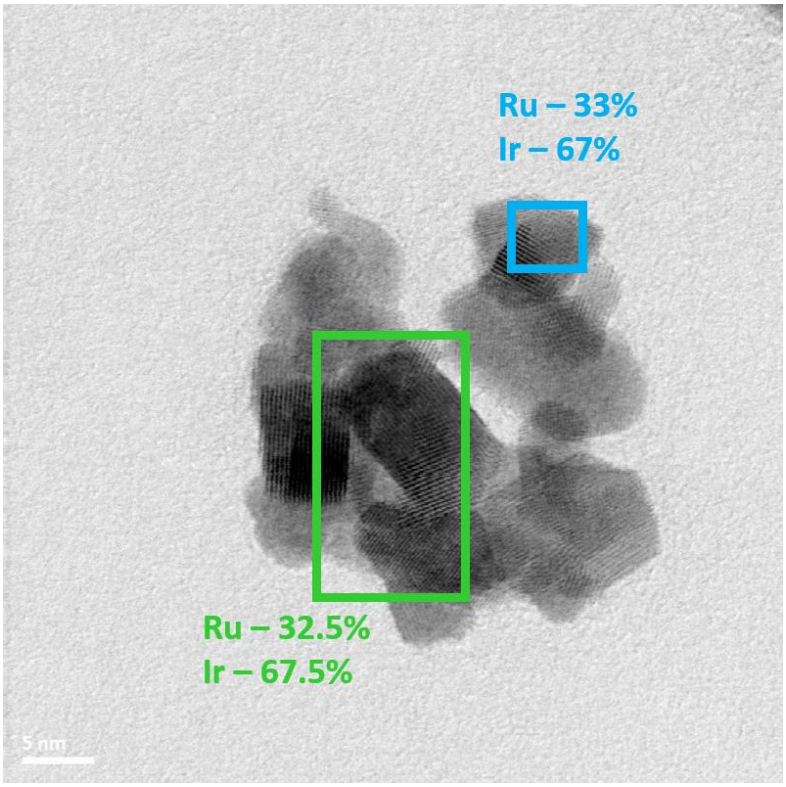

Figure 68. STEM image of the $Ir_{0.7}Ru_{0.3}O_2$ catalyst after the NAP-XPS measurements. Atomic percentage of Ru and Ir in the marked regions as determined by the local EDX analysis is indicated in the figure as well. Similar Ir/Ru distributions were observed in the pristine samples (not shown).

4.2.3. Electrochemical Characterization in Liquid Electrolyte

The electrochemical tests in a three electrode electrochemical cell in the presence of 0.05 M H_2SO_4 electrolyte were done by L. Wang (DLR, Stuttgart). The catalyst powders have been supported on glassy carbon rotating disk working electrode, while Pt foil and RHE were used as a counter and reference electrodes, correspondingly. The ohmic drop resistance used for iR corrections was determined by means of EIS and was equal to 34 Ω. The details of the experimental methods were discussed in Chapter 2. While in the previous Chapter we already showed some electrochemical results obtained on monometallic rutile RuO_2, here we partly repeat them in order to facilitate the direct comparison of pure ruthenium and mixed oxides.

The typical CVs obtained on monometallic and bimetallic Ru(Ir)-based anodes are shown in Figure 69. Higher pseudocapacitance of the $Ir_{0.7}Ru_{0.3}O_2$ sample may be attributed to the smaller particle size of the Ir-containing sample and the ensuing higher specific surface area. The position of the red-ox peaks observed in the CVs is similar for both electrodes, however there is a small shift in case of the mixed oxide, which was also reported in the literature[42]. Thus, the proper

interpretation of the CV curves is quite complex and cannot be done just on the basis of these results.

Panels A and B of Figure 70 show the evolution of the electrochemical activity with the number of potential cycles for RuO_2 and $Ir_{0.70}Ru_{0.3}O_2$ anodes, correspondingly. One may clearly see higher stability and activity of mixed iridium-ruthenium oxide in comparison to a single ruthenium oxide.

The Tafel slope was estimated from the RDE data shown in Panels A and B of Figure 70. The example of the analysis is demonstrated in Panel B of Figure 69. One may see a similar slope of ca. 60 mV dec^{-1} for both oxide-based anodes, however for a single RuO_2 anode we observe its slight evolution at higher potentials related to its degradation under high anodic potentials.

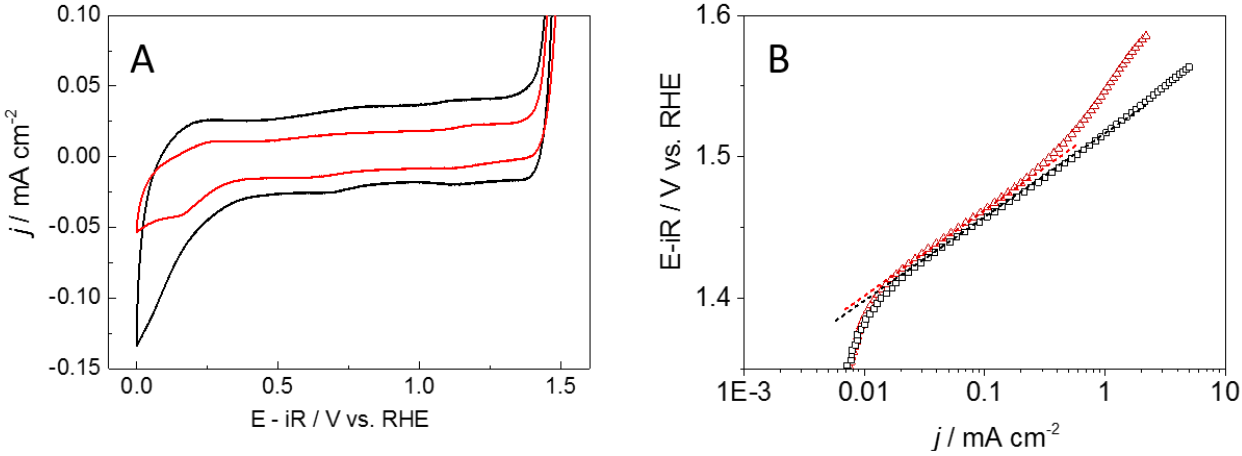

Figure 69. Panel A: CVs (2nd cycle out of 10) for RuO_2 (red) and $Ir_{0.7}Ru_{0.3}O_2$ (black) samples measured in N_2-saturated 0.05 M H_2SO_4 at 25°C at the scan rate of 20 mV s^{-1}. Panel B: Tafel plots constructed from the second current-potential scans. Catalyst loading – 60 μg cm^{-2}. The curve obtained on RuO_2 was previously shown in Figure 50. The data were provided by L. Wang[181].

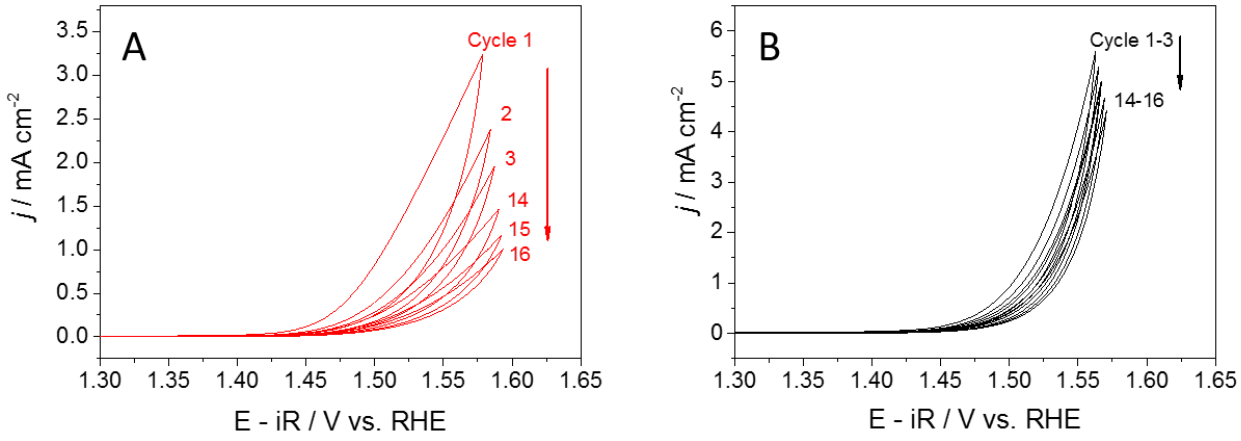

Figure 70. Current-potential characteristics of the RuO_2 (A), and the $Ir_{0.7}Ru_{0.3}O_2$ (B) anode measured in N_2-saturated 0.05 M H_2SO_4 at 25 °C with a scan rate of 5 mV s^{-1}. Catalyst loading – 60 μg cm^{-2}. The results obtained on monometallic ruthenium oxide were shown in Chapter 3. The data were provided by L. Wang[181].

4.2.4. NAP-XPS measurements: Experimental Protocol and Electrochemical Tests

Operando studies of $Ir_{0.7}Ru_{0.3}O_2$ and RuO_2 – based MEAs under water electrolysis conditions were performed at ISISS beamline at BESSY II synchrotron facility (the same beamtime of November 2015). The photoemission spectra were recorded under different polarization conditions and 3 mbar water vapor. The pretreatment procedure used for the surface stabilization and cleaning consisted in the potential cycling of the electrodes in the potential range [0; 1.6] vs DHE with a scan rate of 100 mV s^{-1}. The MEAs resistance has been estimated by means of EIS and was followed during the following NAP-XPS measurements. All the potentials presented further were iR corrected according to the obtained values of R = 56 Ohm for the MEA comprising the $Ir_{0.7}Ru_{0.3}O_2$ anode and ca. 60 Ohm for the MEA comprising the RuO_2 anode.

The typical CVs recorded on Ir,Ru-based anodes in the NAP-XPS chamber under 3 mbar water vapor are shown in Figure 71. Similar to the results obtained in liquid electrolyte (Figure 69), the bimetallic anode possesses higher pseudocapacitance than a single ruthenium oxide-based electrode. The curves obtained in the gas-phase ambient are rather featureless, though a small peak can be distinguished at 1.1 – 1.2 V vs DHE for both electrodes. This peak is also present in the voltammograms obtained in a three-electrode cell. The OER onset is similar for the anode with and without iridium admixture in its composition. The analysis of Tafel slope based on these results is not reliable due to the high scan rates applied here.

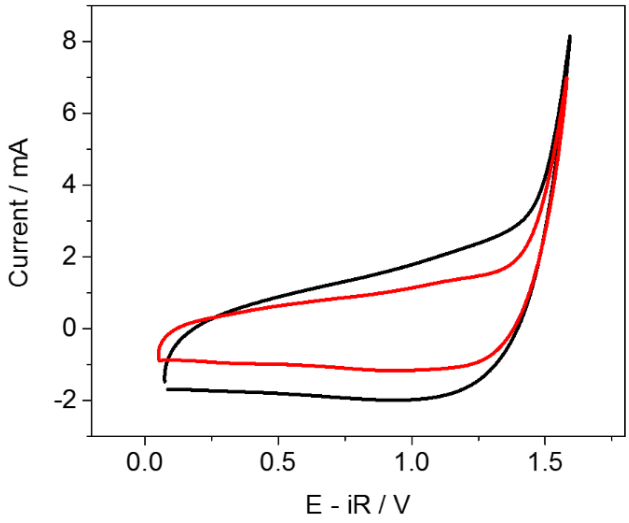

Figure 71. CVs obtained on $Ir_{0.7}Ru_{0.3}O_2$ (black) and RuO_2 (red) anodes in the NAP-XPS chamber under 3 mbar of water vapor. Scan rate 100 mV s^{-1}. The potential values are Ohmic drop corrected. Catalyst loading – 0.1 mg cm^{-2}. The electrode area – 0.9 cm^2. The curve obtained on RuO_2 anode was taken from Figure 50.

Electrochemical characterization performed either in the presence of liquid electrolyte or under water vapor conditions revealed their quite similar behavior. This allowed us to apply the same measurement protocol for *in-situ* studies of Ru- and Ir,Ru-based MEAs. Particularly, the core-level spectra of all the elements present on the electrode surface (Ru3d, Ir4f, C1s, O1s, S2p, F1s, Si2p) were recorded under each applied potential. In order to analyze the propagation of the potential-induced changes in the sub-surface, we also performed the depth-dependent measurements using photon energies 595 eV and 1080 eV for Ir4f spectra; 820 eV and 1300 eV for C1sRu3d spectra, i.e. the kinetic energies of the emitted electrons 530 eV and 1015 eV, respectively. These values correspond to the approximate analysis depths (estimated as three times the inelastic mean free path of the corresponding Ir and Ru oxides) of 4.4 nm and 6.3 nm allowing us to analyze both surface as well as sub-surface region composition. The XP spectra for other elements were measured only with one kinetic energy of 530 eV.

The current transients recorded during the *in-situ* NAP-XPS measurements are shown in Figure 51 for the RuO_2 anode and Figure 72 for the mixed Ir,Ru oxide-based sample. The comparison of the current values during the first OER cycle did not reveal any significant difference in the electrode activities, while the catalyst loading was maintained the same for all the samples (0.1 mg cm^{-2}). The gas-phase composition, and particularly the evolution of oxygen and hydrogen, was controlled during the measurements by online mass spectrometer connected to the NAP-XPS chamber. An example of the MS data obtained on single and mixed Ir,Ru-based anodes is shown in Figure 73. One may clearly see the evolution of the currents corresponding to the

formation of oxygen molecules (m/z = 32) under polarization. Their increasing at 1.5 V and 1.8 V (vs DHE) confirms the occurrence of the OER observed at these potentials in the CVs and CAs discussed above. It is worth mentioning that at the high anodic potential of 1.8 V both the current and the MS signal decay evidence material degradation even in the presence of Ir.

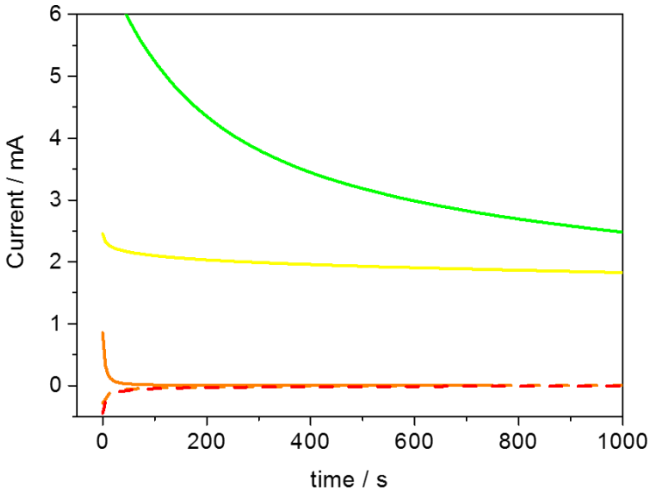

Figure 72. Chronoamperograms obtained in the NAP-XPS chamber at BESSY II synchrotron on $Ir_{0.7}Ru_{0.3}O_2$ anode under 3 mbar water vapor and different polarization conditions: 0.0 V (red); 1.0 V (orange); 1.5 V (yellow); 1.8 V (green). Solid lines represent the forward scan, the dashed – the backward. The potentials are ohmic drop corrected. Temperature 25°C. Catalyst loading – 0.1 mg cm^{-2}.

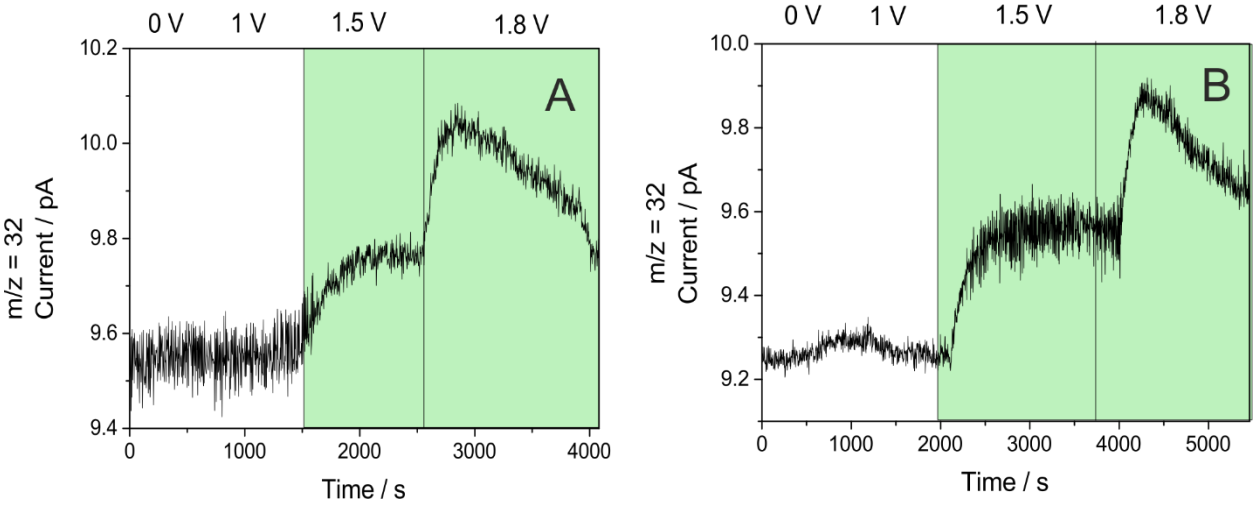

Figure 73. MS data acquired during the measurements for (A) RuO_2 and (B) $Ir_{0.7}Ru_{0.3}O_2$ electrodes. The Ohmic drop-corrected potential values are provided at the top of the figure. The OER region is green-filled. The OER onset potential correlates with the MS data on the oxygen and the hydrogen (from the CE - not shown) evolution.
Note that Panel A was shown as Figure 53

4.3. *In-situ* NAP-XPS studies

While the e*x-situ* characterization of the catalysts and the MEAs with STEM/EDX before and after operation did not reveal any noticeable structural or compositional changes resulting from the OER cycle (Figure 67), the data of *in-situ* measurements presented in this part clearly show changes on the anode surface during the OER, thus providing valuable insight into the electrode behaviors and stabilization mechanism in the presence of iridium. The analysis of both Ru3d and Ir4f XP spectra under different polarization conditions and photon energies is shown in the corresponding sections.

4.3.1. Evolution of Ru active sites

The presence of Ir in Ru-based anodes improves their stability under the reaction conditions, which was confirmed in this work during the electrochemical tests in liquid electrolyte and under water vapor ambient and is also supported by literature results[34,35,49,77]. In order to elucidate the role of iridium, we will first follow the evolution of Ru sites on the $Ir_{0.70}Ru_{0.3}O_2$-based anode and compare it with that for the single-metal RuO_2 anode.

The fitting procedure of Ru3d XP spectra is discussed in Section 2.3.6.2 in detail, so here we will only briefly recall it. The examples of the ruthenium photoemission spectra recorded on RuO_2 and $Ir_{0.7}Ru_{0.3}O_2$ electrodes exposed to a potential of 1.5 V are shown in Panels A, B of Figure 74. As confirmed by the MS data (Figure 73), this potential corresponds to the oxygen evolution reaction region. For clarity, spectra presented in Figure 74 do not show carbon components originating from adventitious carbon and the membrane, which were nevertheless considered during the fitting since C1s and Ru3d spectra (particularly $Ru3d_{3/2}$ peaks) are overlapping. The fitting of Ru3d spectra presented on Figure 74 was done using four doublets (see Table 6 for the parameters) attributed to rutile- type RuO_2, hydrated Ru (IV) oxide – $Ru(OH)_x$, Ru (VI) and Ru (VIII) species based on the literature data. The fitting also included C1s components originating from the adventitious carbon and membrane. All these components were found on the Ru-based electrode surface regardless the presence of IrO_2 admixtures, however the ratio between different ruthenium components is different for single Ru- and mixed Ir,Ru- oxide-based anodes.

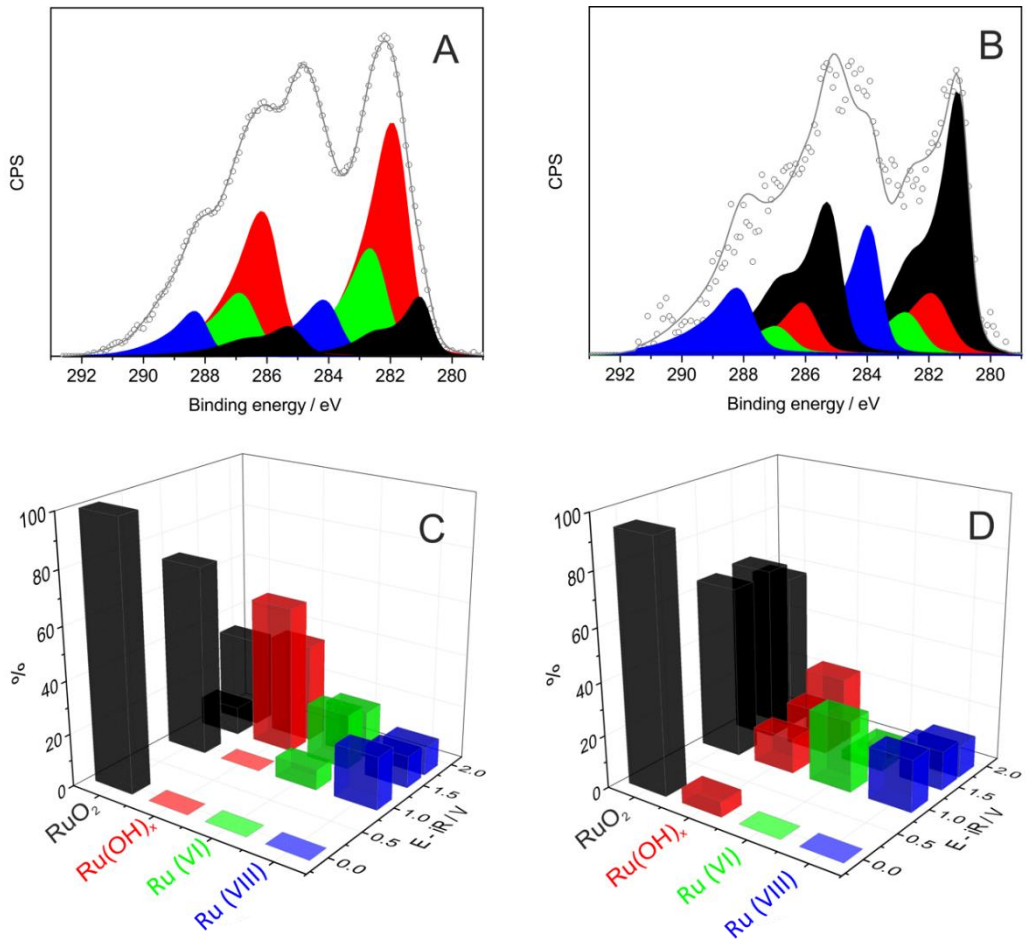

Figure 74. Upper panels: fitted C1s-Ru3d XP spectra of RuO_2 (A) and $Ir_{0.7}Ru_{0.3}O_2$ (B) electrodes at 1.5V. Experimental XPS data are shown as black cycles, fitted spectrum – as a grey line. For the sake of clarity carbon peaks are not shown. Bottom panels: Influence of the applied potential on the surface composition of RuO_2 (C) and $Ir_{0.7}Ru_{0.3}O_2$ (D) electrodes. Only forward scans are shown. Measurements were performed in 3 mbar H_2O ambient at a photon energy of 820 eV. The values of potential are iR corrected and are given on the dynamic hydrogen electrode (DHE) scale. Color codes: RuO_2 (black); $Ru(OH)_x$ (red); Ru(VI); Ru (VIII) or $RuO_{4(s)}$ (blue). Note that Panels A and C was already shown in Figure 54.

For the quantitative analysis of the electrode surface compositions, we will follow the evolution of these four ruthenium-based components with the applied potential. The corresponding diagrams showing evolution of Ru components for RuO_2 and $Ir_{0.7}Ru_{0.3}O_2$ anodes are presented in Panels C and D of Figure 74 correspondingly. The initial state of ruthenium (at 0V vs DHE) is dominated by rutile type RuO_2 oxide both in single and in the mixed oxide. Small traces (ca. 5%) of hydrated oxide phase – $Ru(OH)_x$ – observed on the $Ir_{0.70}Ru_{0.3}O_2$ oxide are within the fitting error. Increasing of the applied potential prior to the OER leads to the formation of ruthenium-based species with higher oxidation state – Ru (VI) and Ru (VIII). Their formation has already been discussed for Ru-based anodes in Chapter 3, while here it is also confirmed in case of mixed Ir,Ru-based oxide anode. Further increase of the potential leads to a decreased contribution of

these species. As it was previously discussed for RuO_2 anode, Ru (VIII) species are observed on the electrode surface under conditions below their standard thermodynamic potential. We tentatively attribute it to the formation of surface $RuO_{4(s)}$ oxide stabilized on the rutile-phase oxide surface either in the presence or in the absence of Ir. Moreover, the potential-induced evolution of Ru (VI) and Ru (VIII) species either during the forward or during the backward scans (Figure 75) is similar both on single and on the mixed oxide. The decreasing of Ru (VIII) species in the OER region has been explained by their decomposition forming lower oxidation state ruthenium oxide and evolving oxygen (see Eq. 23). For Ru (VI) species, we see their higher contribution in case of RuO_2 electrode on the backward scan in comparison to the mixed $Ir_{0.70}Ru_{0.3}O_2$ electrode.

While the quantity and the evolution with potential of Ru (VI) and Ru (VIII) are not strongly affected by the presence of Ir admixtures, the most significant difference is related to the ratio between anhydrous and hydrated Ru (IV) oxide. As it was mentioned before, initially we observed a small contribution of $Ru(OH)_x$ phase on the $Ir_{0.70}Ru_{0.3}O_2$-based anode, however further increasing of the applied potential leads to significant changes of the anhydrous – hydrous Ru (IV) oxide ratio. One may see that the presence of Ir does not completely exclude the hydration, but limits its level at ca. 20%, while for pure RuO_2 anode the contribution of $Ru(OH)_x$ component is growing with time and with the potential cycling. In contrast to the behavior observed for the single-metal RuO_2 anode, the potential reversal (Figure 75) results in a virtual restoration of the initial composition for the $Ir_{0.7}Ru_{0.3}O_2$ anode surface.

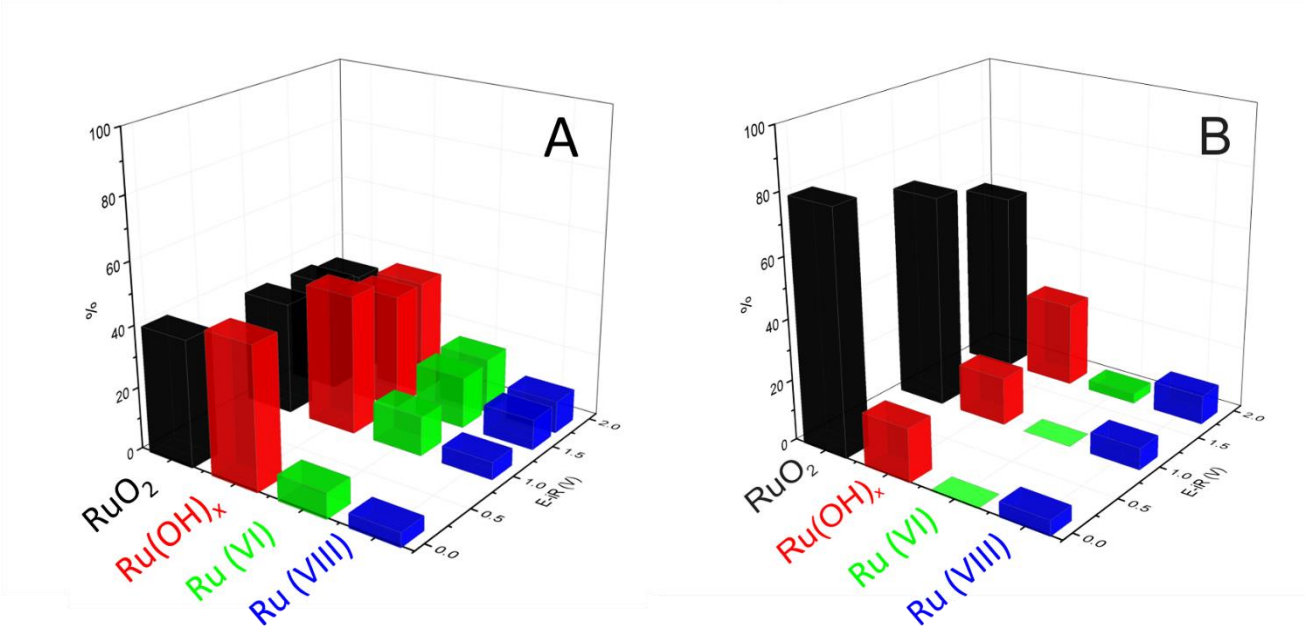

Figure 75. Influence of the applied potential on the surface composition of RuO_2 (A) and $Ir_{0.7}Ru_{0.3}O_2$ (B) electrodes in 3 mbar H_2O ambient in the backward scans. Color codes: RuO_2 (black), hydrated RuO_2 (red), Ru (VI) (green), and Ru (VIII) (blue). Photon energy – 820 eV.

4.3.1.1. Surface vs Sub-surface Composition: Tuning of Photon Energy

One of the advantages of the synchrotron radiation used in these studies is the ability to tune the photon energy allowing one to analyze different surface and sub-surface layers composition and distribution of various iridium and/or ruthenium components.

The depth profiling measurements were done only on the mixed Ir.Ru-based anode. Figure 76 shows the example of Ru3d XP spectra acquired on the $Ir_{0.7}Ru_{0.3}O_2$ anode under the OER conditions at two kinetic energies of emitted electrons: 530 eV (Panels A, C) and 1015 eV (Panels B, D). These values correspond to information depths (estimated as 3*IMFP) of 4.4 and 6.3 nm, respectively. Hereafter, we will refer to the former as surface and the latter as sub-surface region. The composition of the electrode and its changes with the penetration depth under other potentials are shown in Figure A 6. By comparing these results, one may clearly notice the dominant presence of anhydrous Ru (IV) component in the sub-surface of the bimetallic anode, representing the rutile-phase core. The contribution of high oxidation state species, such as $RuO_{4(s)}$ and Ru (VI), is diminished with increasing of the information depth of the photoelectrons and their presence is limited to the surface region. These findings confirm the interface-localized processes studied in this work. The depth dependence of Ir sites will be discussed later.

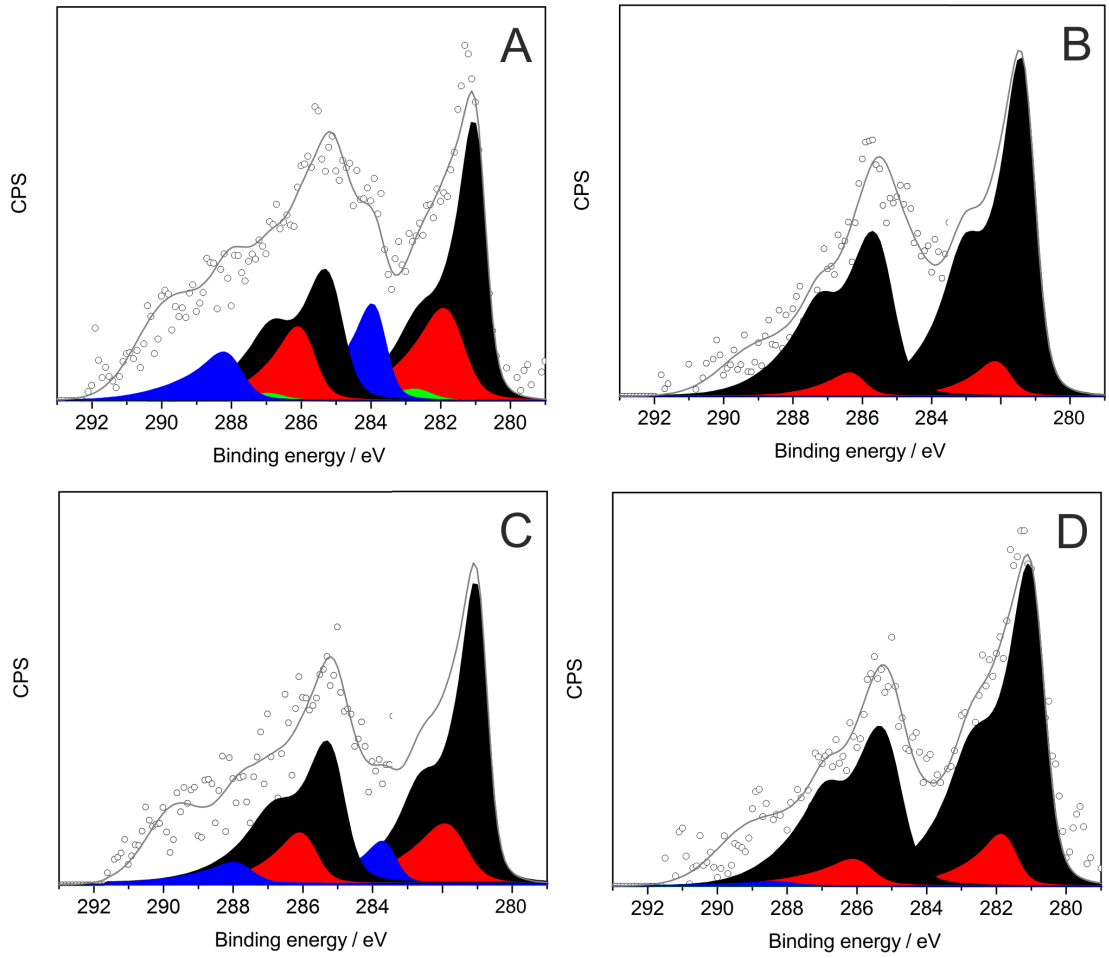

Figure 76. Ru3d XP spectra of $Ir_{0.7}Ru_{0.3}O_2$ electrode in 3 mbar H_2O ambient under 1.8 V (A,B) and 2.5 V (C,D) at different photon energies: 820 eV (A,C) and 1300 eV (B,D). Experimental XPS data are shown as black cycles, fitted spectrum – as a grey line. For the sake of clarity carbon peaks are not shown. Color codes: RuO_2 (black); $Ru(OH)_x$ (red); Ru(VI) (green); Ru (VIII) (blue).

4.3.1.2. Ru3d XP Spectra: Time Effect

The poor stability of Ru (VI) and Ru (VIII) containing compounds limits the number of methods available for their studies. The data obtained here emphasize their role in the electrode degradation and in the oxygen evolution reaction mechanisms.

In order to follow the evolution of Ru3d XP spectra not only with the applied potential or the penetration depth of the photoelectrons, but also with time, we recorded Ru3d spectra twice, directly after the application of the corresponding potential (following the stabilization of the currents, ca. 2-3 minutes after the application of the potential step) and at 50 minutes on $Ir_{0.70}Ru_{0.3}O_2$-based anode. The examples of the evolution of Ru3d spectra with time are shown in Figure 77 at 1.0 V (prior to the OER) and 1.5 V (the OER interval) vs DHE. One may see that the ratio between hydrous to anhydrous forms of Ru (IV) oxide slightly increases with the electrode potential, while Ru (VIII) / Ru (IV) ratio significantly decreases. This can be rationalized by the

transformation of the Ru (VIII) component in other Ru species, which could play a role of the OER intermediates. According to the literature, $RuO_{4(s)}$ species are typically considered as a corrosion product of Ru-based anodes and are supposed to be removed from the surface relatively fast. However, the analysis of the spectra shown in Figure 77 confirmed the idea of surface stabilization of these species proposed earlier. Ru (VI) component disappeared from the electrode surface with the increase of the electrode potential, which can be related to its decomposition to lower oxidation states releasing oxygen in the OER region or to its further oxidation into Ru (VIII).

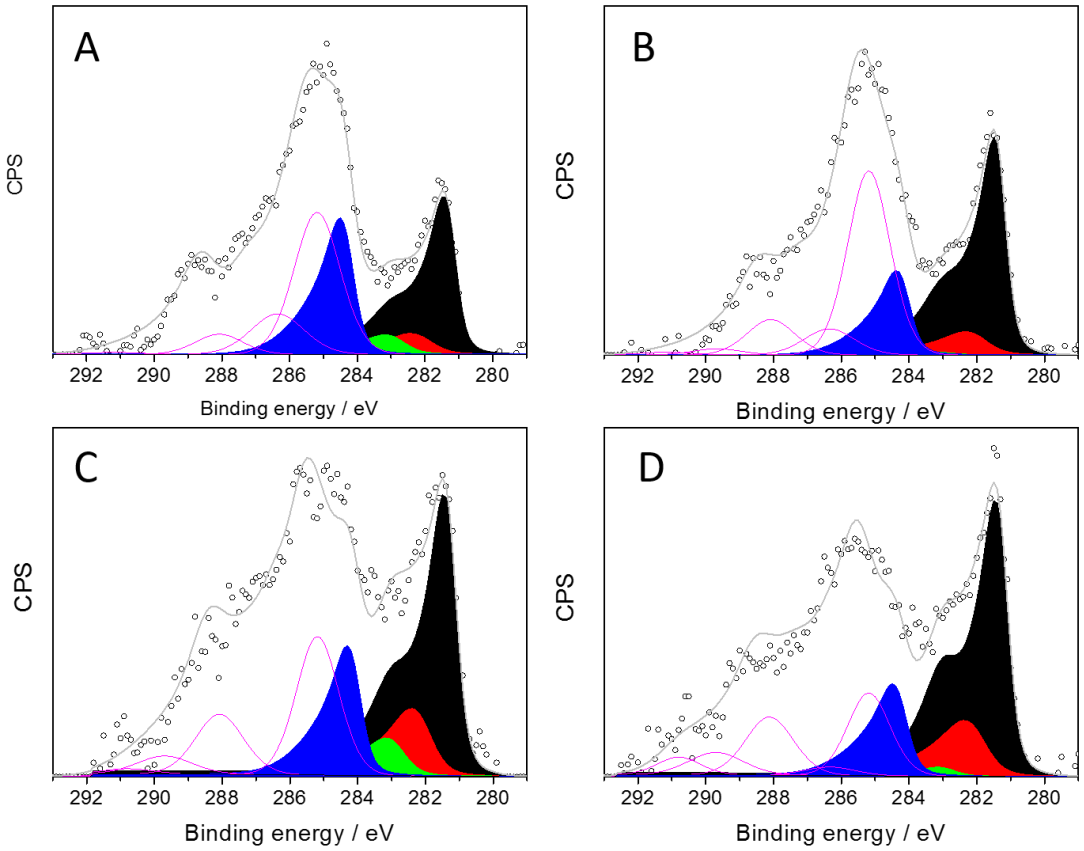

Figure 77. Ru3d XP spectra recorded on $Ir_{0.7}Ru_{0.3}O_2$ electrode in 3 mbar H_2O ambient 2 min (A,C) and ca. 50 min (B, D) after the application of potential of 1.0 V (A, B) and 1.5 V (C, D). Experimental XPS data are shown as black cycles, fitted spectrum – as a grey line. Only $Ru3d_{3/2}$ peak of the doublets are shown. Color codes: RuO_2 (black); $Ru(OH)_x$ (red); Ru(VI) (green); Ru (VIII) (blue), carbon (magenta). Photon energy 820 eV.

4.3.2. Role of Iridium Sites in the OER

In the previous section, we clearly observed the effect of the iridium presence on the evolution of the Ru-based species on the electrode surface. Now we turn to the analysis of the Ir component, starting from the Ir4f XP spectra recorded under different polarization conditions and photon energies and then discussing the Ir/Ru atomic ratio and its evolution with the applied bias.

Figure 78 shows the Ir4f XP spectra recorded on $Ir_{0.7}Ru_{0.3}O_2$ anode under three key potentials: 0 V (below the OER interval), 1.5 V (corresponding to an intermediate OER overpotential), and 1.8 V vs DHE (corresponding to the high OER overpotential). The spectra were collected at two photon energies – 595 eV and 1080 eV. The fitting was performed based on the procedure described by *Pfeifer et al.*[214] using three doublets: main core-level peak corresponding to Ir (IV) state and its two satellites. The asymmetric line shape used here is typical for this kind of materials and is related to the d-electron may-body screening response[215,216]. The details of the fitting procedure and parameters as well as the literature data on the BE position of the Ir4f core-level for different oxidation states of iridium are presented in Chapter 2 (see Table 7, Table 8 and Table 9 and the corresponding comments).

At 0 V vs DHE, iridium is present in the sample in the form of rutile Ir (IV) oxide phase. The depth-dependent analysis did not reveal the presence of metallic iridium component confirming the full oxidation of the sample. Increasing of the applied potential did not lead to any changes of Ir4f spectra regardless of the used photon energy or the position of the analyzed spot on the electrode surface. The stability of the Ir component was further confirmed by *in-situ* measurements of another Ir,Ru-based MEA under the same experimental conditions.

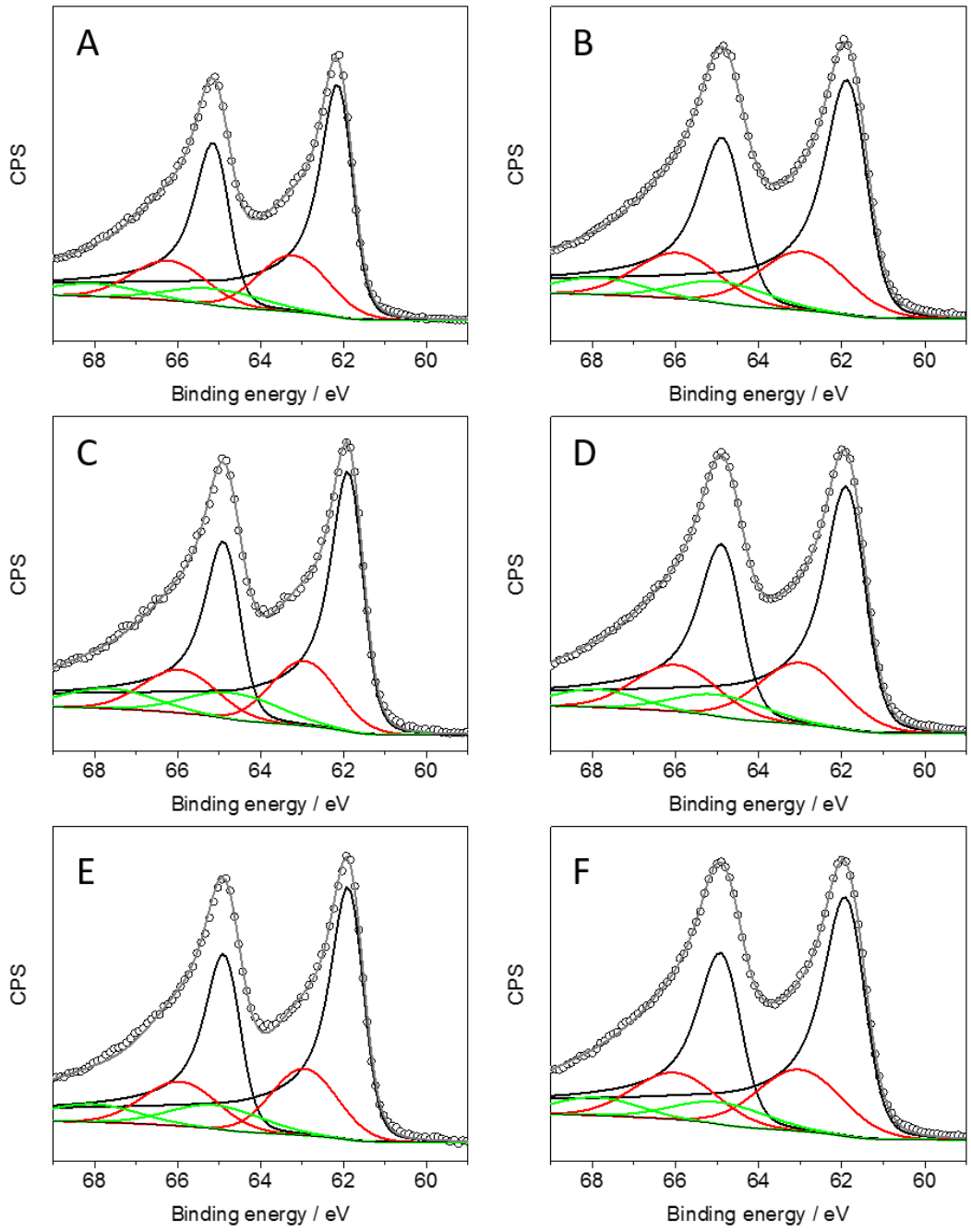

Figure 78. Ir4f XP spectra obtained on $Ir_{0.7}Ru_{0.3}O_2$ electrode in 3 mbar H_2O ambient at E – iR = 0 V (A, B); 1.5 V (C, D) and 1.8 V (E, F) and two photon energies 595 eV (A, C, E) and 1080 eV (B, D, F). Peak fitting was done using three doublets: main peak of rutile-type IrO_2 (black) and 2 satellites (red and green).

The absence of any changes in the Ir4f spectra during the OER cannot be attributed to their passive role in the OER, whereby Ir stabilizes active Ru sites from dissolution itself being inactive. Indeed, it is well established that while being less active than RuO_2, IrO_2 anodes are capable of catalyzing the OER[19,24,108]. However, as it will be shown in Chapter 5, they function via oxygen anion rather than cation red-ox chemistry. This accounts for the absence of any changes in the Ir4f spectra during the OER.

It is also of interest to follow the Ir/Ru ratio on the surface and its eventual dependence on the electrode potential (Figure 79). The nominal composition of mixed Ir,Ru-based oxides, Ir / Ru = 70 / 30, has been confirmed by the EDX analysis discussed above (Figure 68). While the latter is a bulk technique, the surface sensitivity of XPS gives us more relevant information regarding the Ir / Ru distribution at the interface. Initially (at E – iR = 0 V vs DHE) the ratio between iridium and ruthenium on the electrode is close to 1. Increasing the applied potential leads the Ir surface enrichment, also documented in previous studies[35,226]. It is interesting to note, that returning to the initial potential leads to decreasing the Ir/Ru ratio, which reaches a value close to the nominal (Ir / Ru = 2.33).

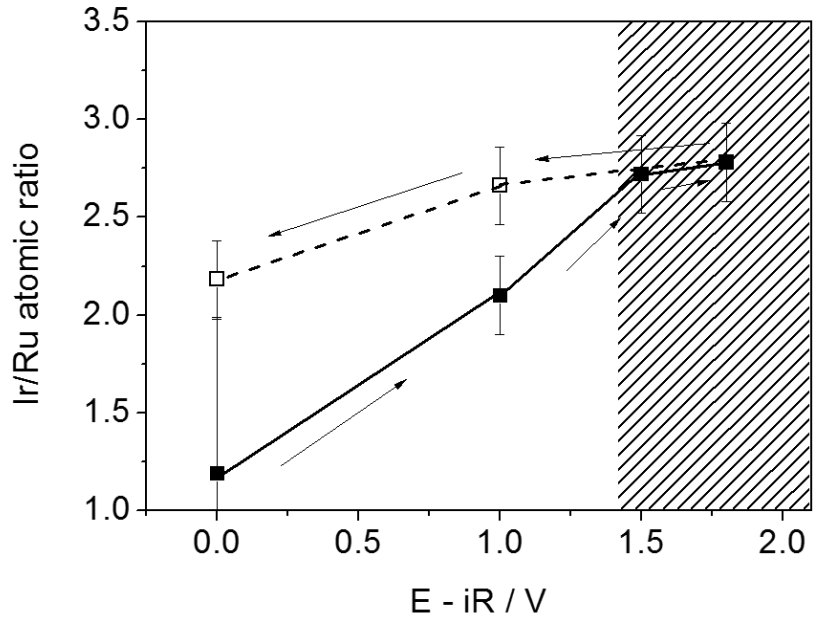

Figure 79. The influence of the applied potential on the Ir/Ru atomic ratio for the $Ir_{0.7}Ru_{0.3}O_2$ catalyst. Forward scan – solid line, backward scan – dashed line. The OER region is marked. The spectra were collected at kinetic energy of 530 eV.

4.4. Stabilization Mechanism in Bimetallic Anode

Rutile-type RuO_2 and $Ir_{0.70}Ru_{0.3}O_2$ catalysts have been prepared by thermal treatment of the corresponding metallic powders and their structure was confirmed by means of X-ray powder diffraction. The analysis of the diffractogram obtained on single ruthenium oxide (Figure 65) revealed small traces of the metallic ruthenium component, however most probably it is originated from the core of the particles, as further photoemission studies of the MEAs based on RuO_2 catalyst powder did not confirm the presence of metallic species. As for the mixed $Ir_{0.70}Ru_{0.3}O_2$ powder, the particles were fully oxidized. Close lattice parameters of tetragonal IrO_2 and RuO_2 do not allow one to distinguish formation of a mixed oxide phase from the mixture of single oxide phases. For this reason, we also performed the STEM/EDX analysis of the pristine oxide powders and the catalyst scratched from the MEA after the electrochemical measurements coupled with *in-situ* NAP-XPS studies. While the precursor, metallic Ru and Ir,Ru particles, possessed the size of 2 -3 nm (as it was shown for pristine Ru in Figure 47), their oxidation in the presence of air led the growth of the particles. It is interesting to note, that the presence of iridium admixtures constrained this growth. The length of pure RuO_2 particles is in the range of 10 – 90 nm with a mean diameter of ca. 14 nm while for $Ir_{0.70}Ru_{0.3}O_2$ the maximum length was only 9 nm. The thorough EDX analysis of the $Ir_{0.70}Ru_{0.3}O_2$ powder confirmed homogeneous distribution of the two components in the sample which suggests the formation of a mixed oxide phase. The post-mortem analysis of the catalysts did not reveal any changes either in the size of the particles or in their composition.

The electrochemical characterization of single and mixed oxides has been performed in liquid electrolyte in a three-electrode cell as well as under water vapor ambient conditions in the NAP-XPS chamber. The cyclic voltammograms recorded on the anodes either with a liquid electrolyte or in the MEA configuration are rather featureless, however one may distinguish small red-ox peaks at ca. 0.7 V and 1.1 V vs RHE on the CVs obtained in sulphuric acid, while only the high potential peaks could be distinguished in the curves measured in the NAP-XPS chamber. Nevertheless, these peaks showed up regardless of the presence or the absence of iridium. As was shown in Chapter 1, the characteristic potentials of red-ox transitions of single iridium and ruthenium oxides are relatively close, leading to their overlap in case of the mixed oxide[42,49,54]. The improved stability of bimetallic Ir, Ru-based oxide catalysts under the reaction conditions in comparison to single Ru-based oxide has been demonstrated by several groups[34,35,49,54,77]. The RDE measurements in liquid electrolyte presented in this work show slower decay of the OER currents in case of $Ir_{0.70}Ru_{0.3}O_2$ anode in comparison to pure RuO_2 (Figure 70) confirming higher stability of the bimetallic anode. Nevertheless, the OER activity of $Ir_{0.70}Ru_{0.3}O_2$ was also

diminishing during potential cycling with the positive potential limit in the OER interval. The comparison of the currents recorded in the liquid electrolyte on the Ru(Ir)-based electrodes with the same loading demonstrates higher activity of the bimetallic-based anode, which may be attributed to its smaller particle size (and the ensuing higher specific surface area). Regardless the decreasing of the electrochemical activity of the Ru- and Ir,Ru-based anodes, the Tafel slope determined based on the current-potential curves recorded at a slow scan rate remained constant and equal to ca. 60 mV dec^{-1}. However, as it was already discussed in Chapter 3, the Tafel slope values obtained in this work for Ru-based oxides are somewhat greater than the ones presented in the literature[36], emphasizing the dependence of the Tafel slope values on the electrode structure, its homogeneity[73] and experimental parameters[27].

At the time of writing this work, the explanations of the improved stability of mixed Ir,Ru-based oxides presented in the literature were quite contradictory[34–36]. One of the reasons of these discrepancies in the literature lies in the current understanding of the degradation mechanism of Ru-based electrodes. While this question has been discussed in detail in the previous chapter of the thesis, here we will rather focus on the comparison of the evolution of the Ru component with potential observed on single and bimetallic Ru(Ir) oxides.

The analysis of the photoemission Ru3d spectra confirmed the presence of all four species on the surface of Ru(Ir) oxides: anhydrous and hydrated Ru (IV), Ru (VI) and Ru (VIII). According to the literature, the latter, $RuO_{4(s)}$, has been considered as the main corrosion product of Ru-based anodes[22,84] and the presence of iridium was expected to diminish its contribution[34,84]. However, the analysis of the surface states of single RuO_2 and mixed $Ir_{0.7}Ru_{0.3}O_2$ under different polarization conditions (Figure 74) did not confirm suppression of the Ru (VIII) surface contribution. The admixtures of Ir do not attenuate the amount of $RuO_{4(s)}$ on the electrode surface, they rather stabilize it on the electrode surface. In addition, the decreasing of the potential during the backward scan did not lead to the full reduction of Ru (VIII) species. We tentatively attribute formation of $RuO_{4(s)}$ species below their equilibrium potential (and prior to the OER onset) observed on both studied anodes as well as its partial reduction during the backward scan as a result of surface stabilization of this species on the electrode surface. In order to support this idea, we also analyzed the sub-surface composition of Ru species on the bimetallic anode under different polarization conditions (Figure 76) revealing the surface localization of high oxidation state ruthenium components, Ru (VI) and Ru (VIII).

Contrary to that of the Ru (VIII), the behavior of the Ru (VI) component is noticeably affected by the presence of iridium. Its formation at potentials below the OER onset and further decrease above the OER onset during the forward scan were confirmed on both Ru(Ir) –based oxides. However, while for RuO_2 the Ru(VI) contribution remained high on the backward potential

scan (Figure 75), this was not the case for the bimetallic electrode where Ru (VI) was at the detection limit. We thus conclude that the presence of Ir protects RuO_2 from its irreversible transformation into either Ru (VI) or into hydrous Ru (IV) oxide as will be discussed below. The analysis of the photoemission spectra recorded on $Ir_{0.70}Ru_{0.3}O_2$ anode at different time after the application of potential (Figure 77) revealed diminishing of Ru (VI) and Ru (VIII) components contribution with time regardless the electrode potential. This is most probably related to the further oxidation of Ru (VI) species and decomposition/sublimation of Ru (VIII) phase, though their degradation under the beam cannot be excluded.

Based on these data concerning Ru (VIII) component, we can already propose that the positive role of iridium can be considered as the stabilization of $RuO_{4(s)}$ on the anode surface rather than its suppressing, contrary to common opinion.

Another effect observed for Ru(Ir) anodes is the hydroxylation of RuO_2 component under polarization which was already discussed in Chapter 3 and was also observed in the literature[238]. This process was shown to be irreversible in case of pure Ru-based systems leading to the disappearance of RuO_2 and its gradual transformation into $Ru(OH)_x$ after consecutive potential cycles into the OER interval. In case of bimetallic Ir,Ru-based anode, the transition of Ru (IV) from its anhydrous to hydrated form was also observed. However, unlike RuO_2-based catalyst, the surface contribution of $Ru(OH)_x$ was restricted to ca. 20% regardless the applied potential. Thus, we can further suggest that the role of Ir admixtures lies in stabilizing Ru in the form of rutile oxide RuO_2, preventing its irreversible transformation into a less stable hydrous oxide form, which is more prone to corrosion.

In contrast to Ru3d, Ir4f XP spectra did not show any noticeable changes either with the polarization or with the photon energy in contrast to the previous *in-situ* NAP-XPS studies of a monometallic IrO_2 anode[101]. The analysis of recorded spectra confirmed the presence of rutile-phase IrO_2 (Figure 78). Various hypotheses may be put forward to explain this observation. The Ir rutile-type oxide may serve as a matrix stabilizing the more active Ru sites, whereby the OER preferentially occurs, while Ir sites remain inert to the reaction. Alternatively, the surface concentration of Ir in higher oxidation state(s) may be too small preventing their detection, or the OER on the Ir oxide occurs via a mechanism, which involves an anion- rather than the cation red-ox cycle as recently documented in refs.[107,108,239] In other to better understand this, in Chapter 5 we will discuss the behavior of monometallic Ir-based anodes.

While the red-ox state of iridium sites does not depend on the reaction conditions, the Ir / Ru atomic ratio rises with the increasing of the potential (Figure 79). The surface segregation of iridium also demonstrated by other groups has been discussed based on the theoretical calculations[240,241]. According to the DFT results, iridium oxides possesses higher affinity to

oxygen than ruthenium oxide[242]. Moreover, it was suggested that the coordinatively unsaturated sites, active for the OER, are occupied by iridium, while ruthenium moves to the less active bridge sites. Thus, according to Man[242], iridium is expected to dominate the OER activity. The idea of IrO_2-like mechanism of the OER for the bimetallic anodes was also suggested based on the analysis of the Tafel slopes estimated for bimetallic as well as single Ir- and Ru-based oxides[49,74]. However, according to the results shown in this work on the potential-induced evolution of the Ru component, we cannot attribute higher surface concentration of Ir to its primary role in the OER mechanism, with the Ru component being inactive. Based on the results of Ru dissolution under the reaction condition[24,99], we would ascribe the evolution of the Ir / Ru ratio to the partial loss of Ru. In case of liquid electrolyte, one would expect the dissolution of Ru (VIII) species[243,244], while under gas-phase conditions of the NAP-XPS chamber – their sublimation.

To sum up, the *in-situ* NAP-XPS studies of Ru(Ir)-based oxides behavior under water splitting conditions allowed us to confirm the degradation mechanism proposed and discussed previously on monometallic ruthenium anodes. By comparison of potential-induced valence state changes observed on pure RuO_2 and mixed $Ir_{0.7}Ru_{0.3}O_2$ oxides, we unveiled the distinctive role of iridium presence in the electrode stability. Particularly, we demonstrated that under operation conditions rutile-type RuO_2 anodes gradually and irreversibly transform into a hydrous Ru (IV) oxide form, while Ir stabilizes Ru in the anhydrous rutile phase. Further, the presence of Ir does not reduce the surface coverage of the $RuO_{4(s)}$ oxide but rather stabilizes it on the surface. By tuning the photon energy, we showed that the core of the catalytic particles mainly consisted of an anhydrous Ru-Ir (IV) oxide phase, while the surface was represented by the Ir (IV) oxide, hydrated form of Ru (IV) oxide and Ru in higher valence states, Ru (VI) and Ru (VIII) labeled as $RuO_{4(s)}$. We finally concluded that the Ir stabilization mechanism consists in protecting RuO_2 from its irreversible transformation into either the unstable hydrous Ru (IV) oxide phase or Ru (VI), and in stabilizing the $RuO_{4(s)}$ intermediate on the anode surface against its dissolution (sublimation).

4.5. Conclusions of Chapter 4

In this Chapter we gave the insights into the stabilization mechanism of Ir,Ru-based anodes by analyzing *in-situ* the surface oxidation states of PEM electrolyzer MEAs, operating at near ambient pressure. By direct comparison of monometallic RuO_2 and bimetallic $Ir_{0.7}Ru_{0.3}O_2$ oxides surface composition obtained by means of NAP-XPS under different polarization conditions, we unveiled the role of iridium in the electrode stability and defined its role in the oxygen evolution reaction.

We demonstrated that Ir protects anhydrous form of Ru (IV) oxide from its irreversible transformation into a hydrated form, prone to corrosion, supporting the degradation mechanism of Ru-based anodes discussed earlier in Chapter 3. In contrast to common opinion, iridium does not diminish the contribution of Ru (VIII) component. Here we demonstrated that the presence of IrO_2 admixtures stabilizes the interface-localized $RuO_{4(s)}$ under the OER conditions and at open circuit potential. The sub-surface analysis of the electrode composition confirmed the presence of anhydrous RuO_2 phase core in the whole range of the potentials and surface localization of high oxidation state components of ruthenium. The analysis of iridium sites revealed their unchanged IrO_2 composition regardless the polarization and analysis depth, emphasizing the role of ruthenium as an active phase of the OER rather than iridium. Further, the surface segregation of iridium under the OER conditions was attributed to the dissolution/sublimation of ruthenium corrosion products.

The results presented herein suggest that stabilization of Ru in the rutile oxide rather than in the hydrous oxide phase is a clue to the development of stable Ru-based anodes for PEM electrolyzers. In order to shed light on the behavior of iridium sites, the next Chapter is devoted to the analysis of pure Ir-based anodes.

Chapter 5. Comparative study of Ir-based anodes under the OER conditions: thermal vs electrochemical oxide

5.1. Introduction

State-of-the-art anodes for PEM electrolysis technology are based on iridium, thus wide dissemination of the PEM electrolyzer technology will raise the issue of its high cost and limited resources. Much effort has recently been focused on the development of the oxygen evolution reaction catalysts with low Ir loading and high mass-weighted catalytic activity. However, further prospects in the catalyst development depend on the progress in the understanding of the mechanism of the OER and key reactive intermediates of this complex electrocatalytic process. Despite several decades of intensive research and significant progress achieved, the mechanism of heterogeneous electrocatalytic OER is still insufficiently understood largely due to the difficulties in unveiling the nature of the active sites under the reaction conditions and detecting reaction intermediates.

The controversies in the understanding of the nature of active intermediates observed in the literature could originate from the different types of the analyzed catalytically active phase (electrochemically grown Ir oxide films or IrO_2 with rutile structure obtained by high temperature oxidation of Ir), various electrode structures (polycrystalline electrodes, sputtered films, nanoparticles), reactive ambients (solid electrodes in contact with liquid acid or membrane-electrode assemblies comprising catalytic particles on proton exchange membranes), applied potential intervals and characteristic measurement times.

In this Chapter, we present a comparative *operando* photoemission study for anode electrocatalysts of two types: (i) Ir metal nanoparticles covered by an electrochemically grown thin oxide layer abbreviated as $Ir@IrO_x$ and (ii) IrO_2 synthesized by thermal oxidation of metal nanoparticles. Both catalysts were integrated in MEAs similar to those utilized for PEM electrolysis and studied under exactly the same conditions using soft X-ray absorption spectroscopy at the O K edge and by NAP-XPS at the Ir4f and O1s core levels to detect possible red-ox transitions of O anions and Ir cations during the OER. The experiments were performed at HZB/BESSY II synchrotron facility in November 2016. The analysis of the obtained spectroscopic data has been complemented by the DFT calculations performed at FHI (Berlin, Germany) by Travis Jones.

The purpose of the work presented in this Chapter is to clarify whether the OER occurs on the same active sites via the same reactive intermediates on the electrochemical and thermal iridium-based oxides and thus reconcile some of the literature controversies. Particularly, by the comprehensive analysis of the absorption and photoemission results collected on Ir-based anodes under the same experimental conditions we:

- followed the evolution of oxygen and iridium sites under different polarization conditions;

- observed the formation of various oxygen-based species and identified their nature;
- analyzed the surface red-ox transformations of Ir sites depending on the oxide type;
- proposed the tentative OER mechanism on Ir-based electrodes.

The results presented in this Chapter are prepared for the submission:

Saveleva, V. A.; Wang, L.; Teschner, D.; Jones, T.; Gago, A. S.; Friedrich, K. A.; Schlögl, R.; Zafeiratos, S.; Savinova, E. R. *Operando* Surface Study of Membrane Electrode Assemblies with Thermally and Electrochemically Oxidizied Iridium Anodes under Water Splitting Conditions. **2018**, *XX*, XXX – XXX

5.2. Materials Characterization

Ir-based electrocatalysts were prepared according to the procedure discussed in Chapter 2 by direct reduction of $IrCl_3$ by $NaBH_4$ in water-free conditions. Two types of the oxides were formed either by thermal oxidation of the pristine metallic iridium nanoparticles (490 °C in the presence of air) referred as thermal iridium oxide IrO_2 or by the electrochemical oxidation of metallic Ir nanoparticles integrated in a working electrode of a MEA under the reaction conditions in the NAP-XPS chamber, labelled here as electrochemical oxide Ir@IrO_x. After the oxidation procedure, IrO_2 particles were further sprayed on the Aquivion membrane. The following parts include the analysis of the synthesized particles by XRD and STEM as well as their electrochemical behavior in liquid electrolyte and under gas-phase ambient.

5.2.1. XRD Analysis

XRD analysis was performed on pristine catalyst powders of metallic iridium and thermal iridium oxide IrO_2. Powder diffraction patterns of both samples as well as the characteristic reflexions of the reference compounds (stars) are shown in Figure 80. For metallic Ir powder we observed wide reflexes attributed to nanoparticles of metallic Ir but also the traces of not-reacted salt ($IrCl_3$). IrO_2 sample is fully represented by a rutile phase oxide.

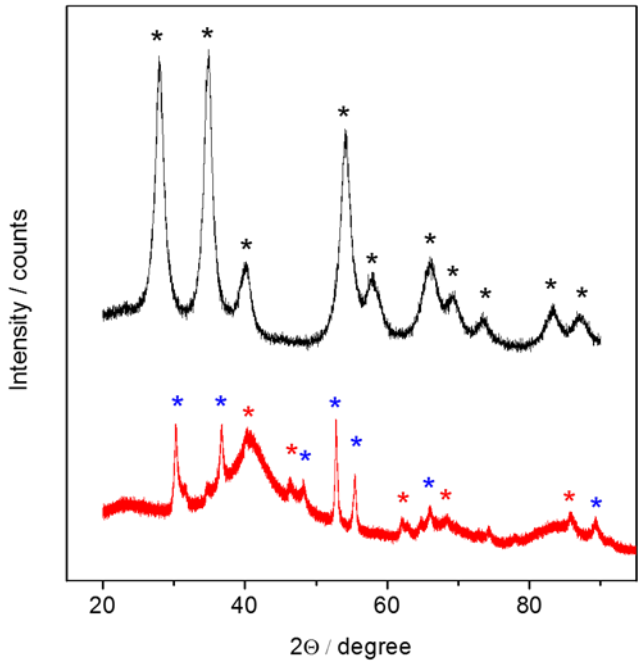

Figure 80. XRD patterns of catalyst powders: metallic Ir (red), thermal oxide IrO_2 (black). The ICDD data for rutile IrO_2 (black, 01-088-0288), face-centered cubic Ir (red, 00-046-1044), $IrCl_3$ (blue, 01-073-0745) are marked in the plot.

5.2.2. Transmission Electron Microscopy

The microscopy analysis was used to characterize the catalysts before the MEA fabrication (metallic Ir and thermal oxide IrO_2) as well as post-mortem by scraping the catalyst particles from the WE surfaces of the MEAs (Ir metal nanoparticles covered by an electrochemically grown thin oxide layer, $Ir@IrO_x$, and IrO_2). Typical TEM images of electrocatalyst powders before and after NAP-XPS measurements are shown in Figure 81. Comparison of TEM images of Ir nanoparticles before and after the measurements revealed a slight growth of the mean particle size during the operation. The values changed from ca. 2.0 nm for the pristine metallic powder to ca. 2.4 nm for $Ir@IrO_x$ catalyst after the electrochemical oxidation. In both cases, the particles are highly agglomerated. It is interesting to note that the presence of IrO_x layer was not detected in the post-mortem sample using the electron energy-loss spectroscopy coupled with the STEM analysis probably due to its low concentration or reduction under the electron beam as it was shown in the work of *Jovanovič et al*.[245]

The analysis of the images obtained for IrO_2 powders revealed their rod-like shape (Panels C and D of Figure 81). The mean width was equal to ca. 5.5 nm and the length to ca. 15.0 nm. No changes either in the particles size or in their shape were detected in the post-mortem sample.

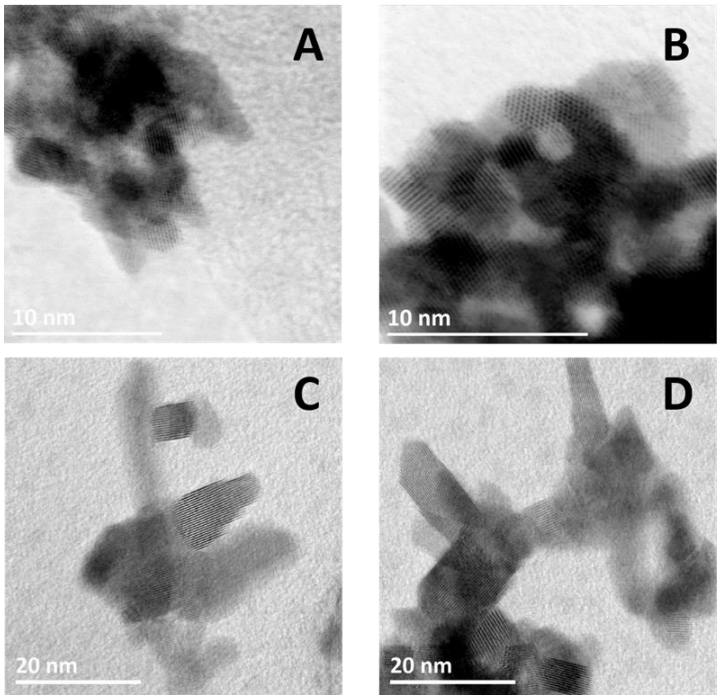

Figure 81. STEM images of pristine metallic Ir particles (A), $Ir@IrO_x$ (B) and IrO_2 (C, D) catalyst before (A,C) and after (B, D) in-situ spectroscopic synchrotron measurements.

5.2.3. Electrochemical Characterization in Liquid Electrolyte

The electrochemical measurements in three-electrode electrochemical cell in the presence of sulphuric acid performed on Ir-based electrodes were done by L. Wang (DLR, Stuttgart). The typical CVs recorded on these electrodes are shown in Figure 82 which compares the 2nd and the 10th cycle for each of the samples. One may notice vanishing of the hydrogen adsorption/desorption peaks in low potential range (ca. 0 V – 0.5 V vs. RHE) for Ir@IrO_x sample after 10 cycles of CV. The diminishing of the peaks in this region clearly indicates the formation of electrochemical oxide IrO_x on the Ir electrode surface. On the contrary, the curves recorded on IrO_2 electrode are stable under the potential cycling, implying that the rutile phase IrO_2 is electrochemically stable and no significant changes occur on the electrode surface during CV sweeping. The comparison of the CV curves recorded on two oxides (the electrode catalyst loading is the same) presented in Panel A of Figure 83 shows higher currents for Ir@IrO_x electrode and a shift of the OER onset to lower potentials in comparison to the IrO_2 anode. A question arises on whether higher currents observed on the electrochemical oxide may be solely due to its higher surface area. Estimation of the specific surface area from the mean particle size neglecting particles agglomeration resulted in ca. 130 and 74 $m^2\ g^{-1}$ for Ir@IrO_x and IrO_2, correspondingly. However, the current values obtained on the former are one order of magnitude higher than the ones observed on IrO_2. Thus, higher specific surface area of Ir@IrO_x does not seem to be the only reason for its higher pseudocapacitance. The other reason is likely to be the different nature of the electrochemical compared to the thermal oxide.

The CV recorded on Ir@IrO_x electrode exhibits two reversible pairs of peaks with the anodic peak potentials around 0.95 and 1.20 V vs RHE. A yet another anodic peak with a corresponding cathodic counterpart at 1.40 V seems to be superposed with the OER onset. For IrO_2 only one pair of peaks can be resolved with corresponding anodic and cathodic peaks at 0.85 and 0.70 V vs RHE.

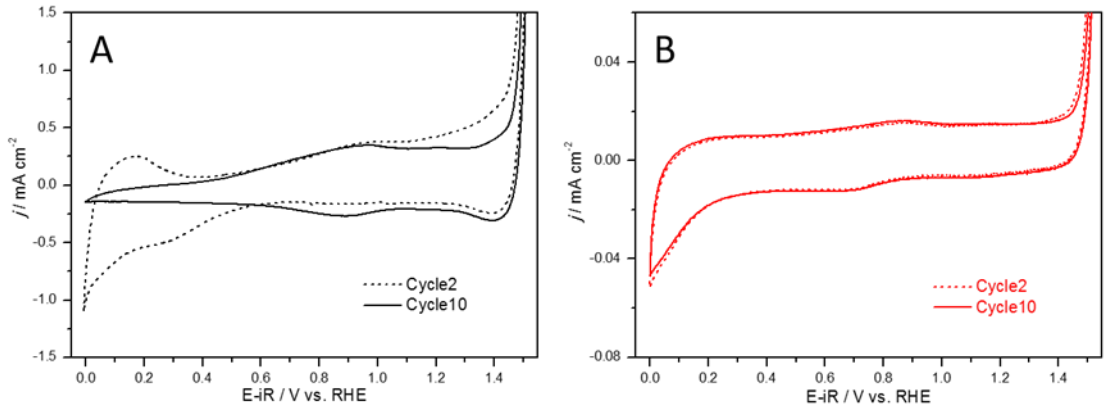

Figure 82. Cyclic voltammograms obtained in N_2-saturated 0.05 M H_2SO_4 on Ir@IrO_x (A) and IrO_2 (B) anode at the sweep rate of 20 mV s^{-1} under 25 °C. Two cycles are shown for each of the electrodes: the 2nd (dotted line) and the 10th (solid line). Catalyst loading on the GC surface is 60 µg cm^{-2}. Current density is normalized to the geometric surface area of the electrode.

The evaluation of the OER activity of Ir-based electrodes was performed after potential cycling in the interval from 0 V to 1.58 V vs RHE (at scan rate of 20 mV s^{-1}). The OER activity of both electrodes was evaluated by CV cycles using a slow scanning rate of 5 mV s^{-1}. The obtained curves shown in Panel B of Figure 83 were capacitance and ohmic drop (iR) corrected and normalized by Ir mass. The ohmic resistance of the electrolyte was estimated as 0.5 Ohm. One may notice a significantly higher OER activity on the Ir@IrO_x electrode in comparison to rutile phase IrO_2. The corresponding Tafel slopes are demonstrated in Figure 84, and amount to ca. 41 mV dec^{-1} and ca. 49 mV dec^{-1} for electrochemical and thermal iridium oxides, respectively. These values correspond to the case of two electrochemical steps, where the last one is considered as rate determining. However, the values obtained in this work in the presence of liquid electrolyte are higher than the ones previously published[54,58]. In the next section, we will compare and discuss the Tafel slopes estimated on the basis of the data obtained under different experimental conditions.

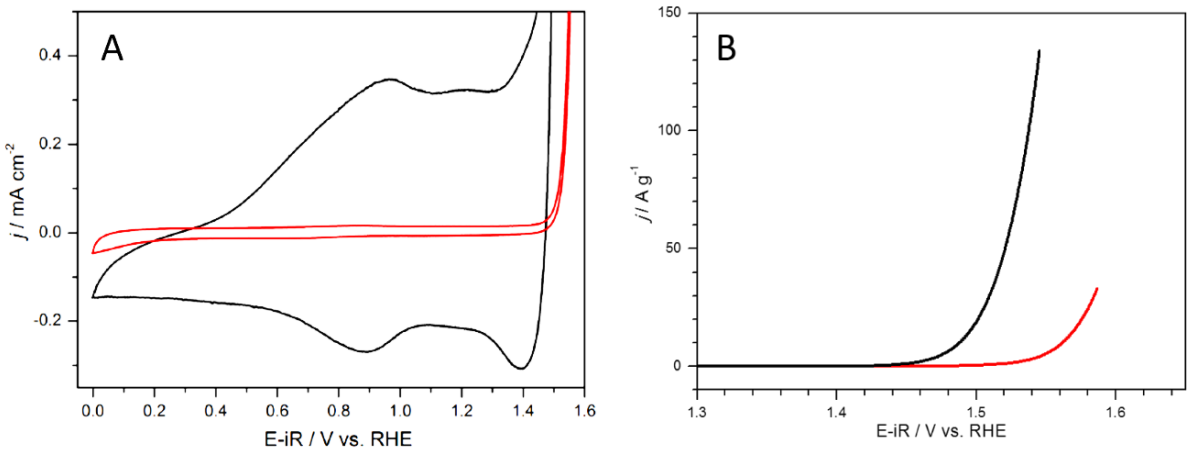

Figure 83. Panel A: The comparison of the 10th CVs recorded on Ir@IrO_x (black) and IrO_2 (red) anodes. The curves were shown in Figure 82. Panel B: OER activity after electrochemically activation measured on Ir@IrO_x anode (black) and IrO_2 (red). The measurements were conducted in N_2-saturated 0.05 M H_2SO_4 with a sweep rate of 5 mV s^{-1}; Catalyst loading on a glassy carbon electrode, 60 µg cm^{-2}; rotating speed, 1600 rpm; measurements temperature, 25 °C.

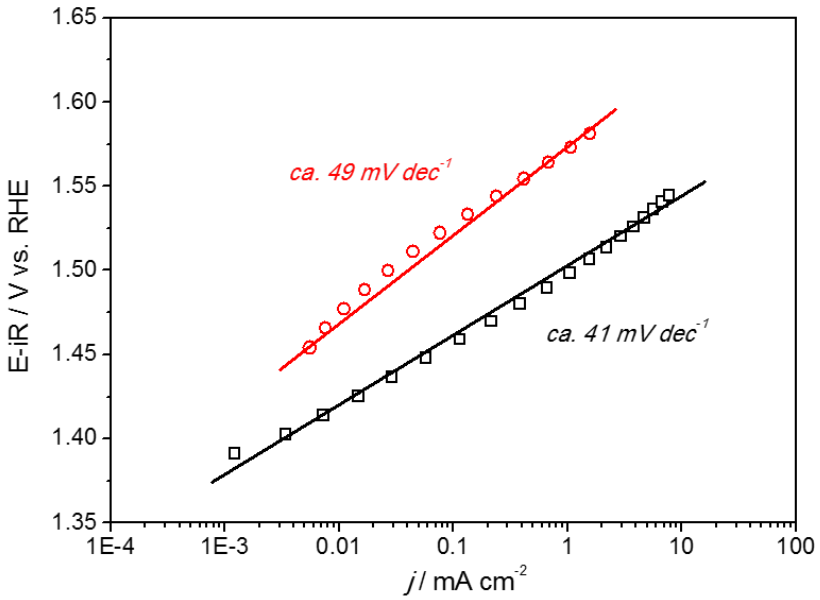

Figure 84. Tafel slope comparison of Ir@IrO_x (black) and IrO_2 (red) obtained in a three-electrode set-up in N_2-saturated 0.05 M H_2SO_4 at 25 °C. The rotating rate 1600 rpm, scanning rate 5 mV s^{-1}. Catalyst loading on glassy carbon electrode, 60 µg cm^{-2}.

5.2.4. Electrochemical Analysis in NAP-XPS chamber and Experimental Protocol

The spectroscopic measurements (NAP-XPS and soft X-ray XANES) were performed at the ISISS beamline (HZB/BESSY II synchrotron) under 3 mbar oxygen-free water vapor under constant voltage applied between the working and the counter electrodes. The MEA resistance examined using high frequency impedance spectroscopy measurements throughout the experiment was equal to 50 Ohm in case of Ir@IrO_x-based MEAs and 80 Ohm for IrO_2-based. These values were used to perform the ohmic drop (iR) correction of the obtained data. The typical CVs recorded on Ir@IrO_x and IrO_2-based anodes are shown in Figure 85. Similar to the results obtained in 0.05 M H_2SO_4, the currents obtained on Ir@IrO_x are higher than the ones registered on IrO_2. However, the difference of pseudocapacitance between the two samples is smaller. The curve recorded on electrochemical iridium oxide possesses two red-ox peaks with anodic peak potentials around 0.5 V and 1.2 V vs DHE, while the CV obtained on thermal oxide has two poorly resolved features with corresponding anodic peaks at ca. 0.5 V and 1.0 V vs DHE. Comparison of the CV curves obtained in liquid electrolyte and under water vapor ambient shows that the position of the anodic peak observed on Ir@IrO_x - based anode at ca. 1.2 V corresponds to the gas-phase data. However, the anodic peak at 0.95 V vs RHE (in 0.05 M H_2SO_4) is shifted to lower potentials (as well as its cathodic counterpart) under water vapor conditions, which is probably related to a lower water activity. An analogous shift of the peak can be also observed for IrO_2 – based anode under two different experimental ambients. While for IrO_2 the anodic/cathodic peaks are observed at very close potential values of ca. 0.5 V vs DHE, for Ir@IrO_x the anodic and the corresponding cathodic peaks are separated suggesting an electrochemically irreversible red-ox transition.

The OER onset potentials, confirmed by the on-line quadrupole mass spectrometer measurements (the data are not shown), are close to the values obtained in liquid electrolyte allowing us to use the ohmic drop-corrected potential values without further correction and correlate the results obtained in liquid electrolyte and under the gas-phase conditions.

Before *in-situ* spectroscopic measurements, all MEAs were pretreated by cycling in the potential interval from 0 V to 1 V vs. DHE directly in the XPS chamber under 3 mbar water vapor in order to obtain stable and reproducible surface state. As it was shown for the results obtained in liquid electrolyte (see Figure 82) such a potential cycling leads to the formation of a layer of non-stoichiometric oxide on the surface of metallic Ir[46,56] which in what follows will be confirmed by the analysis of Ir4f and O1s XP spectra. NEXAFS measurements at the O K-edge and NAP-XPS measurements were realized sequentially without removing the samples from the H_2O vapor

ambient by increasing the electrode potential in regular increments (50 or 100 mV depending on the potential interval).

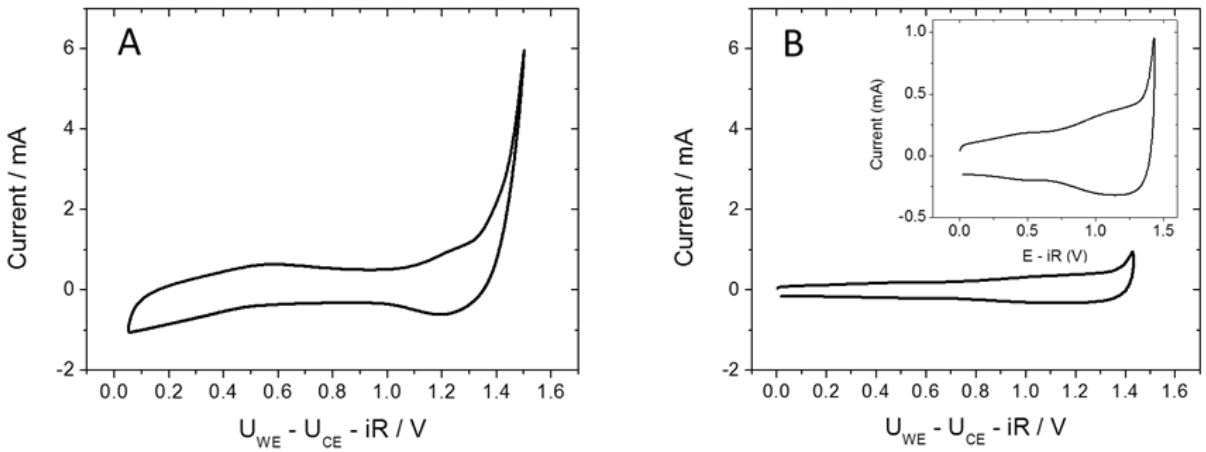

Figure 85. The cyclic voltammograms obtained in the NAP-XPS chamber under 3 mbar water vapor on Ir@IrO$_x$ (A) and IrO$_2$ (B) anodes. The inset of Panel B represents a magnified voltammogram of the IrO$_2$ anode. Scan rate 50 mV s^{-1}.

Operando absorption and photoemission spectroscopic measurements were performed under the constant potential applied between the WE and the CE. The corresponding chronoamperograms recorded during the registration of O K edge and Ir4f spectra are shown in Figure 86 and Figure 87 for Ir@IrO$_x$ and IrO$_2$ anodes, correspondingly. Unlike Ru-based anodes, Ir-based electrodes demonstrate higher stability, at least during the time of the performed *in-situ* experiments, in accordance with the literature data[24]. The currents recorded during spectra collection were stable for both Ir-based anodes. Similar to the data obtained in liquid electrolyte and presented in the literature, the electrochemical activity of the electrochemical iridium oxide is higher than of the thermal one. We observe ca. 5 times higher currents on Ir@IrO$_x$ anode at 1.48 V vs DHE.

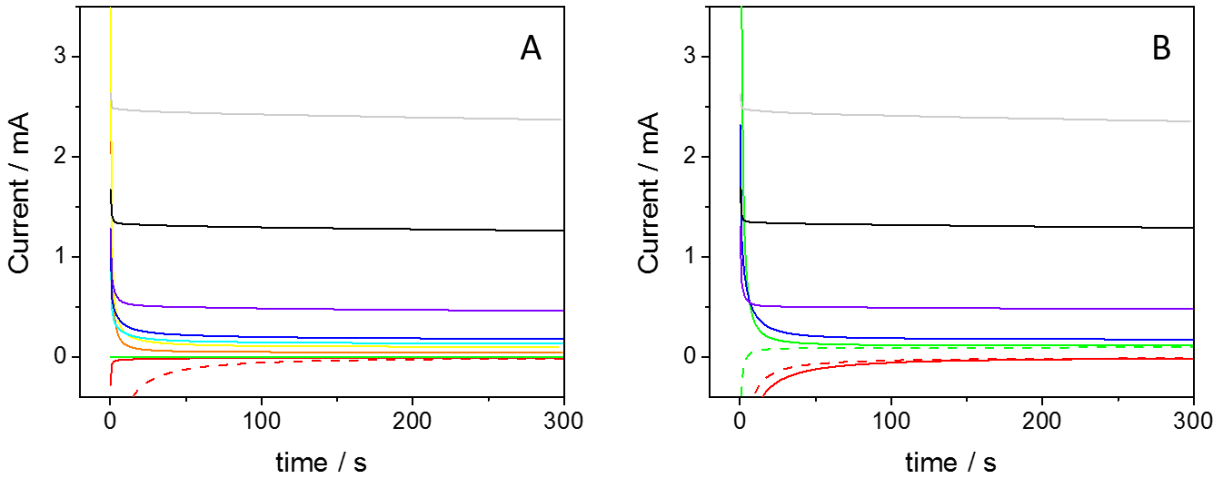

Figure 86. CAs recorded on Ir@IrO$_x$ anode under 3 mbar water vapor and the following potentials: 0 V (red); 0.3 V (orange); 1.0 V (yellow); 1.1 V (green); 1.2 V (cyan); 1.29 V (blue); 1.38 V (violet); 1.43 V (black); 1.48 V (grey). Panel A represents the curves recorded during O K edge measurements, while panel B – during Ir4f spectra collecting. The potentials are iR corrected. Solid lines correspond to the forward scan, dashed lines – to the backward.

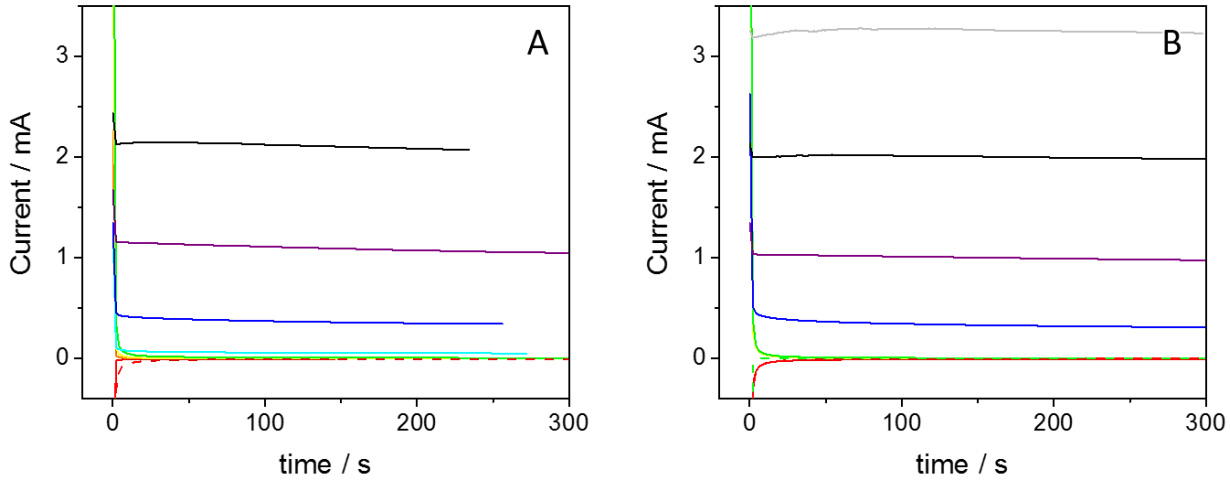

Figure 87. CAs recorded on IrO$_2$ anode under 3 mbar water vapor and the following potentials: 0 V (red); 0.25 V (orange); 0.7 V (yellow); 1.3 V (green); 1.39 V (cyan); 1.48 V (blue); 1.53 V (violet); 1.56 V (black); 1.58 V (grey). Panel A represents the curves recorded during O K edge measurements, while panel B – during Ir4f spectra collecting. The potentials are iR corrected. Solid lines correspond to the forward scan, dashed lines – to the backward.

The analysis of the Tafel slopes estimated for Ir@IrO$_x$ anode on the basis of different data has already been discussed in Chapter 2 (see Table 4). It was shown that the slope does not strongly depend on the RH level, however the values obtained under different experimental conditions (RDE measurements and MEA tests) are quite different. The lowest slope of ca. 41 mV dec^{-1} was calculated from the RDE measurements of Ir@IrO$_x$/GC electrode (0.05 M H_2SO_4, 5 mV s^{-1}). Similar RDE measurements (6 mV s^{-1}, 1600 rpm, 0.1 M $HClO_4$) of Ir NPs – based electrode shown

in literature[58] revealed the slope of ca. 60 mV dec^{-1}. This difference can be related to the differences in the electrode pretreatment procedure. The Ir@IrO_x-based MEA were tested under water vapor ambient (in a laboratory set-up) and in liquid PEM electrolyzer. In the former case the slope was equal to 120 mV dec^{-1}, in the latter – 73 mV dec^{-1}. The CVs recorded in the NAP-XPS chamber at synchrotron facilities were not used for the Tafel analysis as the applied scan rate was too high (50 mV s^{-1}), however we analyzed the currents from the corresponding chronoamperograms (the current values were estimated form the plots shown in Figure 86 at t = 200 s). The Tafel slope was equal to 160 mV dec^{-1} for Ir@IrO_x and ca. 100 mV dec^{-1} in case of IrO_2 – based anode. Thus, one may notice significant variability of the Tafel slope values obtained on the same catalyst during the RDE measurements and the tests of the corresponding MEAs. We suppose that in the latter case the Tafel slopes are not entirely determined by the OER mechanism but are also influenced by other factors such as mass transport in porous layers, Ohmic losses, counter electrode overpotential, which depend on the catalyst layer thickness and porosity, ionomer distribution etc.

5.3. *Operando* Spectroscopic Studies of Ir@IrO_x and IrO_2 – based Anodes

According to the measurement protocol discussed above, *in-situ* spectroscopic studies were performed sequentially, where the absorption O K edge spectra were collected during the first OER cycle and the core-level photoemission spectra (Ir4f) – during the second cycle. The potential was switched in a stepwise manner and the potential-induced changes were followed during two OER cycles. The surface composition of Ir-based anodes between the cycles was controlled by recording of the photoemission spectra of the elements presented on the electrode (Ir4f, C1s, O1s, F1s, S2p and Si2p in order to control the silicon cross contamination observed earlier on similar system). Both thermal and electrochemical Ir-based oxides were studied using the same protocol.

5.3.1. Oxygen Sites: Absorption and Photoemission Spectroscopies

The O K edge spectra were recorded during the first OER cycle, simultaneously in Auger and total electron yield modes. The excitation energy was scanned between 523 eV and 550 eV. Regardless the higher surface sensitivity of the AEY in comparison to the TEY mode, the latter usually provides better signal-to-noise ratios which allowed us to analyze the low intensities of the pre-edge region containing the information on the active oxygen species. As it was shown by *Pfeifer et al*.[108] the low excitation energy region (from 523 to 530 eV) is not affected by the signals from the gas-phase water and oxygen in the NAP-XPS chamber.

The potential evolution of the low excitation energy region of O K edge spectra in TEY mode under polarization for Ir@IrO_x and IrO_2 anodes are shown in Figure 89 and Figure 88, correspondingly. The spectra were normalized to the incident photon flux and to the gas-phase peak intensities.[147] In order to obtain a reliable background containing only water gas-phase peaks, we measured the O K edge spectra in the absence of the sample. The obtained curve was used as a background and was subtracted from all the spectra. The example of subtraction is shown in Figure A 8.

The fitting procedure of the O K edges was based on the parameters provided in the work of *Pfeifer et al*.[104] where the position and the shape of the peaks corresponding to the O^{I-} and O^{II-} species were defined on the basis of the corresponding density functional theory calculations. The work of *Pfeifer et al*.[104] also contains the information on the characteristic resonances of peroxo

and superoxo species formed on the IrO_2 surface, showing that their positions are out of the energy range analyzed in this work.

However, the fitting procedure of the O K edge spectra presented in this work has been slightly modified as explained below. We will start our discussion from the data obtained on the thermal IrO_2-based anode (Figure 88). After the background subtraction, the low excitation energy region [528; 532] eV was fitted with three separate peaks located at 528.9 eV, 530 eV and 531.3 eV with Gaussian/Lorentzian GL(30) function and FWHM of 0.8 – 1.0 eV according to *Pfeifer et al.*[104]. Taking into account the low intensity of the pre-edge we also estimated the error of 10% by varying the fitting parameters several times. While the peaks located at 530 eV and 531.3 eV are present in the O K edge spectra regardless the applied potential, the low excitation energy peak (at 528.9 eV) appears only under the high anodic polarization prior to the OER evolution (starting from 1.3 V vs DHE) and persists during the OER. Based on the theoretical data obtained by T. Jones and experimental results acquired on different Ir-based samples presented in *Pfeifer et al.*[104], the following attribution of the O K edge peaks was applied: 531.3 eV – various OH species; 530 eV – bulk lattice oxygen (O^{II-}) and 528.9 eV – electrophilic O^{I} species formed by oxidation of lattice O^{II-}.

The analogous analysis of the O K edge spectra obtained on Ir@IrO_x anode showed the potential-induced shift of the low excitation energy peak with the electrode potential (from 529.4 eV to 529.0 eV). In order to correlate these changes with the evolution of the surface oxide structures, additional DFT calculations were performed by T. Jones. The introduction of various defect structures on IrO_2 surface allowed us to reproduce the presence of low excitation energy peak, however these data could not explain the systematic shift of this peak with the applied potential. For our future analysis, we considered this shift as being due to a sum of two peaks, where the intensity ratio between these peaks varies with the applied potential. The resulted fitting of O K edge is shown in Figure 89. At low anodic potentials only a 529.4 eV peak is observed. The increasing of the potential up to 1.29 V (vs DHE) leads to the appearance of the second peak at 529 eV and its intensity is further increasing under higher polarization. Meanwhile the 529.4 eV peak contribution is decreasing. Under the OER conditions the intensity of the 529 eV peak is dominating, however the return to the initial potential (0 V vs DHE) leads to the restoration of the spectra, where only 529.4 eV peak can be observed. The analysis of the absorption spectra obtained on Ir@IrO_x sample also revealed the absence of the peak at 530 eV observed on thermal oxide IrO_2 and attributed to bulk lattice oxygen species. Thus, for Ir@IrO_x anode we observed the presence of three following peaks located at: 529 eV, 529.4 eV and 531.3 eV.

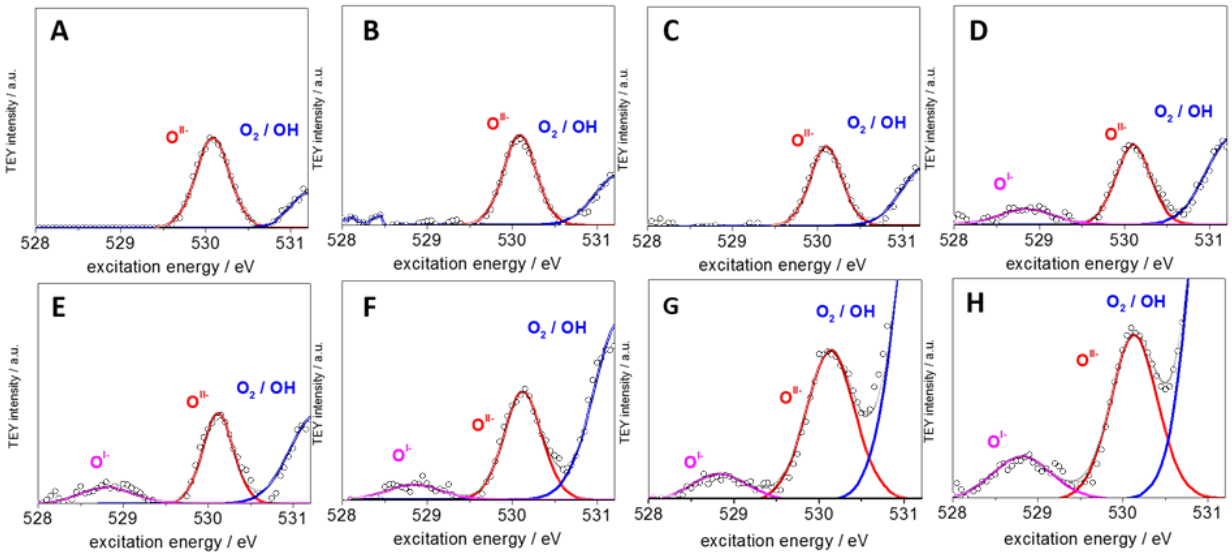

Figure 88. Low excitation energy of O K edges (TEY) of IrO_2 anode under 3 mbar water vapor and different polarization conditions: 0 V (A); 0.25 V (B); 0.7 V (C); 1.3 V (D); 1.4 V (E); 1.45 V (F); 1.5 V (G): 1.6 V (H). Color code: O^{I-} (magenta), gas-phase O_2 / OH (blue), experimental data (black circles), fitted spectrum (grey).

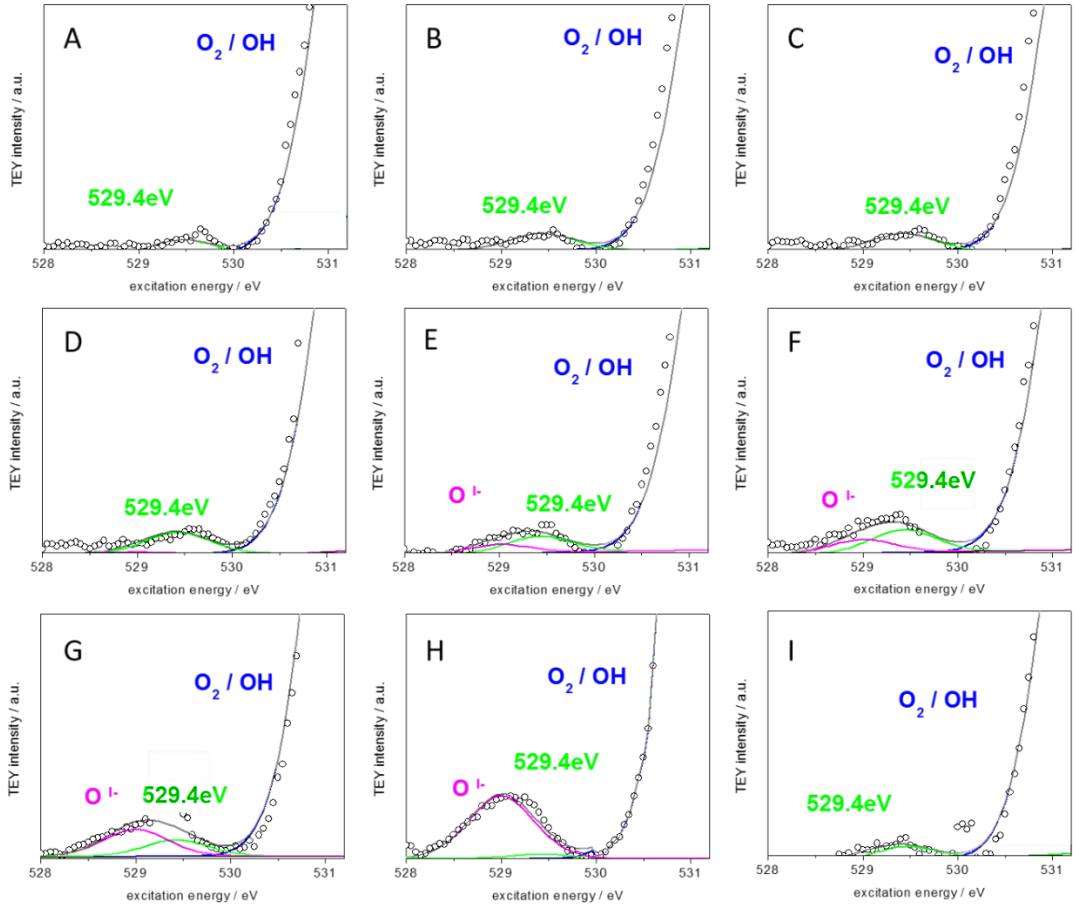

Figure 89. Low excitation energy of O K edges (TEY) of $Ir@IrO_x$ anode under 3 mbar water vapor and different polarization conditions: 0 V (A); 0.5 V (B); 1.0 V (C); 1.1 V (D); 1.29 V (E); 1.38 V (F); 1.43 V (G); 1.48 V (H); 0 V backward (I). Color code: O^{I-} (magenta), gas-phase O_2 / OH (blue), OH groups at 529.4eV (green) experimental data (black circles), fitted spectrum (grey).

The assignment of an additional peak at 529.4 eV was done based on the DFT results discussed in the Appendix (Section A.8.), where two oxygen atoms (μ_1 and μ_2 sites, see panels A and B of Figure A 7) with OH termination may contribute to the intensities of different white lines observed in O K edge spectra. Particularly, the peak located at 529.4 eV was related to μ_1-OH while 531.3 eV – to μ_2-OH. The 529.0 eV assigned to electrophilic O^{I-} species is formed on μ_2 sites.

Based on the theoretical calculations and potential dependence of the 529.0 and 529.4 eV peaks obtained *in-situ* we consider the following scheme of formation of electrophilic O^{I-} species for the electrochemical oxide. The 529.4 eV peak attributed to μ_1-OH sites deprotonates at potentials above 1.3 V and transforms into the OER intermediate μ_2-O (electrophilic oxygen O^{I-}) with a peak at 529.0 eV. This can be expressed by the equation:

$$S\text{-}OH \rightarrow S\text{-}O + H^+ + e^- \quad (Eq.\ 25)$$

Peaks at ~531.0 eV and higher correspond to various OH species (mostly μ_2-OH, see Panel A of Figure A 7), and background increase due to water and gas-phase oxygen formed during the OER.

In spite of the different formation step, the presence of O^{I-} species under high anodic potentials has been confirmed for both iridium oxides. The slight shift of O^{I-} component resonance observed on Ir@IrO_x anode (529.0 eV) in comparison to IrO_2 anode (528.9 eV) can be attributed to different oxide structures as it was discussed in ref.[108] Figure 90 shows the dependence of current values and O^{I-} species versus the applied potential estimated for electrochemical and thermal oxides. The increase of O^{I-} species with applied potential observed on both anodes suggests their electrochemical formation regardless the oxide type. The linear relationship obtained between the current and the O^{I-} peak intensity for the Ir@IrO_x anode (Figure 91) is likely related to a chemical process of the O^{I-} intermediate into molecular oxygen. It is interesting that for rutile-type IrO_2 anode the O^{I-} intermediate emerges at potentials below the current rise which

can be related to the presence of other slow electrochemical steps or to the necessary accumulation of these species on the surface.

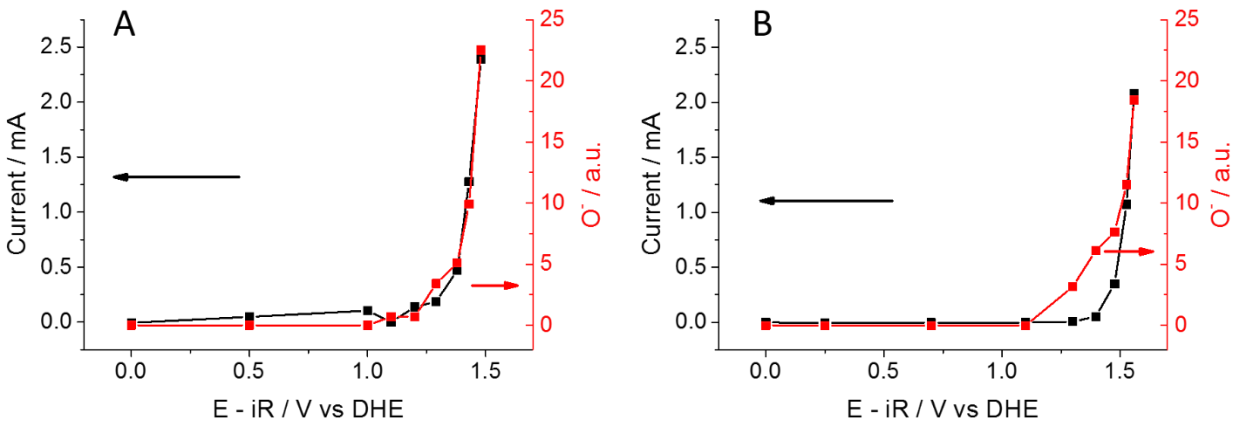

Figure 90. Current values (black) and O^{I-} surface species content (red) versus applied potential for $Ir@IrO_x$ (A) and IrO_2 (B) anodes.

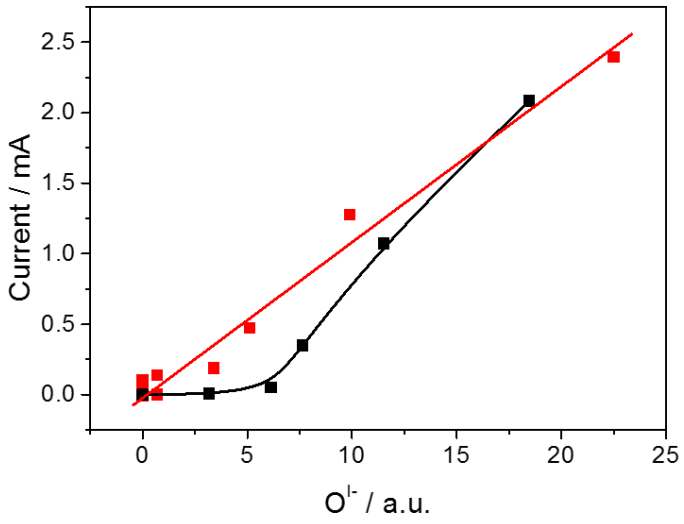

Figure 91. Dependence of the current values recorded on $Ir@IrO_x$ (red) and IrO_2 (black) anodes on the quantity of the formed O^{I-} species.

As it was previously mentioned, the O K edge spectra recorded on $Ir@IrO_x$ do not contain the lattice oxygen species abbreviated as O^{II-} in the whole range of the studied potentials. In order to confirm this, we also analyzed the O1s XP spectra recorded on both thermal and electrochemical iridium oxides at open circuit potentials (see Figure 92). The fitting of the oxygen core-level spectra was done using three components corresponding to bulk lattice oxygen (ca. 530 eV), OH groups (ca. 531.7 eV) and adsorbed water (ca. 532.8 eV). Note that one cannot disregard contributions of C=O and C-O species at 531.7 and 532.8 eV respectively. The lattice oxygen component is clearly observed in the O1s spectra of IrO_2 anode while it is absent for $Ir@IrO_x$, which is in agreement with the absence of the O^{II-} component in the O K edge spectra discussed above. One may also notice a higher relative contribution of the OH components in the case of $Ir@IrO_x$ suggesting the formation of hydroxide or oxyhydroxide rather than rutile oxide layer on

Ir nanoparticles under potential cycling, however their overlap with oxygen functionalities on carbon does not allow us to provide a more precise quantitative analysis.

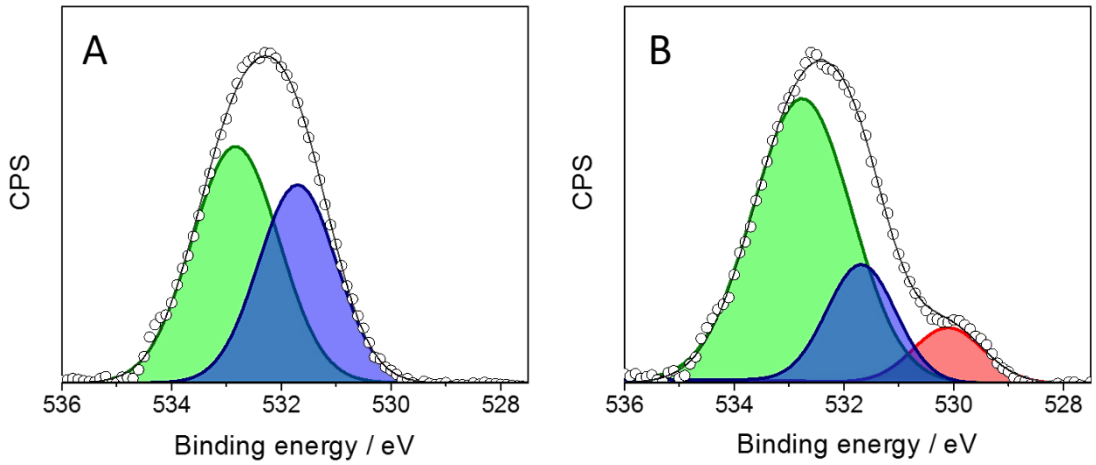

Figure 92. O1s XP spectra of Ir@IrO_x (C) and IrO_2 (D) anodes under 3 mbar water vapor and 0 V. Color codes: lattice oxygen (red), hydroxide and C=O species (blue), water and H_2O/C-O species (green), experimental points (black cycles), fitted curve (gray line). Photon energy 1066 eV.

5.3.2. Potential-induced Changes of Ir sites. Ir4f XP spectra Analysis

We now turn to the analysis of Ir4f XP spectra under various potentials (which were recorded after the series of O K-edge spectra) in order to clarify the role of Ir sites in the OER, and eventually detect red-ox transformations of the surface cations during the OER for the two types of Ir-based anodes. Ir4f, C1s and O1s (discussed above) XP spectra were recorded using selected excitation photon energies so that the photoelectrons were emitted at a kinetic energy of ca. 530 eV. To increase the surface sensitivity Ir4f spectra were also recorded at kinetic energy of 330 eV. These values correspond to an approximate analysis depth (estimated as three times the inelastic mean free path for metallic iridium) of 1.8 nm and 2.4 nm for 330 eV and 530 eV respectively.

Figure 93 represents the Ir core-level spectra obtained on Ir@IrO_x anode under different polarization conditions. The fitting procedure as well as the parameters used for the deconvolution depending on the kinetic energy were discussed in the corresponding section of Chapter 2. Briefly, the fitting was performed using three doublets with $Ir4f_{7/2}$ peak position at 60.85 eV, 62.40 eV and 61.70 eV attributed to Ir (met), Ir (III) and Ir (IV) components respectively and two doublets corresponding to Ir (III) and Ir (IV) satellites. It is interesting to note that due to the final state effects the binding energy position of Ir (III) species is higher than of Ir (IV). [108,218] The potential-

induced evolution of the components is given in Figure 94. After the initial electrochemical pretreatment the surface of metallic Ir particles is covered by Ir (III) / Ir (IV) mixed oxide layer. Based on the intensity ratio of the oxide vs the metal peaks, the thickness of the former (as estimated by SESSA) is roughly 0.5 nm. Increasing the applied potential leads to the diminution of the contribution of the Ir (III) component accompanied with the increase in the Ir (IV) component, in such a way that in the potential interval of the OER the surface is dominated by Ir (IV). Potential reversal back to 0V results in an increase of the Ir (III) contribution and a decrease of the Ir (IV) component, but does not fully restore the initial spectrum. This may be attributed to the "ageing" of the hydrous electrochemical oxide film, which was reported in previous publications[246].

One of the intriguing question concerns the nature of the Ir (IV) species formed on the surface of Ir nanoparticles during the OER. Even if the XPS is sensitive to the composition rather than the structure, analysis of the peak width of the Ir4f doublet corresponding to Ir (IV) for two commercial reference samples: IrO_2 with rutile structure and hydrated IrO_2 $2H_2O$ which is claimed to be amorphous (see spectra in the Appendix, Figure A 10 and Figure A 11) suggests that the Ir (IV) oxide film formed on metallic iridium nanoparticles ($Ir@IrO_x$) in this work is most likely amorphous. Indeed, *Pfeifer et al.*[218] demonstrated that crystalline and amorphous Ir (IV) oxides are characterized by different XP peak width (FWHM), line shapes and satellites. The formation of a hydrous oxide layer on $Ir@IrO_x$ anode can be also supported by the analysis of O1s XP spectra shown in the previous part (see Figure 92), where the contribution of OH groups on $Ir@IrO_x$ anode was higher than on IrO_2.

According to our results, Ir sites do not exhibit oxidation state higher than (IV). Meanwhile, the formation of Ir (V) species under the OER conditions was proposed in early publications of *Koetz et al.*[98,247] and *Pickup and Birss.*[248] Recent *in-situ* NAP-XPS studies performed on IrO_2 oxide under the OER conditions by *Casalongue et al.*[101] also suggested formation of high oxidation state oxide containing Ir (V). Since *Casalongue et al.*[101] performed the measurements at photon energy of 390 eV, in order to compare our data, we collected the Ir4f spectra under the same photon energy at the key potentials: OCP, before the OER and under the reaction conditions. The fitted XP spectra are shown in Figure 95. The left-hand panels also contain the spectra recorded under the same potentials with the photon energy of 595 eV shown previously to facilitate their direct comparison. The spectra collected at lower photon energy were also fitted with three components attributed to metallic Ir, Ir (III) and Ir (IV), while no additional components were observed. It is interesting to note, that the compositions of the surface and "subsurface" region corresponding to the 390 eV and 595 eV photon energies are very similar, excluding a layered Ir (III) / Ir (IV) oxide/hydroxide

shell at low potentials, but rather suggesting formation of a porous layer on metal Ir particles whereby Ir (III) and Ir (IV) species are intermixed.

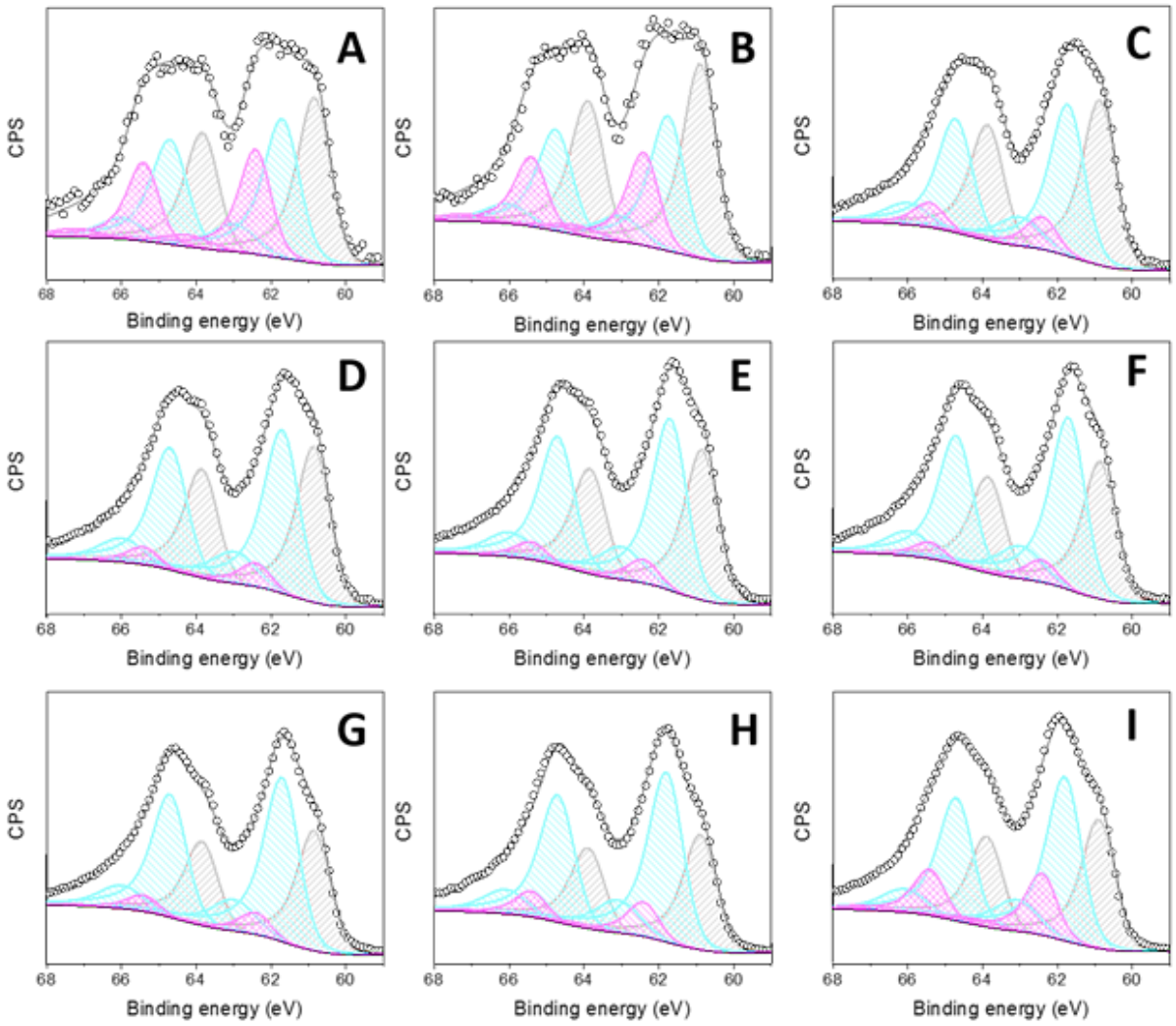

Figure 93. Ir4f XP spectra of Ir@IrO_x anode under 3 mbar water vapor and different polarization conditions: A – 0 V; B – 0.4 V; C – 1.1 V; D – 1.3 V; E – 1.4 V; F – 1.43 V; G – 1.5 V; H – 1.1 V (backward scan); I – 0 V (backward scan). Fitting: Ir met – grey, Ir III magenta, Ir IV – cyan. Photon energy 595 eV.

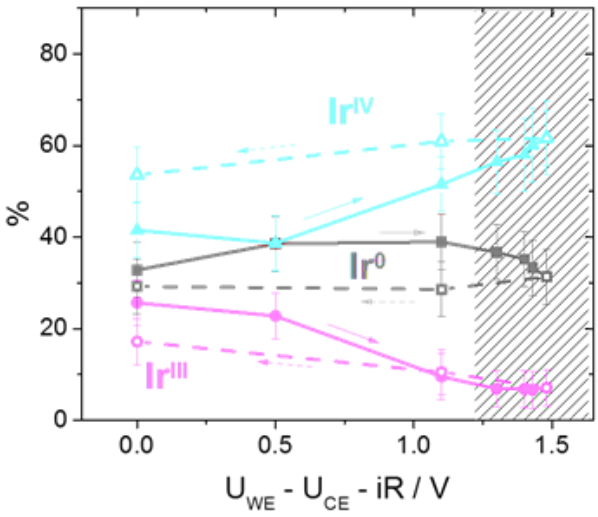

Figure 94. Influence of the applied potential on the surface composition of Ir@IrOx anode. Measurements were performed under 3 mbar water vapor. Photon energy 595 eV. Potentials are ohmic drop corrected, both forward (solid line) and backward (dashed line) scans are shown.

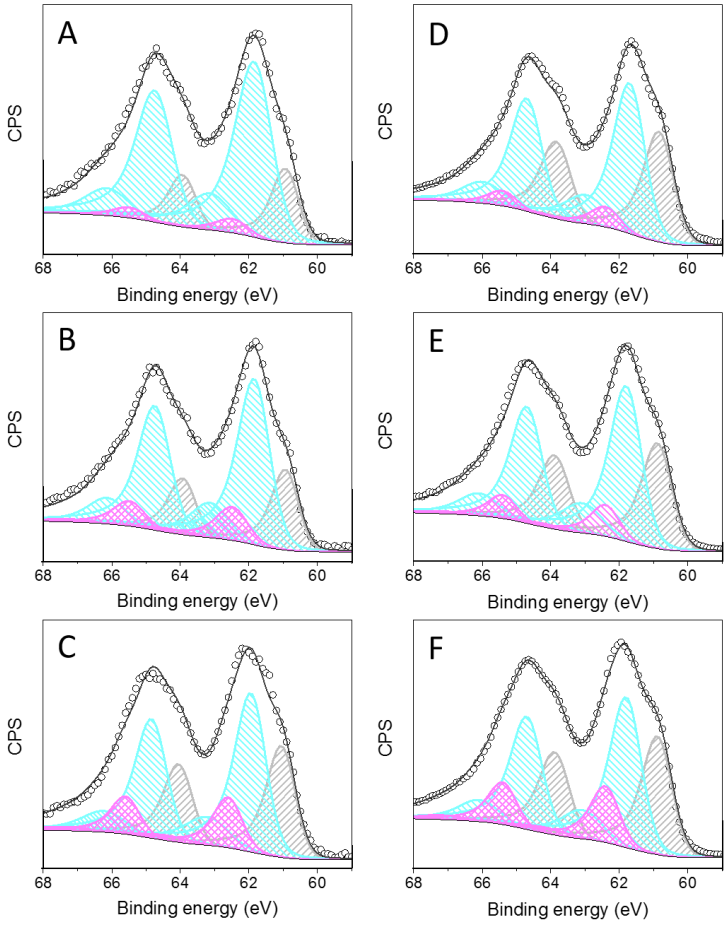

Figure 95. Ir4f XP spectra of Ir@IrO$_x$ anode under 3 mbar water vapor and different polarization conditions: A, D – 1.5 V; B, E – 1.1 V (backward scan); C, F – 0 V (backward scan). Fitting: Ir met – grey, Ir III magenta, Ir IV – cyan. Photon energy: 390 eV (A-C), 595 eV (D-F). Note that the spectra shown in Panels A-C have been demonstrated in Figure 93.

The Ir4f spectra collected on thermal IrO_2 anode are shown in Figure 96. The shape and the width of the peaks correspond to the parameters obtained on the reference powder of rutile oxide (see the Ir4f XP spectra in Figure A 10 of Appendix). The estimated atomic ratio of lattice oxygen (O1s component at 530 eV, Figure 92) to Ir (overall intensity of Ir4f XP spectra), equals to 2.2, which is in agreement with the IrO_2 oxide composition. In contrast to the potential-induced changes observed on $Ir@IrO_x$ electrode, the spectra shown for thermal iridium oxide do not change under the applied potential. The tuning of the photon energy to lower values in order to enhance the surface sensitivity (Panel B of Figure 96) did not reveal any changes either in the position or in the spectra width.

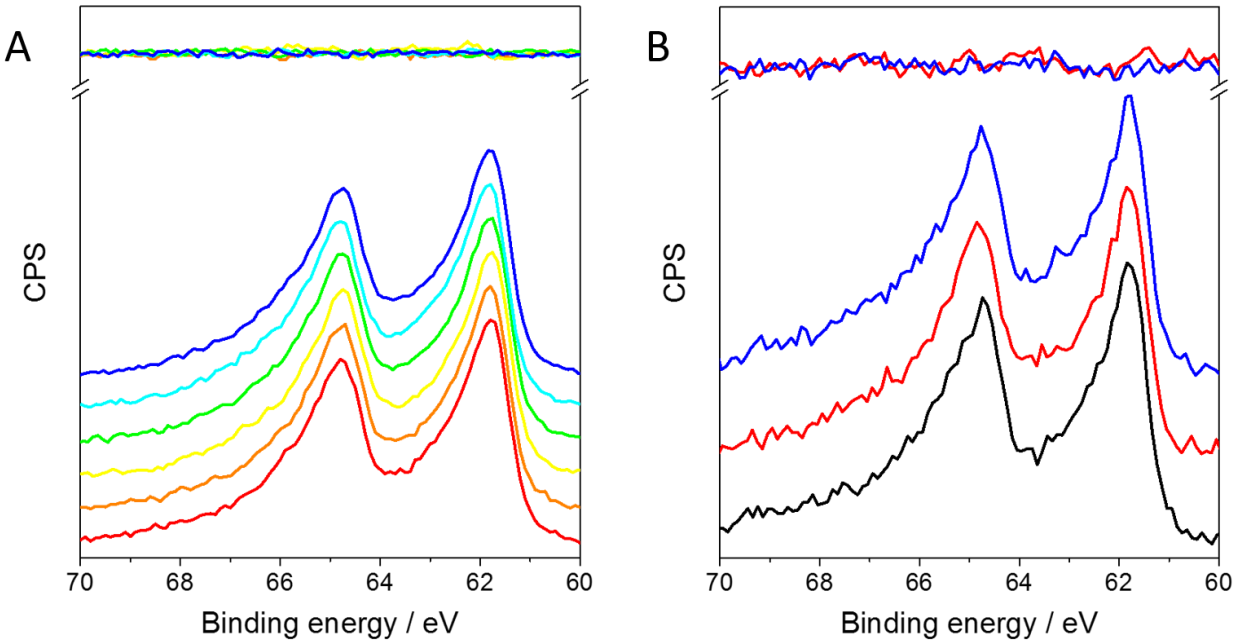

Figure 96. Ir4f XP spectra recorded on IrO_2 anode at different potentials and photon energies of 595 eV (A) and 390 eV (B). Color code for Panel A: 0 V (red); 0.7 V (orange); 1.3 V (yellow); 1.5 V (green); 1.55 V (cyan); 1.6 V (blue). For Panel B: 0 V (black); 1.3 V (red); 1.6 V (blue). The upper part of the panels represents the difference between the spectra obtained under different potentials and the spectrum at the open circuit conditions. Measurements were performed under 3 mbar water vapor. Potentials are Ohmic drop corrected.

5.4. Nature of OER Active Sites on Ir-based Anodes. Discussion

Before we switch to the discussion of the OER mechanism on Ir-based electrodes, we will summarize the properties of these catalytic materials. Thermally obtained IrO_2 catalyst consists of rod-like particles with mean diameter of ca. 5.5 nm and mean length of ca. 15.0 nm. No traces of metallic phase were observed on the corresponding diffractogram and the oxide possesses a rutile structure. The Ir@IrO_x sample consists of metallic iridium covered by an electrochemically grown thin oxide layer. The pristine metallic iridium particles had the mean diameter of ca. 2.0 nm, while the post-mortem analysis of Ir@IrO_x revealed the growth of the particles up to ca. 2.4 nm during the oxidation – reduction cycles performed on the electrode. No changes in the particles size distribution were detected on IrO_2 catalyst powder after *operando* spectroscopic measurements.

Both catalyst powders were characterized electrochemically in liquid electrolyte and under water vapor conditions. Regardless the experimental conditions the Ir@IrO_x demonstrated higher electrochemical activity and lower OER overpotential. The analysis of the cyclic voltammograms recorded on electrochemical oxide revealed the presence of three pairs of anodic and cathodic peaks. The interpretation of the red-ox transitions corresponding to these peaks is under debate. The anodic peak located at 0.95 V vs RHE (Figure 82) is usually assigned to Ir (III) / Ir (IV) red-ox transition[41,49] which involves proton ion intercalation / deintercalation[40,48]. Iridium as an electrochromic system is well known for its color-bleaching cycles corresponding to Ir (III) / Ir (IV) transition observed at ca. 1 V vs RHE[249,250]. The peak observed around the OER onset (superposed to the OER currents at ca. 1.4 V vs RHE) has been attributed to the formation of high oxidation state of iridium (> IV).[40,54] The anodic peak at 1.2 V vs RHE was also attributed to the Ir (III) / Ir (IV) red-ox transition but occurring on different facets[40]. The features observed on the CVs recorded on IrO_2 are less resolved. The curve shown in Panel B of Figure 82 shows a pair of peaks with an anodic peak at 0.85 V vs RHE. This peak is typically related to Ir (III) / Ir (IV) transition, however the proton intercalation associated with it was not confirmed on thermal oxide with rutile structure[51–53]. Moreover, as it was previously mentioned, the theoretical DFT calculations performed for rutile phase RuO_2 have demonstrated low diffusion rate of protons through this structure.[62] Based on the close lattice parameters of rutile Ir and Ru oxides, proton intercalation in IrO_2 structure is questionable. The shift of the anodic/cathodic peaks to more negative potentials observed under 3 mbar water vapor conditions (Figure 85) in comparison to the experiments in liquid electrolyte (Figure 82) is probably related to the decrease of humidity level in the former case. *Birss et al.*[40] proposed the participation of anions in the red-ox transition

associated with the anodic peak located at 0.95 V vs RHE observed in the presence of liquid electrolyte. One should keep in mind, that in the system analyzed under water vapor conditions no free anions are present. This may also lead to the shift of this peak to more negative potentials. However, the main red-ox transition is related to Ir (III) / Ir (IV) red-ox transition observed during the spectroscopic studies discussed further, while the hydration level of these species would be different from the ones, formed in liquid electrolyte.

The analysis of the Tafel slopes performed for the Ir@IrO_x and IrO_2 – based electrodes in the presence of liquid electrolyte revealed the values of ca. 41 and 49 mV dec^{-1}, correspondingly. These values are close to the ones presented in the literature[54,58] where they were interpreted as a proof of the chemical rds[58,76]. However, the slopes obtained on the basis of the results recorded in the NAP-XPS chamber are higher than the ones mentioned above. This change of the Tafel values observed in the experiments under water vapor cannot be completely considered as a change of the reaction mechanism, but is rather related to some other reasons resulting from the decrease of RH level. Thus, the discussion of the OER mechanism based on the obtained Tafel slopes values cannot be done.

Now we can turn to the discussion of the spectroscopic results obtained *operando* on Ir@IrO_x - and IrO_2 - based anodes. During the first OER cycle performed on these electrodes only O K edge spectra were collected under different polarization conditions. After normalization and background subtraction, the spectra (obtained in TEY mode) were fitted using several components (Figure 89 and Figure 88). For IrO_2 anode the experimental spectra clearly show a ca. 530 eV peak and a smaller feature at ca. 528.8 eV, which based on the DFT calculations and in agreement with *Pfeifer et al.*[108] can be attributed to bulk lattice oxygen (labeled as O^{II-}) and to electrophilic O^{I-} species, respectively. Peaks at ~531.0 eV and higher observed on both Ir-based electrodes correspond to various OH species (mostly μ_2-OH, see Figure A 7), and to the background increase due to water and gas-phase oxygen formed during the OER. The analysis of the absorption spectra obtained on electrochemical Ir@IrO_x sample revealed the presence of two low excitation energy peaks at 529.0 and 529.4 eV and the potential dependence of their intensities. While under open circuit potentials the spectra contain only a 529.4 eV peak, the increase of the applied potential (> 1.3V vs DHE) leads to the decreasing of this peak while another, located at 529.0 eV, arises. According to the DFT calculations, the lower excitation energy O K-edge peak of 529.0 eV can be created by deprotonation of OH groups at both cus (coordinatively unsaturated) and bridge position. Thus, we infer that the 529.4 eV peak corresponds to μ_1-OH, which deprotonates at potentials above 1.3 V forming electrophilic oxygen O^{I-} (529.0 eV peak).

In addition to the difference in the low energy peaks behavior observed for Ir@IrO_x and IrO_2 anodes, the analysis of O K edge spectra recorded on the electrochemical oxide did not reveal

the presence of lattice oxygen peak located at 530 eV regardless the applied potential. The analysis of the O1s XP spectra recorded before the spectroscopic measurements also confirms this finding (see Figure 92), whereas in case of IrO_2 anode the lattice oxygen peak is present both in absorption and in the photoemission data.

Moving back to the analysis of potential-dependence of O^{I-} species, we observed that their formation is potential dependent regardless the oxide nature, suggesting that this step as electrochemical. Based on the linear relationship between the current and the O^{I-} peak intensity in case of $Ir@IrO_x$ anode (Figure 91), we suggest the following chemical step of the oxygen molecules formation:

$$2O^{I-} \rightarrow O_{2\,(gas)}, \textit{(Eq. 26)}$$

The observed current is proportional to the amount of oxygen species:

$$i = k\,[O^{I-}], \textit{(Eq. 27)}$$

where *k* is a constant.

The absence of reliable Tafel analysis does not allow us to discuss further the OER mechanism and to define the rate determining step. The fact that the O^{I-} intensity does not level off in the potential region of [1.3; 1.48] V vs DHE applied in our experiments, as one would expect for surface adsorbates, may be tentatively explained by the formation of these species not only on the surface but also in the sub-surface region.

It is interesting that for rutile-type IrO_2 anode the O^{I-} intermediate emerges at potentials below the current rise. While on electrochemical $Ir@IrO_x$ surface the O^{I-} intermediate undergoes fast transformation into molecular oxygen, on thermal oxide further steps seem to be slower. This may be tentatively attributed to the nature of recombination step (Eq. 26), which is likely to require deformation of the oxide structure. Such a deformation may readily occur on the amorphous hydrous oxide but not on the "rigid" structure of the rutile thermal oxide IrO_2. However, one cannot exclude some other steps resulting in the observed changes of the O^{I-} / current correlation on the IrO_2 anode in comparison to an electrochemical oxide.

Based on the results discussed above, we propose the electrophilic O^{I-} species to be an intermediate both on the electrochemical and thermal Ir oxide anodes, its reactivity depending on the oxide nature.

We are moving to the discussion of the role of Ir sites in the oxygen evolution reaction. As it was shown in Chapter 1, one of the open questions concerning iridium red-ox state under the OER conditions is the formation of Ir (V), first proposed by *Kötz et al.*[56] on the basis of *ex-situ* XPS studies and more recently by *Casalongue et al.*[101] and *Minguzzi et al.*[55] using *in-situ* NAP-XPS and XANES, correspondingly.

The analysis of Ir4f XP spectra obtained on electrochemical iridium oxide revealed the presence of three iridium components at the open circuit potential: metallic iridium, Ir (III) and Ir (IV). The increasing of the applied potential leads to a gradual diminishing of Ir (III) content, while the Ir (IV) amount is increasing (Figure 94). This red-ox transition corresponds to the anodic peak observed in the CV at ca. 0.5 V vs DHE (Panel A of Figure 85). This observation supports previous electrochemical studies,[41,46,94,248,251] while here the Ir (III) / Ir (IV) transition is confirmed by means of *in-situ* XPS measurements. According to our results, the potential cycling leads to the accumulation of Ir (IV) species on the surface, as its composition was not fully restored after the OER cycle. For the OER region, however, no additional components related to other high oxidation state of iridium (higher than IV) were observed.

Tuning the photon energy (see Figure 95) did not reveal drastic changes in metallic and Ir (III), Ir (IV) contents. Thus, we cannot support the idea of core-shell structure of $Ir@IrO_x$ particles proposed earlier for similar systems[252]. The absence of the differences with the analysis depth of XPS can be then interpreted by a formation of a porous oxide IrO_x layer with an effective thickness of ca. 0.5 nm (based on simulation of the XP spectra by means of SESSA software), while some area of this layer can be thinner or thicker.

Considering all of the above, we conclude that $Ir@IrO_x$ catalyst, stabilized by potential cycling, consists of a metal covered by an Ir oxide/hydroxide layer. The composition of this oxide strongly depends on the applied potential and changes from a mixed Ir (III) / Ir (IV) oxide/hydroxide below the OER onset to an Ir (IV) oxide above the OER onset, which further persists in the OER potential interval.

Regarding an intriguing question related to the formation of Ir (V) or other high oxidation states of iridium under the OER conditions, we did not observe appearance of any additional peaks even at lower photon energy of 390 eV on $Ir@IrO_x$ anode. Thus, the second anodic peak observed in the CV prior to the OER region at ca. 1.2 – 1.3 V (vs DHE) can be related to the OH / O^{I-} transition discussed earlier rather than to the further oxidation of iridium.

Now we can move to the potential evolution of IrO_2 electrode initially containing the Ir (IV) species. In contrast to the electrochemical oxide, we confirmed the stability of IrO_2 thermal oxide regardless the applied potential and the photon energy used for the measurements (Figure 96). The anodic peak observed under water vapor conditions at ca. 1.0 V vs DHE can be also related to the formation of O^{I-} species analogous to the $Ir@IrO_x$. Neither absorption nor photoemission spectroscopic measurements revealed red-ox transitions in the potential of the second pair of anodic/cathodic peaks resolved on the CV curve recorded on IrO_2 anode in the NAP-XPS chamber with an anodic peak at ca. 0.5 V vs DHE. By analogy with the electrochemical oxide $Ir@IrO_x$ this red-ox transition may be tentatively attributed to Ir (III) / Ir (IV) transition.

However, considering the low intensity of the peaks for the thermal oxide we suggest that this transformation probably takes place only at certain sites, probably defects, resulting in a small contribution of the Ir (III) species to the Ir4f XP spectra. This is in contrast to the behavior of the electrochemical oxide, where significant contribution of the Ir (III) species to the Ir4f XP spectra suggests that this red-ox transition occurs not only on the surface but likely also in the sub-surface, which agrees with the literature data. Furthermore, this work does not support formation of Ir species in oxidation states different from IV under the OER conditions either on thermal or on electrochemical oxide.

Based on the results of absorption and photoemission spectroscopies obtained *operando* on Ir-based anodes, we conclude that the OER mechanism occurs through the anion red-ox transition rather than the cation ones and does not depend on the oxide nature. Regarding the analysis of the O K edge spectra under different polarization conditions, we suggest O^{I-} species as an OER intermediate. Moreover, the linear correlation between the O^{I-} intensity and the OER current observed on Ir@IrO_x anode allows us to propose a tentative OER mechanism. We suggest that O^{I-} species are formed in an electrochemical step, which is followed by a chemical step of molecular oxygen formation. The latter was tentatively considered as the recombination of O^{I-} species. We also suggest the formation of O^{I-} species both on the surface and in the sub-surface regions.

5.5. Conclusions of Chapter 5

In this Chapter, we performed a comparative *operando* study using near-ambient pressure photoelectron spectroscopy and soft X-ray absorption spectroscopy under the reaction conditions for electrochemically ($Ir@IrO_x$) and thermally synthesized (IrO_2) iridium oxides, the two types of Ir anodes, which are widely applied for PEM water electrolysis. Red-ox transition between Ir (IV) and Ir (III) is clearly observed for the electrochemical $Ir@IrO_x$ at potentials below ca. 1.0 V, while in the potential interval of the oxygen evolution Ir is present in the form of Ir (IV) in both materials. Thus, our results do not support the Ir cation red-ox mechanism proposed in some previous publications. The analysis of the O K edge spectra under the reaction conditions supported by DFT calculations reveals formation of electrophilic oxygen O^{I-} as an OER intermediate through an electrochemical step and confirms oxygen anion red-ox mechanism, independent of the type (electrochemical vs. thermal) oxide. The formation of molecular oxygen is suggested to occur through a chemical step. The constant increasing of the O^{I-} intensity observed on both anodes in the analyzed potential intervals was attributed to the formation of these species not only on the surface but also in the sub-surface region. The higher electrocatalytic activity of the electrochemical vs. thermal oxide is not related to the higher concentration of the O^{I-} intermediate but rather to its higher reactivity, which is revealed by the correlation between the O^{I-} intensity and the OER current and may be explained by the more flexible structure of electrochemical hydrous oxide compared to the thermal oxide. The analysis of the iridium photoemission spectra of different analytical depth recorded on $Ir@IrO_x$ spectra under different polarization conditions did not confirm the formation of the core-shell structure of the particles but rather the presence of a porous oxide layer.

The results discussed herein contribute to the fundamental understanding of the processes taking place on iridium-based electrodes.

Chapter 6. Supported Iridium-based Electrocatalyst: SMSI studies

6.1. Introduction

Highly active and stable Ir-based electrocatalysts are required for electrocatalysis of the oxygen evolution reaction in PEM electrolyzers. Various strategies are proposed for reducing utilization of scarce and expensive Ir in the anode catalyst layers. One of the promising approaches relies on the development of supported iridium catalysts, which is the topic of the current Chapter.

Antimony-doped tin oxide (ATO) has attracted significant attention as a promising support material due its high electronic conductivity and high electrochemical stability. Moreover, iridium catalysts supported on ATO have demonstrated an improvement of the activity-stability properties in comparison to unsupported iridium. In the literature, this enhancement has been tentatively attributed to the strong metal-support interaction (SMSI), which is known in heterogeneous catalysis and studied for other catalyst systems[134,135,253]. However, the role of the support in Ir/ATO system is not fully understood yet.

Here we present a comparative *in-situ* study of unsupported Ir-, ATO- and Ir/ATO-based anode catalysts by means of NAP-XPS under the oxygen evolution reaction conditions. The measurements were performed at TEMPO beamline of SOLEIL synchrotron (Paris, France). The data interpretation was also complemented by the modeling of the XP spectra using the SESSA software. The *in-situ* measurements were complemented by microscopy measurements performed by the Electron Microscopy group of the University of Antwerp (Belgium). The ATO support material was provided by MINES ParisTech (France), while the catalysts have been synthesized and characterized in the presence of liquid electrolyte at DLR (Stuttgart, Germany)[132].

The objective of these studies is to unveil the role of the ATO support in the improved performance of Ir/ATO catalysts. In order to achieve this, we performed the analysis of the:

- elemental distribution (Ir, Sn, Sb) by means of *ex-situ* STEM-EDX mapping;
- atomic ratio of the elements presented on the anode surfaces estimated on the basis of the measured photoemission spectra *in-situ* under different polarization conditions;
- red-ox state of iridium and its dependence on the presence of the support;
- electrochemical stability of ATO support under the OER conditions;
- potential-induced changes in the width and binding energy position of tin core-level spectra recorded at different photon energies.

A manuscript containing the data presented in this Chapter is under preparation.

6.2. Materials and their Characterization

SnO_2:Sb support has been synthesized by a sol-gel method from metal alkoxide precursors at MINES ParisTech (France). Iridium nanoparticles were obtained by direct reduction of iridium chloride in the presence of sodium borhydride. Ir/ATO catalyst was then prepared by deposition of iridium catalysts on SnO_2:Sb aerogel. The synthesis of Ir-based catalyst powders was done at DLR (Germany). For details, see Chapter 2.

Ir-based catalysts have been analyzed in 0.05 M H_2SO_4 using the RDE and chronopotentiometry techniques by L. Wang (DLR) and the results are shown in Figure 97. Prior to the measurements, the unsupported Ir and Ir/ATO-based electrodes have been electrochemically oxidized by potential cycling in the region from 0 V to 1.6 V vs RHE (10 cycles). The obtained results of the OER activity and stability (at current density of 1 mA cm^{-2}) demonstrate the improved properties of ATO-supported iridium catalyst in comparison to the unsupported counterpart observed previously in the literature and attributed to the SMSI.[75,132] The analysis of the Tafel slopes based on the cyclic voltammograms recorded at 5 mV s^{-1} scan rate did not reveal significant differences for unsupported Ir and Ir/ATO, which were estimated as 44 and 42 mV dec^{-1}, correspondingly.

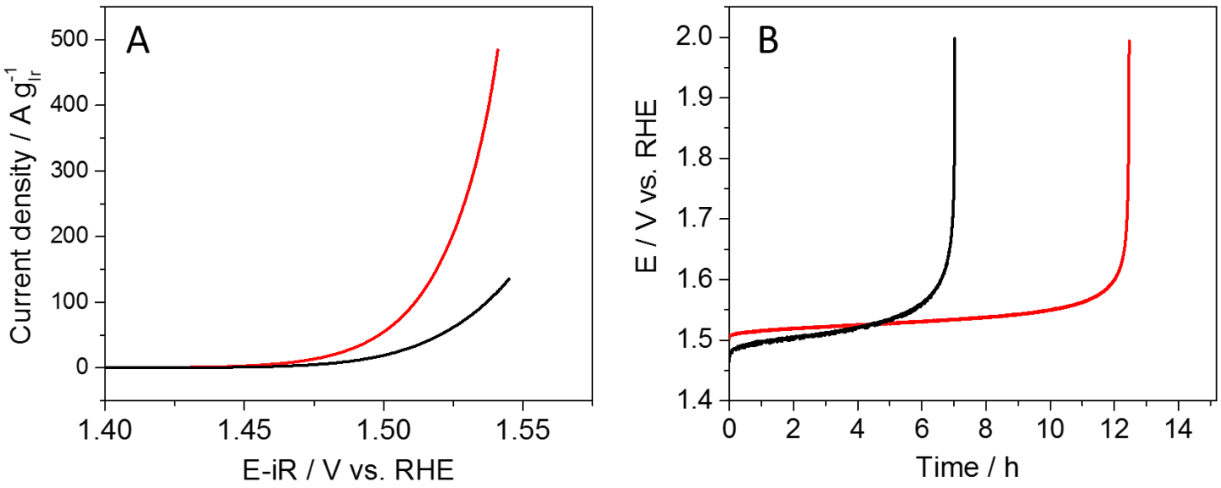

Figure 97. Panel A: OER activity of unsupported Ir (black) and Ir/ATO (red) catalysts measured in N_2-saturated 0.05 M H_2SO_4, scan rate 5 mV s^{-1}, rotation rate 1600 rpm. Panel B: Chronopotentiometry results on unsupported Ir (black) and Ir/ATO (red) anodes at current density of 1 mA cm^{-2} in N_2-saturated 0.05 M H_2SO_4. Iridium loading on electrodes: 60 μg cm^{-2} for unsupported Ir and 17 μg cm^{-2} for Ir/ATO. Temperature 25°C. The measurements were performed by L. Wang (DLR).[132]

The microscopic analysis coupled with EDX mapping was performed on the pristine catalysts (ATO and Ir/ATO) scratched from the corresponding MEAs as well as post-mortem

samples after the NAP-XPS measurements discussed further. The data were obtained and analyzed by Dr. M. Batuk under supervision of Prof. J. Hadermann (University of Antwerp, Belgium).

The analysis of the TEM images of the pristine ATO sample (not presented) showed the presence of agglomerated crystals of 3 – 13 nm with a mean diameter of 7.3 ± 1.7 nm. Ir/ATO sample consists of ATO crystals of the same size, while iridium nanoparticles are highly agglomerated and unevenly distributed over ATO. The diameter of Ir NPs is equal to ca. 1.5 – 3.0 nm. The typical images of pristine Ir-ATO catalyst powder are shown in *Li et al.*[132] while the HAADF-STEM images obtained on the post-mortem Ir/ATO samples are provided in Figure 98. Due to a higher atomic number of Ir in comparison to Sn and Sb, iridium nanoparticles appear brighter on the image. The EDX mapping performed on the samples reveled the uniform Sn/Sb distribution close to nominal (Sn : Sb = 10 : 1). The Ir/Sn ratio was estimated as 13 : 1. The post-mortem microscopic analysis of Ir/ATO catalysts did not show any changes of the particles size either of ATO or Ir particles (see Figure 98). The elemental distributions were not affected by the potential cycling either. However, the presence of detached iridium particles was observed on the post-mortem sample (Panel D of Figure A 12). Elemental mapping was performed in order to detect eventual segregation of Sn and/or Sb in the vicinity of Ir nanoparticles. However, elemental maps presented in Figure A 12 did not reveal such segregation. It should be noted however, that the EDX analysis of the above mentioned elements has some limitations due to the overlapping of the EDX spectra (3.44 keV and 3.60 keV for Sn and Sb, correspondingly). The EELS analysis cannot be applied to this system either (Sn, Sb and O have close edge positions at 484.8 eV, 527 eV and 532 eV, respectively).

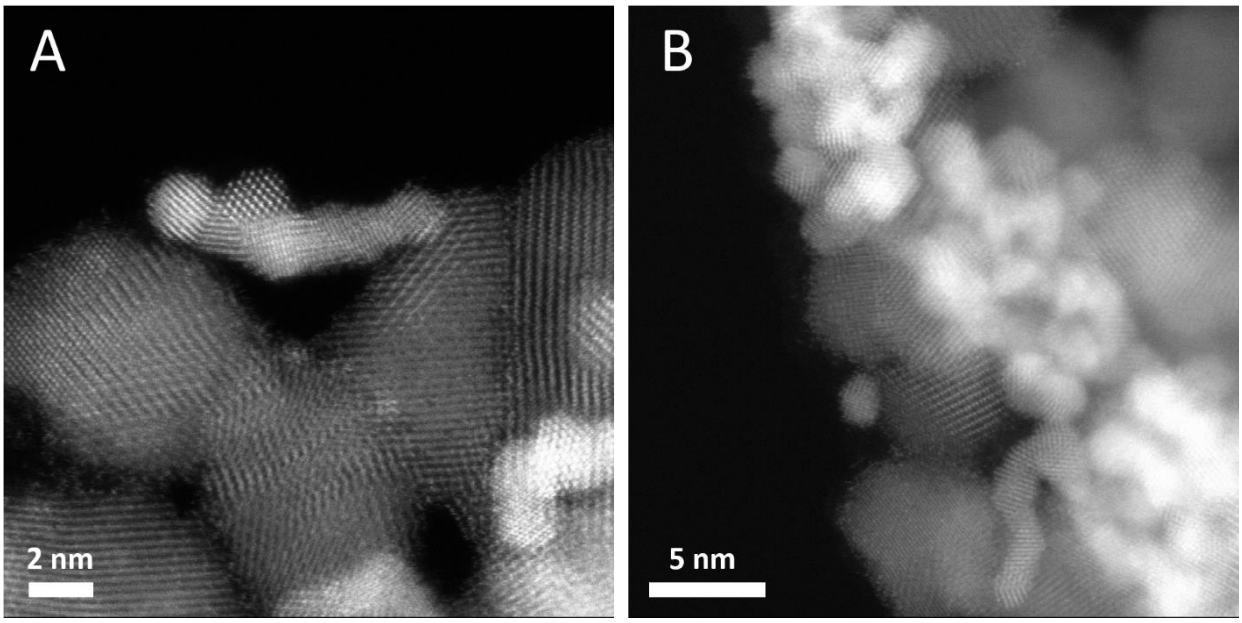

Figure 98. HAADF-STEM images of Ir/SnO_2:Sb powder scratched from the WE side of the MEAs after in-situ measurements. Ir particles appear brighter on the image. The images were obtained by Dr. M. Batuk (University of Antwerp).

6.3. Improvement of the Conductivity of ATO-based catalytic layers

Wide application of doped tin oxides as support materials for the OER is related to its high conductivity and stability under the reaction conditions. The undoped tin oxide possesses conductivity of ca. $1.3 \div 1.9 \cdot 10^{-5}$ S cm^{-1}, while its doping with 10% of antimony (applied in this work) leads to the value of 0.8 S cm^{-1} according to the work of *Ozouf*[128]. For comparison, the conductivity of unsupported IrO_2 nanoparticles with a mean diameter of ca. 6 nm was estimated as 4.9 S cm^{-1}.[254] While iridium oxide – based MEAs were successfully studied by means of NAP-XPS (see Chapters 4, 5), the analogous studies of the ATO supported catalyst revealed problems related to an insufficient conductivity in the catalyst layer.

The analysis of the MEA resistance performed in the NAP-XPS chamber by means of EIS revealed quite high values of 2 600 Ohm under 3 mbar water vapor for an Ir/ATO-based sample, meanwhile the unsupported Ir-based MEAs show the resistance of 60 - 80 Ohm depending on the sample.

The configuration of the electrochemical cell used in this work (see Figure 27) is made in such a way, that the WE containing Ir/ATO powder is grounded to the spectrometer via a current collector, thus the Fermi level of the elements which are electrically connected to the current collector (Ir, Sn, Sb) is supposed to be aligned to the Fermi level of the spectrometer. This means that their XP spectra should not be shifted under polarization. On the contrary, the positions of the XP peaks originating from the elements residing in the membrane (C, F, S) shift in the opposite direction from the polarization bias[255]. The analysis of the binding energy shifts of the corresponding XPS peaks recorded using a MEA with an Ir/ATO anode under polarization is shown in Figure 99 (panel A). One may observe a clear shift for all the elements present on the MEA surface with the potential bias. The fact that the peaks originating from the WE (Ir, Sn, Sb) and those originating from the electrolyte (C, F, S) show similar dependence on the cell voltage, points out at a partial/complete disconnection of the catalyst particles from the current collector. The shape of the XP spectra obtained on this low conductive MEA was not influenced by the potential, see the example of Ir4f spectra shown in Figure A 16.

In order to improve the electronic conductivity of the anode catalyst layer we added the graphene powder into the catalyst ink sprayed on the membrane[256]. Panels A of Figure 101 and Figure 99 show the corresponding changes observed in the electrochemical response and XP peak positions in the presence of graphene. The MEA resistance of the graphene-added (50% wt.) Ir/ATO and ATO based MEAs was 200 Ohm and 160 Ohm, correspondingly. The absence of

potential-induced shifts of the BE for Ir4f, Sn3d XP spectra confirms the proper interconnection between the catalyst particles and the current collector. The *in-situ* NAP-XPS measurements presented in the next sections were performed on graphene-containing samples, however for simplicity we will refer to these anodes as Ir/ATO and ATO without mentioning the graphene presence.

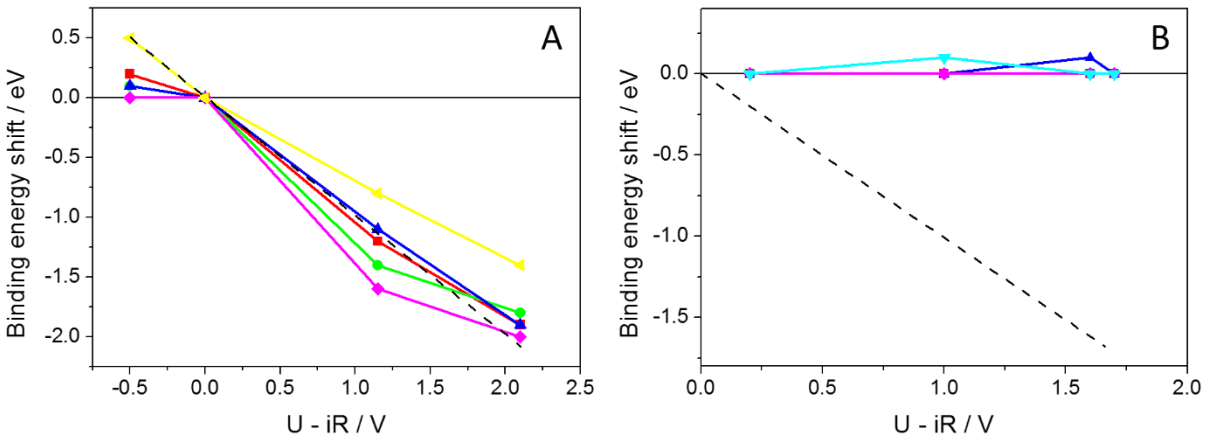

Figure 99. Binding energy shifts relative to the initial potential for Ir4f (red), Sb3d (green), Sn3d (blue), C1s (magenta), Si2p (yellow), O1s (cyan) obtained from the analysis of the NAP-XP spectra measured on Ir/ATO (a) and Ir/ATO + graphene (b) samples. Dotted line corresponds to a 1:1 correlation between the Ohmic-drop corrected voltage and the BE shifts. The kinetic energy of the emitted electrons was ca. 530 eV. Catalyst loading (Ir) 0.5 mg cm^{-2}.

6.4. *Operando* Photoemission Studies

6.4.1. Electrochemical Response in NAP-XPS Chamber

The cyclic voltammogram of Ir/ATO-based anode is shown in Panel A of Figure 101. OER onset observed in the two-electrode cell is close to the value measured in a three-electrode cell vs RHE, suggesting that the counter electrode may be considered as a DHE. This, however, was not the case for the unsupported Ir catalyst integrated in a MEA and measured at TEMPO (SOLEIL synchrotron). Panel A Figure 100 shows the current-potential curve recorded on unsupported Ir – based anodes. One may notice that the potential values are shifted towards negative potentials (ca. 350 mV in comparison to the RHE scale). Previously we demonstrated that CE in our MEA configuration plays a role of a pseudo-reference electrode as dynamic hydrogen electrode (see Figure 38 and corresponding discussion). However, for the unsupported Ir sample measured at TEMPO that was not the case, which may be related to the MEA preparation. Most probably, the amount of Pt/C catalyst on the backward side of the MEA was not high enough in order to serve as a DHE (otherwise this might be related to the MEA fixing). While the potential scale is shifted, the shape of the CV allowed us to define the key potentials at which we recorded the corresponding photoemission spectra: -0.25 V; 0.85 V; 1.05 V and 1.4 V for the unsupported Ir sample. The first two potentials correspond to the states before and after the anodic peak A_1 at ca. 0.25 V observed on the CV (Panel A Figure 100). The OER onset corresponds to 1.05 V, while 1.4 V lies in the oxygen evolution reaction region. The evolution of oxygen was controlled by the on-line mass spectrometry (the data are not shown). In case of Ir/ATO anode (Panel A of Figure 101), the intensity of the peak A_1 is much smaller (at ca. 0.8 V vs DHE) and this peak can be hardly observed on the voltammogram. For Ir/ATO, the following four potentials were applied during the spectra collecting: 0.2 V; 1.0 V; 1.6 V; 1.7 V vs DHE. The ATO-based electrode studies were performed under the same potential values. The CV recorded on Ir-free sample is shown in Figure A 13.

Before *in-situ* NAP-XPS studies, the electrode was subjected to potential cycling in the potential region prior to the OER onset. In case of Ir/ATO and ATO-based anodes, the region was [0.2; 1.0] V vs DHE, while for unsupported Ir – [-0.25; 0.95] V. The cathodic limit of 0.2 V for ATO-based samples was chosen in order to avoid the reduction of the support leading to its dissolution[120]. The chronoamperograms recorded during the photoemission spectra collecting for unsupported Ir, Ir/ATO and ATO – based anodes are shown in Panel B of Figure 100, Figure 101 and Figure A 13, respectively. The decreasing of the currents observed at 1.7 V on Ir/ATO sample in comparison to 1.6 V can be related to the corrosion of the graphene added in the catalyst layer in order to improve its conductivity (see the previous section). One may also notice the drop of the

current with time at 1.6 V, which may also be related to the graphene degradation in the anodic region. For the unsupported Ir sample, the slight decrease of the currents with time in the OER region (1.05 V and 1.4 V) can be also observed, however this drop is less pronounced.

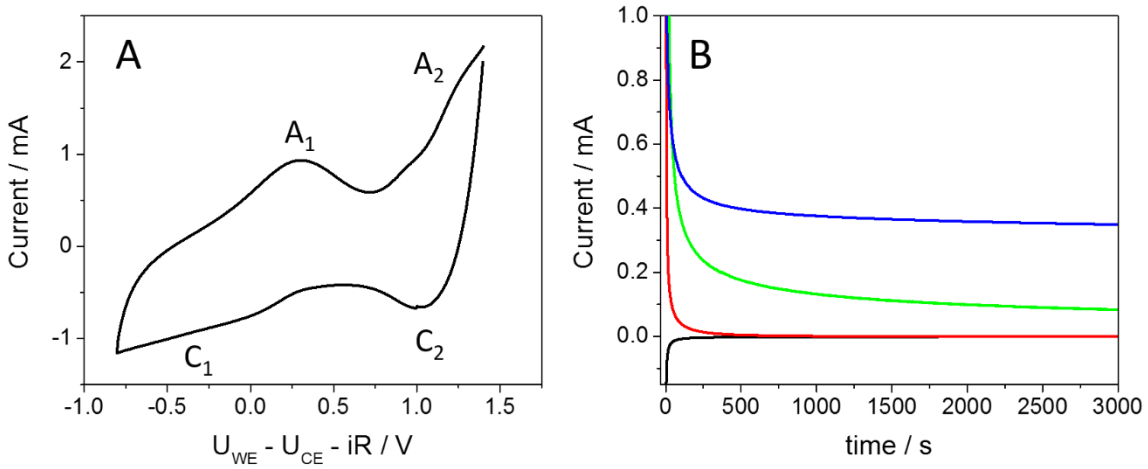

Figure 100. Cyclic voltammogram (A) and chronoamperograms (B) recorded on unsupported iridium anode in the NAP-XPS chamber under 3 mbar water vapor. Scan rate 50 mV s^{-1}. Applied potential for the CAs: -0.25 V (black); 0.85 V (red); 1.05 V (green); 1.40 V (blue). The potentials are Ohmic drop corrected. Catalyst loading (Ir) 0.1 mg cm^{-2}.

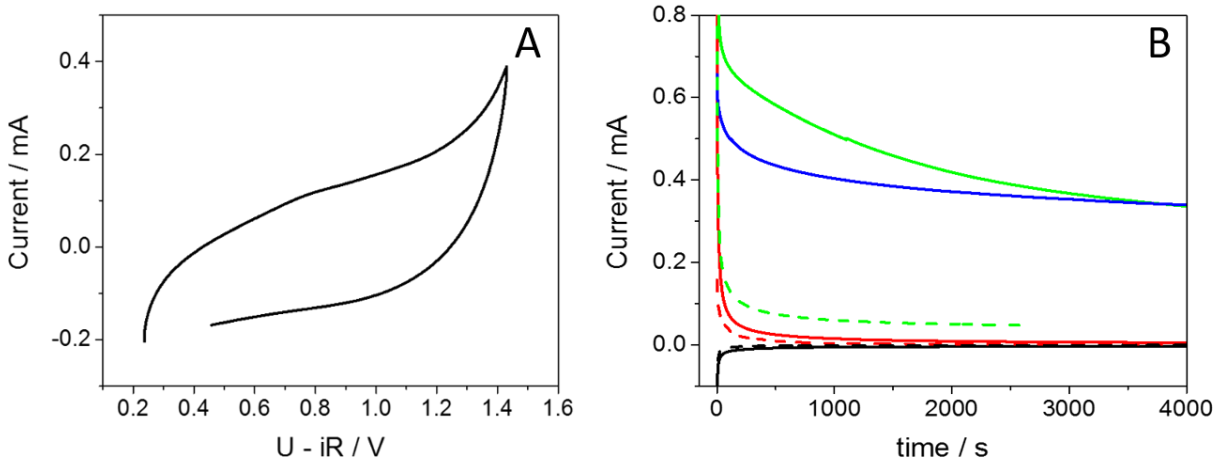

Figure 101. Panel A: CV recorded on Ir/ATO anode of the corresponding MEAs in the NAP-XPS chamber under 3 mbar water vapor. Scan rate 20 mV s^{-1}. Panel B: chronoamperograms recorded on Ir/ATO (solid lines) and ATO (dashed lines) in the NAP-XPS chamber under 3 mbar water vapor and different polarization: 0.2 V (black); 1.0 V (red); 1.6 V (green); 1.7 V (blue). The potentials are Ohmic drop corrected.Catalyst loading (Ir) 0.5 mg cm^{-2}.

6.4.2. Sn3d XP Spectra Analysis

As it was mentioned in Chapter 1, tin oxide is known to be non-stoichiometric and is considered as a mix of Sn (II) and Sn (IV) species, the ratio between them depending on various

factors, such as polarization, doping level etc. The binding energy of Sn3d peak reported in the literature for these two oxidation states of tin revealed their close positions: 485.6eV – 486.9 eV and 486.6eV – 487.5 eV for SnO and SnO_2, respectively[257]. While the valence band spectra may provide better information on the oxidation state of tin, the presence of the gas phase during the NAP-XPS measurements complicates the analysis of the VB region.

Figure 102 and Figure 103 show the Sn3d XP spectra recorded on ATO- and Ir/ATO-based anodes, respectively, under different polarization conditions and kinetic energies. Since changes in the Sn $3d_{5/2}$ peak width could reveal variation of the Sn (II) / Sn (IV) ratio, in Figure 104 we show the FWHM values estimated from the Sn $3d_{5/2}$ XP peak recorded on ATO – and Ir/ATO – based anodes as a function of the applied potential. It should be noted, that an increase of the photon energy leads to the broadening of the peaks due to the instrumentation issues. From the data presented in Figure 104, one may see that neither the application of the potential nor the presence of iridium nanoparticles supported on ATO lead to changes in the width of Sn $3d_{5/2}$ peak, i.e. in the oxidation state(s) of the tin oxide species. The Sn3d XP spectra intensity recorded at 390 eV on Ir/ATO anode (Panel A of Figure 103) at low potentials is quite low. Due to the difficulties related to the FWHM estimation, these points are not shown in the panel B of Figure 104.

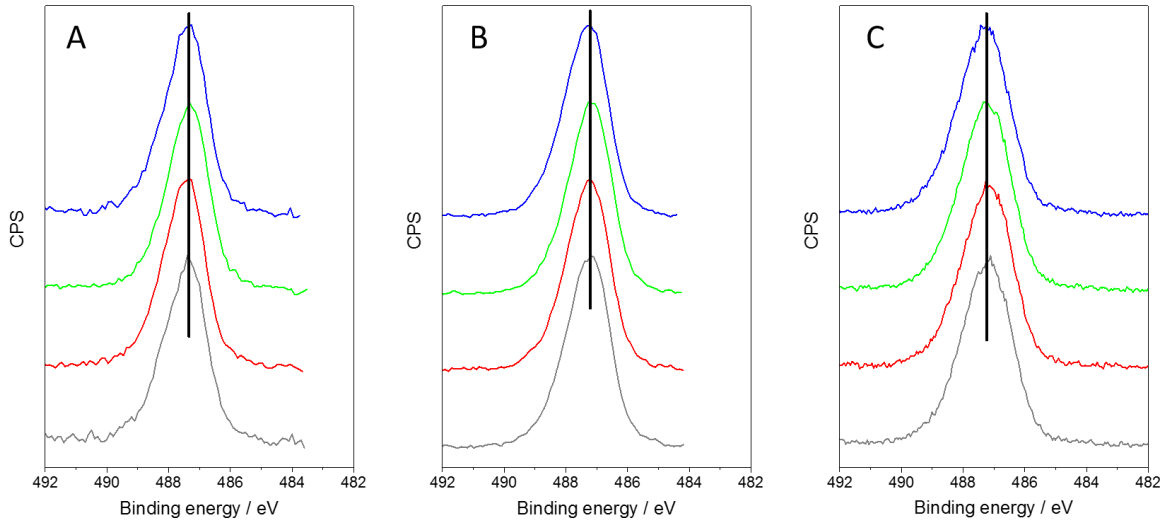

Figure 102. Sn3d$_{5/2}$ XP spectra recorded on ATO-based MEA under 3 mbar water vapor and different polarization: 0.2 V (grey); 1.0 V (red); 1.6 V (green); 1.7 V (blue). The potential values are Ohmic drop corrected. Kinetic energies of the emitted electrons: 390 eV (Panel A); 530 eV (Panel B); 810 eV (Panel C). The spectra intensities are normalized.

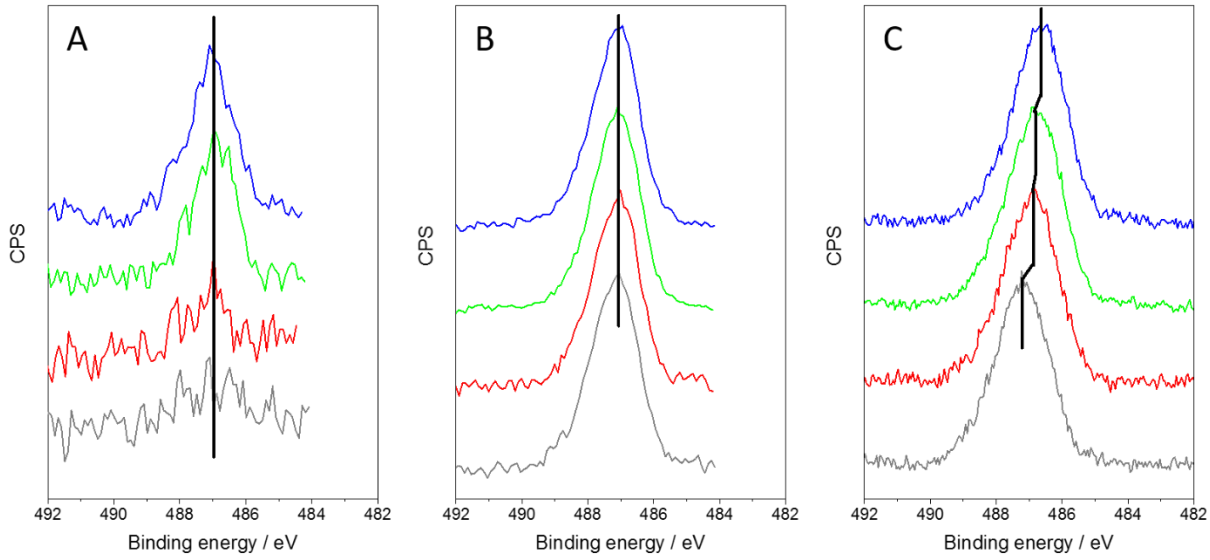

Figure 103. $Sn3d_{5/2}$ XP spectra recorded on Ir/ATO-based MEA under 3 mbar water vapor and different polarization: 0.2 V (grey); 1.0 V (red); 1.6 V (green); 1.7 V (blue). The potential values are Ohmic drop corrected. Kinetic energies of the emitted electrons: 390 eV (Panel A); 530 eV (Panel B); 810 eV (Panel C).

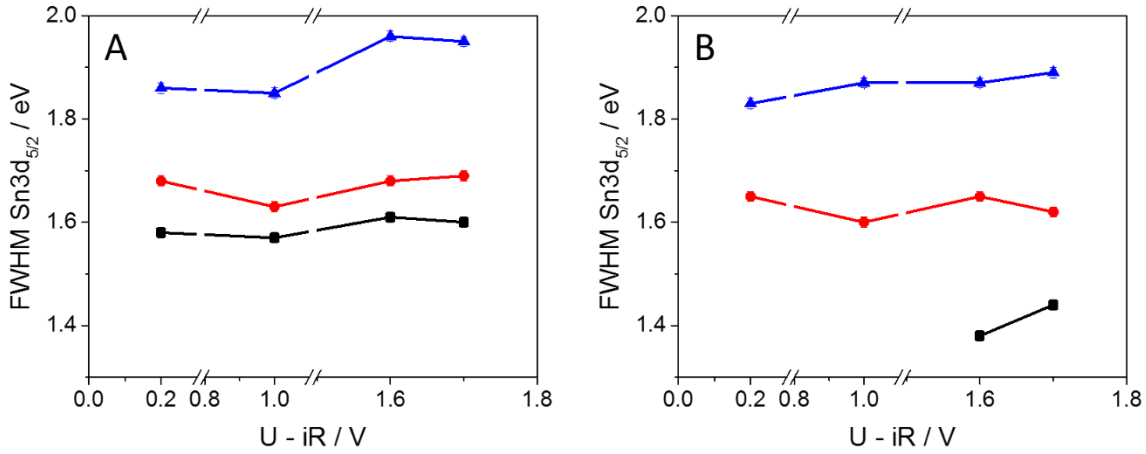

Figure 104. Full width at half maximum of $Sn3d_{5/2}$ XPS peak recorded on ATO (A) and Ir/ATO (B) anodes under different polarization conditions and the following kinetic energies of the emitted electrons: 390 eV (black); 530 eV (red); 810 eV (blue).

While the peak width stayed constant throughout the experiment, one may clearly observe potential-induced shift of the binding energy position for the Sn3d doublet recorded at kinetic energy of 810 eV for Ir/ATO sample. The BE positions of the $Sn3d_{5/2}$ peak collected on both samples are plotted in Figure 105. The changes of the binding energy position of Sn3d XPS peaks might be due to the variations in the oxidation state of tin oxide; the charge transfer effects taking place at the Ir/ATO interface; the doping agent (antimony) surface/sub-surface distribution, as discussed in more detail in Section 6.5 of this Chapter.

The analysis of the Sn3d peak position obtained on pure ATO did not reveal any noticeable shifts with the potential (panel A, Figure 105). It should be also noted that these BE values are higher than the ones reported in the literature for SnO_2. The shift to higher BE can be explained by the antimony doping resulted in the changes of the band gap. Similar values of 487.4 – 487.6 eV have been previously observed for Sb-doped SnO_2.[258,259]

Panel B of Figure 105 shows the evolution of the $Sn3d_{5/2}$ BE recorded on Ir/ATO anode. While the peaks recorded at 530 eV kinetic energy are not influenced by the changes of the applied potential, one may see a consistent decay of the $Sn3d_{5/2}$ peak position with the increasing of the potential for the spectra acquired at 810 eV. The BE shift for semiconductors may be related to different effects taking place at their surfaces, what will be discussed later. It is interesting to note, that the BE energy of $Sn3d_{5/2}$ peak (486.6 eV) recorded under the OER conditions (U – iR = 1.6 and 1.7 V) corresponds to the values observed in the literature for the undoped SnO_2.

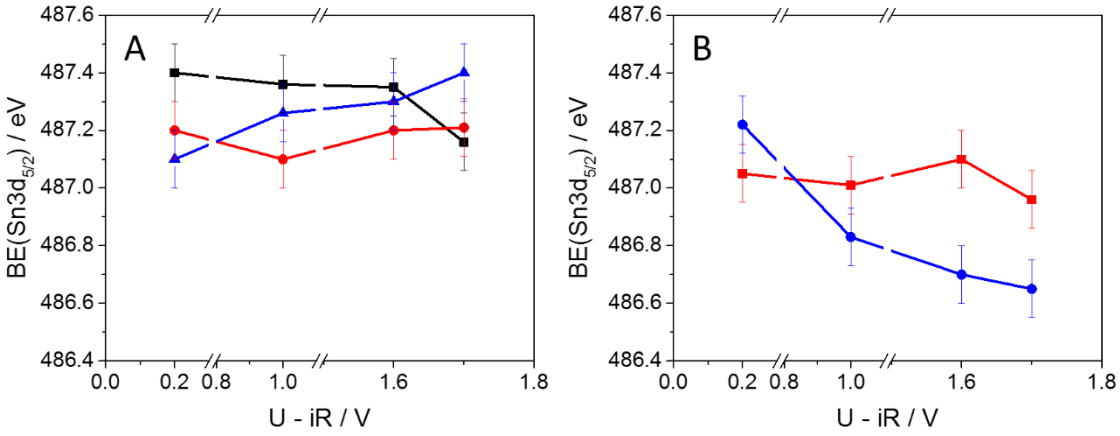

Figure 105. Potential-induced changes of the binding energy position of $Sn3d_{5/2}$ XPS peaks recorded on ATO (A) and Ir/ATO (B) anodes under 3 mbar water vapor under different polarization conditions and the following kinetic energies: 390 eV (black); 530 eV (red); 810 eV (blue).

6.4.3. Evolution of Ir/Sn Ratio

According to the literature the improved activity/stability properties of supported catalysts was interpreted based on the concept of SMSI discussed by *Tauster et al.*[134,135] One of the consequences of this interaction can be the partial or complete encapsulation of the metallic particles[136,137]. The presence of such a layer of the support may explain higher stability of the catalyst[138].

In order to detect eventual (back) spillover of the support species under applied potential, we analyzed the evolution of the Sn/Ir atomic ratio under different polarization conditions. The values were estimated for three analytical depths of 1.9 nm, 2.3 nm, 3.6 nm calculated as three IMFP estimated for metallic iridium (see Table 18). The error bars were estimated based on the

quality of the XP spectra (see the example of Sn3d XP spectra in Figure 103). E.g. low contribution of Sn-based species at low kinetic energy of the emitted electrons of 390 eV leads to rather big errors in the estimation of the elemental atomic ratio.

The increasing of the applied potential leads to an increase of the Sn/Ir atomic ratio, clearly observed at KEs of 390 eV and 530 eV. It is interesting to note, that Sn/Ir ratio is potential-independent for KE of 810 eV and the values obtained at the cell voltage of 0.2 V at 530 eV and 810 eV are very close.

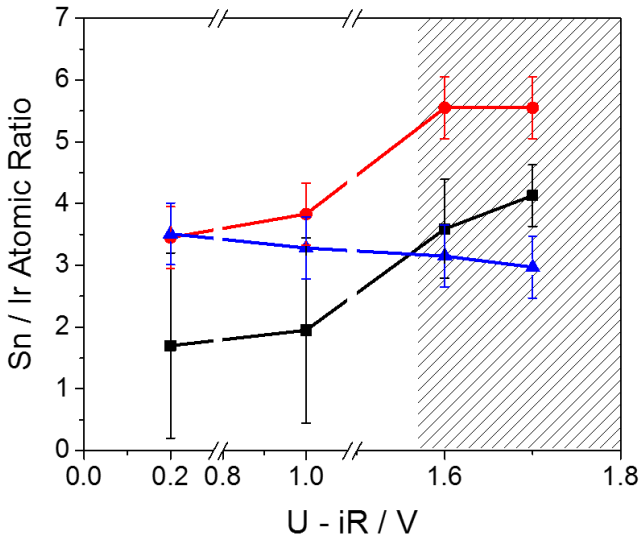

Figure 106. Sn/Ir atomic ratio estimated on the basis of the XP spectra obtained on Ir/ATO anode under 3 mbar water vapor under different polarization conditions and at the kinetic energy of the emitted electrons of 390 eV (black); 530 eV (red); 810 eV (blue). The error bars were estimated from the quality of the corresponding spectra by changing the background.

Table 18. Inelastic mean free path calculated for Ir and IrO_2 based on TPP2M formula[197].

Kinetic Energy of the Emitted Photoelectrons / eV	**IMFP / Å**	
	Metallic Ir	**IrO_2**
390	6.4	11.6
530	7.7	14.5
810	10.3	19.9

In order to reproduce these potential-induced effects and propose a possible model of the surface modification under polarization, we performed modeling of Ir4f and Sn3d XP spectra for different configurations available in SESSA software. The scheme of the morphologies used for

the calculations as well as the parameters used for the simulations are presented in Chapter 2 (Figure 45).

The increasing of Sn/Ir ratio under potential could be due to encapsulation of iridium nanoparticles by ATO. The first model used for the estimation of photoemission peak intensities was a "layered spheres" morphology. As it was shown in Panel B of Figure 45, iridium nanoparticles of various radii were placed on tin oxide substrate and covered by a tin oxide shell of different thickness. By changing the model parameters, it was possible to reproduce two effects observed experimentally: the increasing of Sn/Ir ratio at 530 eV and their constant values at 810 eV (see the example of the calculated results in Table A 7 of the Appendix). However, by changing the calculation settings, the model is not able to get similar Sn/Ir ratio at 530 eV and 810 eV observed at OCP.

The second possible explanation of the observed ratio could be the potential-induced changes in the iridium particles size. For this, we used an "islands" morphology (Panel C of Figure 45), where the dimensions of the parallelepipeds were varied, while their volume was kept constant. Some of the results obtained by this model are shown in Table A 8. While the Sn/Ir ratio was not influenced by the kinetic energy for the initial configuration, the changing of the particles height (here it is parameter *c*) led to a simultaneous increase of the ratio for both energies. Moreover, the growth observed at kinetic energy of 810 eV was much more pronounced, which disagrees with the experiment.

The last model used for the estimation of Sn/Ir ratio was intended to reproduce a partial encapsulation of iridium nanoparticles. While the SESSA software does not offer such a morphology, we used a "spheres" morphology where iridium nanoparticles of 2 nm diameter were located on the tin oxide support (Panel D of Figure 45). For this model, we varied the height of iridium particles protruding above the substrate. The data obtained for this morphology are shown in Table A 9 and the estimated Sn/Ir ratio reproduced both the independence of the Ir/Sn for the kinetic energy of 810 eV and the increase of this ratio for KE of 530 eV observed experimentally, suggesting that partial encapsulation of iridium particles might be responsible for the observed behavior.

6.4.4. Influence of the Electrode Potential on the Oxidation State of Iridium

In order to unveil the influence of support on the surface state of iridium, we analyzed the Ir4f XP spectra recorded on unsupported Ir – and Ir/ATO – based MEAs under the same

experimental conditions. Due to the shift of the potential scale for the unsupported iridium sample compared to the RHE scale, the comparison of the potentials was done based on the characteristic features of the CVs recorded for these anodes. The first measurement was taken at potentials of -0.25 V and 0.20 V for unsupported Ir and Ir/ATO, respectively, corresponding to the potential interval below anodic peak A_1 observed on both voltammograms. The second potential, 0.85 V and 1.00 V, correspondingly, represented the surface state above peak A_1. Finally, the last two measurement points, 1.05, 1.4 V for Ir and 1.6, 1.7 V for Ir/ATO, correspond to the OER region.

Figure 107 shows the Ir4f XP spectra recorded on two anodes below the anodic peak A_1, i.e. -0.25 V for unsupported Ir and 0.20 V for Ir/ATO, and three photon energies representing different analytical depth (see Table 18). The fitting procedure of Ir4f XP spectra as well as the applied parameters have been discussed in Chapter 2. Briefly, the spectra were deconvoluted using 5 doublets corresponding to metallic iridium, Ir (IV) and its satellite; Ir (III) and its satellite.

The analysis of Ir4f spectra recorded on unsupported iridium revealed the presence of all three components regardless the kinetic energy. On the contrary, for supported Ir nanoparticles no traces of Ir (III) species were observed. Moreover, the metal contribution for supported Ir/ATO was noticeably higher than for unsupported particles. The apparent thickness of the oxide layer estimated on the basis of the modeling (see Chapter 2) was equal to 0.3 nm and < 0.1 nm (at the potentials below the anodic peak A_1) in case of unsupported and supported Ir, correspondingly (the results of the modeling are shown in Figure A 15 of the Appendix). Turning back to the unsupported Ir, the results obtained under different photon energies show that the oxide layer has a porous structure rather than core-shell, whereby Ir (IV) and Ir (III) are intermixed. The data presented in the previous Chapter 5 obtained by *in-situ* NAP-XPS measurements of Ir@IrO_x anode at ISISS (BESSY II synchrotron) support the idea of a porous oxide layer formed electrochemically under the operation conditions.

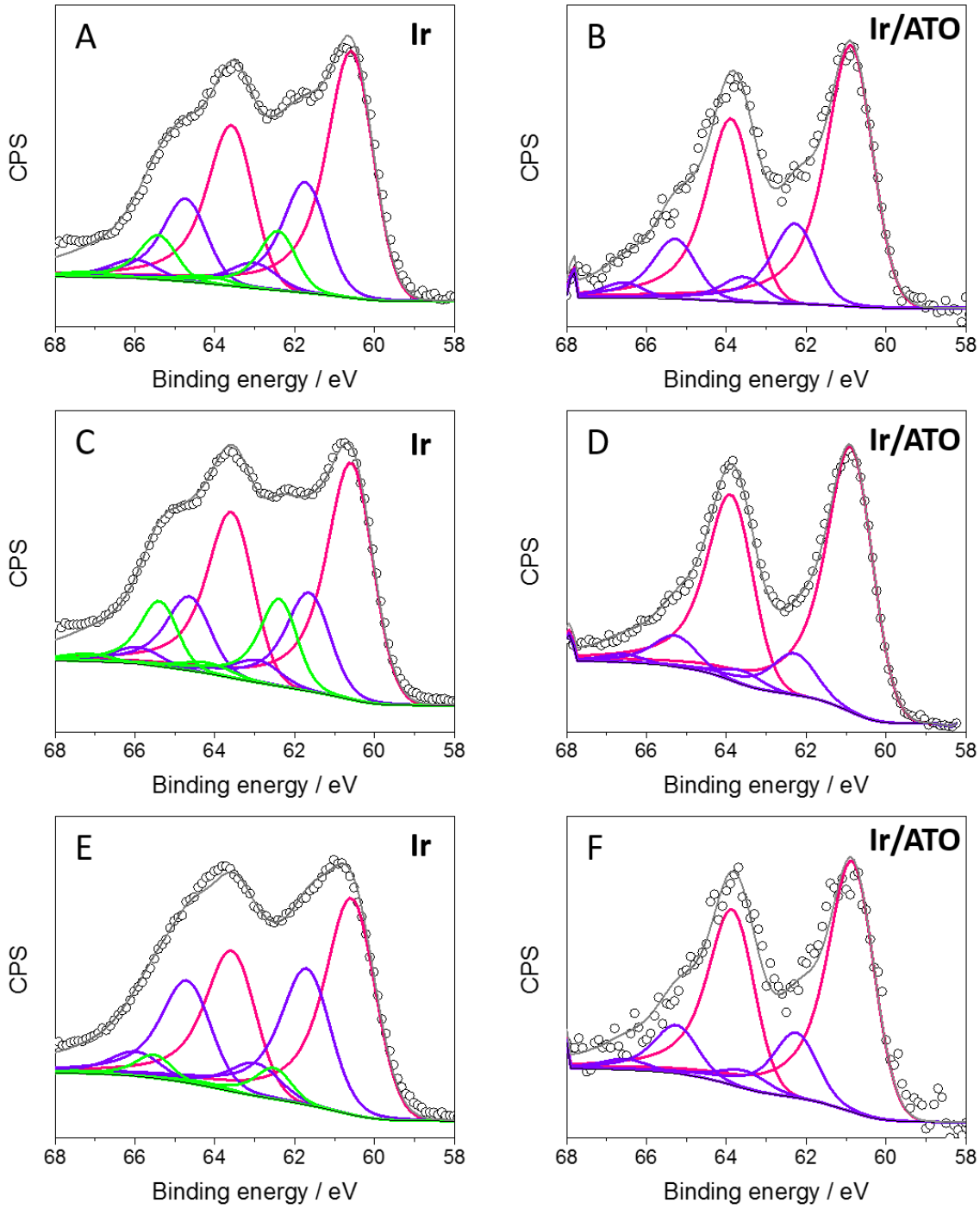

Figure 107. Ir4f XP spectra recorded on unsupported Ir (A,C,E) and Ir-ATO (B,D,F) anodes under 3 mbar water vapor and -0.25 V and 0.2 V (below peak A_1), correspondingly. The kinetic energies of the emitted electrons was the following: 390 eV (A,B); 530 eV (C,D); 810 eV (E,F). Pass Energy 50 eV. The color code: Ir_{met} - pink, Ir (III) – green, Ir (IV) – violet. Experimental results are shown as circles, while the fitting – grey line.

Now we can turn to the analysis of the potential dependence of iridium red-ox states. Figure 108 show the evolution of metallic iridium, Ir (IV) and Ir (III) components for three photon energies observed on unsupported and supported iridium particles. We will start the analysis from the unsupported particles, the data are presented in Panels A, C and E. The increasing of the applied

potential from - 0.25 V to 0.85 V leads to the decrease of Ir (III) contribution. Under the OER conditions, the amount of Ir (III) is less than 10 % and the electrode surface is mostly represented by metallic Ir (ca. 55-60%) and Ir (IV) oxide. It is interesting to note that the amount of metallic component is increasing with polarization, while the contribution of Ir (IV) is potential independent. This behavior can be explained by the specific morphology of the formed electrochemical oxide on iridium nanoparticles. Particularly, we propose the formation of 3D porous oxide layer.

The analysis of Ir4f XP spectra recorded on Ir/ATO anode under different polarization is shown in Panels B, D and F of Figure 108. The contribution of metallic iridium and Ir (IV) component are not strongly influenced by the applied potential. However, one may notice slight decreasing of the metal contribution under the OER conditions, e.g. from ca. 85% to 75% (for KE of 530 eV). No traces of Ir (III) species were observed on the supported Ir catalyst.

Comparison of the results obtained on different synchrotron revealed, that unsupported Ir catalyst measured at TEMPO beamline is less oxidized than the Ir@IrO_x sample analyzed at ISISS. This and other small changes (i.e. potential dependence of Ir (IV) component) can be related to the differences in the experiment conditions, however the overall behavior under the applied potential is similar in both cases.

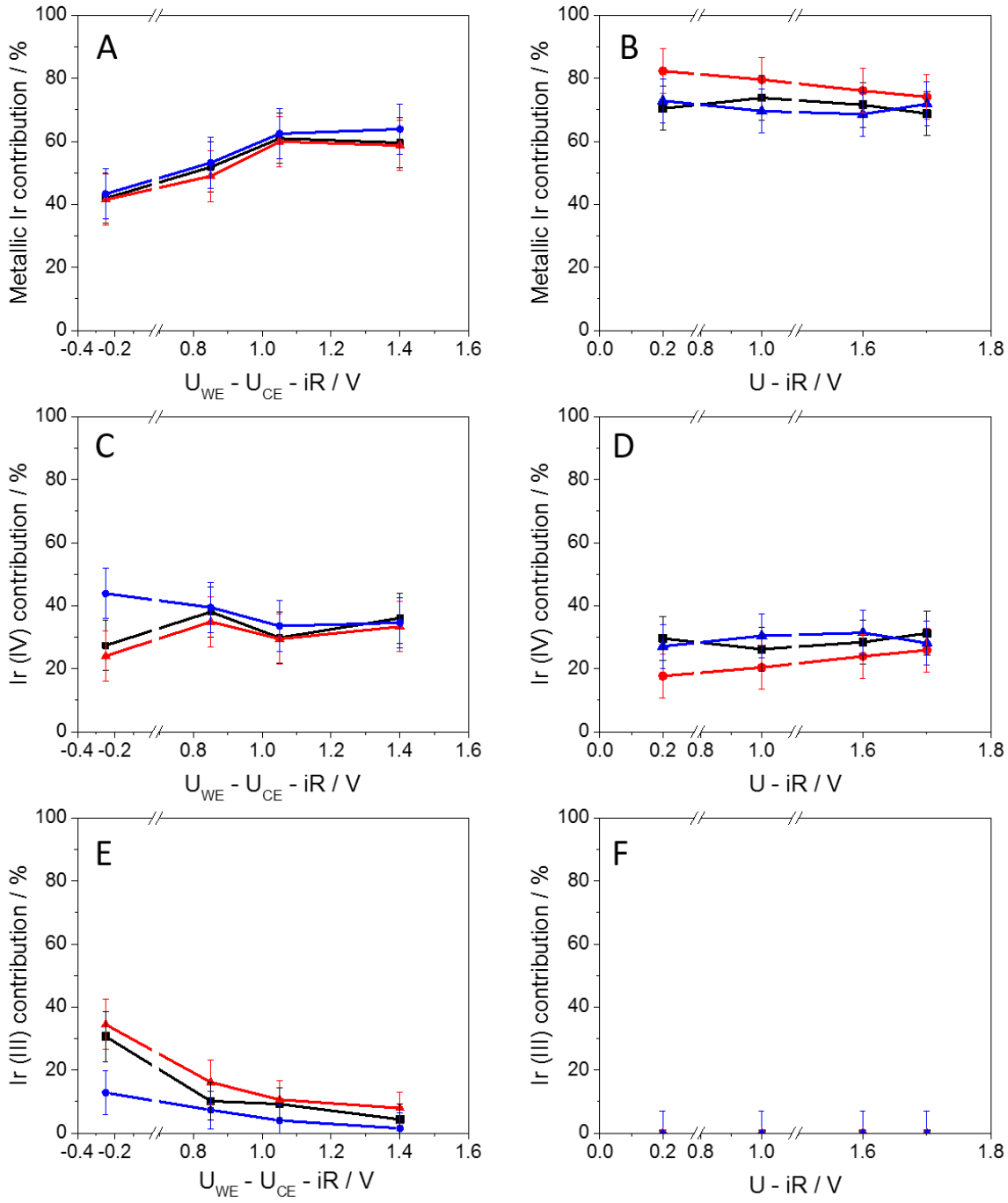

Figure 108. Potential-induced changes of Ir sites composition estimated on the base of XP spectra recorded on unsupported iridium (A, C, E) and Ir/ATO (B, D, F) anodes under 3 mbar water vapor and the kinetic energies: 390 eV (black); 530 eV (red); 810 eV (blue). Metallic iridium contributions are shown on Panels A, B; Ir (IV) – Panels C, D; Ir (III) – Panels E, F. The potential values are Ohmic drop corrected.

6.5. Role of ATO Support in Anode Performance

Three catalyst powders, unsupported iridium, Ir/ATO and ATO, prepared by our project partners (DLR, Stuttgart) and characterized electrochemically in a three electrode cell (in liquid electrolyte) were studied under water vapor ambient. The former data show higher activity of supported iridium particles and improved stability under the OER conditions in comparison to the unsupported catalyst. For water vapor conditions, on the contrary, we observed the decreasing of the currents at high anodic polarization. Moreover, the values recorded at 1.7 V are lower than the ones obtained at 1.6 V (see Figure 101). At first glance such a behavior could be related to the corrosion of the ATO support under high anodic polarization discussed in the literature[120,121]. However, the data obtained in liquid electrolyte did not reveal any drop of the supported electrocatalyst performance under similar polarization conditions.[132] The main difference between the RDE measurements performed at DLR and the ones made in the NAP-XPS chamber was the presence of the graphene additives in the latter case. Graphene was added deliberately in the anode catalyst layer in order to improve its conductivity. The graphene-based materials are supposed to possess improved corrosion stability at high anodic polarization in comparison to state-of-the-art carbon supports[260]. However, graphene oxidation at high anodic potentials cannot be excluded and is considered to be responsible for the decreasing of the currents.

The analysis of the Tafel slopes was performed on the basis of the data obtained in three-electrode cell and did not reveal any changes in the presence of the ATO support. The observed values of ca. 42 – 44 mV dec^{-1} are lower than the ones reported in the literature (ca. 60 mV dec^{-1})[75]. Nevertheless, the similar Tafel slopes observed on unsupported and supported catalysts studied in this work suggest similar OER mechanism (see the discussion of the OER mechanism on Ir-based anodes in Chapter 5).

We will start our discussion of *in-situ* NAP-XPS results with the evolution of the Sn/Ir atomic ratio estimated based on the XP spectra recorded on Ir/ATO samples (Figure 106). A systematic increasing of the tin contribution with the applied potential and especially under the OER conditions can be assigned to one of the following reasons:

1. Sn surface segregation with partial or full encapsulation of iridium nanoparticles by ATO;
2. Changes in the iridium nanoparticle size and/or shape;
3. Cleaning of the surface under potential cycling resulted from the oxidation of carbon impurities;
4. Detachment of iridium nanoparticles under the OER conditions.

While cleaning of the surface under the electrochemical cycling is a well-known effect, the analysis of the C/Ir ratio as well as the changes in C1s XP spectra under different polarizations did not reveal systematic dependence on the applied bias (see Section A.16). Based on this we can exclude this hypothesis from the list.

The detachment of the catalyst particles is a known phenomenon[133,261,262], for example for fuel cell cathode catalysts due to the support corrosion[263].

The post-mortem analysis of the MEAs performed by means of STEM at University of Antwerp confirmed the presence of detached iridium particles, however considering local character of the STEM analysis, it is hardly possible to estimate their contribution quantitatively (see Figure 98). The presence of detached particles could indeed explain the growth of Sn/Ir ratio with potential. However, in order to obtain that Sn/Ir ratio increased by a factor of ca. 2 (as observed experimentally) ca. 50 % of the particles should be disconnected from the ATO surface. In this case, the performance of this catalyst would be similar to the one observed for the unsupported Ir, what is not the case, as it was shown by the electrochemical measurements in three-electrode cell. Furthermore, detachment of 50 % Ir particles is not supported by microscopic data.

The microscopic analysis of pristine and post-mortem samples coupled with EDX did not reveal any changes in the particle shape and size nor in the elemental distribution. Formation of an ATO shell on iridium nanoparticles, which could explain the Sn/Ir growth was not supported by microscopy analysis either.

Thus, none of the hypotheses proposed above could be supported by the post mortem analysis unless the potential-induced surface changes were reversible. In order to verify whether formation of an ATO shell and/or size/shape changes (assuming that they are reversible and occur under potential-controlled conditions) could result in the experimentally observed Sn/Ir ratio increase, we performed the simulation of photoemission spectra for several morphologies varying the modeling parameters. Based on the comparison of the experimental and calculated Sn/Ir ratio under different kinetic energies, we may exclude from our further discussion two following situations proposed before: full encapsulation of iridium nanoparticles by ATO and changes in iridium particles shape and size. Due to a limit set of the available morphologies in the used software, the reproduction of partial encapsulation model was not possible directly. In order to simulate the changes of Ir – ATO interface, we used a “spheres” morphology and varied the height of the iridium particles protruding above the substrate, thus changing the interface. The evolution of Sn/Ir ratio estimated from this model was in agreement with the experimental results.

The encapsulation of the particles under polarization has been previously discussed for TiO_x-based supports.[137] The support layer formed on the particle surfaces might eventually decrease their dissolution. However, encapsulation by a crystalline layer would block the active

surface and lead to a decrease of the catalyst activity. Taking into consideration the enhanced OER activity of Ir/ATO catalyst observed in liquid electrolyte in comparison to the unsupported Ir, we propose either a partial encapsulation or the formation of a porous ATO shell, both being reversible and lifted off once the potential returns to the OCP value.

The analysis of Sn3d XP spectra recorded on the samples with and without iridium nanoparticles did not reveal any changes in the peak widths regardless the applied potential and the presence of iridium. Thus, the oxidation state of Sn or more precisely the ratio between Sn (II) / Sn (IV) oxidation states can be considered stable.

The degradation of the ATO support is generally related to the antimony dissolution[121]. As it was discussed in Chapter 1, antimony can be present in the ATO in the form of Sb (III) and Sb (V) simultaneously and the ratio between the two oxidation states depends on the doping level[129–131]. Sb (III) species are considered to be on the surface of the oxide, while Sb (V) – in the bulk. The increasing of the applied potential could lead to the following reaction of antimony dissolution[120]:

$$Sb_2O_3 + 3H_2O = 2SbO_3^- + 6H^+ + 4e^-,\ E^0 = +0.71\ V_{RHE}\ (Eq.\ 28)$$

The analysis of Sn/Sb atomic ratio for ATO-based anode estimated on the basis of the photoemission spectra recorded at KE of 530 eV and 810 eV is shown in Figure A 18. The ratio is stable in the interval of the applied potentials, however one may observe slight surface segregation of antimony in comparison to the sub-surface region. The EDX analysis, as a bulk-oriented method, performed on a pristine Ir/ATO – based MEA and its post-mortem studies confirmed the nominal ratio of Sn / Sb = 10 : 1, while according to the XPS data, the ATO surface contains ca. 50 % of antimony. The small intensity of $Sb3d_{3/2}$ peak and the overlapping of $Sb3d_{5/2}$ part of the doublet with the O1s spectra do not allow us estimating the oxidation state of antimony precisely. The analysis of Sb peaks in case of the Ir/ATO sample was not possible, as the signal was strongly attenuated by the presence of iridium particles on the ATO surface. Nevertheless, we may consider the electrochemical stability of the ATO support, at least its chemical composition, under the conditions applied in this work.

Turning back to the analysis of Sn3d XP spectra, their BE position (487.1 – 487.4 eV) is higher than the one observed for tin oxide in the literature (486.6 eV). This is most likely related to the semiconductor band-gap shrinkage due to the antimony doping[264]. Figure 109 shows the evolution of the SnO_2 band structure with the electron donor doping level. Thus, the presence of extra free electrons in a doped material leads to the filling of the lowest states in the conduction band, causing a downward shift of the latter as a result of the Coulomb interactions and mutual exchange forces between the energy bands[265]. This induces the shrinkage of the band-gap of the doped SnO_2 compared to undoped (panel C of Figure 109). The narrowing/broadening of the band-

gap is followed by the BE shift of the corresponding core-levels[266], observed in the literature for Sb-doped SnO_2 samples by means of XPS[258,259]. Moreover, *Egdell et al.*[258] showed that the valence band region is much more sensitive to the changes of free electrons concentration in antimony-doped tin oxide than their core-level spectra. The changes of the oxidation state of antimony (Sb (III) and Sb (V)) affect the type of the defects formed in tin oxide, either positively charged defects or oxygen vacancies. Consequently, this will also vary the distance between the conduction and the valence bands. For example, *Ke et al.*[130] have shown that the formation of ultrathin (< 3 nm) SnO_2:Sb films leads to the changes of the preferential oxidation state of antimony to Sb (III), causing the broadening of the band gap (see Figure 110).

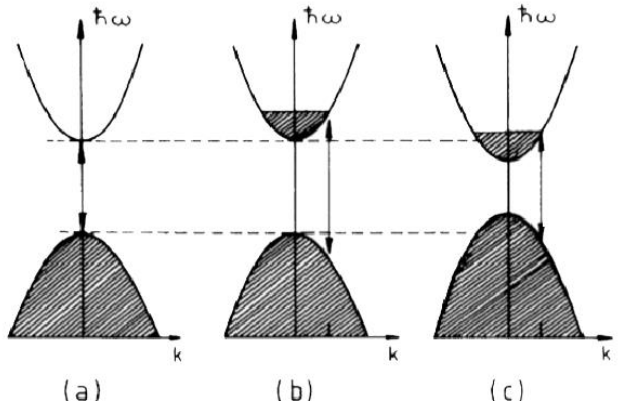

Figure 109. Schematic band structure of SnO_2: undoped (a) and after heavy doping (b,c). Panel (b) shows the filling of the conduction band, while panel (c) demonstrates the results of the many-body interaction, namely the shrinkage of the energy gap. Shaded areas correspond to the occupied regions. Taken from[265].

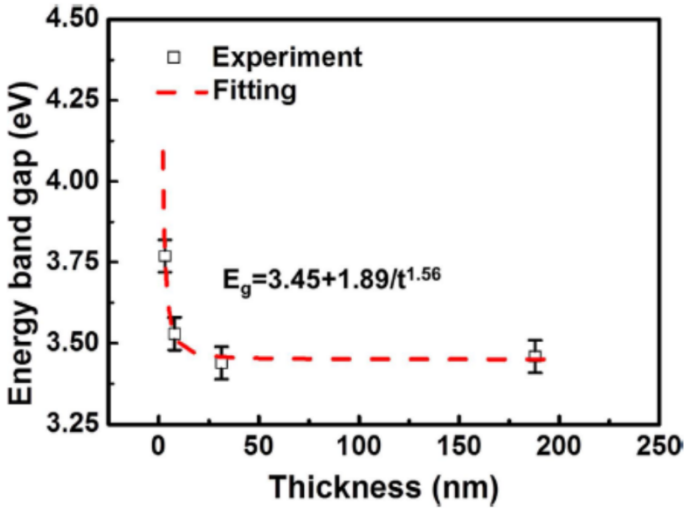

Figure 110. The energy band gap vs the thickness of SnO_2:Sb films obtained form the valence band XP spectra. The dashed line represents a fit to a power-law function. Taken from[130].

The binding energy position of the Sn3d XP spectra recorded on ATO-based electrode stays constant regardless the polarization and the photon energy at which the spectra were collected. However, the analysis of the data obtained on Ir/ATO-based electrode reveals the shift of the Sn3d binding energy position under polarization at kinetic energy of 810 eV (see Panel C of Figure 103). It should be noted that the BE position of the spectra recorded at 530 eV is stable. This potential-induced peak shift can be explained by the redistribution of tin and antimony and/or the bending of the energy band edges. Further, we will discuss both of these possibilities.

The surface segregation of antimony to the topmost layers of the SnO_2:Sb has been demonstrated by several groups and has been referred to the differences in the surface energy of tin and antimony[131,267,268]. The analysis of Sn/Sb atomic ratio performed on ATO-based sample performed in this work also revealed the antimony surface enrichment, however the values were not influenced by the potential cycling contrary to what had been shown by *Fabbri et al.*[121] Moreover, the shift of Sn3d XP spectra of Ir/ATO towards lower BE values of 486.6 eV at anodic polarization corresponds to the position of undoped tin oxide, what can be related to the redistribution of the elements in the ATO. The STEM/EDX analysis performed on pristine and post-mortem Ir/ATO samples did not reveal any changes in the Sn/Sb ratio close to the iridium/SnO_2 interface. Note however that the EDX analysis probes the "bulk" of the material, while XPS is a surface-sensitive method resulting in the different values, analogous to the ATO sample discussed above. The elemental mapping was also complicated by the close values of the characteristic lines of tin and antimony. However, one cannot exclude a reversible elemental redistribution under the applied potential.

Low concentration of free charge carrier density in the semiconductor leads to the prolonged electron screening length in comparison to the atomic range for the metals. The bending of the energy band edges can be induced by[269] contact with metal, application of the external electric field, adsorption effects etc. For our discussion, we will briefly review the first two effects.

The band bending at the metal/semiconductor interface depends on the physical properties of the materials, particularly on their work function (Φ) values. Variations in the surface composition of the catalyst as well as the substrate lead to the differences in the work function. Table 19 shows the WF data of Ir- and Sn-based compounds reported in the literature. Based on the data presented in the Table, metallic iridium has lower Fermi level than ATO. However, for nanoparticles one should also consider the dependence of the work function values on the size[270].

Table 19. Literature values of the work functions.

Compound	Work Function / eV	Sample Description	Ref
Ir_{met}	5.30	Metallic iridium film	[271]
IrO_2	4.23	Ir film annealed at 900°C in O_2	[272]
SnO_2:Sb	5.03	Antimony doping: 2 wt.%	[273]
	4.90	3 wt.%	[274]
	5.00	7 wt.%	[275]
SnO_2	5.70	SnO_2 (101), stoichiometric	[257]

The energy diagram of a metal/semiconductor contact for the mentioned above case where the work function of the metal is higher than that of the semiconductor is shown in Figure 111. Due to this difference, the free electrons will flow from the semiconductor to the metal until both Fermi levels will be aligned (see the bottom panel of Figure 111). Thus, at the metal/semiconductor interface, the metal is negatively charged and the semiconductor is positively charged. However, if the Φ of semiconductor and metal are close, no bending can be observed what is referred as a flat-band position. Figure 112 demonstrates the example of the energy band position under different polarizations.

The capability of the XPS, UPS methods to follow the bending of the energy bands has been debated in the literature. The shifts of the valence band edge with respect to the Fermi level due to band bending should be reflected by a shift of the complete photoemission spectra including all core levels, valence bands, and also the secondary electron cutoff what was demonstrated in[276,277]. In contrast, the theoretical analysis of the photoemission spectra performed by *Margaritondo et al.*[278] for different cases of band bending claimed the independence of the line width/shift on the band bending for the semiconductors with certain concentrations of free charge carriers. The limitations of the core level position analysis for the band bending studies were also supported by *Szuber et al.*[279]

Now we can turn to the discussion of the obtained results, where these two effects are present simultaneously – metal/semiconductor interface and external polarization.

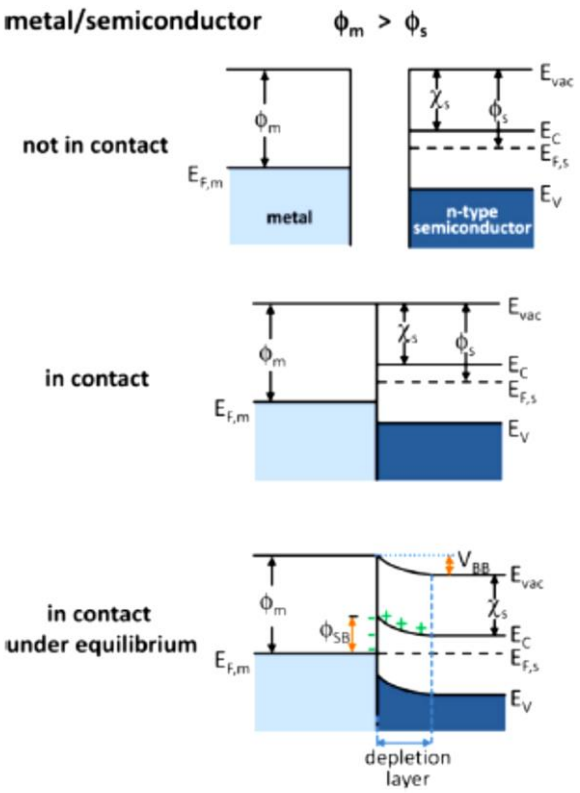

Figure 111. Energy band diagram of metal and n-type semiconductor contacts. E_{vac} – vacuum energy; E_c – energy of conduction band minimum, E_v – energy of valence band maximum, Φ_m and Φ_s work function of metal and semiconductor, correspondingly, χ_s – electron affinity of the semiconductor. Taken from[269].

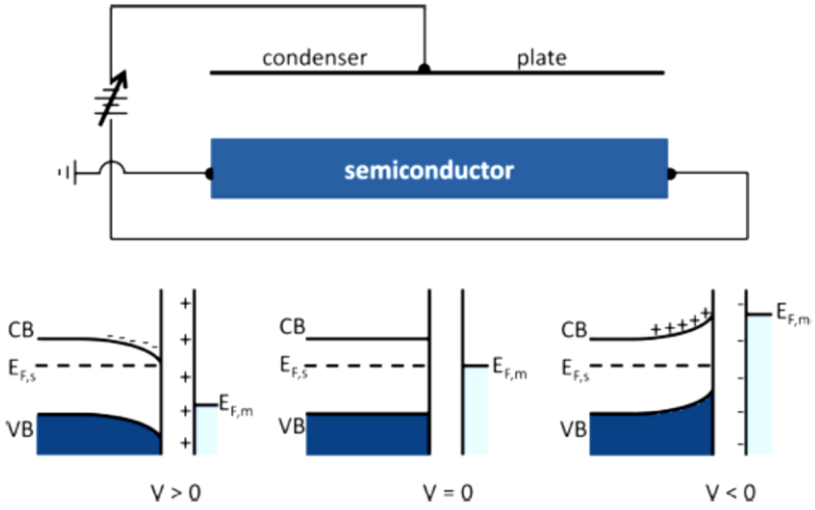

Figure 112. Schematic diagram of field-effect-induced band bending on an n-type semiconductor with no surface states. Taken from[269].

Based on the results obtained in our *in-situ* NAP-XPS studies, we propose the following scheme for Ir/ATO sample. Below the anodic peak A_1 (0.2 V vs DHE) the Fermi level of iridium and valence band of ATO are at the same energy level (see the close values of Φ presented in Table 19), i.e. assume that we are close to the flat-band potential where no electron flow occurs at

the interface and the BE values remain constant. The increasing of the applied potential leads to the downward shift of metal Fermi level causing a downward band bending in semiconductor, i.e. the charge transfer from iridium to ATO. This statement is in contrast to the conclusion made by *Oh et al.*[75] who proposed the inverse charge transfer. However, their measurements were performed without polarization. Thus, according to our scheme, one would expect the formation of δ^+ charge on the metal and δ^- - on semiconductor at Ir-ATO interface under the OER conditions. The heavily doped SnO_2 used in this work possesses high free charge carrier density leading to rather small band bending decay length. In this case, by variation of the analytical depth of XPS, we can follow the band bending phenomena due to the difference in the binding energies at the Ir-ATO interface and in the bulk ATO:

$$BE_{bulk} < BE_{surface}\text{ , (Eq. 29)}$$

what was observed for Sn3d XP spectra recorded at kinetic energy of 530 eV and 810 eV, where the BE of the latter was lower than of the former. It should be noted that the spectra recorded at high KE (810 eV in our case) should possess the contribution of both surface and "sub-surface" regions, averaging the contributions. In this case, one would expect the broadening of the peak or the changes in the peak shape due to the appearance of an additional shoulder. While here, we observe the complete shift of Sn3d peak observed at 810 eV, thus the broadening of the peaks at the kinetic energies lower than 810 eV, i.e. 530 eV, is expected, what is not the case.

The last but not the least topic for the current discussion of the SMSI is the behavior of iridium sites, i.e. their red-ox transitions under different polarization conditions, on unsupported and supported Ir catalysts. The main difference in iridium surface state was observed at the potentials close to the OCP. In the absence of the support, the electrochemical oxide layer consisted of intermixed Ir (III) / Ir (IV) oxide, while for Ir/ATO-based anode, no traces of Ir (III) species were observed regardless the photon energy analogous to the spectroscopic data of *Oh et al.*[75] Moreover, the overall content of the Ir (IV) oxide on supported Ir was lower than on unsupported. If we compare the CVs recorded on these electrodes in the NAP-XPS chamber (Panels A of Figure 101 and Figure 100 for Ir/ATO- and unsupported Ir-based anodes, respectively), one may also observed a well-pronounced red-ox peak A_1 recorded on Ir-based anode, which is poorly distinguished on Ir/ATO. Usually, this peak is referred to the Ir (III) / Ir (IV) red-ox transition what was also shown in the previous Chapter for $Ir@IrO_x$ electrode. Thus, the diminishing of this peak intensity in the CV on Ir/ATO electrode is in agreement with the absence of Ir (III) species in the corresponding Ir4f XP spectra. Analogous to Ru, Ir-based hydrous oxides are used as pseudocapacitive materials, where the III / IV transition is associated with proton intercalation leading to the oxide surface expansion and destabilization[45]. Taking into account higher stability of Ir/ATO-based anodes observed in the literature in comparison to unsupported Ir, we suggest

that the occurrence of Ir (IV) / Ir (III) red-ox transition accompanied by proton intercalation leads to a faster degradation of the catalyst.

The increase of the applied potential leads to the oxidation of Ir (III) species on the unsupported Ir catalyst, while the surface state of iridium sites on Ir/ATO electrode is barely influenced by the external polarization. Under the OER conditions, the amount of the Ir (IV) species on the electrodes surface is quite similar. Meanwhile, based on the model of the band bending, one would expect higher oxidation of iridium in case of supported particles due to the charge transfer from ATO. This inconsistency is not understood yet.

To conclude, by applying *in-situ* NAP-XPS approach we performed a comparative analysis of unsupported Ir, Ir/ATO and ATO-based anodes under the water electrolysis conditions in order to understand the origin of increased activity and stability of Ir/ATO vs. unsupported Ir anode. The changes of Sn/Ir atomic ratio observed on Ir/ATO sample under the applied potential were tentatively attributed to a partial encapsulation of iridium nanoparticles by ATO. The constant width and BE position of the Sn3d XP spectra recorded on ATO-based electrode under different polarization conditions confirmed the stability of the support surface composition under the applied experimental conditions. The potential-induced BE shift of tin core-level spectra at kinetic energy corresponded to sub-surface region can be explained either by the redistribution of tin/antimony or by the bending of the energy bands. The quantitative analysis of Ir4f XP spectra recorded on unsupported and supported iridium nanoparticles revealed higher oxidation of the former below the OER region and the absence of Ir (III) component on the surface of supported catalyst. The latter can be considered as a reason of a higher stability of Ir/ATO. On the basis of the obtained and modeled XP spectra, we estimated the effective thickness of the oxide layer, which under the OER conditions was equal to ca. 0.1 nm and ca. 0.2 nm for Ir/ATO and unsupported Ir, respectively. Thinner oxide layer observed on a supported catalyst may explain its higher activity in comparison to the unsupported one.

6.6. Conclusions of Chapter 6

Higher activity and improved stability properties of supported Ir catalysts on antimony-doped tin oxide are generally related to the presence of the metal-support interaction. In this Chapter by applying *in-situ* NAP-XPS approach for the analysis of unsupported and supported iridium catalysts under the OER conditions, we demonstrated various effects induced by the presence of support as well as analyzed the behavior of the pure support.

The photoemission measurements were also complemented by the microscopic analysis of pristine and post-mortem samples performed at the University of Anwerp and by XP spectra modeling using SESSA software. On the basis of the obtained results, we proposed a partial reversible encapsulation of iridium nanoparticles by ATO under the OER conditions. The Ir (IV) / Ir (III) transition is hindered by the presence of the ATO support, what could be a clue of a higher stability of the supported Ir anode. The enhanced electrochemical activity observed on Ir/ATO anodes in comparison to the unsupported catalyst was related to a thinner iridium oxide layer formed under the reaction conditions. The analysis of the ATO support in the absence of iridium particles revealed the stability of the substrate surface composition under the applied conditions.

To the best of our knowledge, this work can be considered as the first attempt of *in-situ* NAP-XPS studies of Ir-supported catalyst, demonstrating the capability of the method and revealing the SMSI-induced processes taking place at metal-support interface.

General Conclusions and Outlook

The aim of the present thesis was to perform NAP-XPS and NEXAFS studies *operando* on Ir, Ru – based anodes under water electrolysis conditions in order to clarify the OER mechanism on these anodes; explain higher stability of thermal Ir, Ru – based oxides in comparison to the corresponding more active electrochemical oxides; and define the role of the support in the behavior of the Ir/ATO catalysts.

In order to pursue these objectives, we studied Ir, Ru – based membrane-electrode assemblies under 3 mbar water vapor and different polarization conditions using photoemission and absorption spectroscopies at ISISS and TEMPO beamlines at HZB/BESSY II and SOLEIL synchrotrons, respectively.

The present thesis demonstrates different OER mechanisms on iridium and ruthenium – based anodes regardless the oxide nature (thermal *vs*. electrochemical).

It was shown that the OER mechanism on Ir-based anodes is likely to involve anion red-ox chemistry (O^{II-} / O^{I-} transition), while a cation mechanism was confirmed for Ru-based anodes. Higher degradation of the latter was also attributed to the cation red-ox transitions leading to the formation of corrosion products under the reaction conditions. Moreover, the OER mechanism of Ir and Ru does not depend on the oxide nature, whether it was the rutile oxide obtained by thermal treatment of metallic particles or the one formed electrochemically under applied potential.

Comparative analysis of the electrochemical and thermal Ir- and Ru-based oxides behavior allowed us to propose tentative explanations of the differences in their activity and stability properties.

For Ru-based anodes, we demonstrated a potential-induced irreversible transition of anhydrous Ru (IV) into a hydrous Ru (IV) hydroxide form. The formation of these hydroxide species was related to the differences in the stability properties of electrochemical and thermal oxides. Formation of high oxidation state Ru components (Ru (VI) and Ru (VIII)), which are supposedly part of the catalytic cycle, was detected under anodic potentials, however their role as the active reaction intermediates is uncertain. These findings were further supported by *in-situ* NAP-XPS studies performed on bimetallic $Ir_{0.7}Ru_{0.3}O_2$ oxide. The stabilization mechanism of iridium was largely attributed to the protection of anhydrous Ru (IV) oxide from its irreversible transformation into a hydrated form. In contrast to common opinion, the decrease of the Ru (VIII) contribution in the presence of iridium was not confirmed.

Operando studies of Ir-based systems revealed the presence of Ir (III) / Ir (IV) red-ox transition on the electrochemical oxide, while the surface composition of IrO_2 was not altered regardless the applied potential. In agreement with the literature, this was attributed to the occurrence of the Ir (III) / Ir (IV) red-ox transition not only on the surface but also in the sub-surface layers of the electrochemical oxide. The analysis of the iridium photoemission spectra recorded with different photon energies did not reveal the formation of oxidation states higher than IV on either of the oxides. Regarding the structure of the electrochemical Ir oxide, we suggest the formation of a porous oxide layer (rather than a core-shell structure), which is formed on the surface of Ir metal particles and contains intermixed Ir (III) / Ir (IV) species. The analysis of the O K edge spectra revealed the formation of electrophilic oxygen O^{I-} species through an electrochemical step and confirmed their role of an OER intermediate on both oxides. Based on the ratio between the current and the O^{I-} intensity, we suggested the formation of oxygen in a chemical step. The difference in the stability of thermal and electrochemical Ir-based oxides was attributed to the presence of Ir (III) / Ir (IV) transition, while higher activity of the electrochemical oxide was tentatively attributed to a more "flexible" amorphous oxide structure.

The improved stability of supported iridium catalysts was also explained by a hindered Ir (III) / Ir (IV) transition as compared to unsupported Ir, while the increase of its activity – to a thinner oxide layer. It is interesting to note, that the evolution of the surface composition under applied potential observed on unsupported iridium catalysts was confirmed by the measurements performed at two synchrotrons and different end-stations. Based on the experimental data we also suggest a partial reversible encapsulation of Ir by ATO support under the OER conditions.

The results demonstrated in this thesis provide answers to several questions related to the OER mechanism taking place on Ir, Ru – based anodes and to their degradation under the reaction conditions, however, there are still issues to clarify and study in the future.

First of all, the reason of the different OER mechanisms revealed on Ir- and Ru – based catalyst systems is not fully understood yet. Probably this could be related to the differences in the electronic structures of these elements. Whether this is the case or not, additional studies, mainly theoretical ones, are required for these systems in order to explain the origin of this effect.

DFT calculations would also complement the O K edge results obtained on electrochemical ruthenium oxide with the aim of proper attribution of the resolved peaks and improving the overall understanding of this system behavior.

In-situ NAP-XPS analysis performed on supported iridium catalysts emphasized the complexity of the processes taking place between the metal and the support particles under the reaction conditions. One of the intriguing questions is the reversibility of the effects discussed in

this thesis and their proper interpretation. For the future, we propose to perform some additional *in-situ* XPS measurements in order to study the evolution of the electrode surface under several consecutive potential cycles. Analysis of the spectra of antimony species, their oxidation state and surface contribution under the OER conditions, could also provide valuable information. AFM measurements performed under polarization conditions could provide supplementary information on the surface state of Ir/ATO and on the eventual segregation of SnO_2 to the Ir surface during the OER.

Application of *in-situ* NAP-XPS demonstrated in this thesis and in the literature is currently mainly restricted to solid oxide- and PEM-based fuel cell/electrolyzer systems. Meanwhile, to the best of our knowledge, *operando* analysis of alkaline-based systems by NAP-XPS is still quite rare. During this work, we also performed several attempts in order to study the anion-exchange-based MEAs by NAP-XPS. One of the main difficulties, which we encountered, was related to the low conductivity of currently available anion-exchange membranes under low relative humidity conditions of the NAP-XPS chamber. Thus, future progress in the field will largely depend on the availability of appropriate stable anion-exchange membranes with high ionic conductivities at low relative humidities.

Appendix

A.1. XRD Results of metallic Ru Nanoparticles

Table A 1. XRD pattern of rutile ruthenium oxide RuO_2 [03-065-2824].

2th	Intensity	h	k	l
27.89	999	1	1	0
34.95	730	1	0	1
39.86	186	2	0	0
40.39	44	1	1	1
54.03	511	2	1	1
57.64	114	2	2	0
59.26	64	0	0	2
65.22	94	3	1	0
66.74	110	1	1	2
69.21	134	3	0	1
73.81	49	2	0	2
82.95	69	3	2	1
87.34	52	2	2	2

Table A 2. XRD pattern of hexagonal Ru [01-089-3942].

2th	Intensity	h	k	l
38.39	263	1	0	0
42.19	258	0	0	2
44.02	999	1	0	1
58.35	120	1	0	2
69.42	122	1	1	0
78.41	116	1	0	3
52.22	16	2	0	0
84.69	117	1	1	2
85.95	84	2	0	1

Table A 3. XRD pattern of hexagonal ruthenium chloride $RuCl_3$ [01-073-0319].

2th	Intensity	h	k	l
16.71	999	1	0	0
29.16	36	1	1	0
33.26	170	1	1	1
33.79	68	2	0	0
35.96	130	1	0	2
43.53	190	1	1	2
45.23	65	2	1	0
46.94	96	2	0	2
51.70	78	3	0	0
56.22	72	2	1	2

Figure A1 shows the XRD pattern obtained on as prepared Ru powder. Two different phases have been observed on Ru (AP) sample, corresponded to metallic Ru (blue) and ruthenium chloride (red). The peaks related to metallic Ru are broad due to small particles size of ca. 2.6 nm according to the TEM analysis (Figure 47). The unreacted ruthenium salt presented in the as prepared sample did not interfere the reaction taken place at Ru electrode. No chlorine evolution have been observed by means of online mass spectrometry, as well as no Cl presence was found in the XP spectra of neither $Ru@RuO_x$ nor RuO_2.

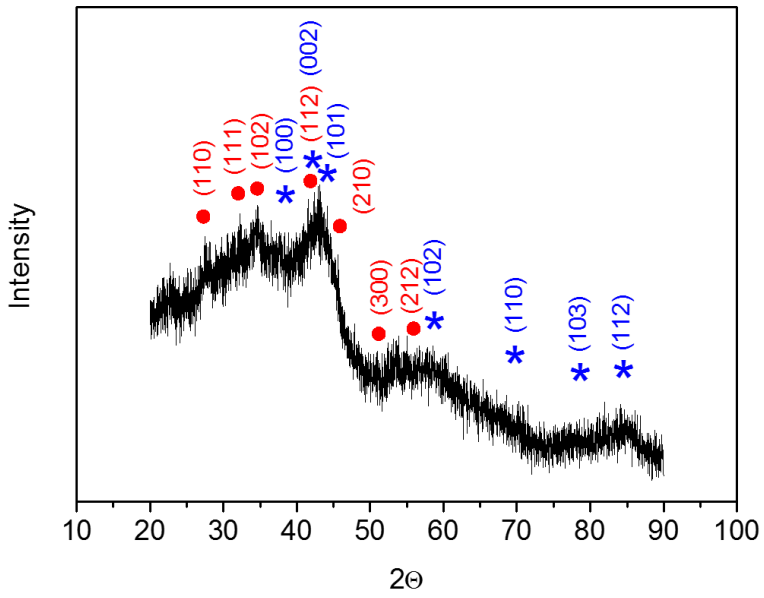

Figure A1. XRD pattern of as prepared Ru powder. Provided pattern markers corresponds to hexagonal metallic Ru 01-089-3942 (blue) and hexagonal ruthenium chloride $RuCl_3$ 01-073-0319 (red).

A.2. TEM Analysis: RuO_2 powder

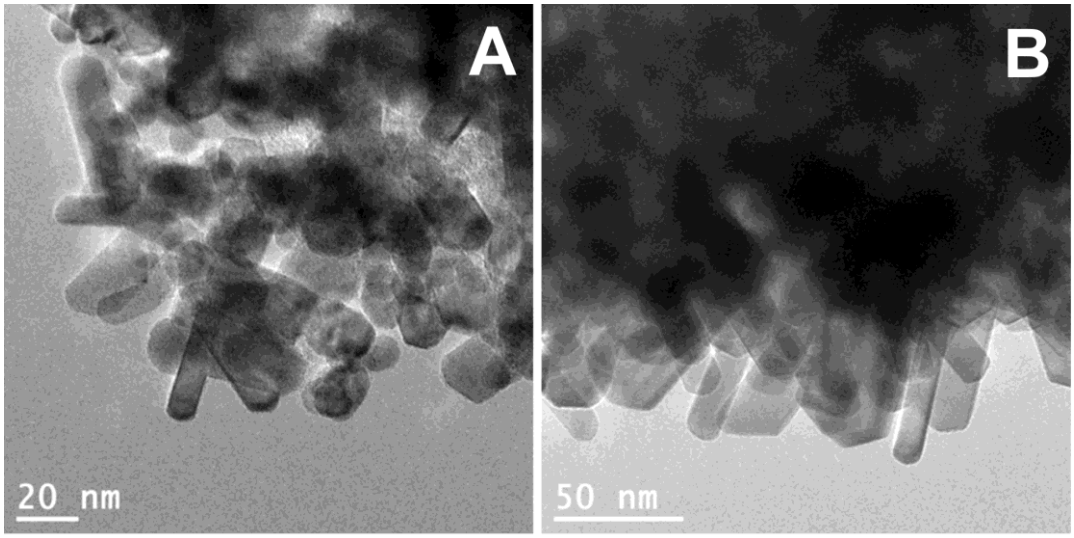

Figure A 2. TEM images of pristine RuO_2 (A,B) powder under different magnifications.

A.3. RuO_2 Thickness Calculation: Results

The thickness of the electrochemical oxide layer formed on metallic ruthenium particles under the experimental conditions was estimated by means of SESSA software for a "layered spheres" morphology. The scheme is shown in Figure 44, for the simplicity, we considered the oxide shell to be comprised of RuO_2 oxide and varied the thickness of this oxide layer maintaining the overall particles size constant and calculated the contribution of RuO_2 into the overall XP spectra. The results are shown in Figure A 3. The NAP-XPS analysis of the $Ru@RuO_x$ anode surface after the electrochemical pretreatment revealed that the contribution of RuO_2 species was equal to ca. 60%. This value correspond to oxide shell thickness of 5 – 6 Å, i.e. 2 monolayers. Further comparison of the experimental data with the calculations was not performed due to the dominant presence of hydrous Ru (IV) oxide/hydroxide species on the surface, attenuating the signal of metallic core.

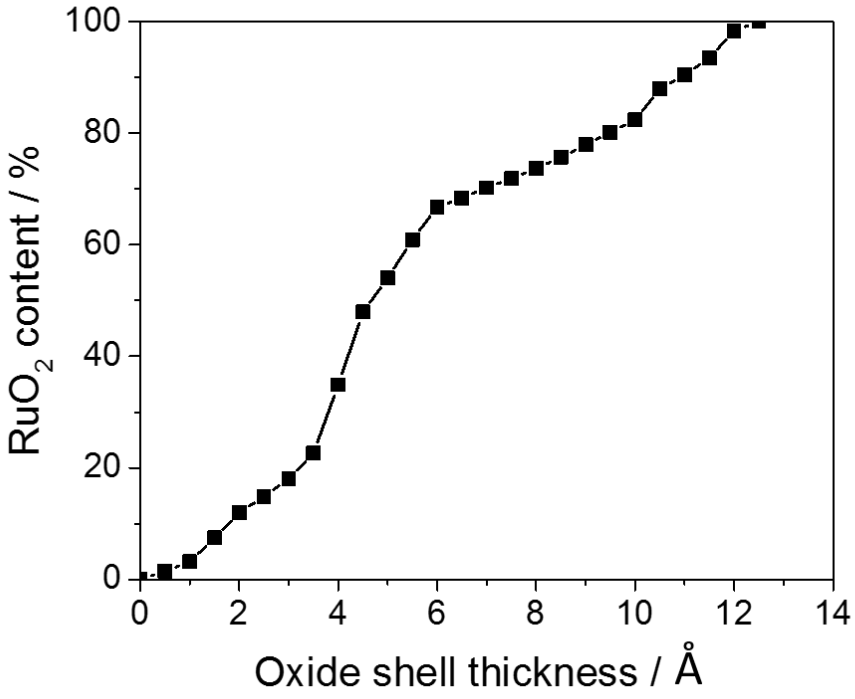

Figure A 3. Contribution of RuO_2 species in XP spectra depending on the oxide shell thickness. Morphology used for calculations – "layered spheres". See Figure 44 for detail.

A.4. Evolution of O1s XP spectra under polarization. Ru@RuO$_x$ anode

The potential-induced changes of O1s XP spectra recorded on Ru@RuO$_x$ anode during the third OER cycle are shown in Figure A 4. As it was mention in the main text, the fitting was done using three peaks located at 530.6eV, 532eV and 533.3eV and attributed to lattice oxygen, hydroxo groups and adsorbed water. The contribution of carbon species into the O1s XP spectra cannot be excluded. The analysis of the OH/O$_{lattice}$ ratio depending on the applied potential did not reveal any trends. This may be related either to a high contribution of carbon-based species or due to the strong degradation of the analyzed sample.

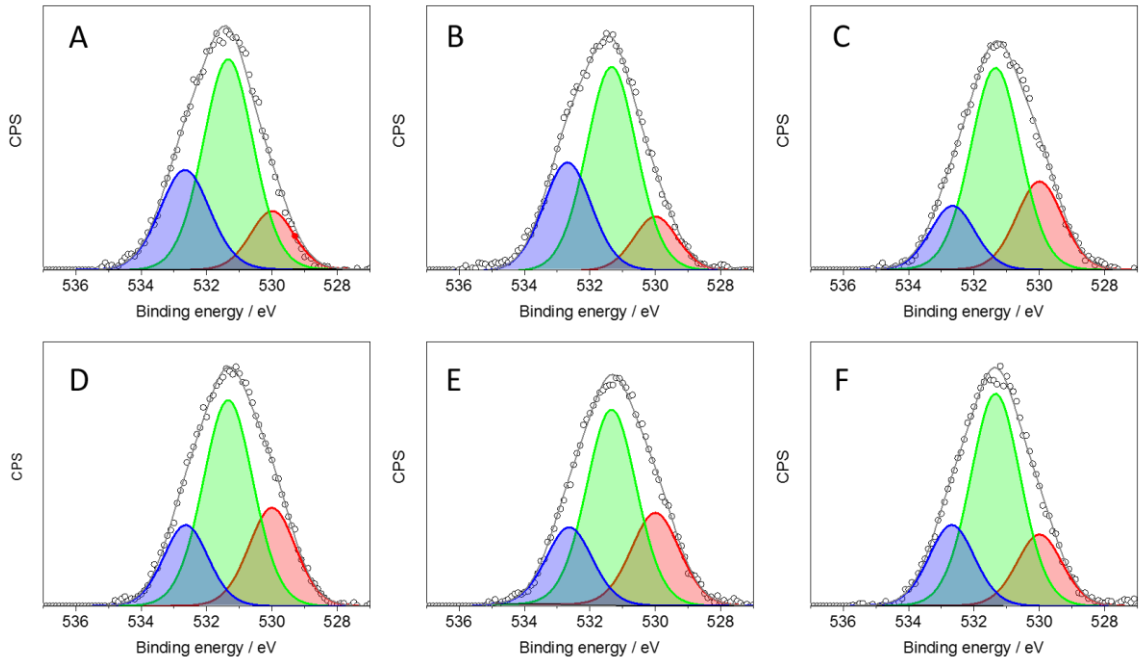

Figure A 4. O1s XP spectra recorded on Ru@RuOx anode under 3 mbar of water vapor and different polarization: 0.75 V (A); 1.0 V (B); 1.34 V (C); 1.39 V (D); 1.41 V (E); back 0.75 V (F). The fitting was done within three peaks: 530 eV (red); 531.3 eV (green) and 532.7 eV (blue). Photon energy 1066 eV.

A.5. Reference Sample Analysis : RuO_2 and RuO_2 xH_2O

The analysis of surface composition of two reference powder samples – RuO_2 and RuO_2 xH_2O (Alfa Aesar) – have been performed by means of XPS under vacuum conditions. Fitted Ru3d-C1s and O1s XP spectra are shown in Figure A 5.

For hydrated rutile oxide abbreviated as RuO_2 xH_2O, the amount of hydroxide groups was not specified by the supplier. Based on the fitting of the corresponding XP spectra (Panel B of Figure A 5) we confirmed the presence of both anhydrous RuO_2 and hydrated $Ru(OH)_x$ components and their ratio has been estimated as 1.2. The atomic ratio of different components is provided in Table A 4.

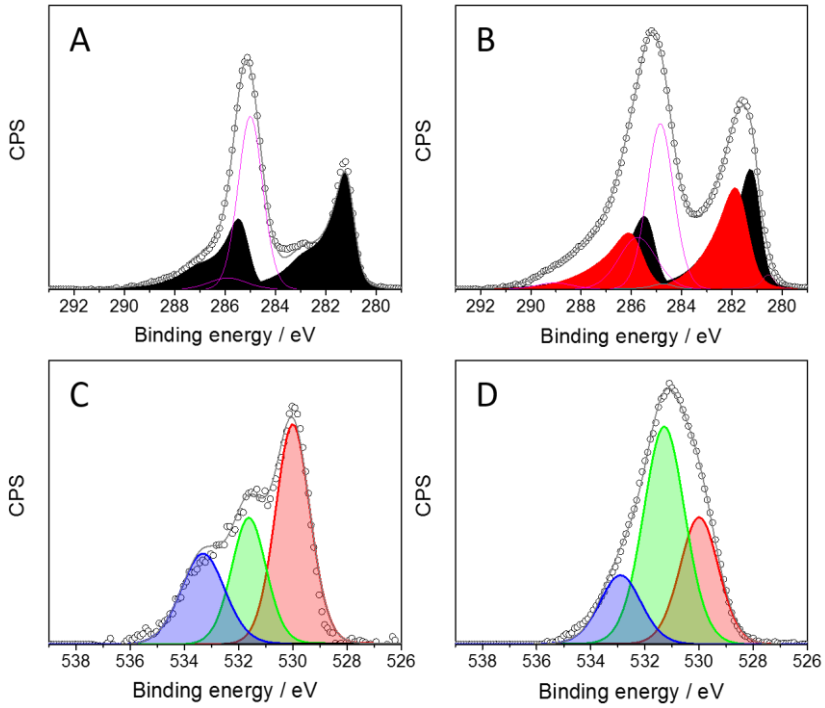

Figure A 5. Fitted C1s-Ru3d (A, B) and O1s (C, D) XP spectra of reference powders RuO_2 (A,C) and RuO_2 xH_2O (B, D) recorded under vacuum. Experimental XPS data are shown as black cycles, fitted spectrum – as a grey line. Panels A, B - Color code: RuO_2 (black), hydrated RuO_2 (red), and carbon species (magenta). Panels C, D – Color code: $O_{lattice}$ (red), OH + Carbon-based species (green), H_2O_{ads} + carbon-based species (blue). Kinetic energy of the emitted electrons 530 eV.

Table A 4. Atomic ratio estimated on the base of Ru3d, C1s and O1s fitted spectra for two reference samples – RuO_2 and RuO_2 xH_2O.

Atomic Ratio	**RuO_2 (ref)**	**RuO_2 xH_2O (ref)**
C1s / Ru3d	8.11	5.76
Ru3d (RuO_2) / O1s (O_{lat})	0.78	0.73
Ru3d ($Ru(OH)_x$) / O1s (OH)	-	0.28
O1s (O_{lat}) / O1s (OH)	1.74	0.55

A.6. XRD Patterns of Iridium-based compounds

Table A 5. XRD pattern of rutile iridium oxide IrO_2 [01-088-0288].

2th	Intensity	h	k	l
27.99	999	1	1	0
34.66	904	1	0	1
39.99	246	2	0	0
53.94	530	2	1	1
57.84	110	2	2	0
58.39	65	0	0	2
65.46	110	3	1	0
65.59	59	2	2	1
65.97	129	1	1	2
69.22	123	3	0	1
73.12	69	2	0	2
83.06	85	3	2	1
86.77	54	2	2	2

A.7. Potential Dependence of the $Ir_{0.7}Ru_{0.3}O_2$ Anode Surface Composition. Surface vs Subsurface

The analysis of the Ru3d XP spectra obtained on $Ir_{0.7}Ru_{0.3}O_2$ anode under different photon energies shown in Figure A 6 revealed that high oxidation state Ru species, Ru (VI) and Ru (VIII), are located on the anode surface, rather in the subsurface region.

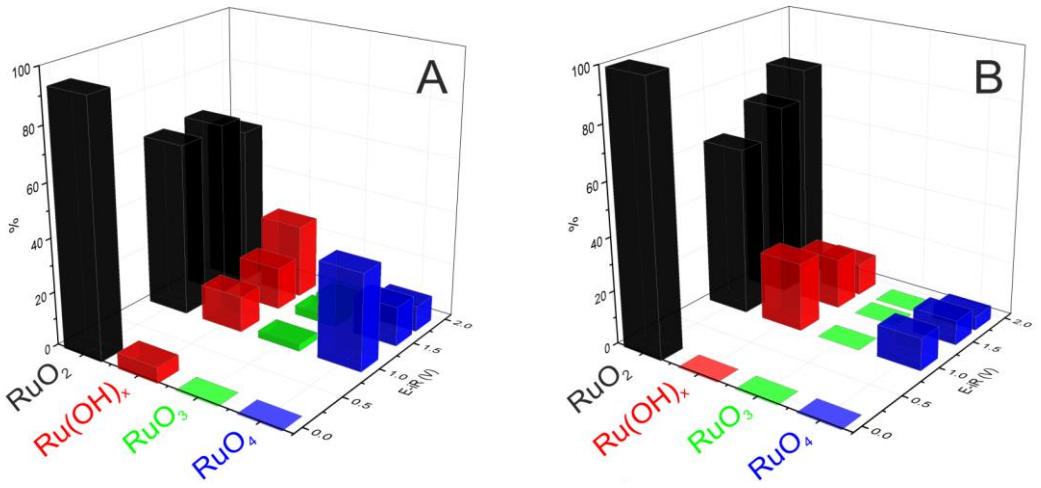

Figure A 6. Influence of the voltage bias on the fractions of RuO_2 (black), hydrated RuO_2 (red), Ru (VI) abbreviated as RuO_3 (green), and $RuO_{4(s)}$ for the $Ir_{0.7}Ru_{0.3}O_2$ electrode under 3 mbar H_2O at 820 eV (A) and 1300 eV (B) photon energy.

A.8. DFT Calculations

Density functional theory calculations were performed using the Quantum ESPRESSO package version 6.1.[280] by Travis Jones (FHI, Berlin). To recover the correct ground state properties[281] the Perdew, Burke, and Ernzerhof (PBE) exchange and correlation potential was employed [PBE].[282] Projector augmented wave datasets were taken from the PS Library[283] and a kinetic energy (charge density) cutoff of 30 Ry (300 Ry) was employed. A k-point mesh equivalent to at least (8×8) for the surface unit cells was employed with cold smearing[284] using a smearing parameter of 0.02 Ry. Calculations used at least 5 layers of IrO_2, the central two layers were fixed and the other were allowed to relax. Various surface orientations [(110), (200), (201), (210), (111)] were investigated in O and OH terminated state. Furthermore, the role of Ir defects introduced at the surface was also tested. Oxygen K-edge spectra were computed using a one-electron Fermi's golden rule expression as implement in XSpectra.[285,286] These were performed with the same k-point mesh as the ground state calculation and no core hole potential was included as this has been shown to give the correct results for IrO_2.[104] The relative edge positions were computed by way of a ΔSCF calculation.[287] These relative energies were then aligned using a calculation of bulk IrO_2, under the assumption the O1s binding energy is 530 eV. The potential at which O^{I-} forms was computed using the concept of a theoretical hydrogen electrode,[83] where in the reaction energy for hydrogen removal from the surface is calculated by way of DFT. This energy is then corrected for the electrode potential and changes in entropy. We neglected changes in zero point energy as previous investigations show they only contribute 0.1-0.2 eV for the types of species we are concerned with and will therefore not qualitatively change our findings.

Figure A 7 shows the structural model of (110) IrO_2 surface with O and OH termination and the corresponding white line positions for two oxygen sites μ_1 and μ_2. The analysis of Panel C of Figure A 7 shows that the low excitation energy O K-edge peak (529 eV peak observed in our work) can be created by deprotonation of OH groups at both cus (coordinatively unsaturated) and bridge position (labelled as μ_2). The white line position of μ_2-OH corresponds to 529.4 eV. The changes in the white line intensity of the O K-edge resonance increases as the edge position decreases due to the increasing of the unoccupied states number.

When we assess the net Löwdin charge (integrated number of occupied p electrons with respect to bulk lattice oxygen) of the various oxygen species, we find a rough correlation between the Löwdin charge and the edge position (Panel D of Figure A 7): the lower the Löwdin charge the lower the edge position. This indicates that the larger electrophilic ('hole') character of the O species the lower is its edge position. Thus, the low excitation energy species located at 529 eV is labeled as O^{I-}. One may also notice the spread of the Löwdin charge (and the edge position) for a

certain species. This has been related to the local effects, like surface orientation, H-bonding and neighboring vacancies. Ir vacancies (which could for example be created through Ir dissolution) create O^{I-} or OH species, for the latter once deprotonated defects push hole character on O, and hence push white line position down and intensity up. On the other hand, when an O is H bond acceptor in H-bonding, the white line position shifts up in energy.

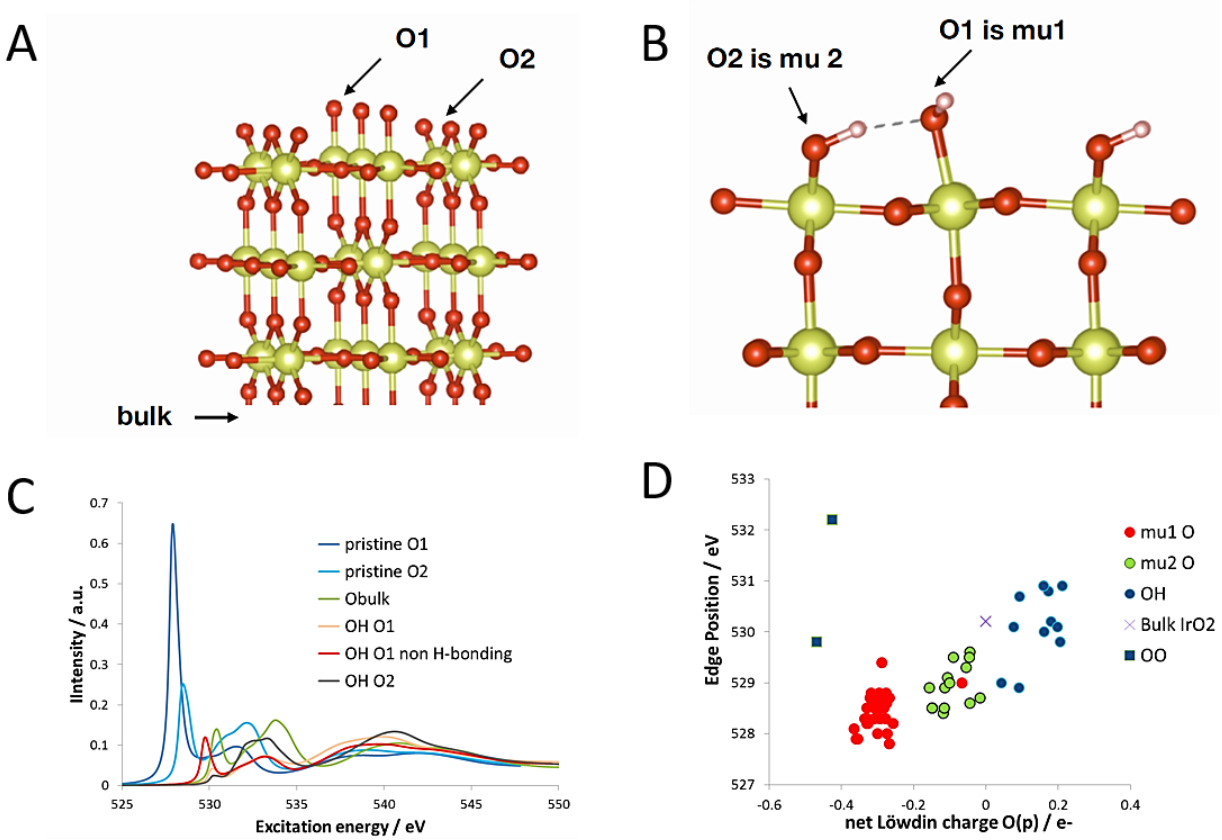

Figure A 7. Ball and stick structural model of the (110) IrO_2 surface with O (A) and OH (B) termination. O K-edges (C) computed for μ_1O (O1) and μ_2O (O2) oxygen with O and OH termination as well as for bulk (O^{2-}) anions. Correlation of the O K-edge white line position at various surface orientations as a function of the net Löwdin charge with respect to Löwdin charge of bulk O^{2-} in rutile IrO_2 (D). The data were provided by T. Jones.

A.9. O K edge Spectra Background

Figure A 8 shows the example of the O K edge background subtraction. The background was recorded on the sample under the same ambient conditions. For this, the sample holder was moved away from the electron analyzer in order to diminish the signal coming from the sample.

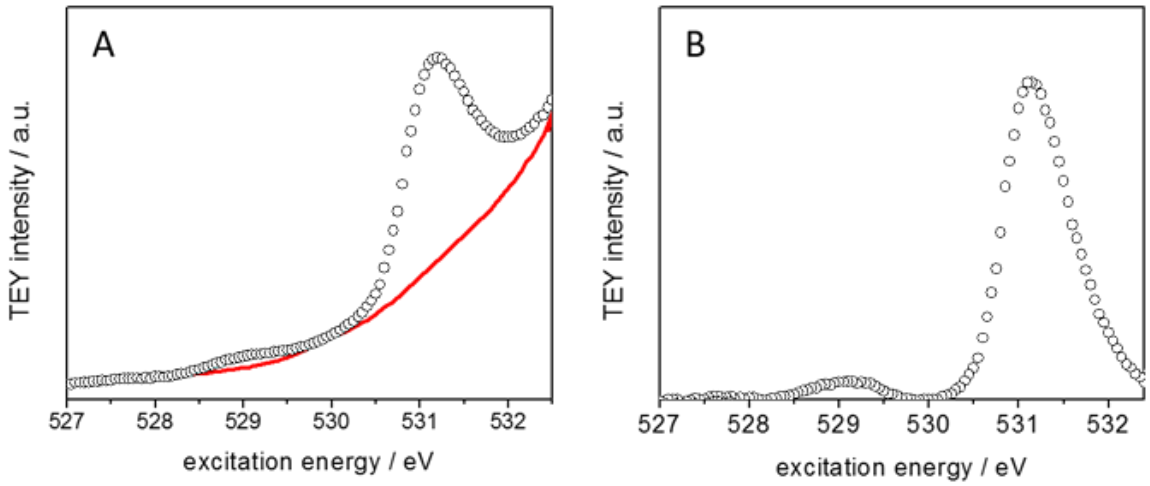

Figure A 8. Low excitation energy of O K edges (TEY) of Ir@IrOx anode under 3 mbar water vapor and 1.5 V before (A) and after (B) background subtraction. The background is marked red in Panel A.

A.10. Ir-based Anodes. O1s XP spectra

Figure A 9 shows the O1s XP spectra recorded on thermal and electrochemical iridium oxide anodes acquired at the end of the experiment at open circuit potential. The spectra obtained at the beginning of the *in-situ* measurements are shown in the main part in Figure 92. One may clearly see the appearance of the low BE component at 530 eV (assigned to lattice oxygen species) on spectra recorded on Ir@IrO_x anode (Panel A of Figure A 9) initially absent. This is most likely related to the formation of lattice-type oxide after two OER cycles performed on Ir@IrO_x anode (during O K edge and Ir4f measurements).

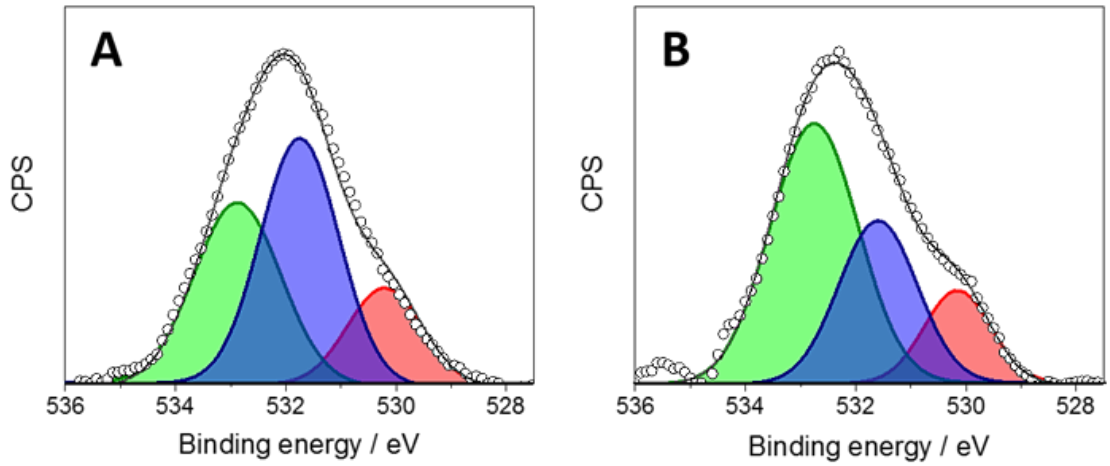

Figure A 9. O1s XP spectra of Ir@IrOx (A) and IrO2 (B) anodes under 3 mbar water vapor and OER conditions (E – iR = 1.5 V) obtained after two full OER cycles. Fitting: lattice oxide – red, hydroxide and C-O species - blue, water and C = O species – green. Kinetic energies: 530eV. Background subtraction was carried out using Shirley method and curve fitting was performed based on a Gaussian/Lorentzian GL(30) function.

A.11. Ir-based Reference Samples

Figure A 10 and Figure A 11 show the Ir4f and O1s XP spectra, respectively, recorded under UHV condition at ISISS beamline of BESSY II synchrotron on two commercial powders purchased from Alfa Aesar: anhydrous iridium (IV) oxide (Panel A) IrO_2 and iridium (IV) oxide dihydrate $IrO_2 \cdot 2H_2O$ (Panel B). The fitting of iridium core-level spectra was done according to the procedure described in[218]. One may clearly the difference in the FWHM of the main core-level peak: 0.7 eV for IrO_2 and 1.3 eV for $IrO_2 \cdot 2H_2O$. The quantitative analysis of the spectra obtained on hydrated oxide revealed also the presence of Ir (III) species (ca. 25%). The fitting of O1s XP spectra was done using three components: O_{lat} (530 eV), OH (ca. 531.4 eV) and adsorbed water (ca. 532.8 eV). The last two components also contain contribution of C=O and C-O species, correspondingly. Table A 6 also provides the atomic ratio calculated on the base of Ir4f, O1s and C1s photoemission spectra analysis. One may notice higher contribution of OH species in case of a hydrated $IrO_2 \cdot 2H_2O$ sample.

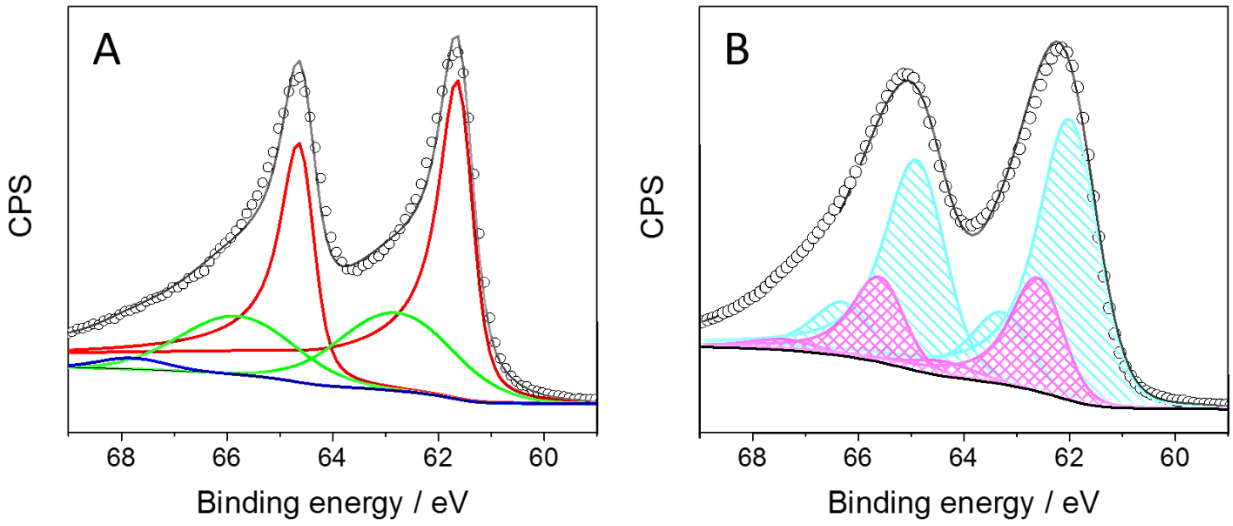

Figure A 10. Ir4f XP spectra recorded under UHV on commercial samples (Alfa Aesar): IrO_2 (Panel A) and IrO_2 $2H_2O$ (Panel B). The fitting was done analogous to the procedure described in Chapter 2. Color code for Panel A: Ir IV (red); Ir IV sat 1 (green); Ir IV sat 2 (blue). Color code for Panel B: Ir IV (cyan); Ir (III) magenta. Photon energy 595 eV, pass energy 20 eV.

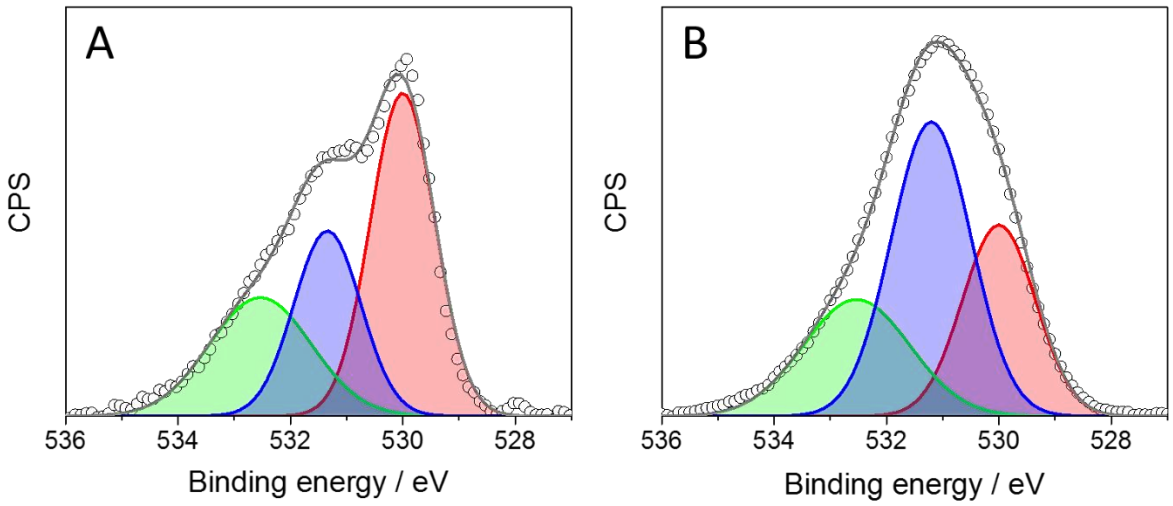

Figure A 11. O1s XP spectra recorded under UHV on commercial samples (Alfa Aesar): IrO_2 (Panel A) and IrO_2 $2H_2O$ (Panel B). The fitting was done analogous to the procedure described in Chapter 5. Color code for Panel A: O_{lat} (red); OH (blue); H_2O (green). Photon energy 1066 eV, pass energy 20 eV.

Table A 6. Results of the quantitative analysis of Ir4f, O1s and C1s XP spectra recorded under UHV at ISISS beamline (BESSY II) on reference samples IrO_2 and IrO_2 $2H_2O$

Sample	**Ir component / %**		**Atomic Ratio**			
	Ir (IV)	Ir (III)	C / Ir	O_{lat} / Ir	OH / Ir	O_{lat} / OH
IrO_2	100	0	17.7	4.4	2.9	1.5
IrO_2 $2H_2O$	75.6	24.4	17.8	2.9	5.0	0.6

A.12. STEM/EDX Mapping. Ir/ATO, Post-mortem Analysis

Figure A 12 shows the STEM-EDX maps obtained on the post-mortem Ir/ATO sample. It should be noted that Sn and Sb peaks overlap in the EDX spectra (3.44 keV and 3.60 keV for Sn and Sb, correspondingly) complicating the precise analysis of Sn/Sb distribution. Panel D of Figure A 12 contains the estimated Sn/Sb atomic content for various areas of the image marked in Panels B and C. Areas 1 and 5 are close to Ir nanoparticles, However, no enrichment of Sn nor of Sb can be observed in the vicinity of Ir nanoparticles.

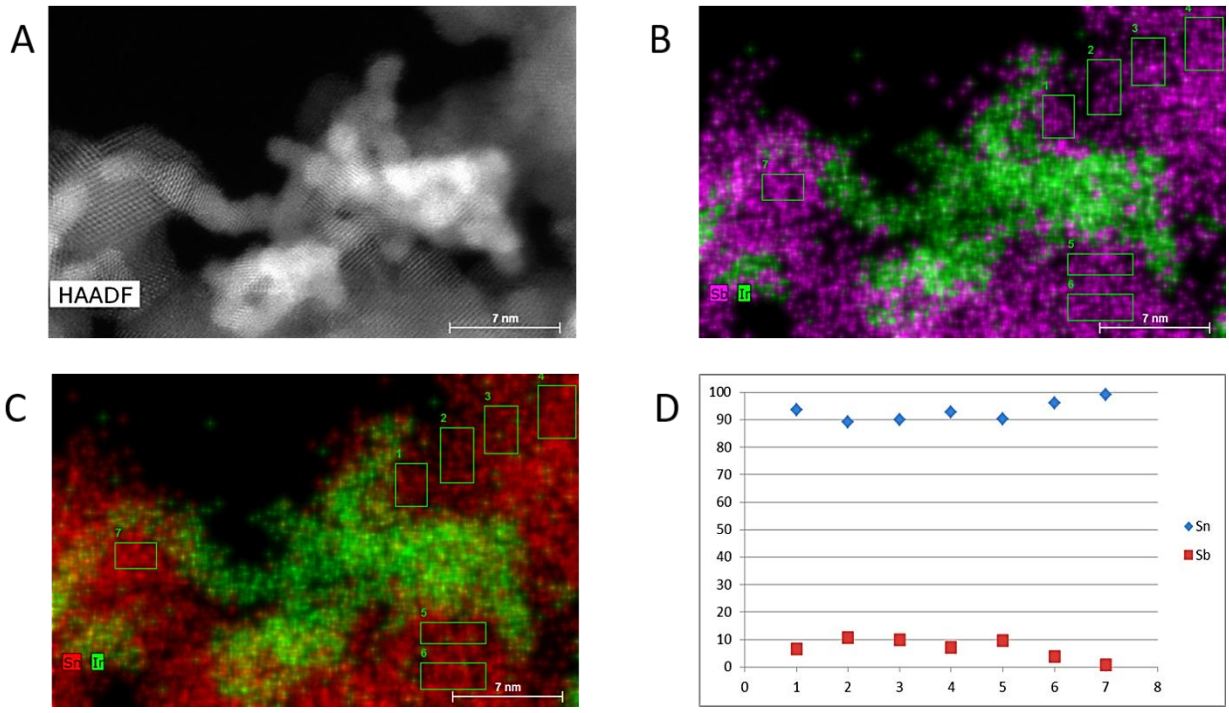

Figure A 12. HAADF-STEM image (Panel A) and STEM-EDX mixed maps (Panels B, D). Color code for the EDX map: Ir (green), Sn (red), Sb (violet). The Sn/Sb atomic content shown in Panel D was estimated for various areas marked in Panels B and C).

A.13. ATO-based anode, Electrochemical Characterization in NAP-XPS chamber

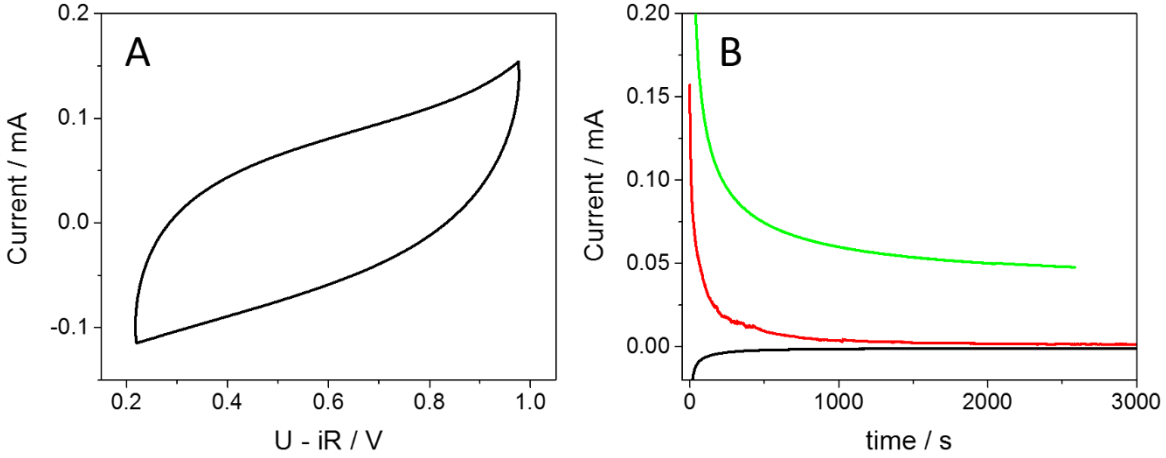

Figure A 13.Cyclic voltamogram (A) and chronoamperograms (B) recorded on Sb-doped SnO_2 anode (with graphene) in the NAP-XPS chamber under 3 mbar water vapor. Scan rate 20 mV s^{-1}. Applied potential for the CAs: 0.2 V (black); 1.0 V (red); 1.6 V (green). The potentials are Ohmic drop corrected.

A.14. SESSA Simulation: Results

The following tables demonstrate the examples of the estimated Sn / Ir ratio for different morphologies and various calculation parameters. For simplicity Figure 45 from the main text is shown here also (Figure A 14) For comparison, Table A 10 contains the experimental data.

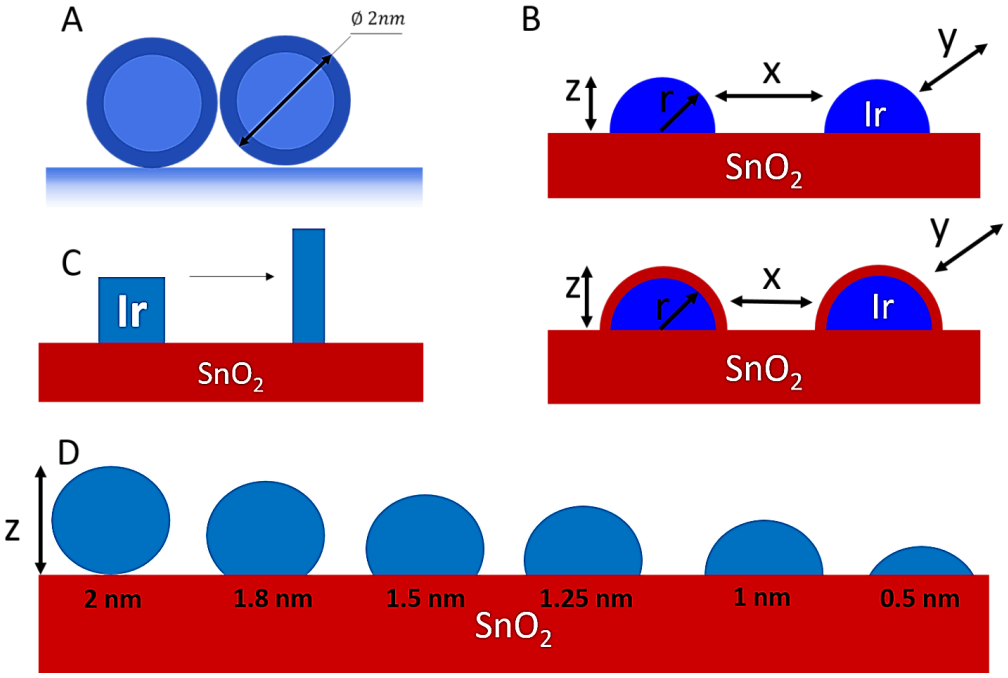

Figure A 14. Sketch of the models used for photoemission spectra simulation with the SESSA software. Panel A: "layered sphere" morphology, metallic iridium particles (d = 2 nm) covered by IrO_2 shell of various thickness, substrate - carbon; Panel B: "spheres" and "layered spheres" morphologies on SnO_2 substrate, in the latter case iridium nanoparticles are covered by tin oxide shell; Panel C: "islands" morphology, varied particles shape with constant volume; Panel D: "spheres" morphology, iridium nanoparticles on tin oxide substrate. This Figure duplicates the one shown in Figure 45.

Table A 7. The Sn / Ir ratio estimated for a "layered spheres" morphology (Panel B of Figure A 14) in SESSA software. The calculations were done for three kinetic energies used in the experiment.

Radius of Ir NPs / Å	**Tin oxide thickness / Å**	**Estimated Sn / Ir ratio**		
		390 eV	**530 eV**	**810 eV**
10	0	0.40	3.71	8.4
10	6	5.34	6.20	7.02
20	0	2.06	3.65	5.74
20	6	6.84	6.85	5.25
20	9	8.66	8.21	7.52

Table A 8. The Sn / Ir ratio estimated for a "islands" morphology (Panel C of Figure A 14) in SESSA software. The calculations were done for two kinetic energies used in the experiment.

Parallelepiped dimensions	**Sn / Ir ratio**	
	530 eV	**810 eV**
a = b = c = 15 Å	3.74	3.71
a = b ≠ c, c = 62 Å	4.85	9.63

Table A 9. The Sn / Ir ratio estimated for a "spheres" morphology (Panel D of Figure A 14) in SESSA software. Parameter z is the height of iridium nanoparticles observed above tin oxide substrate. The calculations were performed for two kinetic energies.

Parameter z / nm	***Sn / Ir ratio***	
	530 eV	**810 eV**
2.00	3.85	3.36
1.80	4.65	3.13
1.50	5.73	3.85
1.25	3.71	3.61

Table A 10. The Sn / Ir ratio estimated based on the experimental results for three kinetic energies of the emitted electrons (the data duplicate) Figure 106.

E - iR / V	**Sn / Ir Ratio**		
	390eV	**530eV**	**810eV**
0.2V	**1.70**	**3.48**	**3.48**
1.7V	**4.11**	**5.56**	**2.96**

The thickness of the electrochemical oxide shell formed on the surface of Ir nanoparticles was also estimated on the base of the modeling of the XP spectra. Panel A of Figure 45 shows the "layered spheres" morphology used for the calculations. The results are shown in Figure A 15.

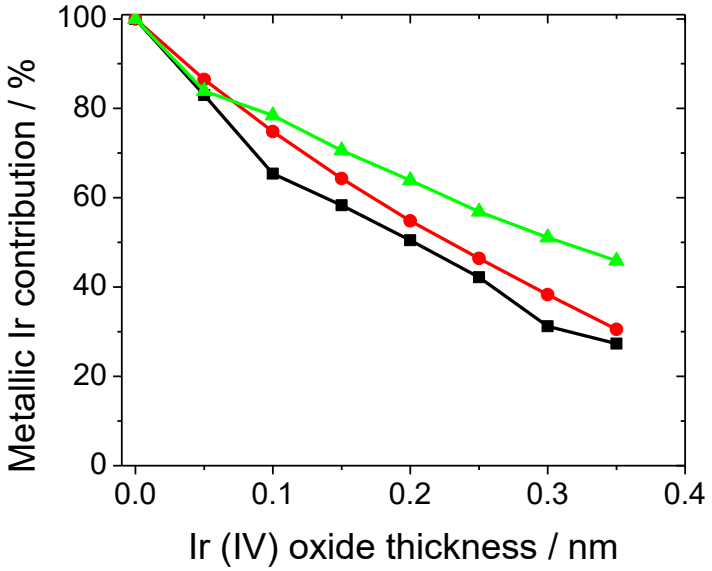

Figure A 15. Calculated dependence of the metallic Ir contribution versus the oxide thickness for three different kinetic energies of the emitted electrons: 390 eV (black); 530 eV (red); 810 eV (green).

A.15. Ir4f XP spectra recorded on Ir/ATO sample with low conductivity

Figure A 16 shows the fitted Ir4f XP spectra recorded on Ir/ATO sample without graphene under 3 mbar water vapor conditions and applied potential of 1.6 V. The fitting was done according to the common procedure discussed in Chapter 2, Section 2.4.6. The quantitative analysis revealed that the electrode surface was represented by metallic Ir (ca. 85 %) with small traces of Ir (III) component regardless the applied potential, confirming the absence of the proper connection in the catalyst layer discussed in Chapter 6.

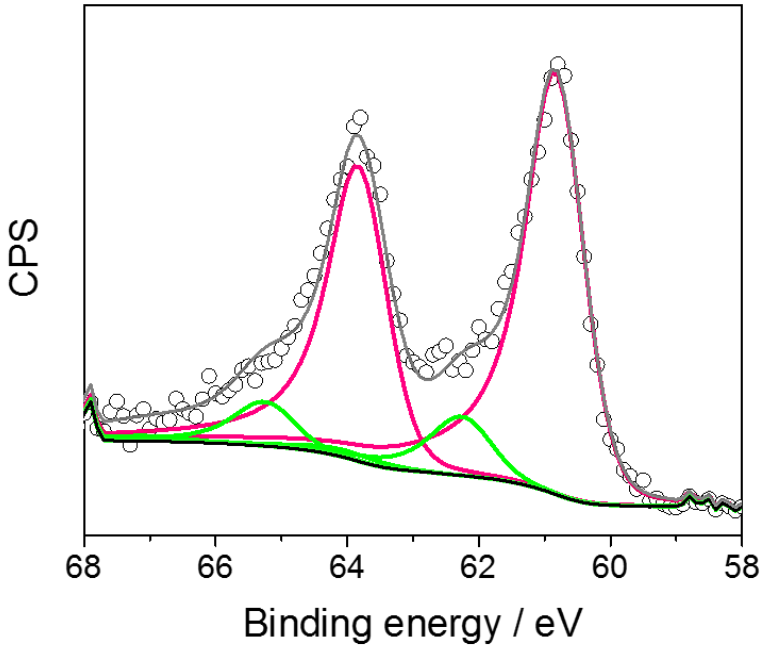

Figure A 16. Ir4f XP spectra obtained under 3 mbar water vapor on Ir/ATO anode for the low conductivity layer. Color code: metallic iridium – pink; Ir (III) – green. The BE position of the spectra was corrected according to the applied potential. The photon energy 595 eV.

A.16. C1s XP spectra recorded on Ir/ATO sample

The quantitative analysis of C1s XP spectra is complicated by the numerous contributions originating from adventitious carbon, graphene (see Section 6.3. Improvement of the Conductivity) and the Aquivion membrane. The XPS peak related to the graphene is assymetric and contains contributions of both sp^3- and sp^2-hybridized carbon located at ca. 284.8eV and 284.1eV, correspondingly[288]. In this work we do not aim to follow the carbon evolution during the reaction, thus we did not perform fitting of the C1s XP spectra. However, eventual drastic changes of the peak intensity or shape should be taken into account. Figure A 17 shows the C1s XP spectra recorded on Ir/ATO anode under 0.2V and 1.7V vs DHE and 3 mbar water vapor. The upper panel represents the corresponding differences of these peaks. One may see the increasing of the contribution of the oxidized carbon species at higher potential, however the evolution of C/Ir ratio under different experimental conditions shown in Table A 11 did not reveal significant changes.

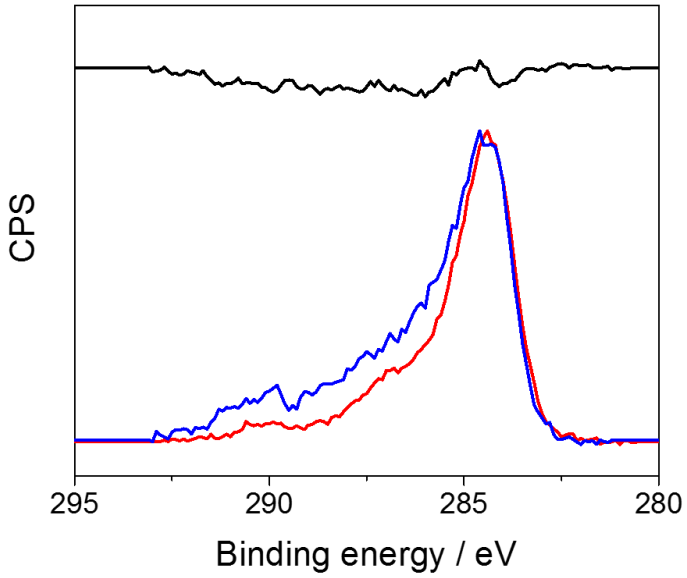

Figure A 17. C1s XP spectra recorded on Ir/ATO anode under 3 mbar water vapor and the following polarization: 0.2V (blue) and 1.7V (red). The upper side of the figure represents the difference spectra between them (black). The XP spectra were collected at the photon energy of 820eV.

Table A 11. C/Ir Atomic ratio calculated from the XP spectra obtained on Ir/ATO anode under different conditions.

Conditions	U – iR / V	C/Ir Atomic Ratio
vacuum	-	57
3 mbar water vapor	0.2	70
	1.7	61

A.17. Sn/Sb Atomic Ratio Evolution

While the Sn3d XPS peak cannot be distinguished on the Ir/ATO anode due to the Sn signal attenuation in the presence of iridium nanoparticles, the analysis of the results obtained on pure ATO-based anodes allowed us calculating the Sn/Sb atomic ratio under polarization and different photon energies. The results are shown in Figure A 18. One can see a higher contribution of antimony in the surface region (530 eV), nevertheless the Sn/Sb ratio stays constant regardless the applied potential. Antimony surface segregation has been previously observed and was related to its higher oxygen affinity. The absence of the potential-induced changes of this ratio emphasizes the stability of the support even at high anodic potentials.

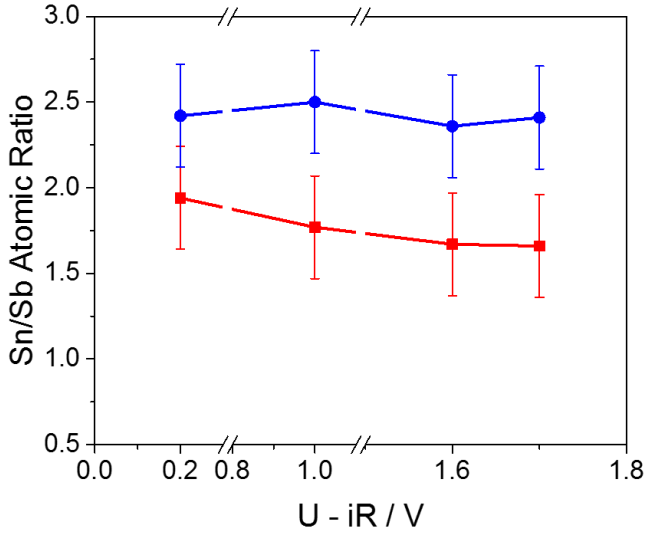

Figure A 18. Sn/Sb atomic ratio calculated from the XP spectra recorded on ATO-based anode under 3 mbar water vapor and different polarization conditions. The potential values are Ohmic drop corrected. The kinetic energies of the emitted electrons are 530 eV (red) and 810 eV (blue).

References

(1) Aneke, M.; Wang, M. Energy Storage Technologies and Real Life Applications – A State of the Art Review. *Appl. Energy* **2016**, *179*, 350–377.

(2) Ursua, A.; Gandia, L. M.; Sanchis, P. Hydrogen Production From Water Electrolysis: Current Status and Future Trends. *Proc. IEEE* **2012**, *100* (2), 410–426.

(3) Wang, M.; Wang, Z.; Gong, X.; Guo, Z. The Intensification Technologies to Water Electrolysis for Hydrogen Production – A Review. *Renew. Sustain. Energy Rev.* **2014**, *29*, 573–588.

(4) Pellow, M. A.; Emmott, C. J. M.; Barnhart, J.; Benson, S. M. Hydrogen or Batteries for Grid Storage ? A Net Energy Analysis. *Energy Environ. Sci.* **2015**, *8*, 1938–1952.

(5) Laguna-Bercero, M. A. Recent Advances in High Temperature Electrolysis Using Solid Oxide Fuel Cells : A Review. *J. Power Sources* **2012**, *203*, 4–16.

(6) Godula-Jopek, A. *Hydrogen Production: By Electrolysis*; John Wiley & Sons, 2015.

(7) Bi, L.; Boulfrad, S.; Traversa, E. Steam Electrolysis by Solid Oxide Electrolysis Cells (SOECs) with Proton-Conducting Oxides. *Chem. Soc. Rev.* **2014**, *43*, 8255–8270.

(8) Ebbesen, S. D.; Mogensen, M. Electrolysis of Carbon Dioxide in Solid Oxide Electrolysis Cells. *J. Power Sources* **2009**, *193*, 349–358.

(9) Moçoteguy, P.; Brisse, A. A Review and Comprehensive Analysis of Degradation Mechanisms of Solid Oxide Electrolysis Cells. *Int. J. Hydrogen Energy* **2013**, *38*, 15887–15902.

(10) Carmo, M.; Fritz, D. L.; Mergel, J.; Stolten, D. A Comprehensive Review on PEM Water Electrolysis. *Int. J. Hydrogen Energy* **2013**, *38* (12), 4901–4934.

(11) Leng, Y.; Chen, G.; Mendoza, A. J.; Tighe, T. B.; Hickner, M. A.; Wang, C. Y. Solid-State Water Electrolysis with an Alkaline Membrane. *J. Am. Chem. Soc.* **2012**, *134* (22), 9054–9057.

(12) Safizadeh, F.; Ghali, E.; Houlachi, G. Electrocatalysis Developments for Hydrogen Evolution Reaction in Alkaline Solutions - A Review. *Int. J. Hydrogen Energy* **2015**, *40* (1), 256–274.

(13) Zeng, K.; Zhang, D. Recent Progress in Alkaline Water Electrolysis for Hydrogen Production and Applications. *Prog. Energy Combust. Sci.* **2010**, *36* (3), 307–326.

(14) Fabbri, E.; Habereder, A.; Waltar, K.; Kötz, R.; Schmidt, T. J. Developments and Perspectives of Oxide-Based Catalysts for the Oxygen Evolution Reaction. *Catal. Sci. Technol.* **2014**, *4* (11), 3800–3821.

(15) Babic, U.; Suermann, M.; Felix, N. B.; Gubler, L.; Schmidt, T. J. Review — Identifying Critical Gaps for Polymer Electrolyte Water Electrolysis Development. *J. Electrochem. Soc.* **2017**, *164* (4), 387–399.

(16) *PEM Electrolysis for Hydrogen Production: Principles and Applications*; Bessarabov, D., Wang, H., Li, H., Zhao, N., Eds.; CRC Press, 2016.

(17) Hickner, M. A.; Kohl, P. A.; Kucernak, A. R.; Mustain, W. E.; Nijmeijer, K.; Scott, K.; Zhuang, L. Anion-Exchange Membranes in Electrochemical Energy Systems. *Energy*

Environ. Sci. **2014**, *7*, 3135–3191.

(18) Matsumoto, Y.; Sato, E. Electrocatalytic Properties of Transition Metal Oxides for Oxygen Evolution Reaction. *Mater. Chem. Phys.* **1986**, *14* (5), 397–426.

(19) Lettenmeier, P.; Wang, L.; Golla-Schindler, U.; Gazdzicki, P.; Cañas, N. A.; Handl, M.; Hiesgen, R.; Hosseiny, S. S. S.; Gago, A. S.; Friedrich, A. K. Nanosized IrOx-Ir Catalyst with Relevant Activity for Anodes of PEM Electrolysis Produced by a Cost-Effective Procedure. *Angew. Chemie* **2015**, *128*, 752–756.

(20) Shen, P. K.; Wang, C.-Y.; Jiang, S. P.; Sun, X.; Zhang, J. *Electrochemical Energy: Advanced Materials and Technologies*; CRC Press, 2016.

(21) Pourbaix, M. J. N.; Van Muylder, J.; de Zoubov, N. Electrochemical Properties of the Platinum Metals - Johnson Matthey Technology Review. *Platin. Met. Rev.* **1959**, *3* (3), 100–106.

(22) Kötz, R.; Lewerenz, H. J.; Stucki, S. XPS Studies of Oxygen Evolution on Ru and RuO2 Anodes. *J. Electrochem. Soc.* **1983**, *130* (4), 825–829.

(23) Wohlfahrt-Mehrens, M.; Heitbaum, J. Oxygen Evolution on Ru and RuO2 Electrodes Studied Using Isotope Labelling and on-Line Mass Spectrometry. *J. Electroanal. Chem. Interfacial Electrochem.* **1987**, *237*, 251–260.

(24) Cherevko, S.; Geiger, S.; Kasian, O.; Kulyk, N.; Grote, J.; Savan, A.; Ratna, B.; Merzlikin, S.; Breitbach, B.; Ludwig, A.; et al. Oxygen and Hydrogen Evolution Reactions on Ru , RuO2 , Ir , and IrO2 Thin Film Electrodes in Acidic and Alkaline Electrolytes : A Comparative Study on Activity and Stability. *Catal. Today* **2016**, *262*, 170–180.

(25) Danilovic, N.; Subbaraman, R.; Chang, K. C.; Chang, S. H.; Kang, Y. J.; Snyder, J.; Paulikas, A. P.; Strmcnik, D.; Kim, Y. T.; Myers, D.; et al. Activity-Stability Trends for the Oxygen Evolution Reaction on Monometallic Oxides in Acidic Environments. *J. Phys. Chem. Lett.* **2014**, *5* (14), 2474–2478.

(26) Hodnik, N.; Jovanovič, P.; Pavlišič, A.; Jozinović, B.; Zorko, M.; Bele, M.; Šelih, V. S.; Šala, M.; Hočevar, S.; Gaberšček, M. New Insights into Corrosion of Ruthenium and Ruthenium Oxide Nanoparticles in Acidic Media. *J. Phys. Chem. C* **2015**, *119* (18), 10140–10147.

(27) Paoli, E. A.; Masini, F.; Frydendal, R.; Deiana, D.; Schlaup, C.; Malizia, M.; Hansen, T. W.; Horch, S.; Stephens, I. E. L.; Chorkendorff, I. Oxygen Evolution on Well-Characterized Mass-Selected Ru and RuO_2 Nanoparticles. *Chem. Sci.* **2015**, *6* (1), 190–196.

(28) Kolotyrkin, Y. M.; Losev, V. V; Chemodanov, A. N. Relationship between Corrosion Processes and Oxygen Evolution on Anodes Made from Noble Metals and Related Metal Oxide Anodes. *Mater. Chem. Phys.* **1988**, *19*, 1–95.

(29) Iwakura, C.; Hirao, K.; Tamura, H. Anodic Evolution of Oxygen on Ruthenium in Acidic Solutions. *Electrochim. Acta* **1977**, *22* (4), 329–334.

(30) Lee, Y.; Suntivich, J.; May, K. J.; Perry, E. E.; Shao-Horn, Y. Synthesis and Activities of Rutile IrO2 and RuO2 Nanoparticles for Oxygen Evolution in Acid and Alkaline Solutions. *Phys. Chem. Lett.* **2012**, *3*, 399–404.

(31) Geiger, S.; Kasian, O.; Shrestha, B. R.; Mingers, A. M.; Mayrhofer, K. J. J.; Cherevko, S. Activity and Stability of Electrochemically and Thermally Treated Iridium for the Oxygen Evolution Reaction. *J. Electrochem. Soc.* **2016**, *163* (11), 3132–3138.

(32) Augustynski, J.; Koudelka, M.; Sanchez, J.; Conway, B. E. ESCA Study of the State of Iridium and Oxygen in Electrochemically and Thermally Formed Iridium Oxide Films. *J. Electroanal. Chem.* **1984**, *160* (1–2), 233–248.

(33) Trasatti, S.; Buzzanca, G. Ruthenium Dioxide: A New Interesting Electrode Material. Solid Structure and Electrochemical Behaviour. *J. Electroanal. Chem. Interfacial Electrochem.* **1971**, *29*, A1–A5.

(34) Kötz, R.; Stucki, S. Stabilization of RuO2 by IrO2 for Anodic Oxygen Evolution in Acid Media. *Electrochim. Acta* **1986**, *31* (10), 1311–1316.

(35) Angelinetta, C.; Trasatti, S.; Atanososka, L. D.; Atanasoski, R. T. Surface Properties of RuO2 + IrO2 Mixed Oxide Electrodes. *J. Electroanal. Chem. Interfacial Electrochem.* **1986**, *214* (1–2), 535–546.

(36) Yeo, R. S.; Orehotsky, J.; Visscher, W.; Srinivasan, S. Ruthenium-Based Mixed Oxides as Electrocatalysts for Oxygen Evolution in Acid Electrolytes. *J. Electrochem. Soc.* **1981**, *128* (9), 1900–1904.

(37) Forgie, R.; Bugosh, G.; Neyerlin, K. C.; Liu, Z.; Strasser, P. Bimetallic Ru Electrocatalysts for the OER and Electrolytic Water Splitting in Acidic Media. *Electrochem. Solid-State Lett.* **2010**, *13* (4), 36–39.

(38) Neyerlin, K. C.; Bugosh, G.; Forgie, R.; Liu, Z.; Strasser, P.; Chemie, I.; Berlin, T. U. Combinatorial Study of High-Surface-Area Binary and Ternary Electrocatalysts for the Oxygen Evolution Reaction. *J. Electrochem. Soc.* **2009**, *156* (3), B363–B369.

(39) Over, H. Surface Chemistry of Ruthenium Dioxide in Heterogeneous Catalysis and Electrocatalysis: From Fundamental to Applied Research. *Chem. Rev.* **2012**, *112* (6), 3356–3426.

(40) Birss, V. I.; Bock, C.; Elzanowska, H. Hydrous Ir Oxide Films: The Mechanism of the Anodic Prepeak Reaction. *Canandian J Chem* **1997**, *75*, 1687–1693.

(41) Cherevko, S.; Geiger, S.; Kasian, O.; Mingers, A.; Mayrhofer, K. J. J. Oxygen Evolution Activity and Stability of Iridium in Acidic Media . Part 1 . – Metallic Iridium. *J. Electroanal. Chem.* **2016**, *773*, 69–78.

(42) Kodintsev, I. M.; Trasatti, S.; Rubel, M.; Wieckowski, A.; Kaufher, N. X-Ray Photoelectron Spectroscopy and Electrochemical Surface Characterization of IrO2 + RuO2 Electrodes. *Langmuir* **1992**, *8* (7), 283–290.

(43) Mo, Y.; Stefan, I. C.; Cai, W.-B.; Dong, J.; Carey, P.; Scherson, D. A. In Situ Iridium L III-Edge X-Ray Absorption and Surface Enhanced Raman Spectroscopy of Electrodeposited Iridium Oxide Films in Aqueous Electrolytes. *J. Phys. Chem. B* **2002**, *106* (14), 3681–3686.

(44) Cukman, D.; Vukovic, M. Electrochemical Behaviour of an Electrodeposited Electrode in Acid Solution. *J Electroanal Chem* **1990**, *279*, 283–290.

(45) Conway, B. E. Transition from “Supercapacitor” to “Battery” Behavior in Electrochemical Energy Storage. *J Electrochem Soc* **1991**, *138* (6), 1539–1548.

(46) Conway, B. E. E.; Mozota, J. Surface and Bulk Processes at Oxidized Iridium electrodes—II. Conductivity-Switched Behaviour of Thick Oxide Films. *Electrochim. Acta* **1983**, *28* (1), 9–16.

(47) Mozota, J.; Conway, B. E. Surface and Bulk Processes at Oxidized Iridium electrodes—I. Monolayer Stage and Transition to Reversible Multilayer Oxide Film Behaviour.

Electrochim. Acta **1983**, *28* (1), 1–8.

(48) Burke, L. D.; Whelan, D. P. A Voltammetric Investigation of the Charge Storage Reactions of Hydrous Iridium Oxide Layers. *J Electroanal Chem* **1984**, *162*, 121–141.

(49) Audichon, T.; Mayousse, E.; Morisset, S.; Morais, C.; Comminges, C.; Napporn, T. W.; Kokoh, K. B. Electroactivity of RuO2-IrO2 Mixed Nanocatalysts toward the Oxygen Evolution Reaction in a Water Electrolyzer Supplied by a Solar Profile. *Int. J. Hydrogen Energy* **2014**, *39* (30), 16785–16796.

(50) Lervik, I. A.; Tsypkin, M.; Owe, L. E.; Sunde, S. Electronic Structure vs. Electrocatalytic Activity of Iridium Oxide. *J. Electroanal. Chem.* **2010**, *645* (2), 135–142.

(51) Sunde, S.; Lervik, I. A.; Tsypkin, M.; Owe, L. Impedance Analysis of Nanostructured Iridium Oxide Electrocatalysts. **2010**, *55*, 7751–7760.

(52) Kötz, E. R.; Neff, H. Anodic Iridium Oxide Films: An UPS Study of Emersed Electrodes. *Surf. Sci.* **1985**, *160*, 517–530.

(53) Glarum, S.; Marshall, J. The A-C Response of Iridium Oxide Films. *J. Electrochem. Soc.* **1980**, *127* (7), 1467–1474.

(54) Lyons, M. E. G.; Floquet, S. Mechanism of Oxygen Reactions at Porous Oxide Electrodes. Part 2—Oxygen Evolution at RuO2, IrO2 and IrxRu1−xO2 Electrodes in Aqueous Acid and Alkaline Solution. *Phys. Chem. Chem. Phys.* **2011**, *13* (12), 5314–5355.

(55) Minguzzi, A.; Lugaresi, O.; Achilli, E.; Locatelli, C.; Vertova, A.; Ghigna, P.; Rondinini, S. Observing the Oxidation State Turnover in Heterogeneous Iridium-Based Water Oxidation Catalysts. *Chem. Sci.* **2014**, *5*, 3591–3597.

(56) Kötz, R.; Neff, H.; Stucki, S. Anodic Iridium Oxide Films. XPS-Studies of Oxidation State Changes and O2-Evolution. *J. Electrochem. Soc.* **1984**, *131* (1), 72–77.

(57) Hüppauff, M.; Lengeler, B. Valency and Structure of Iridium in Anodic Iridium Oxide Films. *J. Electrochem. Soc.* **1993**, *140* (3), 598–602.

(58) Reier, T.; Oezaslan, M.; Strasser, P. Electrocatalytic Oxygen Evolution Reaction (OER) on Ru, Ir, and Pt Catalysts: A Comparative Study of Nanoparticles and Bulk Materials. *ACS Catal.* **2012**, *2* (8), 1765–1772.

(59) Mckeown, D. A.; Hagans, P. L.; Carette, L. P. L.; Russell, A. E.; Swider, K. E.; Rolison, D. R. Structure of Hydrous Ruthenium Oxides : Implications for Charge Storage. *J. Phys. Chem. B* **1999**, *103*, 4825–4832.

(60) Trasatti, S. Physical Electrochemistry of Ceramic Oxides. *Electrochim. Acta* **1991**, *36* (2), 225–241.

(61) Zheng, J. P.; Jow, T. R. A New Charge Storage Mechanism for Electrochemical Capacitors. *J Electrochem Soc* **1995**, *142* (1), L6–L8.

(62) Liu, Y.; Zhou, F.; Ozolins, V. Ab Initio Study of the Charge-Storage Mechanisms in RuO 2 -Based Electrochemical Ultracapacitors. *J. Phys. Chem. C* **2012**, *116*, 1450–1457.

(63) Juodkazytė, J.; Vilkauskaitė, R.; Stalnionis, G.; Šebeka, B.; Juodkazis, K. EQCM Study of Ru and RuO 2 Surface Electrochemistry. *Electroanalysis* **2007**, *19* (10), 1093–1099.

(64) Gileadi, E. *Physical Electrochemistry*; WILEY-VCH, 2011.

(65) Newman, J.; Thomas-Alyea, K. E. *Electrochemical Systems*; WILEY-INTERSCIENCE,

2004.

(66) Shinagawa, T.; Garcia-esparza, A. T.; Takanabe, K. Insight on Tafel Slopes from a Microkinetic Analysis of Aqueous Electrocatalysis for Energy Conversion. *Sci. Rep.* **2015**, *5*, 13801–13821.

(67) Guidelli, R.; Compton, R. G.; Feliu, J. M.; Gileadi, E.; Lipkowski, J.; Schmickler, W.; Trasatti, S. Defining the Transfer Coefficient in Electrochemistry: An Assessment (IUPAC Technical Report). *Pure Appl. Chem.* **2014**, *86* (2), 245–258.

(68) Fletcher, S. Tafel Slopes from First Principles. *J. Solid State Electrochem.* **2009**, *13* (4), 537–549.

(69) Trasatti, S.; Lodi, G. *Electrodes of Conductive Metallic Oxides Part B*; Elsevier: Amsterdam, 1981.

(70) Damjanovic, A.; Dey, A.; Bockris, J. O. Kinetics of Oxygen Evolution and Dissolution on Platinum Electrodes. *Electrochim. Acta* **1966**, *11*, 791–814.

(71) Trasatti, S. Electrocatalysis by Oxides - Attempt at a Unifying Approach. *J Electroanal Chem* **1980**, *111*, 125–131.

(72) Rocchini, G. Influence of Ohmic Drop on the Determination of Electrochemical Parameters. *Stud. Environ. Sci.* **1994**, *59*, 377–413.

(73) Angelinetta, C.; Trasatti, S.; Atanasoska, L. D.; Minevski, Z. S.; Atanasoski, R. T. Effect of Preparation on the Surface and Electrocatalytic Properties of RuO2 + IrO2 Mixed Oxide Electrodes. *Mater. Chem. Phys.* **1989**, *22* (1–2), 231–247.

(74) Kötz, R. Photoelectron Spectroscopy of Practical Electrode Materials. *Adv. Electrochem. Sci. Eng.* **1990**, 75–126.

(75) Oh, H.; Nong, H. N.; Reier, T.; Bergmann, A.; Gliech, M.; Ferreira, J.; Arau, D.; Willinger, E.; Schlo, R.; Teschner, D.; et al. Electrochemical Catalyst − Support Effects and Their Stabilizing Role for IrO X Nanoparticle Catalysts during the Oxygen Evolution Reaction. *J. Am. Chem. Soc.* **2016**, *138* (38), 12552–12563.

(76) Giménez, S.; Bisquert, J. *Photoelectrochemical Solar Fuel Production: From Basic Principles to Advanced Devices*; 2016.

(77) Antolini, E. Iridium as Catalyst and Cocatalyst for Oxygen Evolution / Reduction in Acidic Polymer Electrolyte Membrane Electrolyzers and Fuel Cells. *ACS Catal.* **2014**, *4* (5), 1426–1440.

(78) Reier, T.; Teschner, D.; Lunkenbein, T.; Bergmann, a; Selve, S.; Kraehnert, R.; Schlögl, R.; Strasser, P. Electrocatalytic Oxygen Evolution on Iridium Oxide: Uncovering Catalyst-Substrate Interactions and Active Iridium Oxide Species. *J. Electrochem. Soc.* **2014**, *161* (9), F876–F882.

(79) Trasatti, S. Electrocatalysis in the Anodic Evolution of Oxygen and Chlorine. *Electrochim. Acta* **1984**, *29* (11), 1503–1512.

(80) Man, I. C.; Su, H. Y.; Calle-Vallejo, F.; Hansen, H. A.; Martínez, J. I.; Inoglu, N. G.; Kitchin, J.; Jaramillo, T. F.; Nørskov, J. K.; Rossmeisl, J. Universality in Oxygen Evolution Electrocatalysis on Oxide Surfaces. *ChemCatChem* **2011**, *3* (7), 1159–1165.

(81) Koper, M. T. M. Thermodynamic Theory of Multi-Electron Transfer Reactions : Implications for Electrocatalysis. *J. Electroanal. Chem.* **2011**, *660* (2), 254–260.

(82) Rossmeisl, J.; Logadottir, A.; Nørskov, J. K. Electrolysis of Water on (Oxidized) Metal Surfaces. *Chem. Phys.* **2005**, *319*, 178–184.

(83) Rossmeisl, J.; Qu, Z. W.; Zhu, H.; Kroes, G. J.; Nørskov, J. K. Electrolysis of Water on Oxide Surfaces. *J. Electroanal. Chem.* **2007**, *607* (1–2), 83–89.

(84) Kötz, R.; Stucki, S.; Scherson, D.; Kolb, D. M. In-Situ Identification of RuO4 as the Corrosion Product During Oxygen Evolution on Ruthenium in Acid Media. *J. Electroanal. Chem.* **1984**, *172*, 211–219.

(85) Miles, M. H.; Klaus, E. A.; Gunn, B. P.; Locker, J. R.; Serafin, W. E.; Srinivasan, S. The Oxygen Evolution Reaction on Platinum, Iridium, Ruthenium and Their Alloys at 80°C in Acid Solutions. *Electrochim. Acta* **1978**, *23* (6), 521–526.

(86) Vukovic, M. Rotating Ring-Disc Electrode Study of the Enhanced Oxygen Evolution on an Activated Ruthenium Electrode. *J Chem Soc, Faraday Trans I* **1990**, *86* (22), 3743–3746.

(87) Albery, W. J.; Hitchman, M. L. *Ring-Disc Electrodes*; Clarendon Press, Oxford, 1971.

(88) Diaz-Morales, O.; Calle-Vallejo, F.; Munck, C. de; Koper, M. T. M. Electrochemical Water Splitting by Gold: Evidence for an Oxide Decomposition Mechanism. *Chem. Sci.* **2013**, *4*, 2334–2343.

(89) Diaz-Morales, O.; Ferrus-Suspedra, D.; Koper, M. T. M. The Importance of Nickel Oxyhydroxide Deprotonation on Its Activity towards Electrochemical Water Oxidation. *Chem. Sci.* **2016**, *7*, 2639–2645.

(90) Weaver, M. J. Surface-Enhanced Raman Spectroscopy as a Versatile in Situ Probe of Chemisorption in Catalytic Electrochemical and Gaseous Environments. *J. Raman Spectrosc.* **2002**, *33* (5), 309–317.

(91) Wu, D.; Li, J.; Ren, B.; Tian, Z. Electrochemical Surface-Enhanced Raman Spectroscopy of Nanostructures. *Chem Soc Rev* **2008**, *37*, 1025–1041.

(92) Fierro, S.; Nagel, T.; Baltruschat, H.; Comninellis, C. Investigation of the Oxygen Evolution Reaction on Ti/IrO2 Electrodes Using Isotope Labelling and on-Line Mass Spectrometry. *Electrochem. commun.* **2007**, *9* (8), 1969–1974.

(93) Chang, S. H.; Danilovic, N.; Chang, K.; Subbaraman, R.; Paulikas, A. P.; Fong, D. D.; Highland, M. J.; Baldo, P. M.; Stamenkovic, V. R.; Freeland, J. W.; et al. Functional Links between Stability and Reactivity of Strontium Ruthenate Single Crystals during Oxygen Evolution. *Nat. Commun.* **2014**, *5*, 4191–4200.

(94) Cherevko, S.; Geiger, S.; Kasian, O.; Mingers, A.; Mayrhofer, K. J. J. Oxygen Evolution Activity and Stability of Iridium in Acidic Media . Part 2 . – Electrochemically Grown Hydrous Iridium Oxide. *JEAC* **2016**, *774*, 102–110.

(95) Binninger, T.; Mohamed, R.; Waltar, K.; Fabbri, E.; Levecque, P.; Kötz, R.; Schmidt, T. J. Thermodynamic Explanation of the Universal Correlation between Oxygen Evolution Activity and Corrosion of Oxide Catalysts. *Sci. Rep.* **2015**, *5*, 12167–12174.

(96) Stoerzinger, K. A.; Diaz-Morales, O.; Kolb, M.; Rao, R. R.; Frydendal, R.; Qiao, L.; Wang, X. R.; Halck, N. B.; Rossmeisl, J.; Hansen, H. A.; et al. Orientation-Dependent Oxygen Evolution on RuO_2 without Lattice Exchange. *ACS Energy Lett.* **2017**, *2* (4), 876–881.

(97) O'Grady, W.; Iwakura, C.; Huang, J.; Yeager, E. *Electrocatalysis*; The Electrochemical Society: Princeton, 1974.

(98) Kötz, R.; Lewerenz, H. J.; Brüesch, P.; Stucki, S. Oxygen Evolution on Ru and Ir

Electrodes. *J. Electroanal. Chem. Interfacial Electrochem.* **1983**, *150* (1–2), 209–216.

(99) Kasian, O.; Geiger, S.; Stock, P.; Polymeros, G.; Breitbach, B.; Savan, A.; Ludwig, A.; Cherevko, S.; Mayrhofer, K. J. J. On the Origin of the Improved Ruthenium Stability in RuO_2 –IrO_2 Mixed Oxides. *J. Electrochem. Soc.* **2016**, *163* (11), F3099–F3104.

(100) Arrigo, R.; Hävecker, M.; Schuster, M. E.; Ranjan, C.; Stotz, E.; Knop-Gericke, A.; Schlögl, R. In Situ Study of the Gas-Phase Electrolysis of Water on Platinum by NAP-XPS. *Angew. Chemie - Int. Ed.* **2013**, *52* (44), 11660–11664.

(101) Sanchez Casalongue, H. G.; Ng, M. L.; Kaya, S.; Friebel, D.; Ogasawara, H.; Nilsson, A. In Situ Observation of Surface Species on Iridium Oxide Nanoparticles during the Oxygen Evolution Reaction. *Angew. Chemie Int. Ed.* **2014**, *53* (28), 7169–7172.

(102) Papaefthimiou, V.; Diebold, M.; Ulhaq-Bouillet, C.; Doh, W. H.; Blume, R.; Zafeiratos, S.; Savinova, E. R. Potential-Induced Segregation Phenomena in Bimetallic PtAu Nanoparticles: An In Situ Near-Ambient-Pressure Photoelectron Spectroscopy Study. *ChemElectroChem* **2015**, *2* (10), 1519–1526.

(103) Pedersen, A. F.; Escudero-Escribano, M.; Sebok, B.; Bodin, A.; Paoli, E. A.; Frydendal, R.; Friebel, D.; Stephens, I. E. L.; Rossmeisl, J.; Chorkendorff, I.; et al. Operando XAS Study of the Surface Oxidation State on a Monolayer IrO on RuO and Ru Oxide Based Nanoparticles for Oxygen Evolution in Acidic Media. *J. Phys. Chem. B* **2017**, No. DOI 10.1021/acs.jpcb.7b06982.

(104) Pfeifer, V.; Jones, T. E.; Velasco Vélez, J. J.; Massué, C.; Greiner, M. T.; Arrigo, R.; Teschner, D.; Girgsdies, F.; Scherzer, M.; Allan, J.; et al. The Electronic Structure of Iridium Oxide Electrodes Active in Water Splitting. *Phys. Chem. Chem. Phys.* **2016**, *18*, 2292–2296.

(105) Minguzzi, A.; Lugaresi, O.; Locatelli, C.; Rondinini, S.; Acapito, F. D.; Achilli, E.; Ghigna, P.; Pavia, U.; Chimica, D.; Taramelli, V. Fixed Energy X - Ray Absorption Voltammetry. *Anal. Chem.* **2013**, *85*, 7009–7013.

(106) Grimaud, A.; Diaz-Morales, O.; Han, B.; Hong, W. T.; Lee, Y.-L.; Giordano, L.; Stoerzinger, K. A.; Koper, M. T. M.; Shao-Horn, Y. Activating Lattice Oxygen Redox Reactions in Metal Oxides to Catalyze Oxygen Evolution. *Nat. Chem.* **2017**, *9*, 457–465.

(107) Mueller, D. N.; Machala, M. L.; Bluhm, H.; Chueh, W. C. Redox Activity of Surface Oxygen Anions in Oxygen-Deficient Perovskite Oxides during Electrochemical Reactions. *Nat. Commun.* **2015**, *6*, 6097–6105.

(108) Pfeifer, V.; Jones, T. E.; Velasco Vélez, J. J.; Arrigo, R.; Piccinin, S.; Hävecker, M.; Knop-Gericke, A.; Schlögl, R. In Situ Observation of Reactive Oxygen Species Forming on Oxygen-Evolving Iridium Surfaces. *Chem. Sci.* **2017**, *8*, 2143–2149.

(109) Nong, H. N.; Oh, H. S.; Reier, T.; Willinger, E.; Willinger, M. G.; Petkov, V.; Teschner, D.; Strasser, P. Oxide-Supported IrNiOx Core-Shell Particles as Efficient, Cost-Effective, and Stable Catalysts for Electrochemical Water Splitting. *Angew. Chemie - Int. Ed.* **2015**, *54* (10), 2975–2979.

(110) Wang, L.; Saveleva, V. A.; Zafeiratos, S.; Savinova, E. R.; Lettenmeier, P.; Gazdzicki, P.; Gago, A. S.; Friedrich, K. A. Highly Active Anode Electrocatalysts Derived from Electrochemical Leaching of Ru from Metallic Ir 0 .7 Ru 0 .3 for Proton Exchange Membrane Electrolyzers. *Nano Energy* **2017**, *34*, 385–391.

(111) Cognard, G.; Ozouf, G.; Beauger, C.; Lopez-Haro, M.; Chatenet, M.; Maillard, F. Pt

Nanoparticles Supported on Antimony-Doped and Niobium-Doped Tin Dioxide: Stability in Different Potential Ranges. *Electrochim. Acta* **2017**, *245*, 993–1004.

(112) Antolini, E. Carbon Supports for Low-Temperature Fuel Cell Catalysts. *Appl. Catal. B Environ.* **2009**, *88*, 1–24.

(113) Jackson, C.; Smith, G. T.; Inwood, D. W.; Leach, A. S.; Whalley, P. S.; Callisti, M.; Polcar, T.; Russell, A. E.; Levecque, P.; Kramer, D. Electronic Metal-Support Interaction Enhanced Oxygen Reduction Activity and Stability of Boron Carbide Supported Platinum. *Nat. Commun.* **2017**, *8* (May), 15802–15813.

(114) Moradi, F.; Dehghanian, C. Addition of IrO2 to RuO2+TiO2 Coated Anodes and Its Effect on Electrochemical Performance of Anodes in Acid Media. *Prog. Nat. Sci. Mater. Int.* **2014**, *24* (2), 134–141.

(115) Aizawa, M.; Lee, S.; Anderson, S. L. Deposition Dynamics and Chemical Properties of Size-Selected Ir Clusters on TiO2. *Surf. Sci.* **2003**, *542* (3), 253–275.

(116) Walsh, F. C.; Wills, R. G. A. The Continuing Development of Magneli Phase Titanium Sub-Oxides and Ebonex (R) Electrodes. *Electrochim. Acta* **2010**, *55*, 6342–6351.

(117) Wang, L.; Lettenmeier, P.; Golla-Schindler, U.; Gazdzicki, P.; Cañas, N.; Handl, M.; Hiesgen, R.; Hosseiny, S. S.; Gago, A. S.; Friedrich, A. K. Nanostructured Ir-Supported on Ti4O7 as Cost Effective Anode for Proton Exchange Membrane (PEM) Electrolyzers. *Phys. Chem. Chem. Phys.* **2015**, *18*, 4487–4495.

(118) Wickman, B.; Wesselmark, M.; Lagergren, C.; Lindbergh, G. Tungsten Oxide in Polymer Electrolyte Fuel Cell Electrodes — A Thin-Film Model Electrode Study. *Electrochim. Acta* **2011**, *56*, 9496–9503.

(119) Liu, G.; Xu, J.; Wang, X. An Oxygen Evolution Catalyst on an Antimony Doped Tin Oxide Nanowire Structured Support for Electrolysis. *J. Mater. Chem. A Mater. energy Sustain.* **2015**, *3*, 20791–20800.

(120) Geiger, S.; Kasian, O.; Mingers, A. M.; Mayrhofer, K. J. J.; Cherevko, S. Stability Limits of Tin-Based Electrocatalyst Supports Stability Limits of Tin-Based Electrocatalyst Supports. *Sci. Rep.* **2017**, *7*, 4595–4602.

(121) Fabbri, E.; Rabis, A.; Ko, R.; Schmidt, T. J. Pt Nanoparticles Supported on Sb-Doped SnO2 Porous Structures : Developments and Issues. *PCCP* **2014**, *16*, 13672–13681.

(122) Oh, H.; Nong, H. N.; Strasser, P. Preparation of Mesoporous Sb- , F- , and In-Doped SnO 2 Bulk Powder with High Surface Area for Use as Catalyst Supports in Electrolytic Cells. *Mater. Views* **2015**, *25* (7), 1074–1081.

(123) Ozouf, G.; Beauger, C. Niobium- and Antimony-Doped Tin Dioxide Aerogels as New Catalyst Supports for PEM Fuel Cells. *J. Mater. Sci.* **2016**, *51* (11), 5305–5320.

(124) Velikokhatnyi, O. I.; Kadakia, K.; Datta, M. K.; Kumta, P. N. Fluorine-Doped IrO2: A Potential Electrocatalyst for Water Electrolysis. *J. Phys. Chem. C* **2013**, *117* (40), 20542–20547.

(125) Oh, H.-S.; Nong, H. N.; Reier, T.; Gliech, M.; Strasser, P. Oxide-Supported Ir Nanodendrites with High Activity and Durability for the Oxygen Evolution Reaction in Acid PEM Water Electrolyzers. *Chem. Sci.* **2015**, *6*, 3321–3328.

(126) Godinho, K. G.; Walsh, A.; Watson, G. W. Energetic and Electronic Structure Analysis of Intrinsic Defects in SnO 2. *J Phys Chem C* **2009**, *113*, 439–448.

(127) Gurrola, M. P.; Guerra-Balcázar, M.; Álvarez-Contreras, L.; Nava, R.; Ledesma-García, J. High Surface Electrochemical Support Based on Sb-Doped SnO 2. *J. Power Sources* **2013**, *243*, 826–830.

(128) Ozouf, G. PhD Thesis: Electrodes À Base D'aérogels de SnO2, Résistantes À La Corrosion Pour La Réduction de L'oxygène Dans Les Piles À Combustible À Membrane Échangeuse de Protons (PEMFC), MINES ParisTech, 2017.

(129) Lekshmy, S. S.; Daniel, G. P.; Joy, K. Microstructure and Physical Properties of Sol Gel Derived SnO 2 : Sb Thin Films for Optoelectronic Applications. *Appl. Surf. Sci.* **2013**, *274*, 95–100.

(130) Ke, C.; Zhu, W.; Zhang, Z.; Soon Tok, E.; Ling, B.; Pan, J. Thickness-Induced Metal-Insulator Transition in Sb-Doped SnO2 Ultrathin Films: The Role of Quantum Confinement. *Sci. Rep.* **2015**, *5*, 17424–17434.

(131) Slater, B.; Catlow, C. R. A.; Gay, D. H.; Williams, D. E.; Dusastre, V. Study of Surface Segregation of Antimony on SnO 2 Surfaces by Computer Simulation Techniques. *J. Phys. Chem. B* **1999**, *103*, 10644–10650.

(132) Wang, L.; Song, F.; Ozouf, G.; Geiger, D.; Morawietz, T.; Handl, M.; Gazdzicki, P.; Beauger, C.; Kaiser, U.; Hiesgen, R.; et al. Improving the Activity and Stability of Ir Catalysts for PEM Electrolyzer Anodes by SnO 2 : Sb Aerogel Supports : Does V Addition Play an Active Role in Electrocatalysis? *J. Mater. Chem. A Mater. energy Sustain.* **2017**, *5*, 3172–3178.

(133) Spoeri, C.; Kwan, J. T. H.; Bonakdarpour, A.; Wilkinson, D. P.; Strasser, P. The Stability Challenges of Oxygen Evolving Electrocatalysts: Towards a Common Fundamental Understanding and Mitigation of Catalyst Degradation. *Angew. Chemie Int. Ed.* **2017**, *56* (22), 5994–6021.

(134) Tauster, S. J.; Fung, S. C.; Garten, R. L. Strong Metal-Support Interactions . Group 8 Noble Metals Supported on Ti02. *J. Am. Chem. Soc.* **1978**, *100* (1), 170–175.

(135) Tauster, S. J.; Fung, S. C.; Baker, R. T. K.; Horsley, J. A. Strong Interactions in Supported-Metal Catalysts. *Science (80-.).* **1981**, *211* (4487), 1121–1125.

(136) Diebold, U. The Surface Science of Titanium Dioxide. *Surf. Sci. Rep.* **2003**, *48* (5–8), 53–229.

(137) Matsubu, J. C.; Zhang, S.; Derita, L.; Marinkovic, N. S.; Chen, J. G.; Graham, G. W.; Pan, X.; Christopher, P. Adsorbate-Mediated Strong Metal-Support Interactions in Oxide-Supported Rh Catalysts. *Nat. Chem.* **2017**, *9*, 120–127.

(138) Shi, X. Y.; Zhang, W.; Zhang, C.; Zheng, W. T.; Chen, H.; Qi, J. G. Real-Space Observation of Strong Metal-Support Interaction : State-of-the-Art and What's the next. *J. Microsc.* **2016**, *262* (3), 203–215.

(139) Paul van der Heide. *X-Ray Photoelectron Spectroscopy: An Introduction to Principles and Practices*, WILEY.; 2011.

(140) Briggs, D.; Seah, M. P. *Practical Surface Analysis, Auger and X-Ray Photoelectron Spectroscopy*; WILEY, 1990.

(141) Watts, J. F.; Wolstenholme, J. *An Introduction to Surface Analysis by XPS and AES*; WILEY, 2003.

(142) Knop-Gericke, A.; Hävecker, M.; Neisius, T.; Schedel-Niedrig, T. New Experimental

Technique : X-Ray Absorption Spectroscopy Detector for in Situ Studies in the Soft X-Ray Range (250 eV < Hv < 1000 eV) under Reaction Conditions. *Nucl. Instruments Methods Phys. Res. Sect. A Accel. Spectrometers, Detect. Assoc. Equip.* **1998**, *A 406*, 311–322.

(143) Groot, F. De; Kotani, A. *Core Level Spectroscopy of Solids*; CRC Press, 2008.

(144) Pfeifer, V. PhD Thesis: Identification of Reactive Oxygen Species in Iridium-Based OER Catalysts by in Situ Photoemission and Absorption Spectroscopy, TU Berlin, 2017.

(145) Hähner, G. Near Edge X-Ray Absorption Fine Structure Spectroscopy as a Tool to Probe Electronic and Structural Properties of Thin Organic Films and Liquids. *Chem. Soc. Rev.* **2006**, *35*, 1244–1255.

(146) Russell, A. E.; Rose, A. X-Ray Absorption Spectroscopy of Low Temperature Fuel Cell Catalysts. *Chem. Rev.* **2004**, *104*, 4613–4635.

(147) Stöhr, J. *NEXAFS Spectroscopy*; Springer-Verlag Berlin Heidelberg, 1992.

(148) Hävecker, M.; Cavalleri, M.; Herbert, R.; Follath, R.; Knop-Gericke, A.; Hess, C.; Hermann, K.; Schlögl, R. Methodology for the Structural Characterisation of Vx Oy Species Supported on Silica under Reaction Conditions by Means of in Situ O K-Edge X-Ray Absorption Spectroscopy. *Phys Status Solidi B* **2009**, *246* (7), 1459–1469.

(149) Groat, F. M. F. De. X-Ray Absorption and Dichroism of Transition Metals and Their Compounds. *J. Electron Spectros. Relat. Phenomena* **1994**, *61*, 529–622.

(150) Stuve, E. M.; Krasnopoler, A.; Sauer, D. E. Relating the in-Situ , Ex-Situ , and Non-Situ Environments in Surface Electrochemistry. *Surf. Sci.* **1995**, *335*, 177–185.

(151) Shchukarev, A. XPS at Solid – Aqueous Solution Interface. *Adv. Colloid Iterface Sci.* **2006**, *122*, 149–157.

(152) Wibowo, R.; Aldous, L.; Jacobs, R. M. J.; Manan, N. S. A.; Compton, R. G. In Situ Electrochemical-X-Ray Photoelectron Spectroscopy: Rubidium Metal Deposition from an Ionic Liquid in Competition with Solvent Breakdown. *Chem. Phys. Lett.* **2011**, *517* (1–3), 103–107.

(153) Ogletree, D. F.; Bluhm, H.; Hebenstreit, E. D.; Salmeron, M. Photoelectron Spectroscopy under Ambient Pressure and Temperature Conditions. *Nucl. Instruments Methods Phys. Res. Sect. A Accel. Spectrometers, Detect. Assoc. Equip.* **2009**, *601*, 151–160.

(154) Bluhm, H. Photoelectron Spectroscopy of Surfaces under Humid Conditions. *J. Electron Spectros. Relat. Phenomena* **2010**, *177* (2–3), 71–84.

(155) Starr, D. E.; Liu, Z.; Hävecker, M.; Knop-Gericke, A.; Bluhm, H. Investigation of Solid / Vapor Interfaces Using Ambient Pressure X-Ray Photoelectron Spectroscopy. *Chem. Soc. Rev.* **2013**, *42* (13), 5833–5857.

(156) Salmeron, M.; Schlögl, R. Ambient Pressure Photoelectron Spectroscopy: A New Tool for Surface Science and Nanotechnology. *Surf. Sci. Rep.* **2008**, *63* (4), 169–199.

(157) Ogletree, D. F.; Bluhm, H.; Lebedev, G.; Fadleyzahid, C. S.; Salmeron, H.; Ogletree, D. F.; Bluhm, H.; Lebedev, G.; Fadley, C. S. A Differentially Pumped Electrostatic Lens System for Photoemission Studies in the Millibar Range A Differentially Pumped Electrostatic Lens System for Photoemission Studies in the Millibar Range. *Rev. Sci. Instrum.* **2002**, *73* (11), 3872–3879.

(158) Liu, X.; Yang, W.; Liu, Z. Recent Progress on Synchrotron-Based In Situ Soft X-Ray Spectroscopy for Energy Materials. *Adv. Mater.* **2014**, 1–20.

(159) Shavorskiy, A.; Karslioglu, O.; Zegkinoglou, I.; Bluhm, H. Synchrotron-Based Ambient Pressure X-Ray Photoelectron Spectroscopy. *Synchrotron Radiat. News* **2014**, *27* (2), 14–23.

(160) Kaya, S.; Ogasawara, H.; Näslund, L. Å.; Forsell, J. O.; Casalongue, H. S.; Miller, D. J.; Nilsson, A. Ambient-Pressure Photoelectron Spectroscopy for Heterogeneous Catalysis and Electrochemistry. *Catal. Today* **2013**, *205*, 101–105.

(161) Kerherve, G.; Regoutz, A.; Bentley, D.; Hood, C.; Feeley, K.; Knight, S.; Robson, A.; Turner, C.; Singh, N.; Pontefract, J.; et al. Laboratory-Based High Pressure X-Ray Photoelectron Spectroscopy: A Novel and Flexible Reaction Cell Approach. *Rev. Sci. Instrum.* **2017**, *88* (3).

(162) Axnanda, S.; Crumlin, E. J.; Mao, B.; Rani, S.; Chang, R.; Karlsson, P. G.; Edwards, M. O. M.; Lundqvist, M.; Moberg, R.; Ross, P.; et al. Using "Tender" X-Ray Ambient Pressure X-Ray Photoelectron Spectroscopy as A Direct Probe of Solid-Liquid Interface. *Sci. Rep.* **2015**, *5*, 9788–9800.

(163) Favaro, M.; Valero-Vidal, C.; Eichhorn, J.; Toma, F. M.; Ross, P. N.; Yano, J.; Liu, Z.; Crumlin, E. J. Elucidating the Alkaline Oxygen Evolution Reaction Mechanism on Platinum. *J. Mater. Chem. A Mater. energy Sustain.* **2017**, *5*, 11634–11643.

(164) Ali-Löytty, H.; Louie, M. W.; Singh, M. R.; Li, L.; Guido, H.; Casalongue, S.; Ogasawara, H.; Crumlin, E. J.; Liu, Z.; Bell, A. T.; et al. Ambient-Pressure XPS Study of a Ni-Fe Electrocatalyst for the Oxygen Evolution Reaction. *J. Phys. Chem. C* **2016**, *120* (4), 2247–2253.

(165) Lewerenz, H.; Lichterman, M. F.; Richter, M. H.; Crumlin, E. J.; Hu, S.; Axnanda, S.; Favaro, M.; Drisdell, W.; Hussain, Z.; Brunschwig, B. S.; et al. Operando Analyses of Solar Fuels Light Absorbers and Catalysts. *Electrochim. Acta* **2016**, *211*, 711–719.

(166) Favaro, M.; Jeong, B.; Ross, P. N.; Yano, J.; Hussain, Z.; Liu, Z.; Crumlin, E. J. Unravelling the Electrochemical Double Layer by Direct Probing of the Solid / Liquid Interface. *Nat. Commun.* **2016**, *7*, 12695–12703.

(167) Wu, F.; Yao, N. Advances in Sealed Liquid Cells for in-Situ TEM Electrochemial Investigation of Lithium-Ion Battery. *Nano Energy* **2015**, *11*, 196–210.

(168) Liu, Y.; Dillon, S. J. In Situ Observation of Electrolytic H2 Evolution Adjacent to Gold Cathodes. *ChemComm* **2014**, *50*, 1761–1763.

(169) Hodnik, N.; Dehm, G.; Mayrhofer, K. J. J. Importance and Challenges of Electrochemical in Situ Liquid Cell Electron Microscopy for Energy Conversion Research. *Acc. Chem. Res.* **2016**, *49*, 2015–2022.

(170) Velasco Vélez, J.-J.; Wu, C. H.; Pascal, T. A.; Wan, L. F.; Guo, J.; Prendergast, D.; Salmeron, M. The Structure of Interfacial Water on Gold Electrodes Studied by X-Ray Absorption Spectroscopy. *Science (80-.).* **2014**, *346* (6211), 14664–14666.

(171) Binninger, T.; Fabbri, E.; Patru, A.; Garganourakis, M.; Han, J.; Menzel, A.; Nachtegaal, M.; Schmidt, T. J. Electrochemical Flow-Cell Setup for In Situ X-Ray Investigations I . Cell for SAXS and XAS at Synchrotron Facilities. *J. Electrochem. Soc.* **2016**, *163* (10), 906–912.

(172) Kolmakov, A.; Dikin, D. A.; Cote, L. J.; Huang, J.; Abyaneh, M. K.; Amati, M.; Gregoratti, L.; Gu, S. Graphene Oxide Windows for in Situ Environmental Cell Photoelectron Spectroscopy. *Nat. Nanotechnol.* **2011**, *6*, 651–657.

(173) Velasco-Velez, J. J.; Pfeifer, V.; Hävecker, M.; Weatherup, R. S.; Arrigo, R.; Chuang, C.; Stotz, E.; Weinberg, G.; Salmeron, M.; Schlögl, R.; et al. Photoelectron Spectroscopy at the Graphene – Liquid Interface Reveals the Electronic Structure of an Electrodeposited Cobalt / Graphene Electrocatalyst. *Angew. Chemie Int. Ed.* **2015**, *54*, 14554–14558.

(174) Velasco-Velez, J. J.; Pfeifer, V.; Hävecker, M.; Wang, R.; Centeno, A.; Zurutuza, A.; Algara-Siller, G.; Stotz, E.; Skorupska, K.; Teschner, D.; et al. Atmospheric Pressure X-Ray Photoelectron Spectroscopy Apparatus : Bridging the Pressure Gap. *Rev. Sci. Instrum.* **2016**, *87* (5), 053121–053135.

(175) Trotochaud, L.; Head, A. R.; Karsl, O.; Kyhl, L. Ambient Pressure Photoelectron Spectroscopy : Practical Considerations and Experimental Frontiers. *J. Phys. Condens. Matter* **2017**, *29*, 053002–053031.

(176) Law, Y. T.; Zafeiratos, S.; Neophytides, S. G.; Orfanidi, A.; Costa, D.; Dintzer, T.; Arrigo, R.; Gericke, K.; Schlögl, R.; Savinova, E. R.; et al. In Situ Investigation of Dissociation and Migration Phenomena at the Pt/electrolyte Interface of an Electrochemical Cell. *Chem. Sci.* **2015**, *6*, 5635–5642.

(177) Saveleva, V. A.; Papaefthimiou, V.; Daletou, M. K.; Doh, W. H.; Ulhaq-Bouillet, C.; Diebold, M.; Zafeiratos, S.; Savinova, E. R. Operando Near Ambient Pressure XPS (NAP-XPS) Study of the Pt Electrochemical Oxidation in H 2 O and H 2 O/O 2 Ambients. *J. Phys. Chem. C* **2016**, *120* (29), 15930–15940.

(178) Saveleva, V. A.; Daletou, M. K.; Savinova, E. R. The Influence of Methanol on the Chemical State of PtRu Anodes in a High-Temperature Direct Methanol Fuel Cell Studied in Situ by Synchrotron-Based near-Ambient Pressure X-Ray Photoelectron Spectroscopy. *J. Phys. D. Appl. Phys.* **2017**, *50*, 14001–14010.

(179) Casalongue, H. G. S.; Kaya, S.; Viswanathan, V.; Miller, D. J.; Friebel, D.; Hansen, H. A.; Norskov, J. K.; Nilsson, A.; Ogasawara, H. Direct Observation of the Oxygenated Species during Oxygen Reduction on a Platinum Fuel Cell Cathode. *Nat Commun* **2013**, *4*, 2817–2822.

(180) Lettenmeier, P.; Wang, L.; Golla-Schindler, U.; Gazdzicki, P.; Cañas, N. A.; Handl, M.; Hiesgen, R.; Hosseiny, S. S.; Gago, A. S.; Friedrich, K. A. Nanosized IrOx -Ir Catalyst with Relevant Activity for Anodes of Proton Exchange Membrane Electrolysis Produced by a Cost-Effective Procedure. *Angew. Chem. Int. Ed. Engl.* **2016**, *128*, 752–756.

(181) Saveleva, V. A.; Wang, L.; Luo, W.; Zafeiratos, S.; Ulhaq-bouillet, C.; Gago, A. S.; Friedrich, K. A.; Savinova, E. R. Uncovering the Stabilization Mechanism in Bimetallic Ruthenium − Iridium Anodes for Proton Exchange Membrane Electrolyzers. *Phys. Chem. Lett.* **2016**, *7*, 3240–3245.

(182) Hwang, G. S.; Kaviany, M.; Gostick, J. T.; Kientiz, B.; Weber, A. Z.; Kim, M. H. Role of Water States on Water Uptake and Proton Transport in Nafion Using Molecular Simulations and Bimodal Network. *Polymer (Guildf).* **2011**, *52* (12), 2584–2593.

(183) Kreuer, K.-D.; Rabenau, A.; Weppner, W. Vehicle Mechanism , A New Model for the Interpretation of the Conductivity of Fast Proton Conductors. *Angew. Chemie Int. Ed.* **1982**, *122* (3), 1981–1982.

(184) Merlo, L.; Oldani, C.; Apostolo, M.; Arcella, V. PFSA Aquivion® Membranes: General Features and Degradation Mechanisms. In *Fuel Cells*; 2012; p 34.

(185) Xiao, P.; Li, J.; Tang, H.; Wang, Z.; Pan, M. Physically Stable and High Performance Aquivion/ePTFE Composite Membrane for High Temperature Fuel Cell Application. *J.*

Memb. Sci. **2013**, *442*, 65–71.

(186) Siracusano, S.; Baglio, V.; Stassi, A.; Merlo, L.; Moukheiber, E.; Arico', A. S. Performance Analysis of Short-Side-Chain Aquivion Perfluorosulfonic Acid Polymer for Proton Exchange Membrane Water Electrolysis. *J. Memb. Sci.* **2014**, *466*, 1–7.

(187) Skulimowska, A.; Dupont, M.; Zaton, M.; Sunde, S.; Merlo, L.; Jones, D. J.; Rozie, J. Proton Exchange Membrane Water Electrolysis with Short-Side-Chain Aquivion Membrane and IrO2 Anode Catalyst. *Int. J. Hydrogen Energy* **2014**, *39*, 6307–6316.

(188) Cui, S.; Liu, J.; Selvan, M. E.; Paddison, S. J.; Keffer, D. J.; Edwards, B. J. Comparison of the Hydration and Diffusion of Protons in Perfluorosulfonic Acid Membranes with Molecular Dynamics Simulations. *J. Phys. Chem. B* **2008**, *112* (42), 13273–13284.

(189) Kreuer, K. D.; Schuster, M.; Obliers, B.; Diat, O.; Traub, U.; Fuchs, A.; Klock, U.; Paddison, S. J.; Maier, J. Short-Side-Chain Proton Conducting Perfluorosulfonic Acid Ionomers: Why They Perform Better in PEM Fuel Cells. *J. Power Sources* **2008**, *178* (2), 499–509.

(190) Bilderback, D. H.; Elleaume, P.; Weckert, E. Review of Third and next Generation Synchrotron Light. *J Phys B* **2005**, *38*, 773–797.

(191) Knop-Gericke, A.; Kleimenov, E.; Hävecker, M.; Blume, R.; Teschner, D.; Zafeiratos, S.; Schlögl, R.; Bukhtiyarov, V. I.; Kaichev, V. V.; Prosvirin, I. P.; et al. Chapter 4 X-Ray Photoelectron Spectroscopy for Investigation of Heterogeneous Catalytic Processes. *Adv. Catal.* **2009**, *52*, 213–272.

(192) Siegbahn, H.; Lundholm, M. A Method of Depressing Gaseous-Phase Electron Lines in Liquid-Phase ESCA Spectra. *J. Electron Spectros. Relat. Phenomena* **1982**, *28*, 135–138.

(193) Polack, F.; Silly, M.; Chauvet, C.; Lagarde, B.; Bergeard, N.; Izquierdo, M.; Chubar, O.; Krizmancic, D.; Ribbens, M.; Duval, J. P.; et al. TEMPO : A New Insertion Device Beamline at SOLEIL for Time Resolved Photoelectron Spectroscopy Experiments on Solids and Interfaces TEMPO : A New Insertion Device Beamline at SOLEIL for Time Resolved Photoelectron Spectroscopy Experiments on Solids and In. In *AIP Conference Proceedings*; 2010; Vol. 1234, pp 1–5.

(194) Butler, J. A. V; Drever, G. The Mechanism of Electrolytic Processes. Part I. The Anodic Oxidation of Some Metals of the Platinum Group. *Trans Faraday Soc* **1936**, *32*, 427–435.

(195) Cazaux, J. A Physical Approach to the Radiation Damage Mechanisms Induced by X-Rays in X-Ray Microscopy and Related Techniques. *J. Microsc.* **1997**, *188* (2), 106–124.

(196) Schulze, M.; Bolwin, K.; Gülzow, E.; Schnurnberger, W. XPS Analysis of PTFE Decomposition due to Ionizing Radiation. *Fresenius J. Anal. Chem.* **1995**, *353*, 778–784.

(197) Tanuma, S.; Powell, C. J.; Penn, D. R. Electron Inelastic Mean Free Paths. *Surf. Interface Anal.* **1994**, *21*, 165–176.

(198) Yeh, J. J. *Atomic Calculation of Photoionization Cross-Sections and Asymmetry Parameters*; Gordon & Breach Science, 1993.

(199) Barr, T. L. Nature of the Use of Adventitious Carbon as a Binding Energy Standard. *J. Vac. Sci. Technol. A Vacuum, Surfaces, Film.* **1995**, *13* (3), 1239–1246.

(200) Economou, N. J.; O'Dea, J. R.; McConnaughy, T. B.; Buratto, S. K. Morphological Differences in Short Side Chain and Long Side Chain Perfluorosulfonic Acid Proton Exchange Membranes at Low and High Water Contents. *RSC Adv.* **2013**, *3* (42), 19525–

19532.

(201) Morgan, D. J. Resolving Ruthenium: XPS Studies of Common Ruthenium Materials. *Surf. Interface Anal.* **2015**, *47* (11), 1072–1079.

(202) Cox, P. A.; Goodenough, J. B.; Tavener, P. J.; Telles, D.; Egdell, R. G. The Electronic Structure of Bi2-xGdxRu2O7 and RuO2: A Study by Electron Spectroscopy. *J. Solid State Chem.* **1986**, *62* (3), 360–370.

(203) Kötz, R. XPS Studies of Oxygen Evolution on Ru and RuO[sub 2] Anodes. *J. Electrochem. Soc.* **1983**, *130* (4), 825–829.

(204) Connick, R. E.; Hurley, C. R. Chemistry of Ru(VI), -(VII) and -(VIII). Reactions, Oxidation Potentials and Spectra. *J. Am. Chem. Soc.* **1952**, *74* (20), 5012–5015.

(205) Kim, K. S.; Winograd, N. X-Ray Photoelectron Spectroscopic Studies of Ruthenium-Oxygen Surfaces. *J. Catal.* **1974**, *35*, 66–72.

(206) Atanasoska, L.; O'Grady, W.; Atanasoski, R. T.; Pollak, F. The Surface Structure of RuO2: A Leed, Auger and XPS Study of the (110) and (100) Faces. *Surf. Sci.* **1988**, *202* (1–2), 142–166.

(207) Blume, R.; Rosenthal, D.; Tessonnier, J.-P.; Li, H.; Knop-Gericke, A.; Schlögl, R. Characterizing Graphitic Carbon with X-Ray Photoelectron Spectroscopy : A Step-by-Step Approach. *ChemCatChem* **2015**, *7*, 2871–2881.

(208) Estrade-Szwarckopf, H. XPS Photoemission in Carbonaceous Materials : A "defect" peak beside the Graphitic Asymmetric Peak. *Carbon N. Y.* **2004**, *42*, 1713–1721.

(209) Attekum, P. M. T. M. van; Wertheim, G. K. Excitonic Effects in Core-Hole Screening. *Phys. Rev. Lett.* **1981**, *43* (25), 1896–1898.

(210) Mun, C.; Ehrhardt, J. J.; Lambert, J.; Madic, C. XPS Investigations of Ruthenium Deposited onto Representative Inner Surfaces of Nuclear Reactor Containment Buildings. *Appl. Surf. Sci.* **2007**, *253* (18), 7613–7621.

(211) Bianchi, C. L.; Ragaini, V.; Cattania, M. G. An XPS Study on Ruthenium Compounds and Catalysts. *Mater. Chem. Phys.* **1991**, *29* (1–4), 297–306.

(212) Shen, J. Y.; Adnot, A.; Kaliaguine, S. An ESCA Study of the Interaction of Oxygen with the Surface of Ruthenium. *Appl. Surf. Sci.* **1991**, *51* (1–2), 47–60.

(213) Salomonsson, A.; Petoral, R. M.; Uvdal, K.; Aulin, C.; Käll, P. O.; Ojamäe, L.; Strand, M.; Sanati, M.; Spetz, A. L. Nanocrystalline Ruthenium Oxide and Ruthenium in Sensing Applications - An Experimental and Theoretical Study. *J. Nanoparticle Res.* **2006**, *8* (6), 899–910.

(214) Pfeifer, V.; Jones, T. E.; Velasco Vélez, J.-J.; Greiner, M.; Massué, C.; Arrigo, R.; Teschner, D.; Girgsdies, F.; Scherzer, M.; Allan, J.; et al. The Electronic Structure of Iridium Oxide Electrodes Active in Water Splitting. *Phys. Chem. Chem. Phys.* **2015**, 1–14.

(215) Daniels, R. R.; Margaritondo, G.; Georg, C.; Levy, F. Electronic States of Rutile Dioxides: RuO2, IrO2, and RuxIr1-xO2. *Phys. Rev. B* **1984**, *29* (4), 1813–1818.

(216) Wertheim, G. K.; Guggenheim, H. J. Conduction-Electron Screening in Metallic Oxides: IrO2. *Phys. Rev. B* **1980**, *22* (10), 4680–4683.

(217) Caciuffo, R.; Melone, S.; Rustichelli, F.; Boeuf, A.; Ispra, C. Monochromators for X-Ray Synchrotron Radiation. *Phys. Rep.* **1987**, *152* (1), 1–71.

(218) Pfeifer, V.; Jones, T. E.; Vélez, J. V.; Massué, C.; Arrigo, R.; Teschner, D.; Girgsdies, F.; Scherzer, M.; Greiner, M. T.; Allan, J.; et al. The Electronic Structure of Iridium and Its Oxides. *Surf. Interface Anal.* **2015**, *48* (5), 261–273.

(219) Peuckert, M. XPS Study on Thermally and Electrochemically Prepared Oxidic Adlayers on Iridium. *Surf. Sci. Lett.* **1984**, *144* (2–3), 451–464.

(220) Haverkamp, R. G.; Marshall, A. T.; Cowie, B. C. C. Energy Resolved XPS Depth Profile of (IrO2, RuO2, Sb2O5, SnO2) Electrocatalyst Powder to Reveal Core-Shell Nanoparticle Structure. *Surf. Interface Anal.* **2011**, *43* (5), 847–855.

(221) Bozack, M. J. Sputter-Induced Modifications of IrO2 During XPS Measurements. *Surf. Sci. Spectra* **1993**, *2* (2), 123–127.

(222) Hufner, S.; Wertheim, G. K. Core-Line Asymmetries in the X-Ray-Photoemission Spectra of Metals. *Phys. Rev. B* **1975**, *11* (2), 678–683.

(223) Freakley, S. J.; Ruis-Esquius, J.; Morgan, D. J. The X-Ray Photoelectron Spectra of Ir , IrO 2 and IrCl 3 Revisited. *Surf. Interface Anal.* **2017**, *49* (8), 794–799.

(224) Werner, W. S. M.; Smekal, W.; Hisch, T.; Himmelsbach, J.; Powell, C. J. Simulation of Electron Spectra for Surface Analysis (SESSA) for Quantitative Interpretation of (Hard) X-Ray Photoelectron Spectra (HAXPES). *J. Electron Spectros. Relat. Phenomena* **2013**, *190*, 137–143.

(225) Powell, C. J.; Werner, W. S. M.; Shard, A. G.; Castner, D. G. Evaluation of Two Methods for Determining Shell Thicknesses of Core−Shell Nanoparticles by X-ray Photoelectron Spectroscopy. *J. Phys. Chem. C* **2016**, *120* (39), 22730–22738.

(226) Owe, L. E.; Tsypkin, M.; Wallwork, K. S.; Haverkamp, R. G.; Sunde, S. Iridium-Ruthenium Single Phase Mixed Oxides for Oxygen Evolution: Composition Dependence of Electrocatalytic Activity. *Electrochim. Acta* **2012**, *70*, 158–164.

(227) Stoerzinger, K. A.; Qiao, L.; Biegalski, M. D.; Shao-Horn, Y. Orientation-Dependent Oxygen Evolution Activities of Rutile IrO 2 and RuO 2. *J. Phys. Chem. Lett.* **2014**, *5* (10), 1636–1641.

(228) Campbell, C. T. Transition Metal Oxides: Extra Thermodynamic Stability as Thin Films. *Phys. Rev. Lett.* **2006**, *96* (6), 066106(1)-066106(4).

(229) Juodkazis, K.; Vilkauskaite, R. Difference between Surface Electrochemistry of Ruthenium and RuO2 Electrodes. **2007**, *85* (4), 194–201.

(230) Pauly, N.; Tougaard, S. Core Hole and Surface Excitation Correction Parameter for XPS Peak Intensities. *Surf. Sci.* **2011**, *605* (15–16), 1556–1562.

(231) Hu, Z.; Mazumdar, C.; Kaindl, G.; de Groot, F. M. F.; Warda, S. A.; Reinen, D. Valence Electron Distribution in La2Li1/2Cu1/2O4, Nd2Li1/2Ni1/2O4, and La2Li1/2Co1/2O4. *Chem. Phys. Lett.* **1998**, *297*, 321–328.

(232) Hu, Z.; Lips, H. Von; Golden, M. S.; Fink, J.; Kaindl, G.; de Groot, F. M. F.; Ebbinghaus, S.; Reller, A. Multiplet Effects in the Ru L 2 , 3 X-Ray-Absorption Spectra of Ru (IV) and Ru (V) Compounds. *Phys. Rev. B* **2000**, *61* (8), 5262–5266.

(233) Jones, T. E.; Rocha, T. C. R.; Knop-Gericke, A.; Stampfl, C.; Schlögl, R.; Piccinin, S. Thermodynamic and Spectroscopic Properties of Oxygen on Silver under an Oxygen Atmosphere. *PCCP* **2015**, *17*, 9288–9312.

(234) Mattos-Costa, F. I.; Lima-Neto, P. De; Machado, S. A. S.; Avaca, L. A. Characterisation of

Surfaces Modified by Sol-Gel Derived RuxIr1−xO2 Coatings for Oxygen Evolution in Acid Medium. *Electrochim. Acta* **1998**, *44*, 1515–1523.

(235) Bernt, M.; Gasteiger, H. A. Influence of Ionomer Content in IrO 2 / TiO 2 Electrodes on PEM Water Electrolyzer Performance. *J. Electrochem. Soc.* **2016**, *163* (11), 3179–3189.

(236) Faria, L. .; Boodts, J. F. C.; Trasatti, S. Electrocatalytic Properties of Ternary Oxide Mixtures of Composition Ru0.3Ti(0.7-x)CexO2: Oxygen Evolution from Acidic Solution. *J. Appl. Electrochem.* **1996**, *26* (11), 1195–1199.

(237) Mefford, J. T.; Rong, X.; Abakumov, A. M.; Hardin, W. G.; Dai, S.; Kolpak, A. M.; Johnston, K. P.; Stevenson, K. J. Water Electrolysis on La1−xSrxCoO3−δ Perovskite Electrocatalysts. *Nat. Commun.* **2016**, *7*, 11053–11064.

(238) Doyle, R. L.; Godwin, I. J.; Brandon, M. P.; Lyons, M. E. G. Redox and Electrochemical Water Splitting Catalytic Properties of Hydrated Metal Oxide Modified Electrodes. *Phys. Chem. Chem. Phys.* **2013**, *15* (33), 13737–13783.

(239) Grimaud, A.; Hong, W. T.; Shao-Horn, Y.; Tarascon, J.-M. Anionic Redox Processes for Enhanced Battery and Water Splitting Devices. *Nat. Mater.* **2016**, *15* (2), 121–126.

(240) Mowbray, D. J.; Martínez, J. I.; Rossmeisl, J.; Thygesen, K. S.; Jacobsen, K. W.; Nørskov, J. K. Trends in Metal Oxide Stability for Nanorods , Nanotubes , and Surfaces. *J. Phys. Chem. C* **2011**, *115*, 2244–2252.

(241) Mattheiss, L. F. Electronic Structure of RuO2, OsO2, and IrO2. *Phys. Rev. B* **1975**, *13* (6), 2433–2451.

(242) Man, I. C. Theoretical Study of Electro-Catalysts for Oxygen Evolution. *Physics (College. Park. Md).* **2011**, *PhD*.

(243) Kötz, R.; Stucki, S. Oxygen Evolution and Corrosion on Ruthenium-Iridium Alloys. *J. Electrochem. Soc.* **1985**, *132* (1), 103–108.

(244) Danilovic, N.; Subbaraman, R.; Chang, K. C.; Chang, S. H.; Kang, Y.; Snyder, J.; Paulikas, A. P.; Strmcnik, D.; Kim, Y. T.; Myers, D.; et al. Using Surface Segregation to Design Stable Ru-Ir Oxides for the Oxygen Evolution Reaction in Acidic Environments. *Angew. Chem. Int. Ed. Engl.* **2014**, *53* (51), 14016–14021.

(245) Jovanovi, P.; Hodnik, N.; Ruiz-Zepeda, F.; Arcon, I.; Jozinovi, B.; Bele, M.; Šala, M.; Šelih, V. S.; Hocevar, S. B.; Gaberscek, M. Electrochemical Dissolution of Iridium and Iridium Oxide Particles in Acidic Media : Transmission Electron Microscopy , Electrochemical Flow Cell Coupled to Inductively Coupled Plasma Mass Spectrometry and X-Ray Absorption Spectroscopy Study. *J. Am. Chem. Soc.* **2017**, *139* (36), 12837–12846.

(246) Elzanowska, H.; Birss, V. I. Reversible Ageing of Iridium Oxide Electrodes in Acidic Solutions. *J. Appl. Electrochem.* **1999**, *23* (1993), 646–654.

(247) Kötz, R.; Neff, H.; Stucki, S. Anodic Iridium Oxide Films. *J. Electrochem. Chem.* **1984**, *131* (January), 72–77.

(248) Pickup, P. G.; Birss, V. I. A Model for Anodic Hydrous Oxide Growth at Iridium. *J Electroanal Chem* **1987**, *220*, 83–100.

(249) Gottesfeld, S.; McIntyre, J. D. E.; Beni, G.; Shay, J. L. Electrochromism in Anodic Iridium Oxide Films. *Appl. Phys. Lett.* **1978**, *33* (1978), 208–211.

(250) Ito, S.; Abe, Y.; Kawamura, M.; Kim, K. H. Electrochromic Properties of Iridium Oxide Thin Films Prepared by Reactive Sputtering in O2 or H2O Atmosphere. *J. Vac. Sci.*

Technol. A Vacuum, Surfaces, Film. **2015**, *33*, 041204–041209.

(251) Stalnionis, G.; Juodkazis, K.; Juodkazyte, J. EQCM Study of Iridium Anodic Oxidation in H 2 SO 4 and KOH Solutions. *Electroanalysis* **2005**, *17* (19), 1734–1739.

(252) Nong, H. N.; Oh, H.-S.; Reier, T.; Willinger, E.; M.G., W.; Petkov, V.; Teschner, D.; Strasser, P.; Willinger, M.-G.; Petkov, V.; et al. Oxide-Supported IrNiOx Core-Shell Particles as Efficient, Cost-Effective, and Stable Catalysts for Electrochemical Water Splitting. *Angew. Chemie* **2015**, *54* (10), 2975–2979.

(253) Viswanathan, B. 15 Years of Strong Metal Support Interactions. *Proc. Indian Natn. Sci. Acad*. 1995, pp 121–160.

(254) Puthiyapura, V. K.; Pasupathi, S.; Su, H.; Liu, X.; Pollet, B.; Scott, K. Investigation of Supported IrO2 as Electrocatalyst for the Oxygen Evolution Reaction in Proton Exchange Membrane Water Electrolyser. *Int. J. Hydrogen Energy* **2014**, *39* (5), 1905–1913.

(255) Ladas, S.; Kennou, S.; Bebelis, S.; Vayenas, C. G. Origin of Non-Faradaic Electrochemical Modification of Catalytic Activity. *J Phys Chem* **1993**, *97*, 8845–8848.

(256) Yusoff, A. R. bin M.; Dai, L.; Cheng, H.-M.; Liu, J. Graphene-Based Energy Devices. *Nanoscale* **2015**, *7*, 6881–6882.

(257) Batzill, M.; Diebold, U. The Surface and Materials Science of Tin Oxide. *Prog. Surf. Sci.* **2005**, *79*, 47–154.

(258) Egdell, R. G.; Rebane, J.; Walker, T.; Law, D. Competition between Initial-and Final-State Effects in Valence-and Core-Level X-Ray Photoemission of Sb-Doped SnO 2. *Phys. Rev. B* **1999**, *59* (3), 1792–1799.

(259) Nagata, T.; Bierwagen, O.; White, M. E.; Tsai, M. Y.; Yamashita, Y.; Yoshikawa, H.; Ohashi, N.; Kobayashi, K.; Chikyow, T.; Speck, J. S. XPS Study of Sb-/In-Doping and Surface Pinning Effects on the Fermi Level in SnO2 (101) Thin Films. *Appl. Phys. Lett.* **2011**, *98* (23), 1–4.

(260) Zhao, Y.; Chen, S.; Sun, B.; Su, D.; Huang, X.; Liu, H.; Yan, Y. Graphene-Co3O4 Nanocomposite as Electrocatalyst with High Performance for Oxygen Evolution Reaction. *Sci. Rep.* **2014**, *5*, 7629–7636.

(261) Martelli, G. N.; Ornelas, R.; G, F. Deactivation Mechanisms of Oxygen Evolving Anodes at High Current Densities. *Electrochim. Acta* **1994**, *39* (11/12), 1551–1558.

(262) Zeradjanin, A. R.; Topalov, A. A.; Van Overmeere, Q.; Cherevko, S.; Chen, X.; Ventosa, E.; Schuhmann, W.; Mayrhofer, K. J. J. Rational Design of the Electrode Morphology for Oxygen Evolution – Enhancing the Performance for Catalytic Water Oxidation. *RSC Adv.* **2014**, *4* (19), 9579.

(263) Shao-Horn, Y.; Sheng, W. C.; Chen, S.; Ferreira, P. J.; Holby, E. F.; Morgan, D. Instability of Supported Platinum Nanoparticles in Low-Temperature Fuel Cells. *Top. Catal.* **2007**, *46*, 285–305.

(264) Memming, R. *Semiconductor Electrochemistry*, Second Edi.; Memming, R., Ed.; WILEY-VCH, 2016.

(265) Sanon, G.; Rup, R.; Mansingh, A. Band-Gap Narrowing and Band Structure in Degenerate Tin Oxide (SnO2) Films. *Phys. Rev. B* **1991**, *44* (11), 5672–5680.

(266) Siegbahn, K.; Nordling, C.; Fahlman, A.; Nordberg, R.; Hamrin, K.; Hedman, J.; Johansson, G.; Bergmark, T.; Karlsson, S.-E.; Lindgren, I. and; et al. *ESCA Atomic, Molecular and*

Solid State Structure Studied by Means of Electron Spectroscopy; Almqvist and Wiksell, 1967.

(267) Cox, P. A.; Egdell, R. G.; Harding, C.; Patterson, W. R.; Tavener, P. J. Surface Properties of Antimony Doped Tin (IV) Oxide: A Study by Electron Spectroscopy. *Surf. Sci.* **1982**, *123* (2–3), 179–203.

(268) Szczuko, D.; Werner, J.; Oswald, S.; Behr, G.; Wetzig, K. XPS Investigations of Surface Segregation of Doping Elements in SnO2. *Appl. Surf. Sci.* **2001**, *179* (1–4), 301–306.

(269) Zhang, Z.; Yates, J. T. Band Bending in Semiconductors: Chemical and Physical Consequences at Surfaces and Interfaces. *Chem. Rev.* **2012**, *112* (10), 5520–5551.

(270) Zhou, L.; Zachariah, M. R. Size Resolved Particle Work Function Measurement of Free Nanoparticles : Aggregates vs . Spheres. *Chem. Phys. Lett.* **2012**, *525–526*, 77–81.

(271) John Read Jr., A. PhD Thesis: A Study of Surface Reactions by Field Emission Microscopy, Iowa State University of Science and Technology, 1961.

(272) Chalamala, B. R.; Wei, Y.; Reuss, R. H.; Aggarwal, S.; Gnade, B. E.; Ramesh, R.; John, M.; Sosa, E. D.; Golden, D. E.; Chalamala, B. R.; et al. Effect of Growth Conditions on Surface Morphology and Photoelectric Work Function Characteristics of Iridium Oxide Thin Films. *Appl. Phys. Lett.* **1999**, *47* (10), 1394–1397.

(273) Lu, H.; Vourlias, G.; Krier, A.; Milne, B.; Gillin, W. P.; Adamopoulos, G.; C, J. M. C. Solution Processed SnO2:Sb Transparent Conductive Oxide as Alternative to Indium Tin Oxide for Applications in Organic Light Emitting Diodes. *J. Mater. Chem. A* **2016**, *4*, 3563–3570.

(274) Bissig, B.; Jäger, T.; Ding, L.; Tiwari, A. N.; Romanyuk, Y. E. Limits of Carrier Mobility in Sb-Doped SnO2 Conducting Films Deposited by Reactive Sputtering Limits of Carrier Mobility in Sb-Doped SnO 2 Conducting Films Deposited by Reactive Sputtering. *Apl Mater.* **2015**, *3*, 062802–062809.

(275) Aegerter, M. A.; Dahmani, B.; Guzman, G.; Pütz, J. Patent: Material for Use in the Manufacturing of Luminous Display Devices, 2005.

(276) Gassenbauer, Y.; Schafranek, R.; Klein, A.; Zafeiratos, S.; Hävecker, M.; Knop-Gericke, A.; Schlögl, R. Surface States, Surface Potentials, and Segregation at Surfaces of Tin-Doped In2O3. *Phys. Rev. B - Condens. Matter Mater. Phys.* **2006**, *73* (24), 1–11.

(277) Bartoš, I.; Romanyuk, O.; Paskova, T.; Jiříčeka, P. Electron Band Bending and Surface Sensitivity : X-Ray Photoelectron Spectroscopy of Polar GaN Surfaces. *Surf. Sci.* **2017**, *664*, 241–245.

(278) Margaritondo, G.; Gozzo, F.; Coluzza, C. Band Bending at Semiconductor Interfaces and Its Effect on Photoemission Line Shapes. *Phys. Rev. B* **1993**, *47* (15), 9907–9909.

(279) Szuber, J.; Goepel, W. Photoemission Studies of the Electronic Properties of the Space Charge Layer of SnO2 (110) Surface. *Electron Technol.* **2000**, *33*, 261–281.

(280) Giannozzi, P.; Baroni, S.; Bonini, N.; Calandra, M.; Car, R.; Cavazzoni, C.; Ceresoli, D.; Chiarotti, G. L.; Cococcioni, M.; Dabo, I.; et al. QUANTUM ESPRESSO : A Modular and Open-Source Software Project for Quantum Simulations of Materials. *J Phys. Condens Matter* **2009**, *21*, 395502–395521.

(281) Ping, Y.; Galli, G.; Goddard, W. A. I. Electronic Structure of IrO2 : The Role of the Metal D Orbitals. *J Phys Chem C* **2015**, *119*, 11570–11577.

(282) Perdew, J. P.; Burke, K.; Ernzerhof, M. Generalized Gradient Approximation Made Simple. *Phys. Rev. Lett.* **1996**, *77* (18), 3865–3869.

(283) Corso, A. D. Pseudopotentials Periodic Table : From H to Pu. *Comput. Mater. Sci.* **2014**, *95*, 337–350.

(284) Marzari, N.; Vanderbilt, D.; Vita, A. De; Payne, M. C. Thermal Contraction and Disordering of the Al (110) Surface. *Phys. Rev. Lett.* **1999**, *82* (16), 3296–3300.

(285) Gougoussis, C.; Calandra, M.; Seitsonen, A. P.; Mauri, F. First-Principles Calculations of X-Ray Absorption in a Scheme Based on Ultrasoft Pseudopotentials: From α-Quartz to High-Tc Compounds. *Phys. Rev. B* **2009**, *80*, 075102–075110.

(286) Taillefumier, M.; Cabaret, D.; Flank, A.; Mauri, F. X-Ray Absorption near-Edge Structure Calculations with the Pseudopotentials: Application to the K Edge in Diamond and Alpha -Quartz. *Phys. Rev. B* **2002**, *66*, 195107–195115.

(287) Pehlke, E.; Schefiier, M. Evidence for Site-Sensitive Screening of Core Holes at the Si and Ge (001) Surface. *Phys. Rev. Lett.* **1993**, *71* (14), 2338–2341.

(288) Ma, J.; Habrioux, A.; Luo, Y.; Ramos-Sanchez, G.; Calvillo, L.; Granozzi, G.; Balbuenab, P. B.; Alonso-Vante, N. Electronic Interaction between Platinum Nanoparticles and Nitrogen-Doped Reduced Graphene Oxide: Effect on the Oxygen Reduction Reaction. *J Mater Chem A* **2015**, *3*, 11891–11904.

Résumé détaillé

Introduction et Objectifs

Chaque année, la contribution des énergies renouvelables sur le réseau électrique augmente. Plusieurs technologies peuvent être utilisées pour stocker localement l'électricité produite par les énergies renouvelables et approvisionner le réseau en cas de besoin. Une solution consiste à utiliser des batteries qui pourront ensuite être raccordées au réseau électrique. Toutefois, pour le stockage de l'électricité produite sur une période de plusieurs semaines, l'électrolyse de l'eau reste la meilleure technologie [1]. Cette technologie repose sur la dissociation de l'eau sous l'effet du courant électrique pour obtenir de l'hydrogène (à la cathode) et de l'oxygène (à l'anode), séparées par une membrane échangeuse de protons (PEM).

Les électrolyseurs PEM sont très prometteurs pour la production d'hydrogène : ils sont compacts, performants électriquement et produisent de l'hydrogène très pur. Les principaux inconvénients des électrolyseurs PEM sont l'environnement acide de la membrane et la tension importante à appliquer surtout lors du fonctionnement à forte densité de courant. Seuls les métaux nobles, donc rares et onéreux, peuvent résister dans ces conditions. Le passage à une production de masse des électrolyseurs aurait pour conséquence une augmentation du prix des électrolyseurs PEM [2].

La réaction d'oxydation de l'eau en oxygène se déroule à l'anode. La surtension anodique est la cause principale de la dégradation des performances de la cellule PEM d'électrolyse de l'eau. Il est donc important de mieux comprendre les mécanismes de la catalyse de l'oxydation de l'eau pour envisager une solution aux problèmes de durabilité des électrolyseurs PEM et ainsi améliorer leurs performances. Les méthodes de caractérisation utilisées jusqu'à présent pour l'analyse des électrolyseurs ne sont pas capables de suivre leur évolution pendant la réaction électrochimique et demandent des études plus avancées.

L'objectif principal de ce travail de thèse est l'application de spectroscopies *in-situ* dans le but d'étudier les mécanismes de la réaction d'oxydation de l'eau et de la dégradation de différentes anodes pendant le processus.

La thèse est constituée de six chapitres. Le **1er chapitre** est consacré à une étude bibliographique concernant la technologie des électrolyseurs PEM, leur défis et leurs limitations, ainsi que la caractérisation de catalyseurs en temps réel pendant la réaction. Ces études sont réalisées par spectroscopie d'émission de photoélectrons induits par rayons X (XPS) et par spectroscopie d'absorption des rayons X (XAS) sous une pression proche de l'ambiante (NAP). Le

2ème chapitre décrit les méthodes de caractérisation *ex-situ* et *in-situ* des propriétés physico-chimiques et électrochimiques des matériaux. **Les chapitres 3 à 6** présentent les résultats spectroscopiques obtenus *in-situ* sur différentes anodes : ruthénium métallique et son oxyde thermique ; oxyde mixte d'iridium – ruthénium ; iridium métallique et son oxyde thermique ; iridium supporté sur dioxyde d'étain dopé à l'antimoine.

Cette thèse a été réalisée dans le cadre du projet européen INSIDE dédié aux analyses diagnostiques *in-situ* des électrolyseurs de l'eau.

Résultats et discussions

Tous les catalyseurs étudiés au cours de ce travail ont été synthétisés par nos collègues à DLR (Stuttgart, Allemagne) par réduction de sels métalliques précurseurs par le borohydrure de sodium selon les méthodes décrites dans [3,4]. La méthode sol-gel a été utilisée pour la synthèse des aérogels de dioxyde d'étain dopé utilisés comme supports pour l'iridium [5]. Le support a été préparé à MINES ParisTech (Sophia Antipolis, France). La fabrication de l'assemblage membrane électrodes (AME) a été effectuée par dépôt direct de la couche catalytique sur la membrane. Le pré-requis de ce mode d'élaboration est la préparation d'une encre de catalyseur. Cette dernière est alors déposée directement sur la membrane par pulvérisation. L'objectif est de réaliser le dépôt le plus homogène possible et d'épaisseur optimale.

Après la synthèse, tous les matériaux (les poudres et les AMEs) ont été étudiés par diffraction des rayons X (DRX), microscopie électronique à transmission (MET) et microscopie électronique balayage (MEB). Des exemples de diffractogrammes des poudres de RuO_2 et d'$Ir_{0.7}Ru_{0.3}O_2$ sont présentés sur la **Figure 1**. La position des pics caractéristiques du diffractogramme est analysée à l'aide des fiches ICDD (International Center for Diffraction Data) de l'oxyde rutile et du ruthénium métallique. Les raies de diffraction de l'oxyde d'Ir et de Ru se chevauchent. Ainsi, on ne peut pas distinguer entre la formation de l'oxyde mixte d'iridium – ruthénium ou des phases d'oxydes d'Ir et de Ru séparées. La **Figure 2** présente les images MEB obtenues pour l'AME d'$Ir_{0.7}Ru_{0.3}O_2$ qui peuvent confirmer l'uniformité et l'intégrité de la couche de catalyseurs. Les observations en MET avec l'analyse dispersive en énergie (EDX) ont été réalisées avant et après des mesures *in-situ* pour analyser la forme des particules de catalyseurs et leur distribution en taille. L'analyse de l'iridium supporté sur du dioxyde d'étain dopé à l'antimoine a été réalisée par nos collègues de l'Université d'Anvers.

L'activité électrocatalytique pour l'électrolyse de l'eau en O_2 et H_2 a été mesurée par voltampérométrie cyclique (CV) en présence de vapeur d'eau dans la chambre XPS. La résistance

des AMEs a été mesurée par spectroscopie d'impédance. L'analyse de l'activité des catalyseurs en électrolyte liquide (H_2SO_4) a été réalisée par nos collègues (DLR, Allemagne).

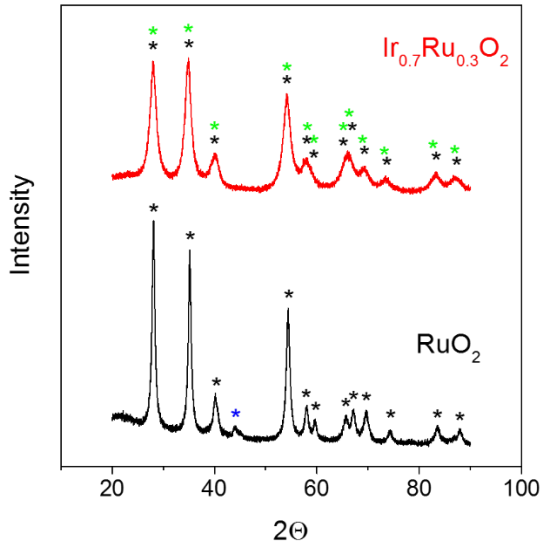

Figure 1. *Diffractogramme obtenu pour les poudres de RuO_2 (bas) et $Ir_{0.7}Ru_{0.3}O_2$ (haut). Les symboles colorés représentent la contribution de : l'oxyde de ruthénium RuO_2 [ICDD 03-065-2824] (noir); le ruthénium métallique [ICDD 01-089-3942] (bleu); l'oxyde d'iridium IrO_2 [ICDD 01-088-0288] (vert).*

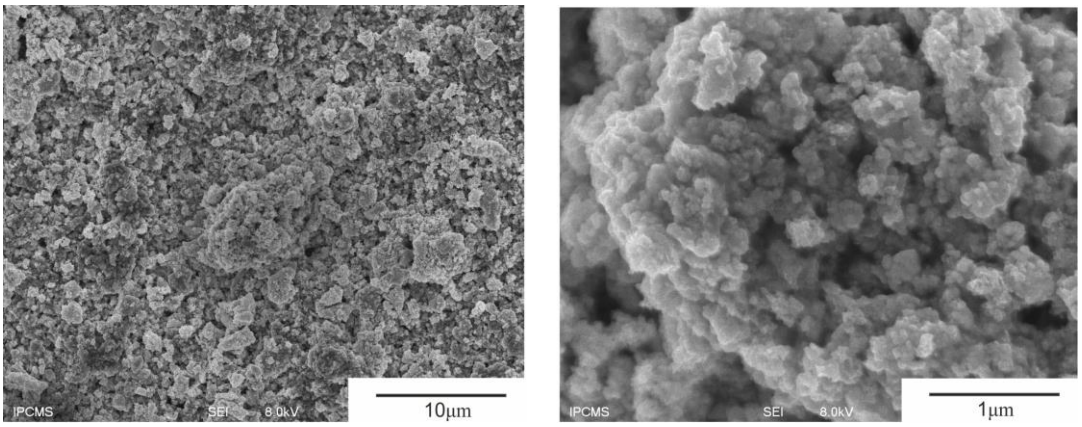

Figure 2. *Images MEB de la surface de l'électrode $Ir_{0.7}Ru_{0.3}O_2$ à des grossissements différents.*

Les résultats spectroscopiques présentés dans ce travail ont été obtenus grâce aux techniques de rayonnement synchrotron sur les lignes ISISS (HZB/BESSY II, Allemagne) et TEMPO (SOLEIL, France) permettant d'effectuer des études en photoémission et en photoabsorption dans la gamme des rayons X de faible énergie. Le rayonnement synchrotron produit une source de lumière dotée de propriétés exceptionnelles : une haute brillance et une large gamme spectrale. La cellule électrochimique a été introduite dans la chambre NAP-XPS pour effectuer les mesures électrochimiques lors de l'enregistrement des spectres de photoémission [6]. La chambre a été aussi équipée d'un spectromètre de masse pour contrôler la composition des gaz

dans la chambre ainsi que la formation de l'oxygène. Les manipulations ont été réalisées sous 3 mbar de vapeur d'eau (correspondant à environ 10% d'humidité relative) et à température ambiante. Grâce aux propriétés de la membrane échangeuse de protons Aquivion (Solvay) utilisée dans ce travail, la performance des anodes sous ces conditions peut être comparée à celle des électrolyseurs PEM réels. Un exemple de voltamogramme cyclique d'anode à base d'$Ir_{0.7}Ru_{0.3}O_2$ obtenu dans la chambre NAP-XPS est présenté sur la **Figure 3**.

Les spectres XPS ont été analysés à l'aide du logiciel CasaXPS. Les rapports atomiques de surface de chaque élément ont été calculés. Afin pour reproduire les résultats expérimentaux et pour estimer l'épaisseur de la couche d'oxyde formée sur les particules pendant la réaction, nous avons réalisé la simulation des spectres de photoémission à l'aide du logiciel SESSA [7]. Ce logiciel est capable de simuler les intensités de photoémission de surfaces de différentes morphologies : des îlots, des bâtonnets, des sphères, des sphères avec des couches supplémentaires.

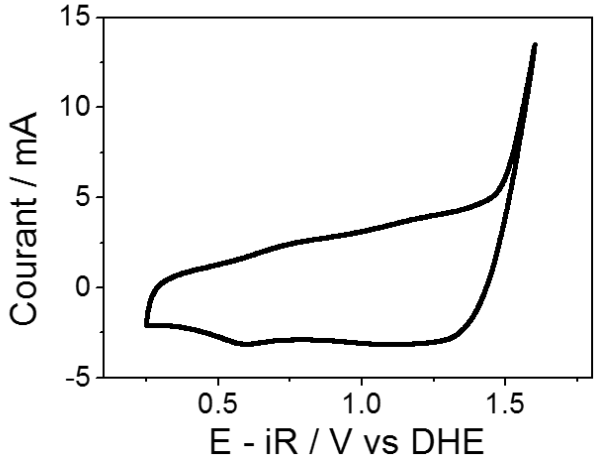

Figure 3. *CV d'anode à base d'$Ir_{0.7}Ru_{0.3}O_2$ mesuré dans la chambre NAP-XPS sous 3 mbar de vapeur d'eau à 20 mV s^{-1}.*

Les anodes à base de ruthénium

Au niveau de l'anode, les oxydes de ruthénium sont les électrocatalyseurs les plus actifs vis-à-vis de l'électrooxydation de l'eau [8-10]. La stabilité de ces anodes dans les conditions d'opération de l'électrolyseur est faible. Pour développer des anodes plus stables, il est nécessaire de mieux comprendre le mécanisme de dégradation des oxydes de ruthénium. Deux types d'oxydes ont été étudiés par NAP-XPS *in-situ* et spectroscopie de structure près du front d'absorption de rayons X (NEXAFS): (i) l'oxyde électrochimique Ru@RuO_x et (ii) l'oxyde thermique RuO_2. Le cœur métallique du premier est couvert par la couche d'oxyde formée pendant les CVs. Le second est un oxyde de type rutile, comme le confirme l'analyse DRX (**Figure 1**).

Les études des anodes RuO_2 et Ru@RuO_x ont été réalisées sur la ligne ISISS du synchrotron BESSY II pendant deux temps de faisceau différents (novembre 2015 pour RuO_2 et mai 2017 pour Ru@RuO_x). Sur la base de l'analyse des résultats NAP-XPS obtenus pour l'oxyde thermique ainsi qu'à cause de la stabilité différente de l'oxyde thermique et de l'oxyde électrochimique nous avons modifié le programme des mesures. Dans le cas de RuO_2, seuls les spectres de photoémission ont été collectés. Les spectres des éléments présents sur la surface de l'électrode (Ru3d, C1s, O1s, F1s, S2p, Si2p) ont été obtenus à des tensions différentes et leur évolution a été suivie pendant deux cycles de l'OER. Cependant, le rôle des transitions oxydation-réduction d'oxygène a été discuté récemment [11-13]. Ainsi, pendant la deuxième session de synchrotron dédiée à l'analyse *in-situ* de Ru@RuO_x, les deux méthodes ont été utilisées – XPS et NEXAFS. Le protocole des mesures était le suivant : pendant le premier cycle de l'OER, seuls des spectres au seuil d'absorption K de l'oxygène ont été enregistrés ; pendant le deuxième – que des spectres Ru3d ; le troisième – O1s. L'état de l'anode Ru@RuO_x entre ces cycles a été contrôlé en recueillant tous les spectres de photoémission et d'absorption.

La **Figure 4 (A)** représente la déconvolution de spectres XPS C1sRu3d obtenus sur RuO_2 réalisée avec quatre contributions : RuO_2, $Ru(OH)_x$, Ru (VI) et Ru (VIII). L'analyse XPS de la surface de Ru@RuO_x (**Figure 5**) démontre le même comportement que RuO_2 mais avec des espèces de ruthénium métallique en plus présentes au début des mesures (avant le cycle OER). Le panneau C de la **Figure 4** montre l'évolution des spectres en fonction de la tension. A 0 V par rapport à l'électrode dynamique à hydrogène (DHE) la surface n'est composée que de RuO_2, tandis que les autres oxydes, avec un état d'oxydation plus élevé (Ru (VI) et Ru (VIII)), n'apparaissent qu'aux tensions plus élevées. Un des effets les plus visibles de l'application de la polarisation est lié à la transformation de l'oxyde de ruthénium de sa forme anhydre, RuO_2, à l'oxyde hydraté, $Ru(OH)_x$. De plus, cette transformation a été considérée comme irréversible ce qui été confirmé

pour les oxydes électrochimiques et thermiques. La formation de l'oxyde hydraté a été confirmée par l'analyse des spectres XPS O1s obtenus pour l'anode à base de Ru@RuO_x.

Fait intéressant, Ru (VI) et Ru (VIII) sont déjà formés à 1.0 V (vs DHE) contrairement au modèle proposé par *Kötz et al*. [14] Aux tensions correspondant à la formation d'oxygène, la quantité de Ru (VIII) diminue pour RuO_2 et ne change pas pour Ru@RuO_x. Donc la participation de Ru (VIII) à la réaction OER comme un intermédiaire est exclue.

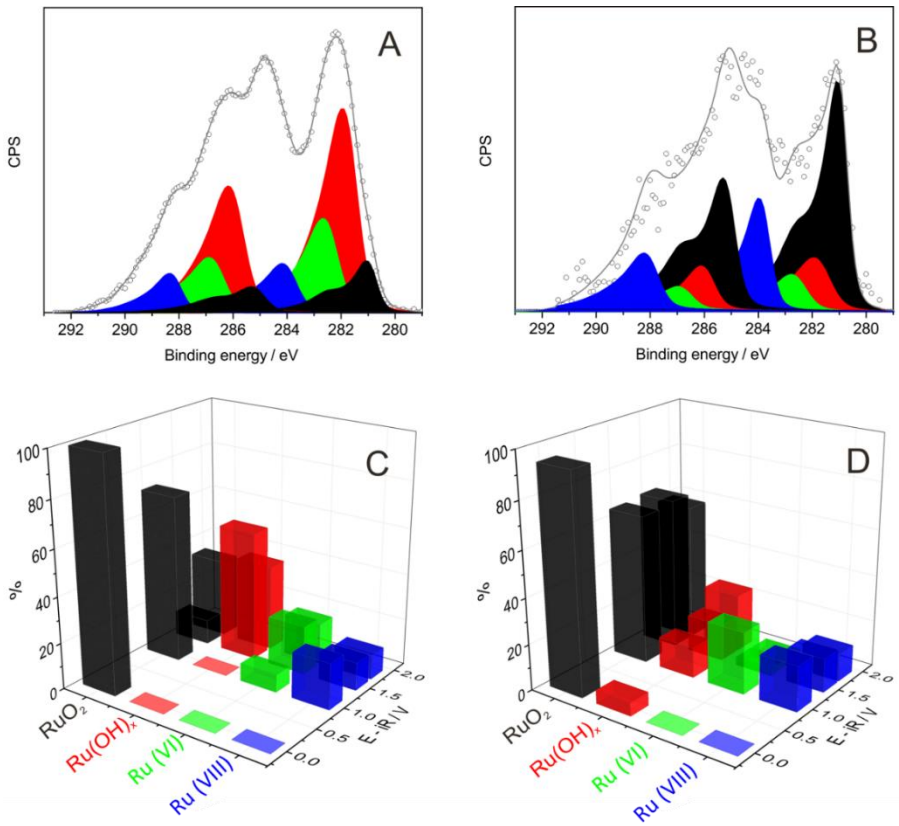

Figure 4. *Panneaux A,B: Déconvolution des spectres C1sRu3d obtenus sur des anodes à base de RuO_2 (A) and $Ir_{0.7}Ru_{0.3}O_2$ (B) mesurés à 1.5 V vs DHE, 3 mbar de vapeur d'eau et une énergie de photons 820 eV. Les cercles noirs représentent les données expérimentales, les lignes grises – les spectres modélisés. Pour des raisons de clarté les pics du carbone ne sont pas présentés. Panneaux C,D:: influence de la tension appliquée sur la composition de la surface de RuO_2 (C) et $Ir_{0.7}Ru_{0.3}O_2$ (D). Code couleur : RuO_2 (noir); $Ru(OH)_x$ (rouge); Ru(VI) (vert); Ru (VIII) (bleu).*

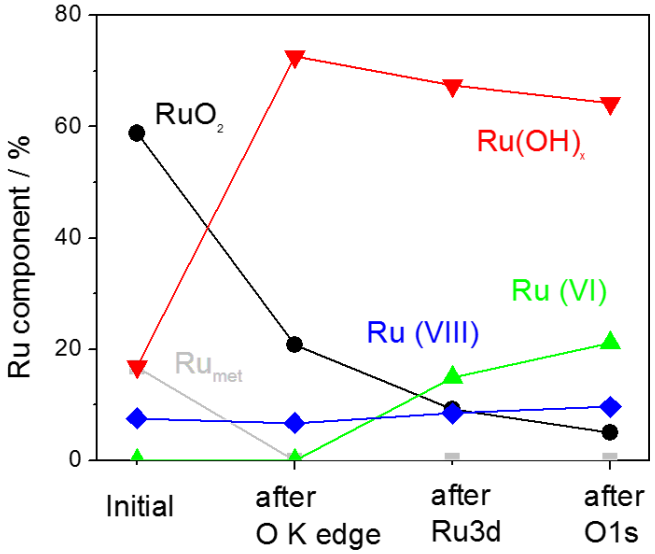

Figure 5. *Influence des cycles OER sur la composition de la surface d'anode Ru@RuO_x évaluée grâce à l'analyse des spectres C1sRu3d mesurés à 0,75 V vs DHE, 3 mbar de vapeur d'eau et une énergie de photons 820 eV. Code couleur : ruthénium métallique Ru_{met} (gris), RuO_2 (noir), $Ru(OH)_x$ (rouge); Ru(VI) (vert); Ru (VIII) (bleu).*

L'analyse des pics au seuil d'absorption K de l'oxygène – « O K edge » (par la méthode du rendement total d'électron, TEY) mesurés sur Ru@RuO_x à différentes tensions est présentée sur la **Figure 6**. Les spectres ont été déconvolués avec trois contributions à l'énergie de 529,2 eV, 530 eV et 531,3 eV. L'attribution des pics au seuil d'absorption K de l'oxygène a été faite sur la base des données XPS expérimentales. Cependant, pour la confirmer, des calculs utilisant la théorie de la fonctionnelle de la densité (DFT) sont hautement souhaitables. Le pic à 529,2 eV a été attribué aux oxydes de Ru (VI) et Ru (VIII). Fait intéressant, ce pic-là est observé sur les spectres « O K edge » indépendamment de la tension. Sur la base de ces résultats nous proposons que Ru (VI) et Ru (VIII) sont plutôt sous la forme d'oxydes que des hydroxydes.

Pour résumer, nous suggérons que les mécanismes de la réaction OER et de la dégradation pour les anodes à base de ruthénium sont basées sur les transitions cationiques. RuO_2 est oxydé en un intermédiaire actif avec l'état d'oxydation élevé, probablement Ru (VII) comme postulé par *Koetz et al.* A cause de sa courte durée de vie, cet intermédiaire ne peut pas être détecté, car il est rapidement transformé en d'autres espèces de Ru, formant de l'oxygène [14]. La formation irréversible de l'oxyde hydraté de Ru (IV) pendant la réaction d'oxydation de l'eau en oxygène est responsable de la dégradation des catalyseurs. Par contre, la forte concentration de $Ru(OH)_x$ empêche la stabilisation de l'oxyde électrochimique. Ce chapitre a montré que le mécanisme de dégradation des électrodes à base de ruthénium est lié à la transition oxyde de rutile – oxyde hydraté.

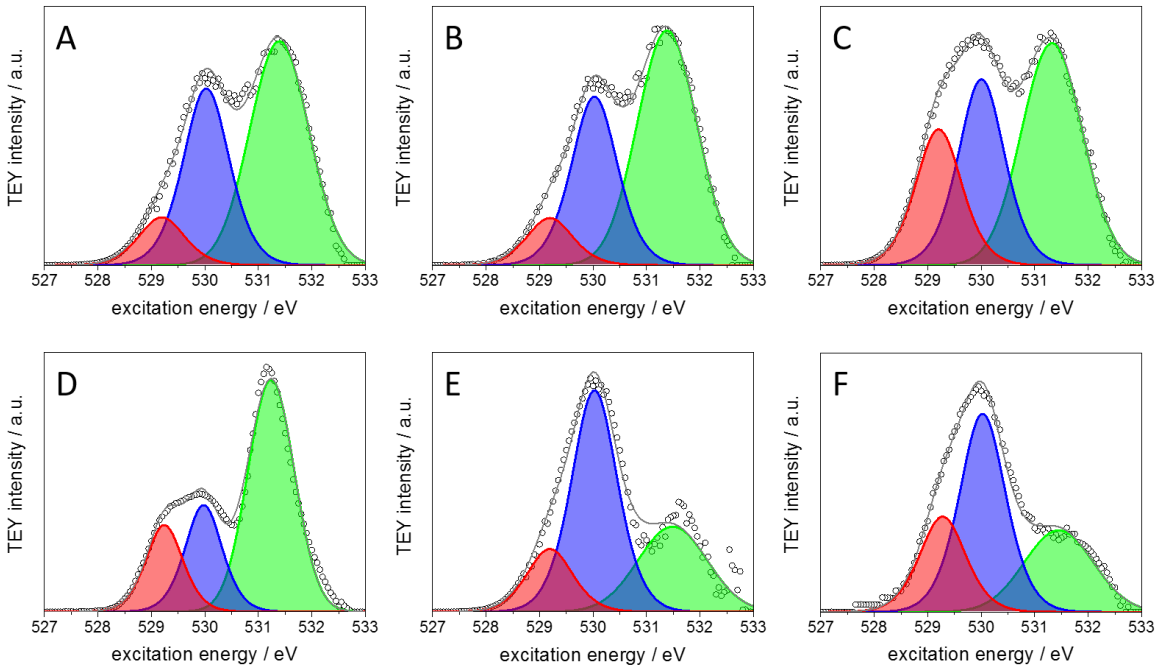

Figure 6. *Signal TEY en fonction de l'énergie d'excitation au seuil d'absorption K de l'oxygène obtenu sur Ru@RuOx à 3 mbar de vapeur d'eau et aux tensions : 0,75 V (A); 1,0 V (B); 1,34 V (C); 1,43 V (D); 0,75 V après le 1er cycle d'OER (E) et après le 3^{me} cycle d'OER (F). Code couleur : 529,2 eV (rouge), 530 eV (rouge), gaz de O_2 / OH absorbé (vert), données expérimentales (cercles noirs), résultats de la modélisation (ligne grise).*

Mécanisme de stabilisation sur les oxydes mixtes d'iridium-ruthénium

Les oxydes mixtes d'iridium et de ruthénium sont généralement utilisés comme catalyseurs de la réaction de dégagement de l'oxygène. Au vu de leur stabilité et activité importantes, de nombreuses recherches se sont focalisées sur ces catalyseurs [15, 16]. Au moment de ce travail, les raisons de la stabilité améliorée des oxydes mixtes d'iridium et de ruthénium présentés dans la littérature sont assez contradictoires [15 – 17]. Pour identifier le rôle de l'iridium dans la stabilisation des oxydes mixte $Ir_{0.7}Ru_{0.3}O_2$, la composition de la surface de RuO_2 et d'$Ir_{0.7}Ru_{0.3}O_2$ a été étudiée *in-situ* par NAP-XPS à différentes tensions.

L'analyse EDX (**Figure 7**) a confirmé la formation d'une seule phase d'$Ir_{0.7}Ru_{0.3}O_2$ plutôt qu'un mélange de deux phases séparées RuO_2 et IrO_2, tandis que la position des pics caractéristiques du diffractogramme (**Figure 1**) confirme la structure de rutile.

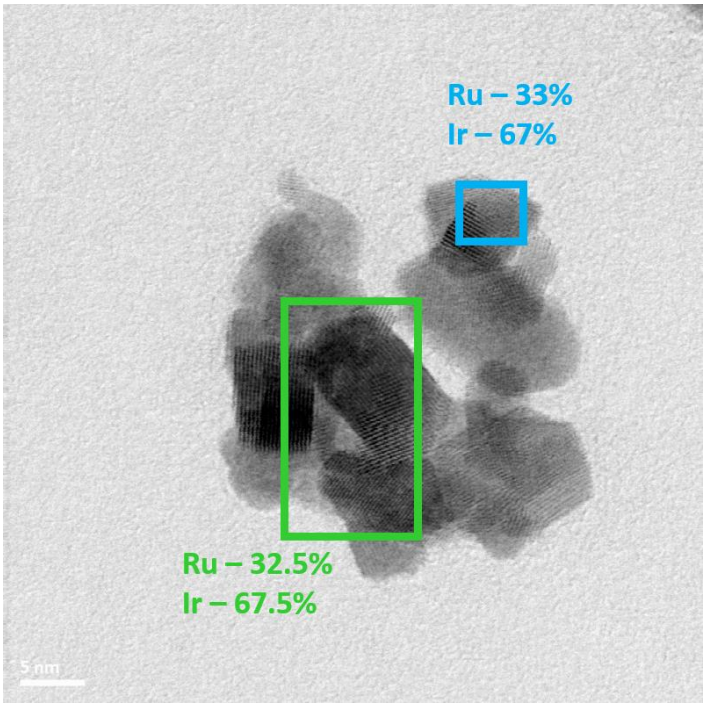

Figure 7. *Images MET de la surface de l'électrode $Ir_{0.7}Ru_{0.3}O_2$ après l'analyse NAP-XPS. Le pourcentage atomique de Ru et d'Ir estimé par l'analyse EDX est indiqué sur la figure dans les différentes régions.*

La comparaison des spectres (**Figure 4**, panneaux A,B) à 1.5 V vs DHE (dans les conditions de la réaction de dégagement de l'oxygène) montre que la présence d'iridium n'atténue pas la formation de RuO_4, comme proposé dans la littérature [18, 19]. Par contre, la transformation RuO_2 – $Ru(OH)_x$ est limitée par l'iridium (**Figure 4**, panneaux C,D). Quant à RuO_4, la présence de l'iridium le stabilise à la surface du catalyseur anodique.

En faisant varier l'énergie des photons il est possible d'augmenter l'épaisseur de la couche de catalyseur étudiée. Le cœur des particules d'$Ir_{0.7}Ru_{0.3}O_2$ est composé de l'oxyde d'Ir(Ru) sous forme rutile, tandis que Ru (VI) et Ru (VIII) ne sont présents qu'à la surface.

Afin d'identifier la phase active pour la réaction de dégagement de l'oxygène, l'analyse de spectres Ir4f a été réalisée. L'absence de changement peut être expliqué par les hypothèses suivantes : (i) le rôle de l'iridium n'est que dans la stabilisation du ruthénium ; (ii) la quantité des espèces intermédiaires avec un état d'oxydation plus que (IV) est trop petite pour être identifiée ; (iii) le mécanisme de dégagement de l'oxygène est associé aux transitions red-ox des anions uniquement. Pour le vérifier, le chapitre suivant est consacré aux études des anodes à base d'iridium pur.

Mécanisme de dégagement de l'oxygène sur les oxydes d'iridium

Le mécanisme classique de la réaction de dégagement de l'oxygène propose un modèle basé sur les transitions red-ox des cations. Dans le cas de l'iridium, sur la base des expériences observées par *in-situ* NAP-XPS [20] and XANES [21] les auteurs ont proposé la formation de Ir (V) comme espèce active lors de la réaction. Par contre, l'implication des anions de l'oxygène pour des électrolyseurs à haute température est bien connue dans la littérature [12]. Les résultats obtenus récemment pour des électrodes à base de couche d'iridium par le groupe de R. Schlögl [13] proposent la participation de O^{I-} comme l'intermédiaire de la réaction de dégagement de l'oxygène. Tous ces résultats ne peuvent pas être directement comparés en raison des différentes techniques utilisées et des différents types de catalyseurs. L'objectif de ce chapitre est d'effectuer une étude spectroscopique comparative de deux types d'oxydes d'iridium obtenus soit par l'oxydation électrochimique (Ir@IrO_x) soit thermique (IrO_2). Les deux catalyseurs ont été intégrés dans l'assemblage membrane électrodes et ont été étudiés sous les mêmes conditions en utilisant la spectroscopie d'absorption des rayons X (O K edge) et d'émission de photoélectrons induits par rayons X (O1s, Ir4f) pour détecter les transitions des anions d'O et des cations d'Ir dans les conditions de la réaction de dégagement de l'oxygène. Les mesures ont été réalisées au centre de synchrotron BESSY II en novembre 2016. L'analyse des données spectroscopiques a été complétée par des calculs DFT effectués par Travis Jones à FHI (Berlin, Allemagne).

Les panneaux de la **Figure 8** représentent les pics au seuil d'absorption K de l'oxygène – O K edge (TEY) – mesurés sur Ir@IrO_x et IrO_2 à une tension correspondant à la réaction de dégagement de l'oxygène. On trouve la présence des espèces O^{I-} sur les deux anodes. Par contre, O^{II-} n'est présent que sur l'oxyde thermique, ce qui est confirmé par les spectres O1s (panneaux C, D de la **Figure 8**). L'influence de la tension sur les courants et la quantité des espèces O^{I-} est montrée sur les panneaux A et B de la **Figure 9**. La formation de O^{I-} correspond à un début de dégagement de l'oxygène plus tôt dans le processus. Nous avons observé que la formation des espèces O^{I-} est dépendante de la tension, donc cette étape est électrochimique. Sur la base de la relation linéaire entre le courant et la quantité de O^{I-} obtenu pour Ir@IrO_x (Panneau A de la **Figure 9**), nous suggérons que la formation des molécules d'oxygène est une étape chimique :

$$2O^{I-} \rightarrow O_{2\,(gas)} \quad (Eq.1)$$

Fait intéressant, pour l'anode à base de IrO_2, on observe la formation des espèces O^{I-} avant l'augmentation de courant (Panneau B de la **Figure 9**). La réaction (équation 1) demande la déformation de la structure de l'oxyde, ce qui est assez difficile pour l'oxyde thermique avec sa

structure rigide de rutile. Cependant, on ne peut pas exclure la présence d'autres étapes conduisant à des changements de comportement O^{I-}/courant pour IrO_2 par rapport à l'oxyde électrochimique.

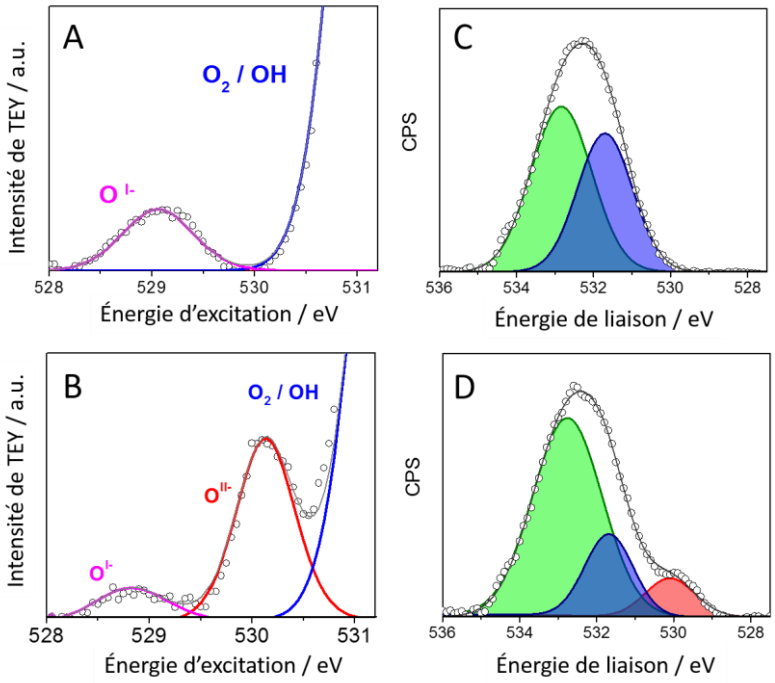

Figure 8. *Panneaux à gauche : Signal TEY en fonction de l'énergie d'excitation au seuil d'absorption K de l'oxygène obtenu sur Ir@IrO_x (A) et IrO_2 (B) à 3 mbar de vapeur d'eau et 1,5V (dans les conditions de la réaction de dégagement de l'oxygène). Code couleur : O^{I-} (magenta), O^{II-} (rouge), gaz de O_2 / OH absorbé (bleu), données expérimentales (cercles noirs), résultats de la modélisation (ligne grise). Panneaux à droite : Déconvolution des spectres O1s sur Ir@IrO_x (C) et IrO_2 (D) mesurés à 0V vs DHE. Code couleur : oxyde de la structure (rouge) ; hydroxyde / espèces de C = O (bleu) ; eau adsorbée / espèces de C - O (vert). Energie cinétique : 530 eV.*

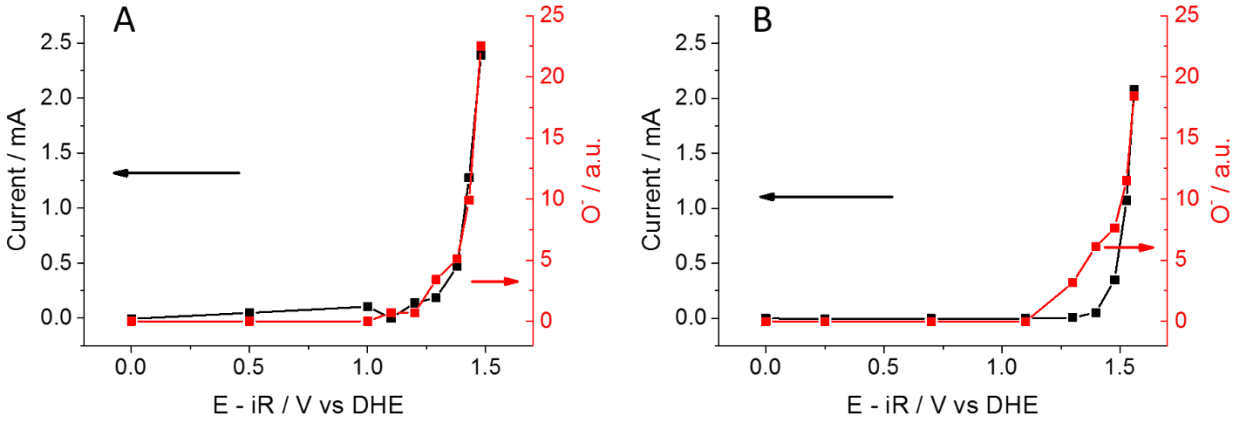

Figure 9. *Courants (noir) et quantité de O^{I-} (rouge) en fonction de la tension appliquée pour Ir@IrO_x (Panneau A) et IrO_2 (Panneau B).*

Pour écarter l'hypothèse de la participation des transitions red-ox des cations d'iridium dans la réaction d'oxydation de l'eau, nous avons analysé les spectres Ir4f résolus pour deux anodes. L'analyse des spectres Ir4f XP obtenus sur l'oxyde électrochimique d'iridium a montré la

présence de trois composants d'iridium à 0 V vs DHE : iridium métallique, Ir (III) et Ir (IV) [22]. Leur évolution en fonction de la tension appliquée est présentée sur **Figure 10**. Les transitions Ir (III) / Ir (IV) ont été enregistrées avant le début du dégagement de l'oxygène, cependant nous n'avons pas observé de transition supplémentaire pendant la réaction. Le changement de l'énergie cinétique pour faire varier la profondeur analytique des rayons X n'a pas affecté le rapport entre les espèces d'iridium. Ainsi, nous ne pouvons pas soutenir l'idée de la structure « core-shell » pour Ir@IrO_x proposée avant dans la littérature [23]. Donc nous proposons la formation d'une couche poreuse d'oxyde électrochimique. Son épaisseur effective a été estimée au moyen du logiciel SESSA et était environ 0.5 nm. Contrairement à l'oxyde électrochimique Ir@IrO_x, nous avons confirmé la stabilité de l'oxyde thermique IrO_2 aux tensions appliquées.

Ainsi, ce travail ne supporte pas la formation d'espèces d'Ir avec l'état d'oxydation > IV dans les conditions de la réaction de dégagement de l'oxygène soit pour l'oxyde thermique ou électrochimique. L'étude des anodes à base d'iridium a montré que le mécanisme de dégagement de l'oxygène ne dépend pas de la nature de l'oxyde et qu'il est associé aux transitions red-ox des anions (O^{II-}/O^{I-}), et pas des cations d'iridium.

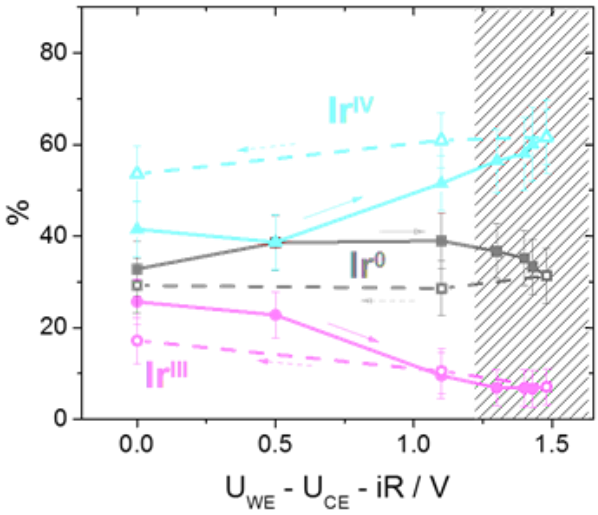

Figure 10. *Influence de la tension appliquée sur la composition de la surface de l'anode à base de Ir@IrOx. Les mesures ont été effectuées sous 3 mbar de vapeur d'eau. Energie des photons 595 eV. Les lignes continues représentent la direction vers l'avant et les lignes pointillées – vers l'arrière.*

Anodes d'iridium supporté sur le dioxyde d'étain dopé à l'antimoine. Interaction entre le métal et le support

Tandis que les anodes d'iridium sont stables et actives, le prix élevé de ce métal est une grande limitation pour leur utilisation. Pour diminuer la quantité nécessaire des catalyseurs sans perte d'efficacité, les nanoparticules de catalyseur peuvent être dispersées sur un support, de manière à obtenir une plus grande surface active. L'utilisation d'un matériau support limite aussi les phénomènes d'agglomération entre les espèces métalliques, conférant ainsi une meilleure stabilité aux catalyseurs [24 – 26].

Le support à base d'aérogels de SnO_2 dopé à l'antimoine (ATO) possède une conductivité électronique élevée et la stabilité nécessaire pour être utilisé à l'anode d'électrolyseur PEM [5]. Des mesures NAP-XPS ont été effectuées sur trois systèmes catalytiques : Ir / ATO, Ir non supporté et ATO pur (sans iridium) dans le but de comprendre les raisons de l'activité et de la stabilité élevées des anodes à base de Ir/ATO observées par nos partenaires [27]. Les mesures NAP-XPS ont été effectuées sur la ligne TEMPO du SOLEIL synchrotron (Paris, France). L'interprétation des données a également été complétée par la modélisation des spectres XP à l'aide du logiciel SESSA. L'analyse microscopique a été effectuée par le groupe de microscopie électronique de l'Université d'Anvers (Belgique).

Les résultats précédents ont montré que la présence du support peut limiter l'oxydation de l'iridium [24]. La **Figure 11** montre les spectres XPS obtenus sur Ir non supporté (panneaux à gauche) et Ir/ATO (panneaux à droite). La surface de l'iridium non supporté est couverte par le mélange des oxydes d'iridium (III) et (IV), par contre dans le cas de l'anode à base de Ir/ATO, uniquement l'oxyde Ir (IV) a été observé. L'absence des espèces de Ir (III) peut expliquer la stabilité élevée de l'oxyde supporté. Similaire aux résultats obtenus sur Ir@IrO_x à la ligne ISISS (du synchrotron BESSY II) et discutés dans la partie précédente de ce travail, la transition Ir (III) / Ir (IV) se produit avant le début du dégagement de l'oxygène.

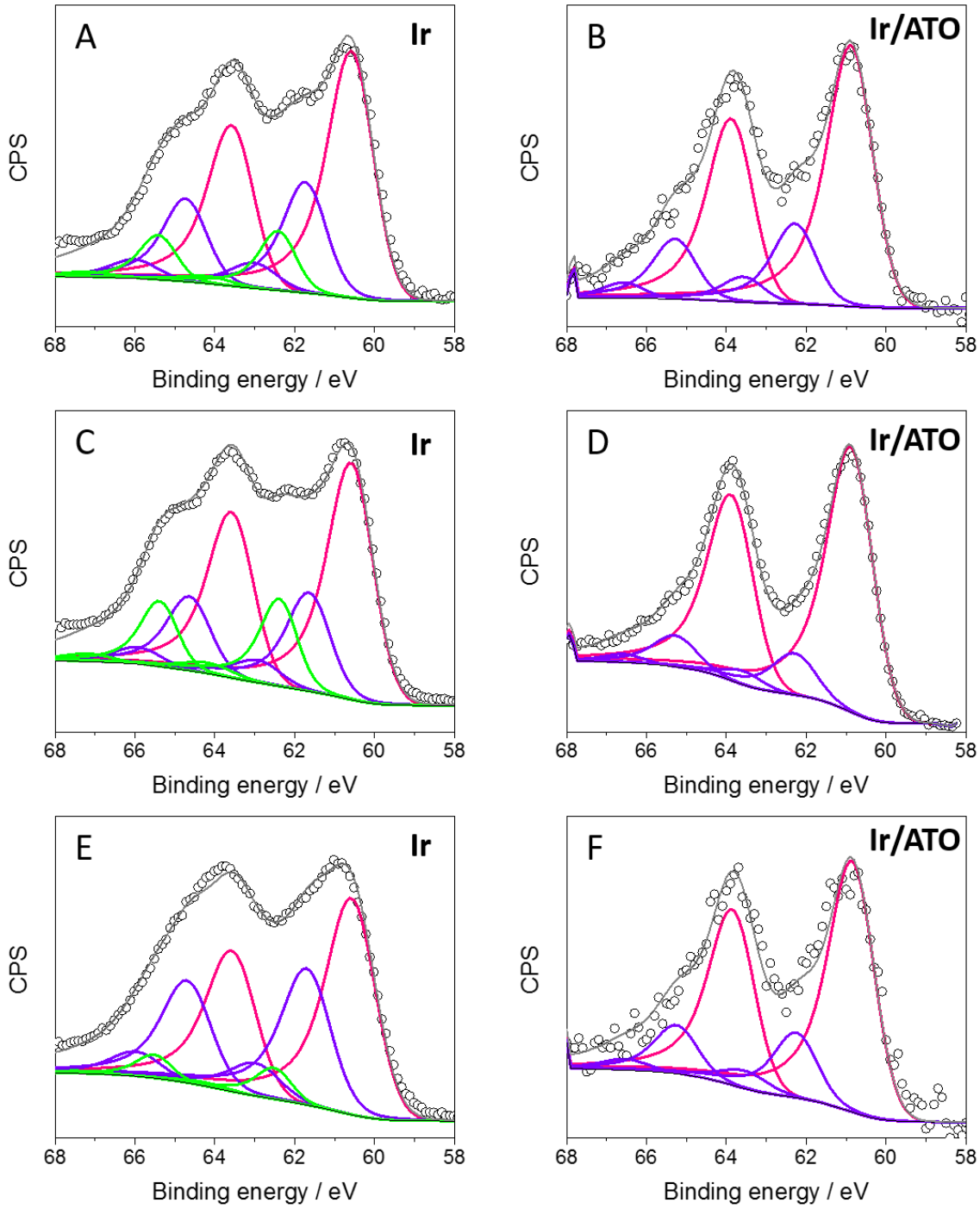

Figure 11. *Déconvolution des spectres Ir4f sur Ir non supporté (A, C, E) et Ir/ATO (B, D, F) mesurés à -0,25 V et 0,2 V, respectivement. Code couleur : iridium métallique – rose, Ir (III) – vert et Ir (IV) – violet. Energies cinétiques : 390 eV (A,B) ; 530 eV (C,D) ; 810 eV (E,F).*

La **Figure 12** représente les spectres XPS $Sn3d_{5/2}$ obtenus sur ATO à différentes tensions. L'oxyde d'étain est connu pour être non stoechiométrique et est considéré comme un mélange d'espèces Sn (II) et Sn (IV) [28], le rapport entre eux dépendant de divers facteurs, tels que la polarisation, le niveau de dopage [29, 30], etc. La largeur à mi-hauteur (FWHM) et la position des pics sont stables, confirmant la stabilité du substrat ATO dans les conditions de la réaction de

dégagement de l'oxygène. L'analyse du rapport atomique entre étain et antimoine montre la ségrégation de Sb sur la surface de l'anode. Cependant, ce rapport est stable à différentes tensions appliquées.

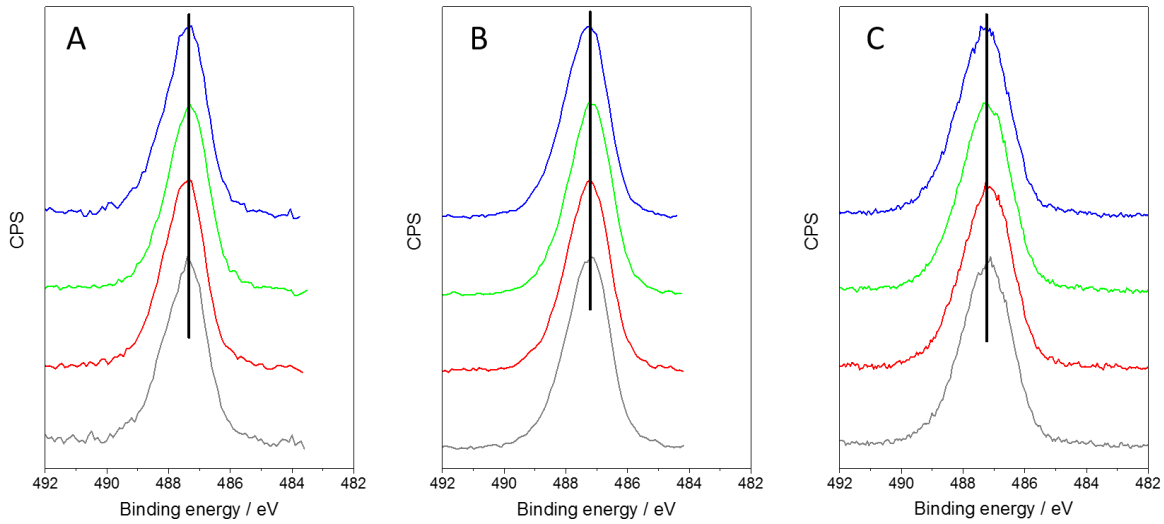

Figure 12. *Spectres $Sn3d_{5/2}$ obtenus sur l'anode à base d'ATO à 3 mbar de vapeur d'eau et aux tensions : 0,2 V (gris); 1,0 V (rouge); 1,6 V (vert) ; 1,7 V (bleu). Energies cinétiques : 390 eV (A) ; 530 eV (B) ; 810 eV (C).*

La largeur des spectres Sn3d est stable indépendamment de la présence d'iridium ou des tensions appliquées (**Figure 13**), cependant l'énergie de liaison se déplace avec l'augmentation de la tension pour Ir/ATO. Ce décalage peut être attribué à la courbure des bandes électroniques à la suite de l'interaction iridium – ATO ou au changement de niveau de dopage [31].

L'analyse du rapport atomique Sn/Ir calculé pour trois énergies de photons différentes démontre la croissance d'étain sur la surface de l'anode aux tensions de la réaction de dégagement de l'oxygène (**Figure 14**). L'augmentation de la contribution de l'étain peut être expliqué par :

1. encapsulation partielle ou totale de nanoparticules d'iridium par ATO ;
2. changements de la taille et / ou de la forme des nanoparticules d'iridium ;
3. nettoyage de la surface d'Ir sous cyclage potentiel (l'oxydation de carbone) ;
4. détachement des nanoparticules d'iridium dans les conditions de la réaction de dégagement de l'oxygène.

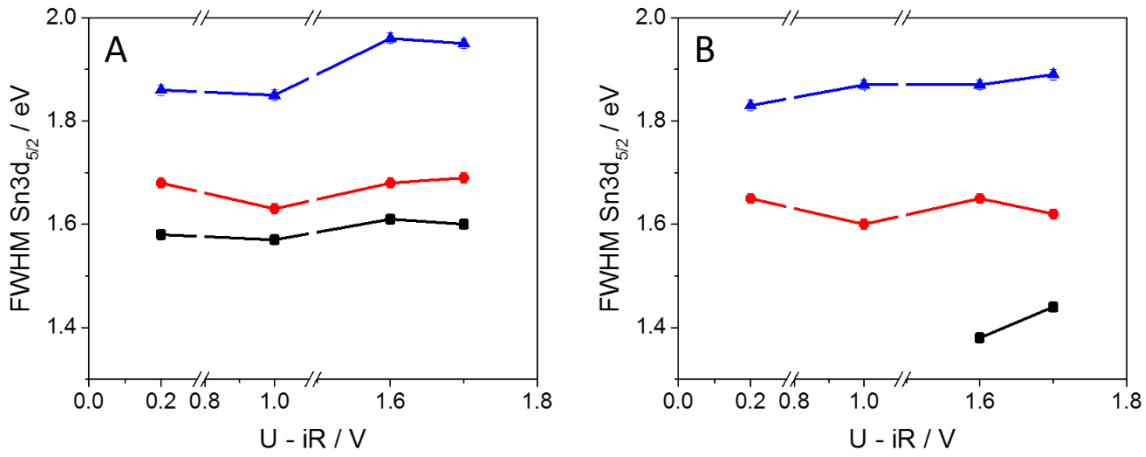

Figure 13. *Changements des largeurs à mi-hauteur (FWHM) des spectres Sn3d$_{5/2}$ obtenus sur ATO pur (A) et Ir / ATO (B) en fonction de la tension. L'énergie cinétique a été variée : 390 eV (noir), 530 eV (rouge), 810 eV (bleu).*

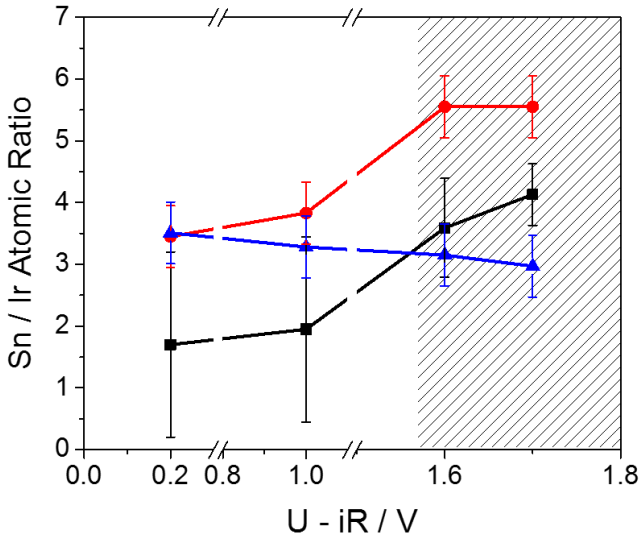

Figure 14. *Rapport atomique Sn/Ir estimé sur la base des spectres XP obtenus sur Ir/ATO à 3 mbar de vapeur d'eau et à différentes tensions. L'énergie cinétique a été variée : 530 eV (rouge), 810 eV (bleu).*

Le rapport C / Ir analysé aux différentes tensions appliquées était assez stable, donc l'hypothèse d'un nettoyage de la surface peut être exclue.

L'état des électrodes a été étudié avant et après la réaction par microscopie MET par nos collègues à l'Université d'Anvers. La taille des particules est restée constante. Par contre, nous avons observé le détachement partiel d'iridium. Cependant, la quantité de particules détachées ne peut pas être très élevée, sinon l'activité électrochimique de l'anode à base d'Ir / ATO doit être la même que pour Ir non supporté et ce n'est pas le cas (selon les données obtenues dans l'électrolyte liquide). De plus, nous n'avons pas observé les changements dans les distributions élémentaires. Par l'analyse post-mortem nous n'avons pas confirmé la formation de coquille d'ATO sur les

particules d'iridium. Ainsi, aucune de les hypothèses proposées ci-dessus ne peut être soutenue par l'analyse post mortem à moins que les changements de la surface ne soient pas réversibles.

Pour vérifier l'idée que la formation d'une coquille d'ATO et / ou des changements de la taille / de la forme des particules d'iridium (en supposant qu'ils soient réversibles) pourrait modifier le rapport Sn / Ir, nous avons simulé des spectres de photoémission pour plusieurs morphologies variant les paramètres de modélisation.

Sur la base des résultats obtenus, nous proposons soit une encapsulation partielle des particules d'Ir soit la formation d'une couche poreuse d'ATO, les deux doivent être réversibles. La transition Ir (III) / Ir (IV) est empêchée par la présence du support ATO, ce qui pourrait être la raison de la stabilité élevée d'Ir supporté. Son activité électrochimique élevée par rapport au catalyseur non supporté était liée à la couche mince d'oxyde d'iridium formée dans les conditions de la réaction.

Conclusion générale

Ce travail de thèse, consacré aux analyses des anodes d'électrolyseur PEM *in-situ* par techniques spectroscopiques, a montré que le mécanisme de dégagement de l'oxygène sur les anodes à base de ruthénium est associé aux transitions red-ox des cations tandis que sur les anodes à base d'iridium – à la transition red-ox des anions (O^{II-} / O^{I-}).

Particulièrement, on a démontré que :

- le mécanisme de dégradation des électrodes à base de ruthénium est lié à la transition oxyde de rutile – oxyde hydraté ;
- Ru (VIII) est l'intermédiaire dans la réaction de dégagement de l'oxygène ;
- la transformation RuO_2 – $Ru(OH)_x$ est limitée par la présence d'iridium ;
- le mécanisme de dégagement de l'oxygène sur les anodes à base d'iridium ne dépend pas de la nature de l'oxyde et qu'il est associé aux transitions red-ox des anions (O^{II-} / O^{I-}) ;
- la stabilité importante de l'iridium supporté sur ATO est attribuée à l'absence de Ir (III) et au fait que la surface des nanoparticules d'iridium soit couverte partiellement par les particules du support aux tensions de dégagement de l'oxygène.

Perspectives

Ce travail a permis de comprendre les mécanismes de dégagement de l'oxygène sur les anodes à base de ruthénium et d'iridium. Cependant, il faut comprendre pourquoi ces anodes fonctionnent selon des mécanismes différents. Pour cela on devrait probablement analyser les structures électroniques de Ru et d'Ir.

Concernant l'utilisation de la méthode NAP-XPS pour étudier le comportement des anodes et des cathodes dans l'électrolyseur alcalin *in-situ*, nous avons effectué les premières tentatives. Les résultats obtenus ont indiqué la nécessité de modifierla cellule *in-situ* utilisée dans les mesures présentées dans ce travail.

Références

(1) Aneke, M.; Wang, M. Energy Storage Technologies and Real Life Applications – A State of the Art Review. *Appl. Energy* **2016**, *179*, 350–377.

(2) Wang, M.; Wang, Z.; Gong, X.; Guo, Z. The Intensification Technologies to Water Electrolysis for Hydrogen Production – A Review. *Renew. Sustain. Energy Rev.* **2014**, *29*, 573–588.

(3) Lettenmeier, P.; Wang, L.; Golla-Schindler, U.; Gazdzicki, P.; Cañas, N. A.; Handl, M.; Hiesgen, R.; Hosseiny, S. S. S.; Gago, A. S.; Friedrich, A. K. Nanosized IrOx-Ir Catalyst with Relevant Activity for Anodes of PEM Electrolysis Produced by a Cost-Effective Procedure. *Angew. Chemie* **2015**, *128*, 752–756.

(4) Wang, L.; Lettenmeier, P.; Golla-Schindler, U.; Gazdzicki, P.; Cañas, N.; Handl, M.; Hiesgen, R.; Hosseiny, S. S.; Gago, A. S.; Friedrich, A. K. Nanostructured Ir-Supported on Ti4O7 as Cost Effective Anode for Proton Exchange Membrane (PEM) Electrolyzers. *Phys. Chem. Chem. Phys.* **2015**, *18*, 4487–4495.

(5) Ozouf, G.; Beauger, C. Niobium- and Antimony-Doped Tin Dioxide Aerogels as New Catalyst Supports for PEM Fuel Cells. *J. Mater. Sci.* **2016**, *51* (11), 5305–5320.

(6) Salmeron, M.; Schlögl, R. Ambient Pressure Photoelectron Spectroscopy: A New Tool for Surface Science and Nanotechnology. *Surf. Sci. Rep.* **2008**, *63* (4), 169–199.

(7) Werner, W. S. M.; Smekal, W.; Hisch, T.; Himmelsbach, J.; Powell, C. J. Simulation of Electron Spectra for Surface Analysis (SESSA) for Quantitative Interpretation of (Hard) X-Ray Photoelectron Spectra (HAXPES). *J. Electron Spectros. Relat. Phenomena* **2013**, *190*, 137–143.

(8) Carmo, M.; Fritz, D. L.; Mergel, J.; Stolten, D. A Comprehensive Review on PEM Water Electrolysis. *Int. J. Hydrogen Energy* **2013**, *38* (12), 4901–4934.

(9) Matsumoto, Y.; Sato, E. Electrocatalytic Properties of Transition Metal Oxides for Oxygen Evolution Reaction. *Mater. Chem. Phys.* **1986**, *14* (5), 397–426.

(10) Fabbri, E.; Habereder, A.; Waltar, K.; Kötz, R.; Schmidt, T. J. Developments and Perspectives of Oxide-Based Catalysts for the Oxygen Evolution Reaction. *Catal. Sci. Technol.* **2014**, *4* (11), 3800–3821.

(11) Grimaud, A.; Diaz-Morales, O.; Han, B.; Hong, W. T.; Lee, Y.-L.; Giordano, L.; Stoerzinger, K. A.; Koper, M. T. M.; Shao-Horn, Y. Activating Lattice Oxygen Redox Reactions in Metal Oxides to Catalyze Oxygen Evolution. *Nat. Chem.* **2017**, *9*, 457–465.

(12) Mueller, D. N.; Machala, M. L.; Bluhm, H.; Chueh, W. C. Redox Activity of Surface Oxygen Anions in Oxygen-Deficient Perovskite Oxides during Electrochemical Reactions. *Nat. Commun.* **2015**, *6*, 6097–6105.

(13) Pfeifer, V.; Jones, T. E.; Velasco Vélez, J. J.; Arrigo, R.; Piccinin, S.; Hävecker, M.; Knop-Gericke, A.; Schlögl, R. In Situ Observation of Reactive Oxygen Species Forming on Oxygen-Evolving Iridium Surfaces. *Chem. Sci.* **2017**, *8*, 2143–2149.

(14) Kötz, R.; Lewerenz, H. J.; Brüesch, P.; Stucki, S. Oxygen Evolution on Ru and Ir Electrodes. *J. Electroanal. Chem. Interfacial Electrochem.* **1983**, *150* (1–2), 209–216.

(15) Kötz, R.; Stucki, S. Stabilization of RuO_2 by IrO_2 for Anodic Oxygen Evolution in Acid Media. *Electrochim. Acta* **1986**, *31* (10), 1311–1316.

(16) Angelinetta, C.; Trasatti, S.; Atanososka, L. D.; Atanasoski, R. T. Surface Properties of RuO_2 + IrO_2 Mixed Oxide Electrodes. *J. Electroanal. Chem. Interfacial Electrochem.* **1986**, *214* (1–2), 535–546.

(17) Yeo, R. S.; Orehotsky, J.; Visscher, W.; Srinivasan, S. Ruthenium-Based Mixed Oxides as Electrocatalysts for Oxygen Evolution in Acid Electrolytes. *J. Electrochem. Soc.* **1981**, *128* (9), 1900–1904.

(18) Kötz, R.; Stucki, S.; Scherson, D.; Kolb, D. M. In-Situ Identification of RuO4 as the Corrosion Product During Oxygen Evolution on Ruthenium in Acid Media. *J. Electroanal. Chem.* **1984**, *172*, 211–219.

(19) Sardar, K.; Petrucco, E.; Hiley, C. I.; Sharman, J. D. B.; Wells, P. P.; Russell, A. E.; Kashtiban, R. J.; Sloan, J.; Walton, R. I. Water-Splitting Electrocatalysis in Acid Conditions Using Ruthenate-Iridate Pyrochlores. *Angew. Chemie - Int. Ed.* **2014**, *53* (41), 10960–10964.

(20) Sanchez Casalongue, H. G.; Ng, M. L.; Kaya, S.; Friebel, D.; Ogasawara, H.; Nilsson, A. In Situ Observation of Surface Species on Iridium Oxide Nanoparticles during the Oxygen Evolution Reaction. *Angew. Chemie Int. Ed.* **2014**, *53* (28), 7169–7172.

(21) Minguzzi, A.; Lugaresi, O.; Achilli, E.; Locatelli, C.; Vertova, A.; Ghigna, P.; Rondinini, S. Observing the Oxidation State Turnover in Heterogeneous Iridium-Based Water Oxidation Catalysts. *Chem. Sci.* **2014**, *5*, 3591–3597.

(22) Pfeifer, V.; Jones, T. E.; Velasco Vélez, J. J.; Massué, C.; Greiner, M. T.; Arrigo, R.; Teschner, D.; Girgsdies, F.; Scherzer, M.; Allan, J.; et al. The Electronic Structure of Iridium Oxide Electrodes Active in Water Splitting. *Phys. Chem. Chem. Phys.* **2016**, *18*, 2292–2296.

(23) Nong, H. N.; Oh, H.-S.; Reier, T.; Willinger, E.; M.G., W.; Petkov, V.; Teschner, D.; Strasser, P.; Willinger, M.-G.; Petkov, V.; et al. Oxide-Supported IrNiOx Core-Shell Particles as Efficient, Cost-Effective, and Stable Catalysts for Electrochemical Water Splitting. *Angew. Chemie* **2015**, *54* (10), 2975–2979.

(24) Oh, H.; Nong, H. N.; Reier, T.; Bergmann, A.; Gliech, M.; Ferreira, J.; Arau, D.; Willinger, E.; Schlo, R.; Teschner, D.; et al. Electrochemical Catalyst − Support Effects and Their Stabilizing Role for IrO X Nanoparticle Catalysts during the Oxygen Evolution Reaction. *J. Am. Chem. Soc.* **2016**, *138* (38), 12552–12563.

(25) Jackson, C.; Smith, G. T.; Inwood, D. W.; Leach, A. S.; Whalley, P. S.; Callisti, M.; Polcar, T.; Russell, A. E.; Levecque, P.; Kramer, D. Electronic Metal-Support Interaction Enhanced Oxygen Reduction Activity and Stability of Boron Carbide Supported Platinum. *Nat. Commun.* **2017**, *8* (May), 15802–15813

(26) Cognard, G.; Ozouf, G.; Beauger, C.; Lopez-Haro, M.; Chatenet, M.; Maillard, F. Pt Nanoparticles Supported on Antimony-Doped and Niobium-Doped Tin Dioxide: Stability in Different Potential Ranges. *Electrochim. Acta* **2017**, *245*, 993–1004.

(27) Wang, L.; Song, F.; Ozouf, G.; Geiger, D.; Morawietz, T.; Handl, M.; Gazdzicki, P.; Beauger, C.; Kaiser, U.; Hiesgen, R.; et al. Improving the Activity and Stability of Ir Catalysts for PEM Electrolyzer Anodes by SnO_2 : Sb Aerogel Supports : Does V Addition Play an Active Role in Electrocatalysis? *J. Mater. Chem. A Mater. energy Sustain.* **2017**, *5*, 3172–3178.

(28) Godinho, K. G.; Walsh, A.; Watson, G. W. Energetic and Electronic Structure Analysis of Intrinsic Defects in SnO 2. *J Phys Chem C* **2009**, *113*, 439–448.

(29) Gurrola, M. P.; Guerra-Balcázar, M.; Álvarez-Contreras, L.; Nava, R.; Ledesma-García, J. High Surface Electrochemical Support Based on Sb-Doped SnO 2. *J. Power Sources* **2013**, *243*, 826–830.

(30) Ozouf, G. PhD Thesis: Electrodes À Base D'aérogels de SnO_2, Résistantes À La Corrosion Pour La Réduction de L'oxygène Dans Les Piles À Combustible À Membrane Échangeuse de Protons (PEMFC), MINES ParisTech, 2017.

(31) Zhang, Z.; Yates, J. T. Band Bending in Semiconductors: Chemical and Physical Consequences at Surfaces and Interfaces. *Chem. Rev.* **2012**, *112* (10), 5520–5551.